MASTER OF SCIENCE IN ENGINEERING DISSERTATION

Design of a UHF Phased Array Ground Station Antenna for Small Satellites

CHARLES GRECH

Supervised by:

DR ING. MARC ANTHONY AZZOPARDI

Co-supervised by:

PROF. ING. VICTOR BUTTIGIEG

*A dissertation submitted in partial fulfilment of the requirements
for the degree of Master of Science in Engineering*

by the

Faculty of Engineering

JUNE 2021

Copyright Notice

Dedication

To my loving wife, parents, brother and sister for their support.

To my children whom I would like to inspire in the pursuit of STEM subjects.

To myself for, four years and thousands of radio hours later, despite the life challenges, getting to this stage.

To the next venture.

73 de 9H1Y

Abstract

Universities and amateur radio communities have been major drivers in the launch of small satellites. These communicate mostly in the VHF and UHF bands with ground stations consisting of mechanically steerable Yagi-Uda antenna systems.

Advances in miniaturization have allowed the more recent trend of launching multiple nanosatellites operating in a similar frequency range. UoMBSat is a 1p PocketQube operating in UHF half-duplex mode designed by the Astrionics Research group at the University of Malta. It is intended to be launched as a 2x2x2 cluster whereby the individual satellites will disperse gradually and must be individually tracked. Such satellite formations pose a new challenge for the conventional ground station which must be capable of distinguishing one satellite from several others in close proximity and identify individual members of a constellation, with capability to possibly track multiple satellites. A system with the capability to electronically steer the beam is required. Phased array antennas (PAAs) allow this to be achieved. They are rarely implemented in small satellite ground stations of this nature due to complexity, cost and the physical challenges associated with the large wavelength.

Constraints and requirements arising from the UoMBSat have been considered and a novel design for a low-cost, functionally-scalable, Geodesic Dome PAA (GDPAA) with a compact footprint is proposed, to meet the general needs of small satellites. A design paradigm for a PAA design for small satellites is proposed and adequately documented to serve as a chronologically optimised sequence of design decisions which other academics interested in implementing a low-cost PAA in their ground stations may consider.

It is demonstrated that if antenna elements are placed in a circular lattice on each face of the icosahedron structure, the overall footprint of the system is reduced by 20% and the overall array performance is improved when compared to the next best triangular lattice counterpart. A low-cost electronics solution utilizing 4-channel Direct Digital Synthesizers is used for phase and amplitude control with reduced complexity. A Python software library to drive the GDPAA has been designed and developed to be interoperable with existing tools and the SatNOGS ground station network. A planar face together with the supporting radome hardware components has been designed and fabricated and measured results are in good agreement with simulations. It is overall demonstrated that a low-cost UHF Phased Array ground station antenna for small satellites is feasible through an active GDPAA with analogue beamforming (BF).

Acknowledgements

First and foremost. I would like to thank two extraordinary gentlemen; my supervisor Dr. Ing. Marc Anthony Azzopardi and my co-supervisor Prof. Ing. Victor Buttigieg for the constant support, source of knowledge and guidance, and for pushing me further in my quest for knowledge. Additionally:

- Other members of the ASTREA team I have had the pleasure of working with; Oliver Vassallo, Dr. Ing. Owen Casha, Ryan Agius, Luke Abela and Aaron Abela;

- Dominic Azzopardi 9H1M, Fortunato Bonnici 9H1ES, Ivan Privitera 9H1PI for imparting the basics and love of amateur radio;

- Dr. Ing. Charles John Betts from the University of Malta's Faculty of Arts for his assistance in carrying out a site survey and providing a total station;

- Dr. Iman Farhat from the University of Malta's Faculty of Science for the ongoing collaboration and genuine interest in this project;

- Emanuele Collica from the University of Malta's Department of Geosciences for his support in carrying out UAV testing;

- Dr. Jon Quick from the Hartebeesthoek Radio Astronomy Observatory for the individual tour of the observatory's equipment, detailed demonstration of the lab and control software, and the inspiration;

- Pierros Papadeas from the Libre Space Foundation for the ongoing collaboration;

- The Dean of the Faulty of Engineering Prof. Ing. Andrew Sammut and other staff who have supported me along the process.

Last but not least, I would like to thank my wife Olesya who, as many partners of radio amateurs will probably attest, has seen a lot of "Charles and his radios", witnessing the washroom repurposed as a radio shack full of antennas, gadgets and gizmos.

Table of Contents

List of Figures

List of Tables

List of Abbreviations

ADC	Analogue to Digital Converter
AOS	Acquisition Of Signal
AR	Axial Ratio
BB	Baseband
BER	Bit Error Rate
BF	Beamforming
BFN	Beamforming Network
COTS	Commercial-Off-The-Shelf
CP	Circular Polarization
DAC	Digital to Analogue Converter
DOA	Direction of Arrival
ECB	Element Control Board
ECSS	European Cooperation for Space Standardization
EIRP	Effective Isotropically Radiated Power
EM	Electromagnetic
ESA	Electrically Small Antenna
ETPA	Equilateral Triangle Patch Antenna
FDS	Frequency Domain Solver
FNBW	First Null Beamwidth
FSK	Frequency-shift Keying
GDPAA	Geodesic Dome Phased Array Antenna
GENSO	Global Education Network for Satellite Operations
GFRP	Glass Fibre Reinforced Polymer
GS	Ground Station
GSaaS	Ground Station as a Service
GSN	Ground Station Network

HPBW	Half-Power Beamwidth
IF	Intermediate Frequency
ITU	International Communication Union
LEO	Low Earth Orbit
LHCP	Left-Handed Circularly Polarized
LNA	Low Noise Amplifier
LOS	Loss of Signal
GSaS	Ground Station As a Service
MCU	Microcontroller Unit
MIT	Mesh Independence Testing
NORAD	North American Air Defense Command
PAA	Phased Array Antenna
PF	Planar Face
PPM	Part Per Million
PSD	Power Spectral Density
RF	Radio Frequency
RHCP	Right-Handed Circularly Polarized
SDR	Software Defined Radio
SGP	Simplified General Perturbation
SLL	Side Lobe Level
SNR	Signal-to-Noise Ratio
SPAA	Spherical Phased Array Antenna
SSO	Sun-Synchronous Orbit
TCXO	Temperature Controlled Oscillator
TLE	Two-Line Element
TNC	Terminal Node Controller
TPA	Triangular Patch Antenna

TR	Truncation Ratio
T/R	Transmit/Receive
TS	Transient Solver
TT&C	Telemetry, Tracking and Command
UAV	Unmanned Aerial Vehicle
UCA	Uniform Circular Array
ULA	Uniform Linear Array
URA	Uniform Rectangular Array
VNA	Vector Network Analyzer
VSWR	Voltage Standing Wave Ratio
VTGS	Virginia Tech Ground Station

Glossary of Symbols

E   Electric field strength

H   Magnetic field strength

Γ Voltage reflection coefficient

ε Permittivity

θ Elevation angle in Ludwig 3 coordinate system

λ Free-space wavelength

μ Permeability

$\hat{\rho}_w$ Unit vector of an incident (incoming) wave

$\hat{\rho}_{gs}$ Unit vector of the receiving ground station antenna

φ Azimuth Angle in Ludwig 3 coordinate system

ψ_p variable angle between $\hat{\rho}_w$ and $\hat{\rho}_{gs}$

Chapter 1: Introduction

The purpose of this chapter is to familiarize the reader with sufficient background and context of the area of study; the design of a UHF phased array ground station antenna for small satellites. The research problem, boundary and project objectives are presented together with what the reader is to expect from this dissertation.

1.1 Background

Since the turn of the millennium, improvements in miniaturization have allowed various players to enter the market of launching satellites with a smaller form factor. What used to be a daughter satellite launched with a main satellite is now a mission in itself. In 1999 the California Polytechnic State University's Multidisciplinary Space Technology Laboratory and Stanford's Space Systems Development Laboratory jointly created the CubeSat standard for nanosatellites with a wet mass of less than 10kg [1]. The original purpose of such a standard was for academic purposes to allow students to witness the development and launch life cycle of a satellite [2].

The standard also had the advantages of standardizing the physical features of small satellites into units of 10×10×10 cm together with other safety requirements [3] and the standard was adopted worldwide. As a result of a common standard, rocket launch companies capitalized on the opportunity to start offering launch services for smaller satellites conformant to the standard.

Universities and amateur radio communities have always been main players in the launch of small satellites communicating primarily in the VHF and lower UHF bands. During the first ten years of the millennium there were one hundred projects worldwide involving small satellites [4]. During the following ten years this amount has gone up by one order of magnitude [5]. Almost all these satellites are using the CubeSat standard or derivatives. This amount is predicted to further increase threefold over the next six years [6] as per Figure 1.1. Apart from universities and amateur communities there is also significant interest and traction in small satellites by civil governments, the military and the general commercial community who have realised the potential of small satellites [7]. Ground Station Networks (GSNs) such as Genso or SatNOGS have come into existence which facilitate the tracking of

satellites via various ground stations which are commonly shared to provide enhanced coverage.

This miniaturization and the ecosystem created around it allows swarms of satellites to be launched to achieve increased global coverage and a significant improvement in temporal resolution of targets. It is of particular interest to note that over twenty nanosatellite constellations have been launched to date with various planned and announced missions underway [6] as per Figure 1.2. One of these missions is the European Union QB50 project [8] which is managed by the von Karman Institute in Belgium. Thirty-six CubeSats were launched in 2017 bringing together various Universities and institutions across Europe to collaborate on common standards.
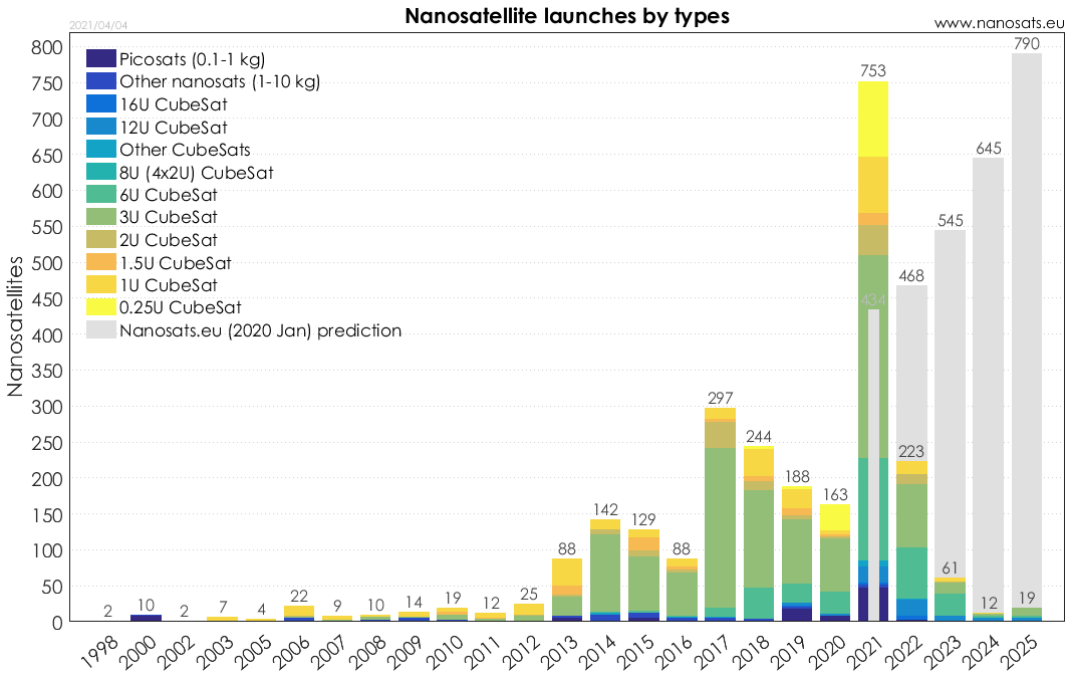
Figure 1.1: Nanosatellite launches by type

UoMBSat is a small satellite being designed by the Astrionics Research group at the University of Malta and will be the first Maltese satellite in space [9]. The project was conceived in 2016 as a 1p PocketQube. The PocketQube standard is a derivate of the CubeSat standard where the satellite measures 5×5×5 cm. The scientific mission of UoMBSat is to measure the electron density of the ionosphere [10], which allows for improvements to be made to ionospheric and space weather models. This provides radio amateurs and the community a source of data for radio propagation predictions. The project has recently been funded and evolved to consist of a constellation of small satellites whose purpose is to collect telemetry on the

performance of electrical components in space. To achieve economies of scale in launch costs, the mission will be launched as a CubeSat 1U (10×10×10 cm) in a 2×2×2 cluster. Gradually, the individual satellites will disperse and must be individually tracked.
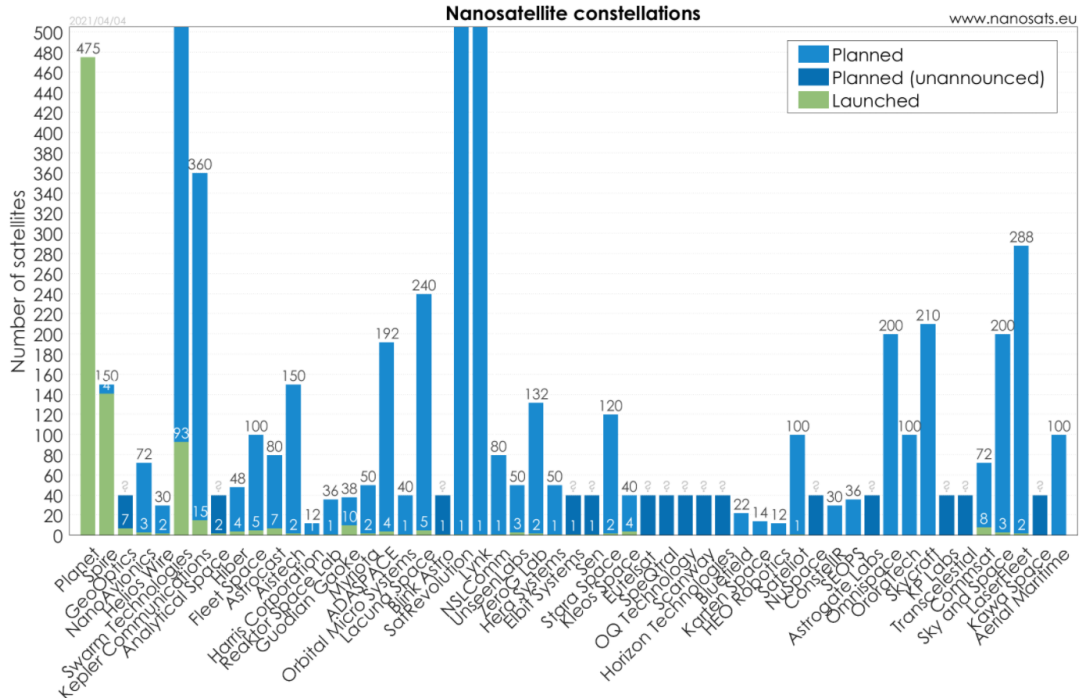
Figure 1.2: Nanosatellite constellations

One of the main challenges for universities in launching a small satellite is the cost of launch, which is estimated to be in the region of twenty-five thousand Euros for a 1p PocketQube [11]. For satellite missions requiring more than one satellite to form a constellation, it is more viable to launch multiples of eight nanosatellites simultaneously which fit exactly in the size of a 1U CubeSat to achieve economies of scale. CubeSats and PocketQubes will be referred to as small satellites in this dissertation. The study in this dissertation is applicable for all satellites operating in the UHF 70cm band, however UoMBSat is the main mission considered in this study.

1.2 Motivations

A constant challenge for all ground station (GS) satellite operators regardless of satellite size is to determine the location of the satellite. This problem augments itself with small satellite constellations which are launched simultaneously in a similar frequency range. The GS must be capable to recognize between its different satellites and between others in a group before the first estimation of Two-Line Elements (TLEs) is provided by the launch provider [12] or by the North American

Air Defense Command (NORAD), which subsequently allows the ground station to accurately predict the trajectory of the satellite.

The TLE acquisition time, defined as the time between launch of the small satellite from the rocket and the time it takes for the TLE to be published, is proportionate to the size of the satellite, with larger satellites being acquired first [13]. Whilst the average TLE acquisition time is less than a day for small satellites there are cases where the TLEs take several days to be provided, leaving the GS operator without knowledge about the whereabouts of the satellite and hence unable to communicate with it accordingly.

A conventional GS comprises typically of a low-cost system built with Commercial-Off-The-Shelf (COTS) hardware connecting mechanically steerable Yagi-Uda antennas to computers via a Terminal Node Controller (TNC) such as [14, 15]. Such systems have served and continue to serve the needs of the community for many years however they are limited to tracking single satellites as long as the TLE of the satellite is publicly available. As small satellite constellations become more mainstream, the traditional mechanically steerable antenna does not serve all the needs of the modern ground station.

An alternative to the traditional mechanically steerable antenna is a Phased Array Antenna (PAA). In its simplest form, the concept of a phased array is a system comprising of multiple antennas whereby the phase of different waves received at the different elements may be modified via the introduction of specific time delays. As a result, through careful selection of the phase, the signals may be combined in a way that the direction the antenna points to can be altered electronically without any physical movement.

The fact that PAAs have no moving parts makes them particularly useful at tracking multiple spacecraft simultaneously especially when satellites are launched and are still not catalogued. At that stage, GS operators have a desperate need to know where to point their antennas to gain control over their satellites. PAAs allows the hemisphere to be scanned in seconds, something which is not possible with mechanically steerable antennas.

The property of having no moving parts results in less wear and tear requiring less maintenance. PAAs are more tolerant to the high wind speeds that the identified ground station site is subject to. GSs tracking multiple satellites will operate mostly

in an unattended mode, so PAAs offer additional resilience due to their capability of graceful degradation whereby if one component malfunctions the system remains online with reduced performance. Arrays offer significant directionality and gain resulting in an improvement of the Signal-to-Noise Ratio (SNR). This is particularly desired for downlink communication due to the low Effective Isotropically Radiated Power (EIRP) emitted from small satellites and large propagation losses as a result of the distance of the satellite to the GS. Advanced beam steering implementations allow the cancellation of unwanted signals via interference suppression which also have a positive effect on the SNR.

On the other hand, PAAs have various challenges. The costs of PAAs are prohibitive. They are more complex to manufacture requiring various Transmit/Receive (T/R) modules requiring synchronization sharing a common sampling clock. Calibration between elements is required such that the progressive phase shift between shifters is equal. They may require a larger footprint depending on the frequency of operation and number of elements.

The UHF amateur satellite band of 435 MHz - 438 MHz, also referred to as P-Band, has always been a popular choice as an operating frequency for small satellites due to the lower cost of the underlying electronics and instrumentation. This band has a higher tolerance for manufacturing precision when compared to its S, C and X-Band counterparts. However, due to its large wavelength of 70 cm, additional complexities are added. Since many antennas are required for PAA geometries capable of full hemispherical coverage, the resulting PAA operating in this frequency band may be rather large occupying a footprint which may not always be available or practical. This is the case for the University of Malta's UoMBSat GS.

Whilst various PAA architectures and implementations are available [16-18], the majority of PAAs and BF applications in the literature are focused on operating frequencies in the S, C and X-Bands with few exceptions [19-21]. A gap has been identified in the lack of availability of a low-cost GS PAA capable of scanning and tracking multiple small satellites simultaneously in P-Band.

1.3 Project Objectives

The main objectives which define the research boundary are to:

- identify the main design constraints in the construction of a GS PAA including UoMBSat mission requirements and site selection;

- design a low-cost PAA architecture within the identified constraints including identifying underlying components;

- design the system in a way that it is repeatable and easily reconstructable at other GS locations;

- document the design paradigm used in the design of the various PAA elements to provide perspective to other researchers tackling the design of a GS PAA;

- design and build the individual antenna element required for the PAA architecture, together with a fully functional higher-level building block;

- design and develop the underlying software libraries required to drive the PAA and perform the required beam steering with ancillary functions;

- ensure the PAA is designed in line with other University of Malta initiatives to ensure one final homogenous satellite communication system;

- integrate the controlling software of the PAA into Ground Station Networks

- to determine whether it is indeed possible to construct a low-cost PAA system which is capable of scanning and tracking multiple small satellites simultaneously in P-Band

1.4 Thesis Outline

This dissertation is divided into five subsequent chapters.

Chapter 2 discusses the *literature review* carried out during this study. The chapter introduction explains in more detail how the chapter is structured and the chapter ends with the conclusions derived from the research carried out. The antenna theory relevant to this dissertation is presented together with various findings of relevance.

Chapter 3 deals with the entire system *design* of the PAA. A design paradigm is presented, and the entire chapter adheres to the flow presented in the paradigm. First the mission requirements and constraints are identified and an appropriate site for the GS is selected. Several steps then follow. The appropriate geometry is selected. The problem is then broken down into smaller components and tackled in a logical order. All relevant mechanical, electrical and software components in scope are designed and prototyped.

Chapter 4 presents the *testing methodology*. The tools used within the study are described, and the methods used to ensure the reliability of results are presented which include a Mesh Independence study and antenna simulations. Various tests are designed and discussed.

Chapter 5 presents the *results* and discusses findings and observations. With knowledge of the system performance, a final link budget is presented together with a project cost estimate workings. The requirements established in the beginning of the design chapter are presented with a summary of how they have been achieved.

The *conclusion* is presented in Chapter 6, with a summary of main contributions and list of items that may be considered for future work. Documentation for the developed software library and its code are included in the appendices. Every attempt has been made to illustrate the concepts being explained pictorially through diagrams to facilitate the reading of this dissertation.

Chapter 2: Background and Literature Review

In this chapter an overview of the available technologies together with associated antenna theories will be presented. The chapter contains five sections as per Figure 2.1.

Figure 2.1: Section structure of literature review

The relevant associated theory is first presented followed by the existing ground station scenario through a review of conventional ground stations, outlining the emerging needs. The state of the art in terms of ground station development is presented, followed by a review of phased array antennas which includes planar face configurations as the building block of phased array antennas. Finally the review hones into the individual antenna elements forming such planar faces. Where possible, relevant concepts and theory is presented in-situ within an applied context to make it easier to comprehend the material being presented.

In this study, the nomenclature selected for frequency band representation is the IEEE Standard Letter Designations for Radar-Frequency bands, as opposed to the nomenclature of the International Telecommunication Union (ITU). The reason is that it is more granular and narrows down a band to a narrower frequency range giving more context to discussion point. The bands are reproduced in Table 2.1 for ease of reference.

Band Designation	Nominal frequency range
VHF	30-300 MHz
UHF	300-1000 MHz
L	1-2 GHz
S	2-4 GHz
C	4-8 GHz
X	8-12 GHz
Ku	12-18 GHz
K	18-27 GHz
Ka	27-40 GHz

Table 2.1: Extract of IEEE Standard Letter Designations for Radar-Frequency bands (IEEE Std 521 2019)

Since the operating frequency of 435MHz - 438 MHz falls within the UHF amateur band, it was considered appropriate to not only consider technical papers which have been published, but also material originating from respectable satellite amateur societies such as the Radio Amateur Satellite Corporation (AMSAT) of which the author is a member of the UK branch.

2.1 Antenna Theory

To prepare the reader for the subsequent literature review and discussion, antenna and antenna array theory are first presented. Various antenna parameters and performance measurement techniques are presented which are then utilized to design the PAA and subsequently to conduct a review of the results.

2.1.1 EM Waves and Regions

According to the IEEE standard for definitions of terms for antennas [22], an antenna is "that part of a transmitting or receiving system that is designed to radiate or to receive electromagnetic waves". Electromagnetic (EM) waves consist of electrical waves travelling together with an orthogonal magnetic wave component and a common frequency as per Figure 2.2. E and H are the electric and magnetic field strengths respectively and λ is the wavelength of the travelling wave.
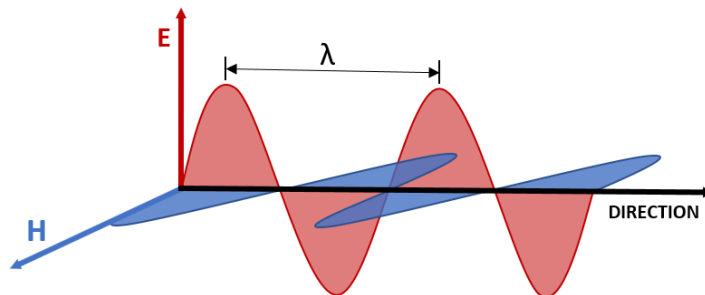
Figure 2.2: Electromagnetic waves

When an EM wave is emitted from an antenna, the electric and magnetic fields are not yet in phase with each other, a property which is required for EM propagation. In Figure 2.2 it is assumed that the electric and magnetic fields are orthogonal travelling on fixed planes. This is not always the case, depending on the distance from the antenna. The EM fields around an antenna are divided into three regions:

- Reactive Near Field is the region where the reactive fields dominate, and E and H fields are out of phase;

- Radiating Near Field (Fresnel Region) is the region where the radiation field dominates;

- Far Field (Fraunhofer Region) is the region most distant from the antenna where both E and H fields are orthogonal to each other and the region is dominated by radiated fields. For the wave to have reached a far field distance the following three conditions must be satisfied [23]:

$$R > \frac{2D^2}{\lambda} \tag{2.1}$$

$$R > 5D \tag{2.2}$$

$$R > 1.6\,\lambda \tag{2.3}$$

where R is the boundary of the far field, D is the maximum linear dimension of the antenna and λ is the wavelength of operation, all values in metres. At UHF frequency, the satellite will certainly be in the far field of a UHF antenna, hence the wave being received at the ground station and throughout this study is considered to have the properties of a plane wave. The wavelength may be derived through the electromagnetic wave velocity formula:

$$c = \lambda f \tag{2.4}$$

where the physical constant c is the speed of light, λ being the wavelength of the frequency of interest and f being the centre frequency.

2.1.2 Antenna Parameters

Polarization

Consider the EM wave of Figure 2.2. The tip of the electric field vector traces a path in a vertical plane with respect to the ground. This is known as vertical polarization. Similarly, a horizontally polarized wave will have its electric field vector travelling horizontally with respect to the ground, with the magnetic counterpart travelling vertically to the ground. The electric field vector may not always travel horizontally or vertically but may follow a continuous rotational path in which case the polarization is classified as Circular Polarization (CP). When travelling towards the observer, if the field vector is turning anti-clockwise then this is Right-Handed Circularly Polarized (RHCP), if turning clockwise then this is Left-Handed Circularly Polarized (LHCP). If the tip of the field vector travels in the shape of an ellipse then the wave is known to be Elliptically Polarized where the same

concept of right-hand and left-hand sense applies. The different types of polarizations are represented in Figure 2.3.
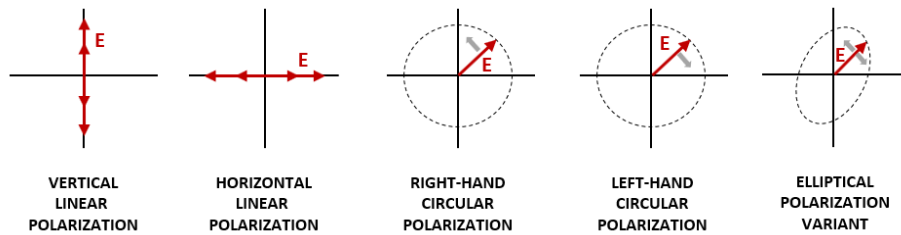
Figure 2.3: Antenna polarization types

For non-linear polarizations, the ratio of the axes is a measure of the quality of CP and is known as the axial ratio (AR). An antenna is considered to have good CP when the AR is 3 dB or less, meaning that there is not more than 3 dB difference between the two axes of the polarization. The AR for a perfectly linearly polarized antenna is therefore infinite.

Understanding the antenna polarization of both the transmitting and receiving antenna will allow the ground station operator to avoid polarization mismatch. This occurs when the plane of the power being transmitted, and the plane of the power being received are at an angle of each other and a power loss occurs. If the angle is 90°, such as is the case for a pair of horizontally and vertically linearized antennas, all power in the transmission plane is not fully absorbed by the receiving plane due to misalignment.
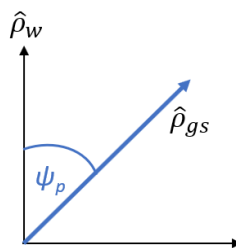
Figure 2.4: Polarization unit vectors

In Figure 2.4 $\hat{\rho}_w$ is the unit vector of an incident (incoming) wave, $\hat{\rho}_{gs}$ the unit vector of the receiving ground station antenna and ψ_p the variable angle between the vectors. The polarization mismatch from misalignment when the vectors are at angle ψ_p may be derived from the polarization loss factor (PLF) calculated as follows [24]:

$$PLF = \left| \hat{\rho}_w \cdot \hat{\rho}_{gs} \right|^2 = \left| \cos \psi_p \right|^2 \tag{2.5}$$

Various values in antenna theory are expressed in Decibels (dB) which is a ratio between signal levels. To convert the PLF of (2.5) to decibels we use the following formula:

$$PLF \ (dB) = 10 \ log_{10} \ PLF \tag{2.6}$$

Polarization mismatch and the PLF are taken into consideration when designing ground stations and calculating link budgets. The Faraday effect is also a contributor to polarization losses as it influences the plane of the polarization. Strong magnetic fields in the Earth's atmosphere change the rotation of the polarization plane. CP is immune to these losses and is hence used in many satellite to GS communications.

Directivity

An antenna may be omni-directional or directional. An omni-directional antenna radiates equally in almost all directions, except for null points. Only an isotropic antenna radiates equally in all directions however it is theoretical and only used as a base on which the directivity of omni-directional and directional may be referenced. A directional antenna radiates the majority of the transmitted power into a certain direction. The maximum directivity D_{max} is expressed as:

$$D_{max} \ = \ \frac{4\pi U}{P_{rad}} \tag{2.7}$$

where U is the radiation intensity in W/solid angle and P_{rad} is the total radiated power in W.

Radiation Lobes

It is particularly useful to express radiation patterns visually, which may include various radiation properties such as power flux density, radiation intensity, field strength, directivity, phase or polarization. These are expressed as polar or cartesian plots in one, two or three dimensions according to the pattern being visualized. Let us analyze the directivity pattern of the elevation plane for a four-by-four element array as a 1D polar plot in Figure 2.5.

A radiation lobe is a portion of the radiation pattern bounded by regions of relatively week radiation intensity [24]. The main lobe is the lobe containing the direction of maximum radiation. The Half-Power Beamwidth (HPBW) is the measured angular distance at the points of the main lobe which is 3 dB less than the

maximum (boresight). In Figure 2.5 the HPBW is 28°. This value is generally used to indicate the general usability of antenna, where the power loss of the antenna from the maximum is not more than 50% (3 dB).
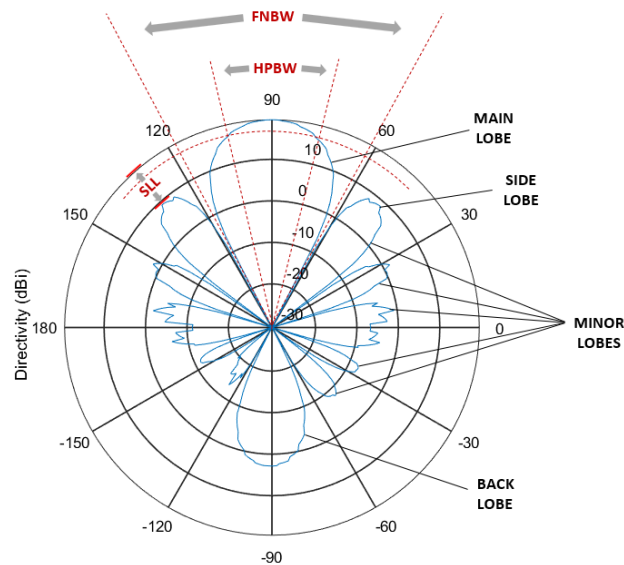
Figure 2.5: Analysis of 1D polar plot of elevation plane directivity pattern

All other lobes are called minor lobes, although these are further classified into side or back lobes. The back lobe is the lobe in the opposite direction of the main lobe whereas all other minor lobes are referred to as minor lobes. Another way of measuring beamwidth is to also measure the angular distance where the first nulls occur, known as the First-Null Beamwidth (FNBW). This value is useful in determining the resolution of an antenna particularly in BF applications. In Figure 2.5 the FNBW is 57°.

With the introduction of phased arrays and the variable of inter-element spacing of antennas, two additional lobe classifications exist [22]. Shoulder lobes are lobes which have merged with the main lobe, and grating lobes are lobes produced by array antennas when the inter-element spacing is sufficiently large to permit the in-phase addition of radiated fields in more than one direction. Grating lobes are very strong sidelobes which can dissipate power in unintended directions and are prevented through the careful selection of inter-element spacing in phased array antennas [25].

Side Lobe Levels (SLLs) must also be considered by the antenna designer. The maximum SLL is the relative directivity of the highest sidelobe with respect to the maximum directivity of the antenna. In Figure 2.5 the directivity of the main and side lobes is 19 dBi and of 9 dBi respectively. This means the side lobe level is

$-10\,\text{dB}$ which is not considered desirable in many applications, the minimum required being at least -20 dB [24].

The radiation patterns for when antennas receive and transmit are the same through the property of reciprocity. This is particularly useful as the study of antenna receive and transmission properties is interchangeable. The Lorentz reciprocity theorem states that the current and voltage read at any two nodes is interchangeable and [26] concludes that the potential induced at the terminals of one antenna due to a current applied to a second antenna is equal to the potential induced in the second antenna by the same current applied to the first antenna.

Impedance and Resonance

Antenna impedance is one of the most important design parameters for an antenna. It is a vector representing the scalar quantities of resistance (R) and reactance (X) and expresses the ratio of voltage to current. Impedance Z is represented in Figure 2.6. It is calculated through the following formula:

$$Z = \sqrt{R^2 + X^2} \tag{2.8}$$
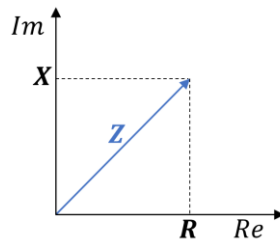
Figure 2.6: Impedance

The resistance is the real part and represents how much power is radiated or absorbed by the antenna. It is constant and does not vary with frequency. It is the sum of the radiation resistance R_r caused by the electrical resistance at the antenna's feedpoint and the loss resistance R_L because of ohmic losses in the antenna:

$$R = R_r + R_L \tag{2.9}$$

The reactance part on the other hand is an imaginary component as it represents the phase shift between the current and voltage which normally are orthogonal to each other in an EM wave. Reactance varies with frequency and is derived from the difference between the inductive reactance X_L and the capacitive X_C reactance:

$$X = X_L - X_C \tag{2.10}$$

14

When the capacitive and inductive reactances cancel each other resulting in zero reactance, the impedance consists of only a resistance component and the antenna is at resonance. This occurs when the length of an antenna is a multiple of a quarter of a wavelength. When an antenna is resonant it will radiate the maximum power, which is desirable.

Permittivity

For certain antennas such as patch antennas a substrate such as FR4 glass-reinforced epoxy laminate material or Alumina may be used. The permittivity property of dielectric materials opposes the radiated E-fields effectively lowering the speed of propagation and corresponding wavelength. As a result, when designing a resonant antenna, the wavelength λ is replaced by the effective wavelength λ_{eff} which takes into consideration the permittivity of the substrate in use. Permittivity is expressed as the relative permittivity ε_r relative to free space. The effective wavelength λ_{eff} is calculated using (2.11).

$$\lambda_{eff} = \frac{\lambda}{\sqrt{\varepsilon_r}} \tag{2.11}$$

Reflection Coefficient and VSWR

Radio Frequency (RF) antennas are designed in such a way that the antenna, the radio (receiver and/or transmitter) and the transmission line connecting the antenna and radio are all matched to the same impedance to reduce power loss through reflection. The Voltage Standing Wave Ratio (VSWR) is a parameter which measures exactly how well the impedance is matched. It is derived from the reflection coefficient, Γ, which is used to determine how much power is reflected by the antenna as a result of impedance continuity. It may be calculated through the ratio of the incident to reflected voltage or power if known. Alternatively, it is calculated with the antenna input impedance Z_{in} and characteristic impedance of the transmission line Z_0:

$$\Gamma = \left| \frac{Z_{in} - Z_0}{Z_{in} + Z_0} \right| \tag{2.12}$$

The VSWR is subsequently calculated as a ratio of the difference between the maximum and minimum amplitude of the reflected voltage wave as follows:

$$VSWR = \frac{1 + |\Gamma|}{1 - |\Gamma|} \tag{2.13}$$

As a rule of thumb, for an antenna to be usable it must have a VSWR of 2:1 or less. This equates to a reflection coefficient of 0.333 or -9.5 dB where 11% of power is reflected. The frequency range where an antenna operates with a VSWR of 2:1 or less is known as the antenna's bandwidth and is often expressed as a percentage of the center frequency of band, ideally close to resonance. It is also expressed inversely as the Q of the antenna as follows:

$$Q = \frac{f_c}{f_2 - f_1} \tag{2.14}$$

where f_c is the centre frequency, f_2 is the highest usable frequency and f_1 the lowest usable frequency. An antenna with high Q is narrowband and input impedance is sensitive to small frequency fluctuations.

The VSWR of an antenna at a specific frequency can be measured via an SWR meter. It is an inexpensive tool and widely available [27] often as the tool of choice for a radio amateur to tune an antenna to resonant frequency. An antenna spectrum analyzer as per Figure 2.8a may also be used which is more sophisticated as it can transmit a low-level output signal and via a directional coupler measures the reflected signal at each step. Such analyzers are also not expensive.

Efficiency and Gain

To assess how much power is being radiated from the antenna, the total efficiency e_0 must be calculated taking into consideration the reflection, conduction and dielectric losses. It can be expressed as:

$$e_0 = e_{cd}(1 - |\Gamma|)^2 \tag{2.15}$$

where e_{cd} is the combined conduction and dielectric efficiency often determined experimentally and Γ is the reflection coefficient [24]. Once the efficiency and directivity are known, the maximum gain G_{max} is calculated by:

$$G_{max} = e_0 D_{max} \tag{2.16}$$

where e_{cd} is the electrical efficiency and D_{max} is the maximum directivity. The gain is a measure which is comprehensive of both directivity and electrical efficiency when compared to an isotropic source.

2.1.3 Mutual Coupling

When the antenna system consists of more than one antenna, the individual antennas reflect power on one another. This effect is measured via the use of

Scattering (S) Parameters which are used to denote how RF waves propagate through a multiple antenna system where every antenna feed point is a port. S-Parameters express how much power is reflected through every port of the network. They are complex numbers with a real magnitude part and imaginary phase part.

They are commonly expressed in matrices, with each individual parameter taking the format S_{ij} where i is the output port and j is the input port, so S_{ij} would represent the power reflected from port j to port i.

$$\begin{matrix} S_{11} & S_{12} & S_{13} \\ S_{21} & S_{22} & S_{23} \\ S_{31} & S_{32} & S_{33} \end{matrix}$$

PORT 1   PORT 2   PORT 3

Figure 2.7: 3 port network and S-Matrix

In the 3-port network of Figure 2.7 the S_{11}, S_{22} and S_{33} parameters in the matrix diagonal denote the reflection coefficient of ports 1, 2 and 3 respectively. As an example, the VSWR of ports 1, 2 and 3 would be calculated by using the values of S_{11}, S_{22} and S_{33} for Γ respectively. The other S-Parameters are referred to as transmission coefficients because they refer to what happens at one port when it is excited by a signal incident at another port [28]. The difference between power levels expressed as transmission coefficients determines the antenna isolation which is the measure used in determining the mutual coupling.

S-Parameters are measured by a network analyzer which can be scalar, measuring amplitude only, or vector, measuring both amplitude and phase, with Vector Network Analyzers (VNAs) being the most common. High end VNAs, such as the 4-port Rhode & Schwartz ZVA50 model of Figure 2.8b, which is installed in the University of Malta's Electromagnetics Research Group Lab [29], are capable of working with operating frequencies of almost 100 GHz and cost six-digit figures. However, nowadays low-cost VNAs operating up to 3 GHz such as the mini-VNA Tiny of Figure 2.8c is available for a few hundred Euros.
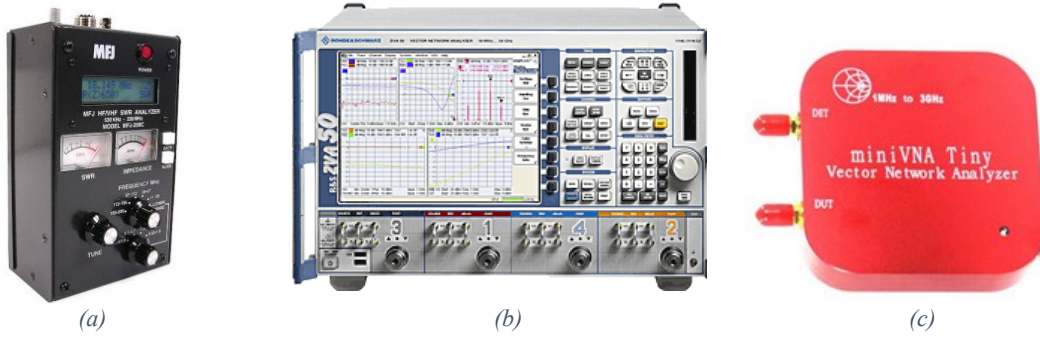
Figure 2.8: Spectrum Analyzer and VNAs (a) MFJ-269D Spectrum analyzer (b) Rohde & Shwartz ZVA50 VNA (c) miniVNA Tiny VNA

2.1.4 Friis Transmission

Now that the reflected and radiated power in an antenna have been investigated it is time to determine what power is received at the receiving antenna at a distance, such as between the ground station and satellite. The maximum power $P_{R,max}$ at the receiving antenna is determined through the Friis equation as follows:

$$P_{R,max} = P_T G_T \left(\frac{\lambda}{4\pi d}\right)^2 G_R \tag{2.17}$$

where P_T and G_T are the power and gain of the transmitting antenna respectively, d is the distance between the antennas and G_R the gain of the receiving antenna.

The factor $(\lambda/4\pi d)^2$ is independently known as the Free Space Path Gain. Its inverse is known as the Free Space Path Loss (FSPL) and is an important component in any link budget calculation of a satellite to ground station communication. It is expressed as follows:

$$FSPL = \left(\frac{4\pi d}{\lambda}\right)^2 \tag{2.18}$$

It is worth mentioning that the Friis transmission equation incorporates in it the gain of both the transmission and receiving antennas which includes electrical losses but not losses due to impedance or polarization mismatches. The Friis transmission equation is summarized by [26] as giving the power delivered to a conjugate-matched receiver in response to a distant transmitter, assuming co-polarized antennas and free space conditions.

2.1.5 Beamforming

Over the years there have been various techniques to steer an antenna's radiation pattern, known as beam steering. A comprehensive review for millimetre wave applications is provided by [30], however in principle they also apply to UHF

applications. The conventional steering technique for ground-satellite communication is mechanical steering which involves physically changing the orientation of the antenna. This is discussed further in Section 2.2.

Let us consider the *n*-element array of Figure 2.9 with five elements where the first element is E_0 and the last element E_4. The elements are separated equally by the distance d in a line on the x-axis. The array is a broadside array, signifying that the boresight of the antennas is perpendicular to the plane of the antennas. A satellite is transmitting a signal with an elevation Direction of Arrival (DOA) angle θ to the boresight (z-axis) of the antenna.
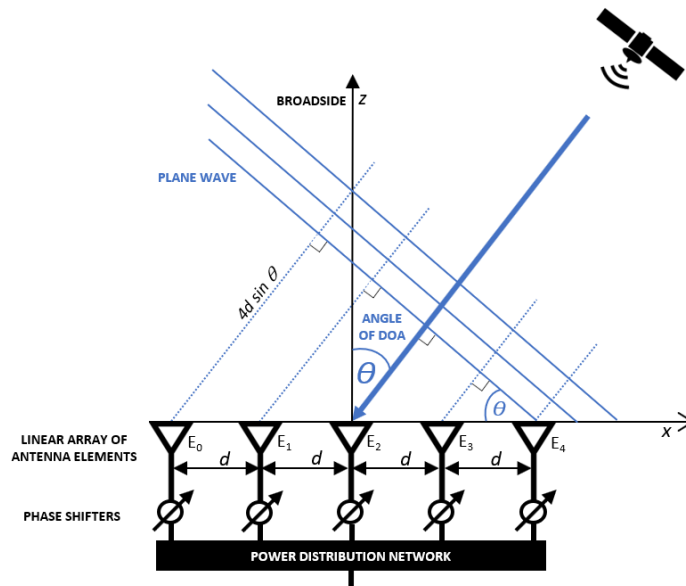
Figure 2.9: ULA and BF concept

Element E_0 is the furthest away from the signal meaning that the signal will first be received by E_4 and last by E_0. For the plane wave to reach element E_0 it will have to travel the additional distance $4d \sin \theta$. This distance may be converted to a fraction of the operating wavelength λ and multiplying further by 360° provides the phase delay φ_n for element E_n.

$$\varphi_n = \frac{dn \sin \Theta}{\lambda} \times 360° \tag{2.19}$$

Since the frequency and waveform of the various waves received on the different elements are identical and the phase difference is constant, the waves are coherent. By introducing a phase shift φ_n delay for every element E_n, as given in (2.19), the waves are delayed in such a manner that they combine when the wave is received at element E_0. This results in *constructive interference* as per Figure 2.10.

On the other hand, noise waves which are picked up randomly from the different elements do not have a constant phase and when summed, on average cancel out each other, resulting in *destructive interference*. [31] concludes that noise that is mutually uncorrelated between the element channels is diminished by a factor of the array size, while correlated components remain unchanged. This coherent amplification behaviour is desirable as the SNR is increased.
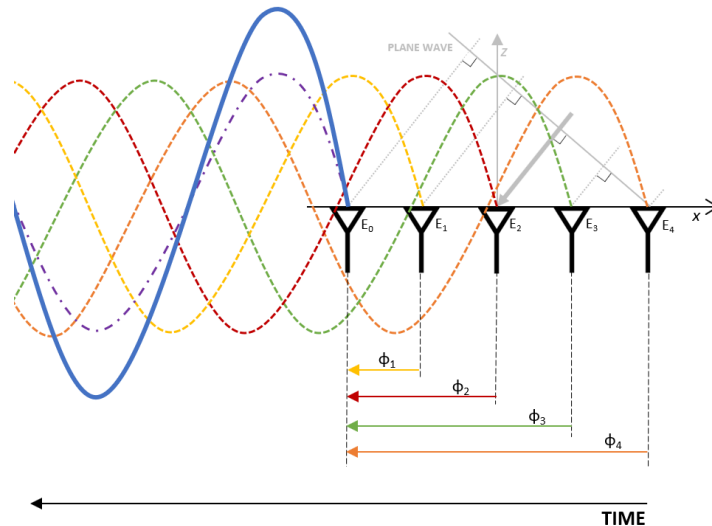
Figure 2.10: Constructive interference

In its simplest form, BF is the principle of placing antenna elements in a specific configuration such that the combined effect of the received waves increases and a main lobe with increased directionality is achieved. Further introducing phase differences between elements as previously described allows the beam to be steered. The concept is summarised in Figure 2.11.
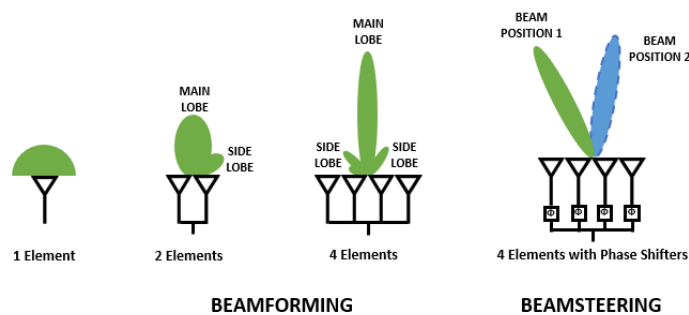
Figure 2.11: BF and beamsteering

One must note that in the workings to derive the phase shift, the frequency is an input variable via the λ parameter. If the waveform of the signal is wideband, the frequency on the edge of the band is significantly different than one on which the phase shift has been calculated and the beam direction changes with the shift of frequency [25]. This concept is known as beam squint.

Both BF and beamsteering functions are commonly referred to collectively as BF and will be referred to in this study as BF. Adding control over the amplitude at an element level allows a system of complex weights to be assigned to each element which are derived through BF algorithms.

2.2 UHF Ground Stations

2.2.1 Conventional Ground Stations

A review of various small satellite ground stations in Europe and beyond [14, 32-42] has been carried out, specifically for amateur satellite tracking which is the application for UoMBSat. Many satellites support more than one band, however it has been found that UHF is the only frequency band supported by all Ground Stations reviewed. This is also demonstrated in Figure 2.12 where it is noted that 59% of small satellites operate on a UHF downlink frequency with 29% of satellites on the 435 MHz - 438 MHz.
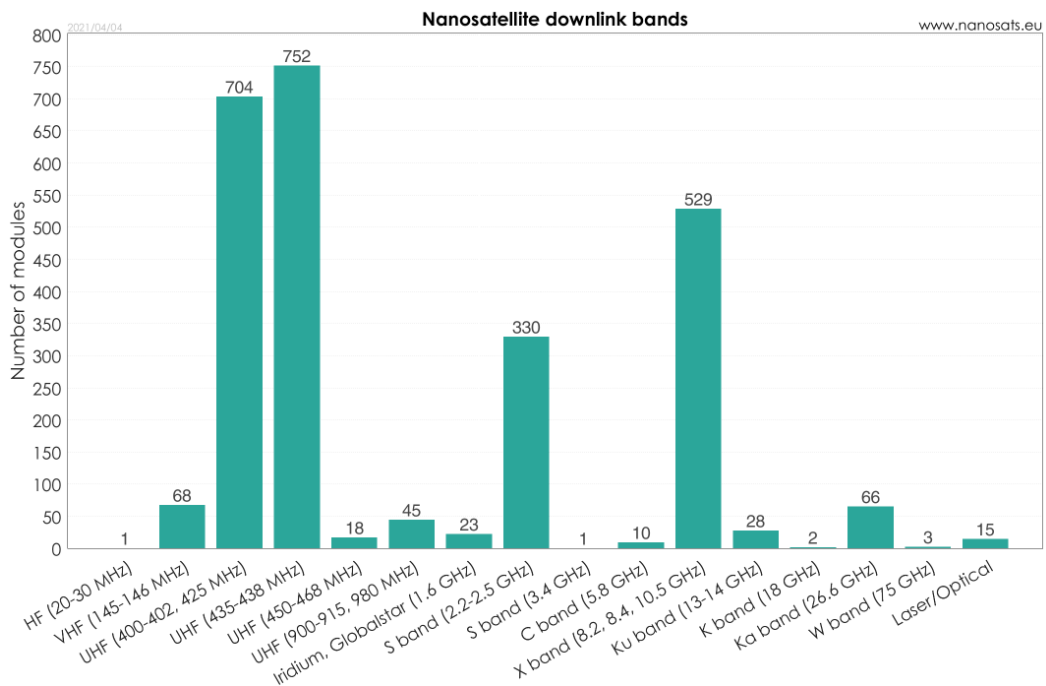
Figure 2.12: Small satellite downlink bands [6]

Ubiquitous use of UHF frequency for small satellite communication with ground stations is justifiable. On one hand, the form factor of small satellites conforming to the CubeSat standard is based on units of 10×10×10 cm, making a full-sized quarter-wave UHF antenna of circa 17 cm possible to be housed on the satellite through a variety of methods. On the other hand, this frequency is not subject to much atmospheric attenuation as at higher frequencies. A wide variety of electronic devices for this frequency are available and generally inexpensive. The

allocated bandwidth at this frequency for satellite applications is typically 25 kHz and has proved to be sufficient for the missions carried out on small satellites to date.

The actual or proposed setup to operate in the UHF frequency is very similar in all reviewed ground stations, represented in Figure 2.13 and explained further in this section, with the exception of [41] whereby a phased array ground station concept has been proposed. This work described in [41] will be discussed later in Sections 2.3 and 2.4.5.
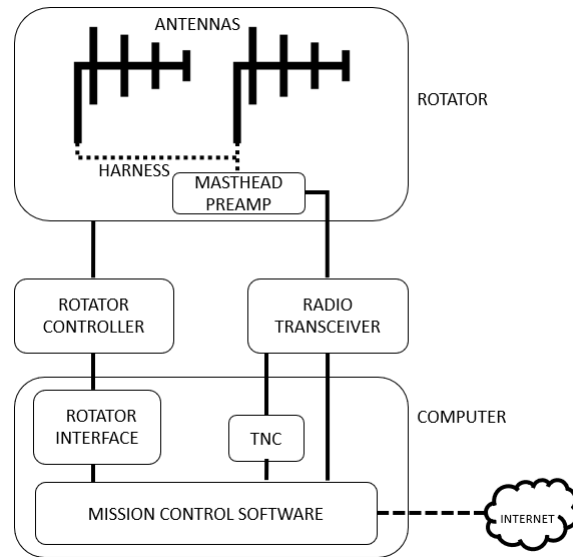
Figure 2.13: Anatomy of a conventional ground station for amateur small satellites

Compared to the other ground stations considered here, the Virginia Tech Ground Station (VTGS) [14] is technologically more advanced, having been built with the intention of evolving into a Ground Station as a Service (GSaaS). As a result, it can support various research and educational missions in satellite communications, radio astronomy and weather applications. The concept of GSaaS will be discussed further in Section 2.2.2.

Antennas

The antenna in use by all ground stations reviewed is a cross-polarized Yagi-Uda antenna with eighteen or more elements, as per Figure 2.14a. Depending on the number of antenna elements in use the gain of the antenna is between 16.2 dBi [36] and 22.0 dBi [34]. Cross-polarized Yagis allow for circular polarization. The polarization sense is generally RHCP however VTGS boasts a duplicated antenna setup for both RHCP and LHCP. The is achieved using a coaxial relay. RHCP/LHCP sense-selectable functionality is selected depending on the mission at hand. A polarization selector may also be used [36].

Harness

A phase harness is connected directly to the two Yagi antennas in orthogonal format to create a crossed Yagi. Its purpose is to insert a delay line, shifting the signal of one of the antennas by 90° to bring both components in phase creating RHCP or LHCP depending on how the harness is connected.

Masthead Preamp

The purpose of the masthead preamp is not to simply perform amplification of both signal (and noise), but to improve the quality of the signal especially if the distance between the antenna and the electronics is significant due to the radio shack not being in the vicinity of the antenna. This is done by selecting a pre-amplifier that has low noise to improve the (SNR). The overall noise figure is determined by the first device in the system, hence the masthead pre-amplifier is mounted as close as possible to the antenna as long as it is within manufacturer's instructions. The exact specifications of the selected pre-amplifiers are not discussed in many of the works reviewed. However, it is known that the SP-7000 Super Amp GaAsFET Mast-Mounted Preamplifier is a common example of a masthead preamplifier used [38, 40].

Rotator

The antennas are mounted on a rotator which is in turn mounted on a mast as per Figure 2.14a. The rotator of choice in more than half the stations reviewed is the entry-level Yaesu G-5500. It can rotate the antenna both in azimuth (complete turn in 58 s) and elevation (half a turn in 67 s). The pointing accuracy is plus/minus four per cent [43] which is almost 15° in azimuth. A rule of thumb for pointing accuracy is that it is within half the HPBW of the antenna. Consider the Tonna 435 MHz 2x19 Element Yagi antenna [44] in use at [32, 33, 35] as a reference antenna to illustrate this point. The HPBW beamwidth is almost 30°, which makes the G-5500 adequate for use.

More heavy-duty versions such as the G-1000DXA are available, able to rotate the antenna for a complete turn in forty seconds for only azimuth [45]. It is interesting to note that VTGS uses Big-RAS rotators, with pointing accuracy of one

fifth of a degree however with a rotation time of 240 s for a complete azimuth turn [40, 46].

Figure 2.14: Mechanically steerable antenna (a) System comprising of cross-polarized Yagi-Uda antennas on a mast [42] (b) Yaesu G-5500 rotator and controller [43]

Rotator Controller

The rotator normally comes with its own controller which is housed indoors. The purpose of the controller is to control the two motor driven rotors for azimuth and elevation by providing an analogue DC voltage in proportion to the required position of the rotor. The ground stations reviewed using a G-5500 rotator also used the accompanying controller as per Figure 2.14b.

Rotator Interface

The rotator interface allows automated control of the movement of the antenna by providing a bridge between the rotator controller and third-party software application or user. A popular controller interface in use with Yaesu Rotators and Controllers is the Yaesu GS-232 [40, 47].

Mission Control Software

The Mission Control Software is the heart of the ground station system, commanding all peripherals directly or indirectly. Various functions are required, which may generally be classified into three types: pre-pass, real-time and post-pass [37]. Various software is available [48, 49] with programs such as SatPC32 [50] catering for a variety of functions.

Pre-pass

Pre-pass functions revolve around ephemeris calculations to create the trajectory of the satellite which is to be tracked. Typical values will consist of azimuth and elevation of Acquisition of Signal (AOS) and Loss of Signal (LOS),

together with the azimuth and elevation at point of highest elevation. Ephemeris calculations revolve around the use of TLEs, which must not be aged as according to [33] a TLE age of 4 days may result in an angular error of 10° which creates a significant *pointing loss* from ground stations with high directivity. Using Simplified General Perturbation models, SGP4, in the case of LEO satellites with an orbital period of less than 225 minutes, the ephemeris may be derived from the TLE and the latitude, longitude, and altitude of the observing location.

NORAD is responsible for cataloguing space objects and producing TLEs which are made available to the general public via the Space-Track API [51] or through other redistributing sources such as Celestrak [52] or NASA [53]. Various real-time software includes pre-pass functionality.

Real-Time

The main purpose of real-time software is to constantly refresh the pointing direction of the antenna and issue commands to the rotator interface, radio transceiver via computer aided transceiver (CAT) control and TNC to offer the ground station operator full control of the satellite for Telemetry, Tracking and Command (TT&C). For small satellites, the ground station is expected to handle the Doppler Frequency correction. The Doppler Effect is the effect in change of frequency emitted by a moving transmitter in relation to the receiver. If a satellite is approaching the ground station, the frequency of the satellite will be higher whereas if the satellite is moving away from the ground station the frequency will be lower. The frequency can vary by 10 kHz on either side of the centre frequency on Low Earth Orbit (LEO) satellites operating in the UHF band. The Doppler frequency shift may be calculated by first deriving the velocity of the satellite from the TLEs. Whilst the software does these calculations automatically, this may be calculated directly by the GS software developer using an Ephemeris library such as the Python PyEphem astronomy library [54].

A variety of software is available [48, 49] to communicate with other sub-systems and to control the mission. Nova is the most popular software in use by the ground stations reviewed [38-40]. VTGS and other stations [32, 33, 35, 36] make use of GSN software for all downlink functions with certain elements of in-house created software. GSNs will be discussed further in Section 2.2.3.

Post-Pass

The function of software in this category is to provide data processing on downloaded files and provide feedback to any networks such as GSNs. Many times, such functions are embedded within all-encompassing software as described above.

TNC

The TNC in amateur satellite use has the capability of encoding and decoding AX.25 radio packets [55]. AX.25 is a data link layer protocol designed and used by radio amateur operators. Normally, the TNC is software based on a PC via the use of a sound card and an audio interface exists between the TNC and Radio Transceiver. However, hardware versions also exist such as the Kantronics KPC-9612+ [56] which is used in [40].

Radio Transceiver

The radio transceiver block in Figure 2.13 is considered as the set of functionalities which is responsible for amplification, filtering and mixing required to allow signals to be transmitted and received by the ground station. The ICOM brand of radios are the most popular radio transceivers in use; the ICOM 910-H [57] at stations described in [35-37, 39, 40] and ICOM 9100 [58] at stations [32, 33, 42]. Yaesu [59] radios are also in use in stations described in [37, 38, 40].

Alternatively, for more flexibility in the processing of signals and data, a Software Defined Radio (SDR) may be used. An SDR essentially replaces to a large extent the blocks of the hardware layer of a radio transceiver with a software implementation [60, 61]. An SDR requires both an element of hardware such as the Universal Software Radio Peripheral (USRP) Platform by Ettus Research [62] and a software development toolkit that provides signal processing blocks such as GNU Radio [61]. It is found that VTGS and the systems described in [32, 33] utilize an SDR with a combination of Ettus USRP and GNU radio in their ground station setup. Cheap SDR versions are available such as the FUNcube Dongle Pro+ [63], RTL-SDR [64] and HackRF One [65] and are in use by [40] and extensively in Open Source Ground Station Networks discussed in Section 2.2.3.

Computer

A computer or collection of them is required to host the rotator interface, mission control software, TNC and elements of SDR for a fully functional system.

Internet

Finally, an internet connection is required to interface with TLE databases, GSNs and for the uploading/downloading of data as may be required.

2.2.2 Commercial Ground Station Options

Due to the constant increase of missions as per Figure 1.1, several commercial options for ground stations have become available. Companies such as ISISPACE [66] and Alba Orbital [67] are offering a turnkey solution for a dedicated ground station.

The ISISPACE solution costs EUR 62,500 for a VHF/UHF solution with additional cost for S-Band support. A proprietary SDR transceiver is included running GNU Radio. A steerable Yagi antenna system is proposed with a 60 s rotational time for a complete azimuth turn and a rotor pointing accuracy of less than one fifth of a degree. A modest gain of 15.5 dBiC is offered with switchable RHCP and LHCP and commercial bands in similar operating frequencies are also supported. The Alba Orbital solution costs EUR 59,000 for a UHF only solution with additional cost for S-Band support. A high gain UHF Yagi antenna with full rotor control is indicated however no further details are available. For comparison, the cost of purchasing individual components for a basic VHF/UHF ground station for amateur use can cost approximately up to EUR 10,000 [37, 42].

As of recent, both ISISPACE and Alba Orbital have extended the As-A-Service paradigm to their ground station offering. Satellite-as-a-service is offered by ISISPACE [68] and Alba Connect Network [69] for Alba Orbital. Few details are available on the respective websites however GSaaS is a well understood concept whereby a fully managed service is offered allowing the operator to carry out various satellite operations remotely without the burden of building or maintaining a ground station. Additional value is also provided by having a global network of antennas allowing multiple communication windows within one orbit. Amazon Web Services is also active in the GSaaS market through its AWS Ground Station offering [70] and new players such as Leaf Space's Leaf Line product [71]. The concept of having a global network of antennas has been around for many years through several open-source initiatives which will be discussed in the following section.

2.2.3 Open-Source Ground Station Networks

It has been found that there is a common sentiment between ground station operators to increase the level of interoperability between stations [72]. This desire creates the need for standardization and over one hundred standards are in existence by the European Cooperation for Space Standardization (ECSS) alone [73]. The same need has given rise to the supply of GSaaS together with the birth of open-source ground station.

Over the years there have been some initiatives for open-source ground station networks. One that gained significant traction [14, 32, 33, 35, 36] was the Global Education Network for Satellite Operations (GENSO) [74]. Conceived in 2006 the idea was for a network of university and amateur ground stations to be created and that would be made available for remote scheduling via a central server, like the GSaaS concept previously described. It was developed and maintained by the European Space Agency. The GENSO project is no longer operational [75] due to various reasons which according to [33] were the limitations on the hardware imposed and specific integration requirements.

Other initiatives which are underway but do not seem to have gained significant traction from the literature reviewed are the Distributed Ground Station Network [76], ThumbNet [77], and a localised Japanese Ground Station Network [78].

By far the most successful to date is the SatNOGS project [79]. This is one of many initiatives by the Libre Space Foundation [80] whose mission is to promote, advance and develop free technologies and knowledge for space and is involved in various space related initiatives. SatNOGS is a comprehensive solution comprising of all hardware and software components covered in Section 2.2.1 and to date has grown into a network of over one thousand stations of which a quarter are online. The author has created a station with ID 124 [81] in June 2018 and it has been used in conducting various tests over the past three years.

A ground station is first established via the installation of an antenna, SDR and host machine. Via installation of a SatNOGS client, the antenna is controlled (where the antenna is not static) via the 'rotctl' interface from 'hamlib' [82] and observations may be scheduled on one's own station or through any other available station in the network via the SatNOGS online portal. Data received from satellites is

demodulated and returned to the SatNOGS server. Via a SatNOGS user interface the GS operator may view the acquired data. A waterfall display is also available which plots frequency spectrum plotted against time, colour coded to show signal amplitude. An audio file with data may also be downloaded for further processing. The existing functionality allows a station to operate in receive mode, however it is known that the SatNOGS system is also capable of serving as a full TT&C solution in Stand-Alone Client Mode as has been the case [83] for the UPSat [84] satellite developed by the Libre Space Foundation.

The author has had various discussions with directors of the Libre Space Foundation specifically on the scope of integrating the concept of a PAA into the SatNOGS network. SatNOGS are on a constant quest to improve pointing accuracy through various methods by improving on the accuracy of the TLEs obtained from Space-Trak or by even being independent. Adding PAA capability to the SatNOGS network as a scanning node is perceived to add considerable value to the quest of SatNOGS as they do not have such arrays as ground stations to date.

This section has investigated ground stations for small satellites operating in UHF band whereby it is concluded that the conventional antenna system in place consists of a mechanically steerable directional Yagi antenna. For added GS functionality and versatility in operating with constellations, a PAA seems indicated.

2.3 State of the Art

A literature review on the state of the art in terms of PAAs in ground stations has been carried out. This section elaborates further on the most relevant works.

- Kumar et al. [85] present a spherical PAA for satellite applications with very good performance in all directions with 64 helical antennas, however in X-Band. No details are provided on the individual elements. The antenna is built primarily for use on a LEO satellite however the concept may also be utilised for GS use.

- [41] propose a UHF PAA ground station for CubeSat applications with a 1x4 ULA of helix antennas with DBF architecture. This is a very relevant work to the present work to my study however it is designed for the tracking of satellites in the north-south direction only and fails to address hemispherical coverage or alternative geometries were considered out of scope of the study. The system utilizes Ettus SDRs which are relatively expensive.

- Martínez Rodríguez et al. [86] have presented a dodecahedron geodesic array with a DBF architecture for L-Band satellite applications. The array comprises of 60 planar faces each with 15 sub-arrays of 3 elements, with a total of 2700 elements.

- [87] is a very comprehensive work of a geometric design for an L-Band GDPAA for satellite communication and air/space surveillance. The work has been carried out for the US Air Force Satellite Control network in the context of military surveillance for all types of satellites in various orbit types. The dome spans 10 m with 675 flat panel faces, suggesting a high cost. No details are provided on the individual elements although in a related paper [88] it is indicated that a wideband double stacked patch antenna is used.

The above observations are classified in Table 2.2. The intention of this table is to visualize the gap within the study of PAA ground stations for small satellites. Low cost is considered to be in the region of EUR 10,000 with high cost being above EUR 100,000.

Ref	Year	Beam-forming Solution Details	Hemi-spherical Coverage	Antenna Element Details	Footprint	Frequency Band	Cost Estimate	Application Relevance
[85]	2017	Yes	Yes		Small	X	Low	High
[41]	2016	Yes			Small	UHF	Low	High
[86]	2010	Yes	Yes			L	High	High
[87]	2004		Yes			L	High	Medium

Table 2.2 Visual comparison of main topics in relevant works to denote gap pictorially

From Table 2.2 it may be observed that a low-cost ground station for small satellites in UHF frequency with hemispherical coverage based on a PAA has not yet been proposed.

2.4 Phased Array Antennas

Phased array technology has been developing steadily for the past sixty years with the introduction of electronic steering [89] and when one hears of phased array antennas the first thing that comes to mind is huge installations of thousands of elements used for military or other mobile communication applications.

PAAs come in various shapes and forms. Gosh and Sen [90] give an exhaustive survey on array antenna design for millimetre-wave communications [90] PAAs are described through a multiple category approach based on design parameters. This method is adopted and further modified by the author as per Figure 2.15 to better suit the material presented.
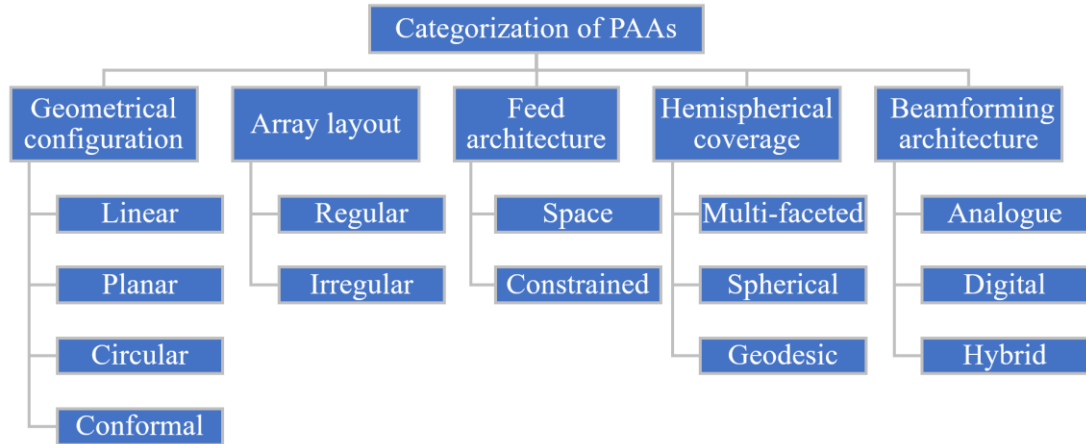
Figure 2.15: Categorization of PAAs into via six different properties; Geometrical configuration, Array layout, Feed architecture, Hemispherical coverage, BF architecture and BF techniques

2.4.1 Geometrical Configuration

Geometrical configurations are broadly divided into four categories: linear, planar, circular and conformal, as shown in Figure 2.16.
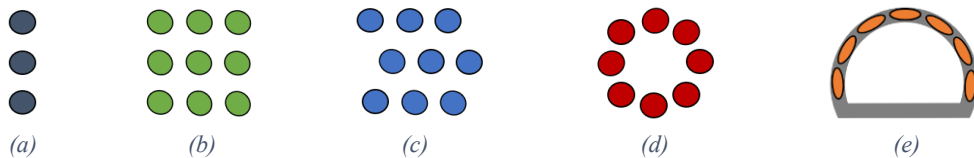
Figure 2.16: Geometrical configurations of PAAs (a) linear (b) rectangular with square lattice (c) rectangular with triangular lattice (d) circular (e) conformal

A linear array consists of several radiating elements along one axis with equal spacing between elements as per Figure 2.16a. It is also known as a Uniform Linear Array (ULA). Its operating principle has already been covered in the Section 2.1.5. They are relatively simple to design and are the building block of many types of arrays. They perform well near the boresight but are limited for satellite tracking use due to their one-dimensional ability in terms of azimuthal scanning and considering they produce a wide pattern in a plane perpendicular to the array axis and a narrow pattern in the plane of the array [91]. They are used in applications such as aircraft control or the military, where only one scanning direction is required with the other direction being mechanically driven. As an example, the Precision Approach Radar

PAR-80 uses a ULA for azimuthal scanning and the air-defence radar AN/FPS-117 uses a ULA for elevation scanning [92].

Planar arrays consist of elements laid out generally in a rectangular lattice which allows for beam forming to be carried out in both azimuth and elevation. They are also known as Uniform Rectangular Arrays (URAs). The elements normally are placed into one of two lattice configurations: square as per Figure 2.16a or triangular as per Figure 2.16b. The spacing between antennas and their geometric lattice arrangement contribute directly to the PAA's radiation properties and have been the subject of various studies such as [93] and [94].
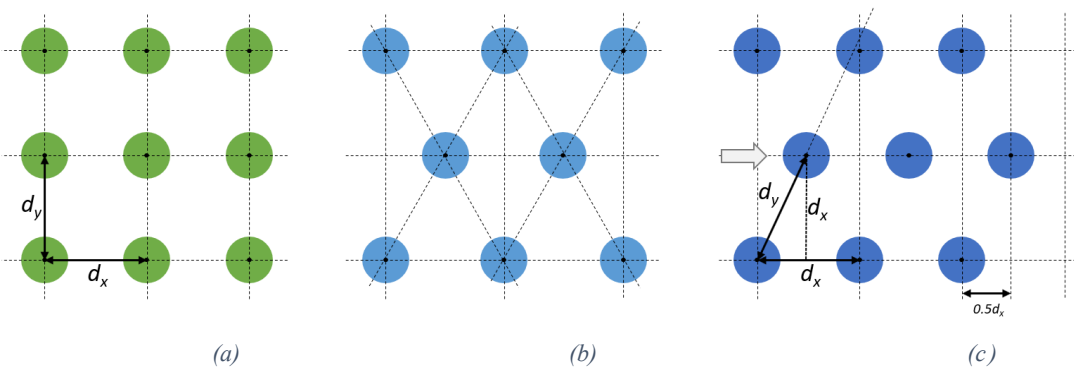
Figure 2.17 Lattice Configuration of URAs (a) Square Lattice (b) Equilateral Triangular Lattice (c) Triangular Lattice with displaced alternate rows

In the square lattice of Figure 2.18a, d_y is equal to d_x with the value being carefully selected as a trade-off between mutual coupling and grating lobes. Way back in 1961, Sharp [93] proposed placing the elements in an equilateral triangle pattern instead of a rectangular pattern as per Figure 2.18b with the intention of reducing the number of elements required. Depending on the positioning of the main beam the number of elements could be reduced by a factor of between 5.7% and 13.4%.

More recently in 2011, Noordin et al. [94] conducted similar work however with the approach of reducing mutual coupling in patch antenna arrays. Multiple techniques exist for mutual coupling reduction of antennas [95] such as introducing defected wall structures [96] or electromagnetic band gap [97] between elements. However Noordin et al. [94] conclude that arranging elements in a triangular lattice as per Figure 2.17c, results in a wider separation of the elements than the square counterpart of Figure 2.17a with mutual coupling reduction technique variants. Instead of re-arranging the whole lattice, it is proposed that alternate layers are

displaced by $0.5d_x$. The area of the footprint of the URA's triangular lattice is increased by $0.5d_x \times d_y$ which is marginal as the array becomes larger. This reduces the need for any additional complexity, leading to better antenna isolation, directivity, and gain.

If the elements are arranged in a concentric layout as per Figure 2.16d, then this is known as a Uniform Circular Array (UCA). If multiple rings are required, then this array is also a type of planar array known as a Planar UCA (PUCA). The advantages of UCAs over ULAs and URAs is due to their symmetrical configuration and their capability to scan azimuthally with minimal changes in the beamwidth and SLLs [94, 98].

Array elements may also be placed on curved or other non-planar surfaces as per Figure 2.16e making them conformal to the surface. Many properties of ULAs, URAs or UCAs still apply, however the radiation patterns are modified as a result of the extent of variation of the antenna elements [99].

2.4.2 Array Layout

The different arrays in the previous section had regular spacing between the different elements, regardless of the geometrical configuration. Such arrays are known as regular arrays.

Irregular arrays on the other hand consist of arrays where the inter-element separation is not fixed. This can be achieved via the irregular spacing of elements derived from some algorithm which demonstrates improvement in the SLL antenna performance for linear [100] or planar [101] arrays or alternatively by utilizing a fixed planar array which may be reconfigured by turning on only specific elements [102]. The complexity in such arrangements is increased. Such configurations are illustrated in Figure 2.18.

(a)   *(b)*   *(c)*
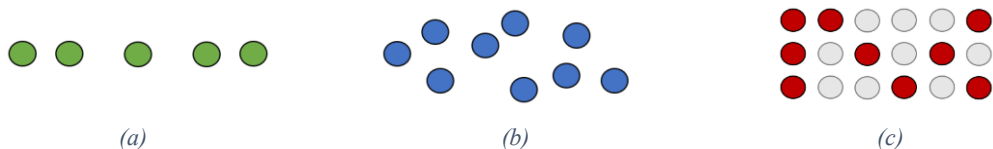
Figure 2.18: Irregular array configurations (a) Fixed irregular linear array (b) Fixed planar irregular array (c) Reconfigurable planar array

2.4.3 Feed Architecture

There are three types of feed architectures for a phased array regardless of type: space, constrained and hybrid feeds [90].

Space feeds

Space feeds uses free-space propagation to distribute power from the signal source to the antenna elements whereas constrained feeds use transmission lines. Figure 2.19a demonstrates the concept where the signal is fed via, for example, a horn antenna and transmitted in free space. Antenna elements are illuminated with the signal, the relative phases are applied and radiated via other elements. Such arrays exhibit less insertion loss however are complex to build as each array channel requires both an illumination and radiating side.
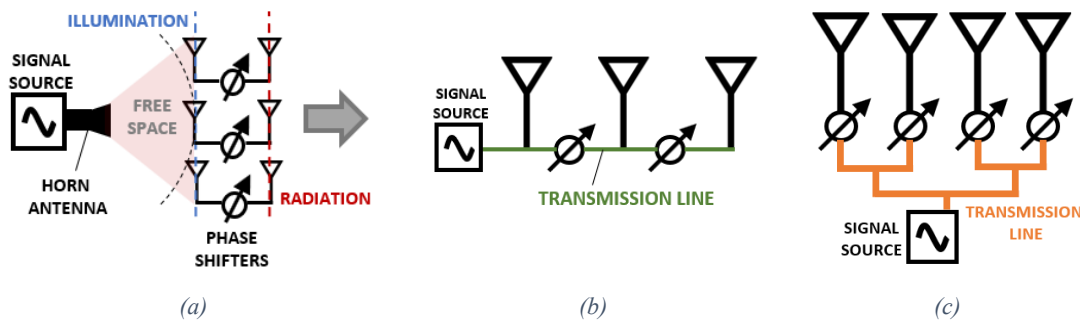
Figure 2.19: PAA Feed architectures (a) Space-fed (Transmission) (b) Constrained series feed (c) Constrained parallel feed

Constrained feeds

Constrained feeds are the most popular feeds for arrays and can be further divided into series or parallel architectures. Series constrained feeds deliver the signal to the individual elements sequentially. There are various applications for this type of architecture and there are various advantages due to the delays introduced in the transmission line including the determination of polarization based on element pattern. However, it is subject to beam squinting due to the progressive phased change between elements [90]. Parallel feeds consist of power combiners/dividers in the transmission line to deliver a signal equal in amplitude and phase to the antennas. Figures 2.2b and c demonstrate the concept of such feeds.

2.4.4 Hemispherical Coverage

The choice of an orbit for a LEO small satellite will largely depend on the mission objectives and payload operational requirements. Polar orbits are orbits where satellites travel past the Earth from North to South, such that the orbit of the satellite must be inclined from the Earth's equator by 90° to achieve near-global coverage [103]. One type of polar orbit is the sun-synchronous orbit (SSO) whereby

the satellite is always in the same fixed relative position to the sun. SSOs are useful due to their property of visiting the same location at the same local time.

Due to the rotation of the Earth, the satellite will be visible to the ground station during various passes as illustrated in Figure 2.20a. The circle marked in yellow depicts the area in for which the satellite is visible to the ground station. This is largely dependent on the altitude of the satellite, altitude of the ground station and assumes that there are no obstacles between the line of sight of the ground station and satellite.

(a)   *(b)*
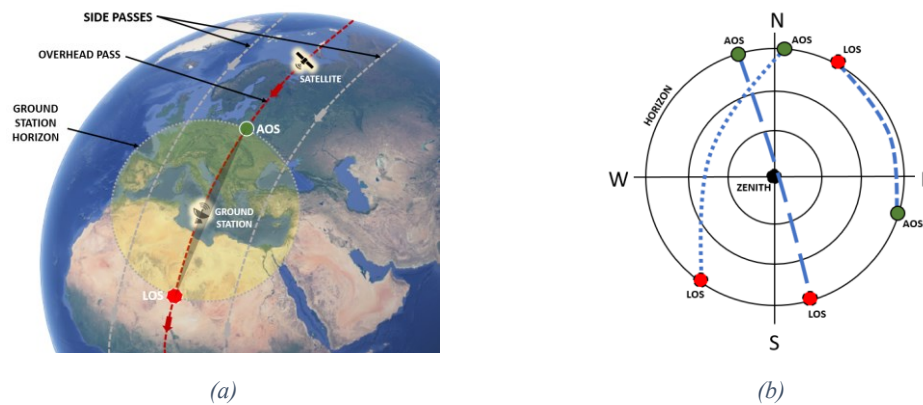
Figure 2.20: Representation of satellite passes (a) Passes view from space (b) Polar plot of sample satellite passes with respect to the ground station

Figure 2.20b depicts three sample passes with respect to the ground station. It may be concluded that for the ground station to be able to track the satellite for all combination of passes, full coverage of the upper hemisphere is required.

(a)   *(b)*   *(c)*   *(d)*   *(e)*
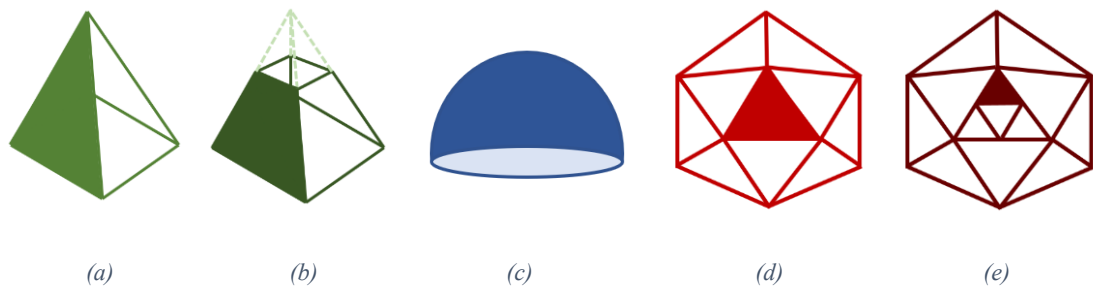
Figure 2.21: PAA geometries providing hemispherical coverage (a) Pyramid faceted (b) Pyramidal frustum faceted (c) Spherical (d) Geodesic: icosahedron (e) Geodesic: icosahedron with subdivision

Let us consider the notion of hemispherical coverage in the context of a PAA, where no moving parts are required. The first approach is to design a system of multiple planar phased arrays placed in a pyramid or pyramidal frustum format as per Figures 2.2a and b. Such formats are discussed in [104, 105], where it is concluded that the larger the number of faces the better the overall PAA performance and the less elements are required on each face. Technology is mainstream and they are easy to manufacture. However, when the scan angle is greater than 60° the radiation

35

performance significantly decreases due to additional mismatch and polarization losses introduced [87].

The second approach is to utilize a Spherical PAA (SPAA) as per Figure 2.21c. The spherical arrangement of elements in SPAAs reduces grating lobes considerably [106] and is also more efficient in terms of radiation than its planar counterparts. It does however pose additional complexities in the mounting of antennas in spherical configuration, although SPAAs at higher frequencies such as X-Band have been built [85], where it is also confirmed that there is good beam formation in all directions. Derivations of spherical geometries such as spheroids or toroids have not been encountered in the literature.

The third approach is to utilize a faceted dome antenna which retains the advantages of a SPAA whilst leveraging existing planar manufacturing technology. By selecting a polyhedron such as an icosahedron (Figure 2.21d), a Geodesic Dome PAA (GDPAA) is created to approximate the properties of a spherical antenna. The sphericity of the GDPAA may be increased by further sub-dividing each face of the polyhedron as per Figure 2.21e. Tomasic et al [88] propose a GDPAA in L-Band based on triangular planar subarrays, arranged in an icosahedral geodesic dome configuration, whereas Sierra- Pérez et al. [107] propose a GDPAA in L-Band based on dodecahedron with faces sub-divided into triangles faces extended onto a cylinder. GDPAAs are covered with a protective radome to avoid degradation of antenna performance because of weather conditions which could make the PAA unusable [108]. Furthermore, it should be noted that the dielectric superstrate of which the radome is manufactured contributes to changes in the resonant frequency, bandwidth, and gain [109].

2.4.5 Beamforming Architecture

BF architectures may be classified into three main categories; analogue, digital and hybrid whereby a variety of techniques may be used to shape the beam or suppress unwanted signals.

Analogue Beamformers

Analogue beamformers are the simplest to implement and are mostly used where there is one RF signal to be received or transmitted and hence one beam of interest.

The signal from each antenna element is phase shifted and the amplitude can also be adjusted in other to set a complex weight, where BF algorithms may be used. Ghosh and Sen [90] further categorize analogue BF architectures depending on where the phase shifter is allocated and hence at which stage the phases are adjusted. Such configurations are possible since the phase shift may be introduced at any stage of the RF signal chain [110].
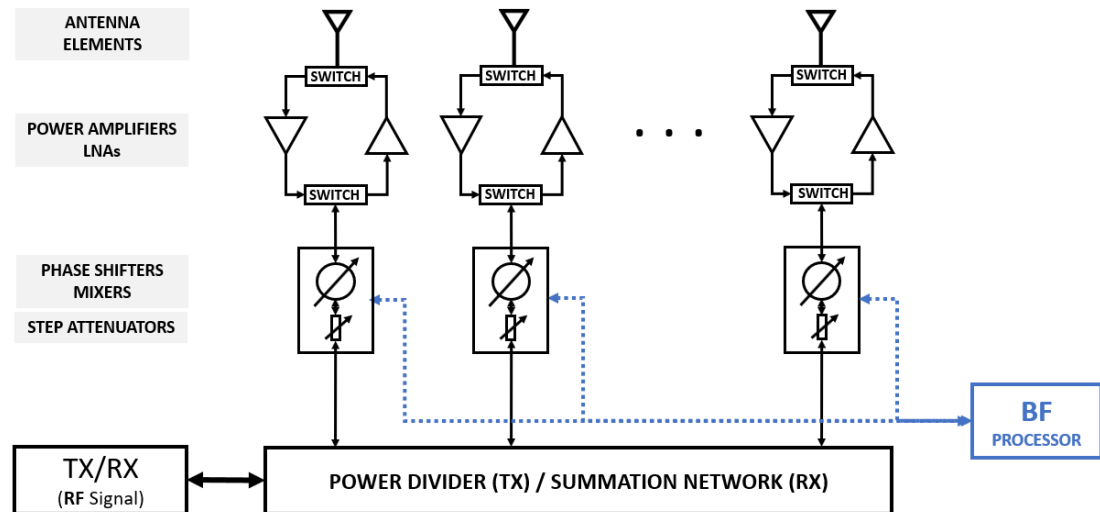
Figure 2.22: Block diagram of an analogue RF beamformer comprising of switches, power amplifiers or LNA, step attenuators and phase shifters for every antenna element, together with a power divider or summation network and BF processor

An Analogue RF Beamformer, as per Figure 2.22, performs phase shifting in the RF domain, with the least number of components required resulting in a lower insertion loss. On the other hand, it has a narrow bandwidth due to the fact that the accuracy of the phase shifters is good only at the centre frequency [30]. Alternatively, the phase shifting may be carried out at the Intermediate Frequency (IF) or Base Band (BB) stage. The bandwidth in these setups increases, however they are subject to increased noise sensitivity from a distributed Local Oscillator (LO) signal. The circuit design must attempt to isolate the LO distribution from other circuitry. The last option is to perform phase shifting at the LO stage where bandwidth performance is also maintained however at the cost of additional mixers amongst others.

Phase shifting can be carried out via the use of commercially available phase shifter hardware modules and may be implemented either using analogue or digital techniques. Analogue phase shifters are controlled through an analog control voltage within a specific range providing a continuous phase shift according to system

specifications. The control line is subject to a lot of noise and digital phase shifters are preferred. Digital phase shifters provide a defined set of phase shifts according to their resolution, typically four to six bits. With a six-bit resolution the phase may be altered in steps of 5.625° which provides poor pointing accuracy for PAA use. Cost-effective phase shifters are offered by main brands such as Analog Devices, Mini-Circuits and Qorvo. Various options are available for operating frequencies in S, C, X, Ku, K and Ka band, however it has been observed that very few options exist in the UHF band.

Alternatively, phase shifting may be caried out via the use of a Digital Direct Synthesizer (DDS). A DDS can create an analogue sine wave from a reference clock, phase accumulator, phase-to-amplitude converter and a DAC with additional phase shifting and amplitude control. A commercially available low-cost DDS is the 4-channel 500MSPS AD9959 chip from Analog Devices. It has a 32-bit frequency tuning word, 14 bits of phase offset and 10-bit DACs. The AD9959 chip has been used in various communication applications and beyond, such as magnetic resonance imaging, the study of quantum systems and design of power supplies. It has been used in a study of a low-cost digital array radar [111] and to build an active PAA [112], both in the S-Band. Jiagua et al. have concluded [112] that DDS-based PAAs have various advantages over their phase shifter and step attenuator counterparts, through the use of the digital beamformer shown in Figure 2.23. These include higher precision and faster amplitude and phase control, avoiding the need for a calibration system for phase shifters and exhibiting low RF loss.

Alternative configurations are possible to perform an element of analogue BF without the needs of phase shifters by using a BF network as previously described or alternatively more novel approaches for ultra-low cost PAAs such as feeding a central element only with the other passive antennas being excited through mutual coupling. Yusuf and Gong [113] have demonstrated that by manually substituting different value capacitors, it is possible to change the reactance of the capacitors loading the passive antennas. It is possible to control the phase shift via the use of varactors.

Digital Beamformers

In digital BF the phase shifting, and subsequent calculation of weights are carried out in software. The main advantage of digital beamformers is their ability to

process multiple copies of the signal dependent on the processing power available. Processing power however increases cost, together with the introduction of an Analogue to Digital Converter (ADC) and Digital to Analogue Converter (DAC) pair for each antenna element. Nonetheless digital BF is used in a variety of applications particularly in mobile communications due to its ability of being able to receive and transmit multiple beams with improved array performance.
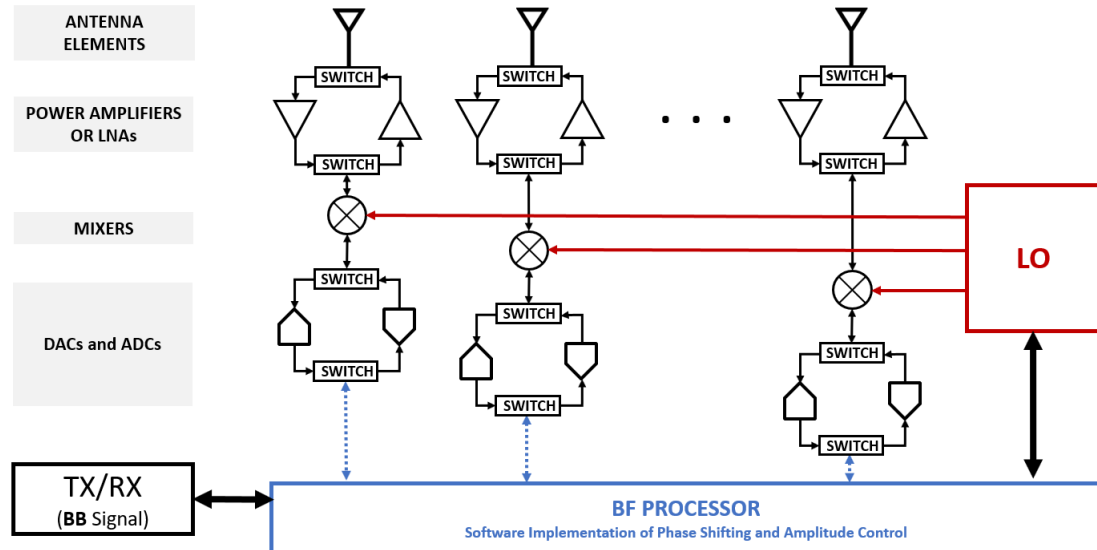
Figure 2.23: Block diagram of a digital beamformer comprising of switches, power amplifiers or LNA, DACs and ADCs for every antenna element, together with a software BF processor

A UHF receiver chain comprising of a ULA of one-by-four crossed loop antennas with a digital beamformer architecture for the tracking of CubeSat applications has been presented by [41]. An SNR improvement of six decibels is noted on the four-element array using Ettus N210 [62] SDRs, however it is indicated that low cost SDRs may be used as long as they are able to be calibrated for phase difference and alignment for coherent processing. A concept of beam-on-demand is also proposed, where a digitized streamed I/Q data set may be provided and consumed as required. Satellite missions would still retain their ground station capabilities for TT&C however subscribe to such beam-on-demand services to extend their reception coverage.

Hybrid Beamformers

Certain architectures are implemented to benefit from both analogue and digital BF. The concept of analogue BF is adopted where the phase shifting is carried out in hardware for each element, however further signal processing is carried out by the BF processor in software.

BF Techniques

BF architectures use time-domain techniques when a time delay to the signals based on the known location of the antenna elements is added to achieve constructive interference. One such technique is the delay-and-sum explained in [114]. BF Networks (BFNs) which consist of parallel feed circuits composed of directional couplers, delay lines, combiners and dividers are arranged in a way to introduce time delays and a fixed set of fixed position beams may be produced. A very common type of BFN is Butler matrix [115]. Crossover couplers consisting of two parallel transmission lines coupled with connecting branch lines between them are used allowing them to be implemented with passive components on a Printed Circuit Board (PCB) significantly reducing cost. The introduction of such time delays allows for constructive interference in the direction of the main beam. The main disadvantage of BFNs is that the time delay circuits are fixed to the design frequency. The general disadvantage of time-domain techniques in general is that the only method to estimate the Direct of Arrival (DOA) of the incoming signal is by iteratively changing the time delay until the constructive interference in the form of an increased power signal is observed.

Alternatively, spectrum-based BF techniques may be used where BF is carried out in the frequency domain instead of the time domain. Time domain functions are converted to frequency-based functions via the Fourier Transform (FT) allowing representation of both the magnitude and phase offset. This allows various spatial signal processing algorithms to be applied for the estimation of DOA. Some of the most common implementations are the Capon, Bartlett and MUSIC beamformers [116].

BF techniques may also be adaptive which, as the name implies, offers the additional feature of being able to sense interfering sources in the environment and adapt the beam pattern accordingly. By modifying both phase shift and gain (via amplitude) of the different antenna elements, a complex weight may be assigned to each antenna element. Through a feedback mechanism to the BF processor, weights may be adjusted adaptively until the margin of error is optimized at which state the system is said to converge. This is possible through adaptive algorithms such as the Least Mean Square and Sample Matrix Inversion algorithms [117]. Weights may also be selected in a manner where a null is placed in the direction of an unwanted

signal on a similar frequency [118], known as null steering. As an alternative to the use of signal processing algorithms, null steering may also be achieved through the selection of antenna elements in an irregular array layout [119]. Satellite communications are generally within line of sight. However, terrestrial interference is higher at lower elevations when the satellite is close to the horizon and interference suppression is more prevalent. Finding the optimal weight selection is and remains an active research field.

Ingram et al. [120] investigate the feasibility of a satellite ground station for LEO in X-Band using adaptive BF to maximize the SNR of the satellite transmission where a measured improvement in SNR is noted. Cheng et al. [121] investigate the use of a Capon beamformer for interference suppression on multi-faceted and hemispherical arrays using dipoles in satellite ground tracking concluding that the concept of PAAs as a substitute to mechanically steered equivalents is very convincing.

2.5 Antenna Elements

In this section various antenna element types will be briefly investigated. They will be classified into four categories depending on their major performance characteristics [23]; electrically small, resonant, broadband and aperture.

2.5.1 Electrically Small Antennas

Electrically small antennas (ESAs) are antennas which are smaller than 10% of the wavelength of the operating frequency. This is mostly used for VHF and lower bands due to the large wavelength size which makes it impractical to construct. As a result, it has a low input resistance and high reactance (capacitive), which may easily be tuned through the insertion of an inductive reactance whose values are derived through the use of (2.8) to (2.10). Monopoles and loop antennas are commonly used ESAs.

(a)   *(b)*
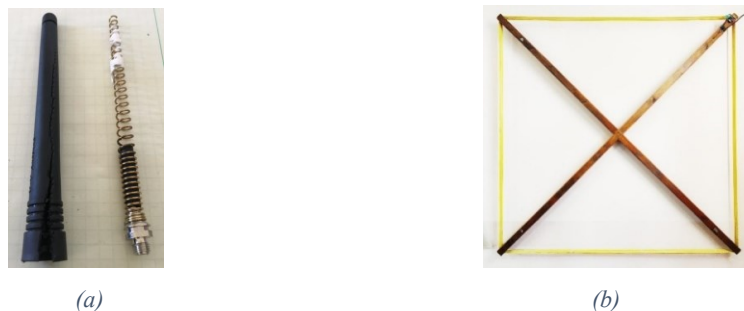
Figure 2.24: Electrically small antennas (a) outside and inside view of a Rubber Ducky coiled monopole antenna in use in VHF/UHF portable radio[115] (b) wire-loop antenna for use in VLF band

The antenna of Figure 2.24a is the stock antenna of the Baofeng UV-5R amateur handheld radio, which consists of a coiled monopole antenna sealed in rubber protection. At 12.5cm length it is approximately $0.06\ \lambda$ for a VHF operating frequency of 144 MHz. Such antennas are present in most handheld radios operating in VHF and UHF frequencies. The antenna of Figure 2.24b is a wire-loop antenna built by the author to monitor Sudden Ionospheric Disturbances on VLF frequencies. With a 1.5 m length it is only $0.00015\ \lambda$ for a VLF operating frequency of 30 kHz. ESAs in general have low efficiency and gain, often below 5 dBi, however are used when it is not practical to build a resonant antenna.

2.5.2 Resonant Antennas

Resonant antennas, as the name implies, are designed for resonance on a particular frequency. They have higher gains than ESAs and have good input impedance on a narrow band of frequencies. Being resonant, the effective length of the antenna is proportionate to the frequency of operation with the same radiation pattern. Quarter-wave and half-wave dipoles, patch, Yagi-Uda and helical antennas all fall under the classification of resonant antennas and are illustrated in Figure 2.25.

Resonant antennas have overall good performance at the frequency they are designed to operate at and are narrowband. Whilst dipoles generally have less than 5 dBi gain, patch antennas typically have 5 dBi to 8 dBi gain, with Yagi-Uda antennas and helicals exceeding 8 dBi according to the geometry of the antenna.

| (a) | (b) | (c) | (d) |
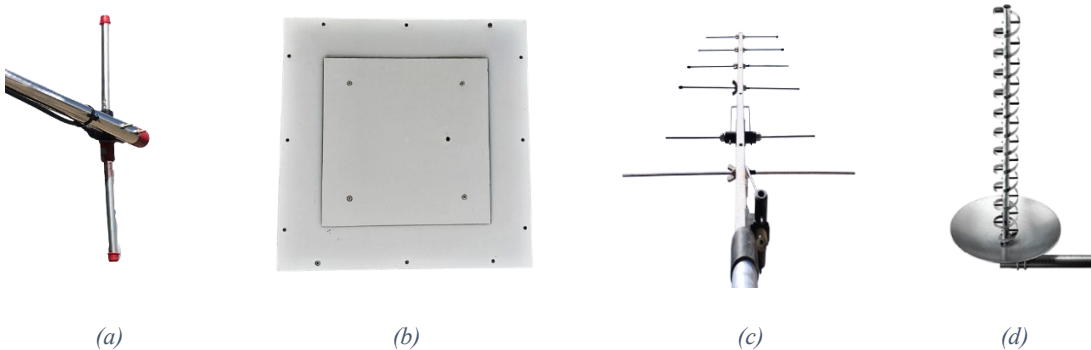
Figure 2.25: Resonant antennas (a) Thunderpole UHF Dipole [121] (b) custom-built UHF aluminium square patch (c) Sandpiper 6- element UHF Yagi-Uda (d) Wade WH14 Series UHF Helical [122]

The geometry of a dipole antenna allows it to be printed and Mirmozafari [123] presents an elegant solution for an S-Band PAA consisting of a ULA of crossed dipoles manufactured on PCB with Rogers laminate. Patch antennas are naturally low-profile and are easily manufactured on PCB for frequencies in S-Band and above [113, 120].

3D printing technology and copper plating techniques are now allowing antennas to be printed. Mirmozafari et al. [124] demonstrate nonplanar S-Band printed dipoles, where a 1×6 ULA is fabricated. Fenn et al. [125] present a solution for a 1×10 ULA of 3D-printed circular microstrip patches in L-Band with copper plating techniques.

2.5.3 Broadband Antennas

Broadband antennas are antennas where many characteristics of their performance remain relatively the same over a wide frequency band and are generally used in television, radar, or radio astronomy. A general rule of thumb for an antenna to classify as a broadband antenna is that it must have certain characteristics including that the beamwidth and VSWR should remain within specified limits over a frequency range of at least an octave.

Log periodic antennas, spirals and fractals are broadband antennas. Log period antennas (Figure 2.26a) function similarly to Yagi-Uda antennas however all the elements are driven giving it a larger bandwidth by comparison. They have good gains generally between 8 dBi and 15 dBi. Spiral antennas on the other hand are very compact antennas with very large bandwidth generally with limited gains of up to 3 dBi however antennas with more moderate gains in the region of 6 dBi to 8 dBi have been proposed such as the antenna in Figure 2.27b [126]. Fractal antennas are also inherently wideband due to their geometrical architecture of self-repeating patterns which makes good use of their property that they could be made to resonate at various frequencies through careful design. The Institute of Space Sciences & Astronomy at the University of Malta has designed an antenna element for an ultra-wideband tightly coupled fractal octagonal Phased Array Antenna [127] as per Figure 2.26c. This will be used in the Square Kilometre Array project, the world's biggest radio telescope.

| (a) | (b) | (c) |
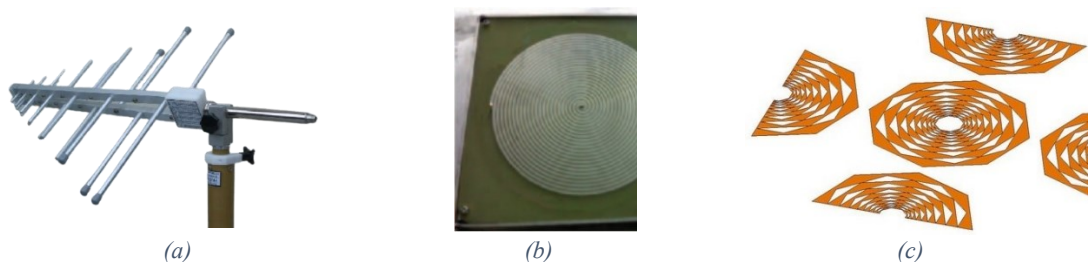
Figure 2.26: Broadband antennas (a) Schwartzbeck UHALP 9108A log periodic 250 MHz -2400 MHz [128] (b) archimedean spiral UHF antenna 300 MHz–4000 MHz [126] (c) fractal octagonal antenna operating in 250 MHz –1250 MHz

2.5.4 Aperture Antennas

Contrary to ESAs, the size of aperture antennas is many times the frequency of use. EM waves flow through a physical aperture. As a result, they offer a good gain of 15 dBi and above, with good bandwidth. Common aperture antennas in use are the horn antenna and the slot antenna. Horn antennas can be used in UHF frequencies and above, although they are mostly used for microwave frequencies due to the physical size requirements. They consist of a waveguide which is terminated into a tapered horn, as per Figure 2.27a and can also be used in conjunction with reflector antennas. Larger reflector antennas can be quite costly and complex however can provide a lot of gain. The radio telescope at the University of Malta of Figure 2.27b is a 5.3m dish antenna with feed horns for L-Band and K-Band and provides a gain of 44 dBi [129].

(a)   (b)   (c)   (d)

Figure 2.27: Aperture Antennas (a) AH Systems SAS-584 Horn Antenna 5.85GHz – 8.20 GHz [130] (b) radio telescope reflector antenna at the Univerisity of Malta (c) Vivaldi antenna [131] (d) Egg-crate structure [132]

Slot antennas are antennas which have a slot embedded in the design from which EM waves are radiated. A common slot antenna is the tapered slot Vivaldi antenna of Figure 2.27c. It is a versatile antenna that can be manufactured from sheet metal or metallized dielectric such as a PCB. Two Vivaldi antennas place in an orthogonal format can be used to achieved circular polarization. To achieve an array configuration, elements are placed in an 'egg-crate' format as per Figure 2.27d where rows and columns fit together in interlocking slots [132]. The arising complexities are to ensure that the ground plane is continuous and replacing an element in the case of maintenance or fault [133]. Nonetheless it is a versatile antenna and used in frequencies in the S-Band and above due to the size of the antenna. Presse et al. [134] present a VHF/UHF Vivaldi linearly polarized antenna on a 1.5 mm thick silicone substrate with an area of 600 mm × 600 mm. Ödman and Hallbjörner [135] propose an antenna with reduced size for a lower operating frequency of 700 MHz but still with dimensions 300 mm × 230 mm, making it unfeasible to manufacture several elements on the same PCB.

2.6 Conclusion

In this chapter, a thorough investigation has been carried out on ground stations and PAAs with special attention to any works or literature on PAAs in the UHF band and for small satellites. Various studies and surveys have been published such as [89, 90] however all targeted to higher frequencies. It is shown that the conventional ground station operating in the UHF band consists of a mechanically steerable antenna system.

From the literature review, the attendance of PocketQube workshops and discussions held by the author with radio amateurs and other GS operators and networks, it is concluded that a low-cost ground station for small satellites operating in UHF frequency with hemispherical coverage has not yet been proposed. This study aims to close this gap in the literature. Special attention is given to the design of the antenna element as this is seldom included within the published works as part of the PAA to give a comprehensive solution.

Chapter 3: Phased Array Antenna System Design

For the proposed system to be complete various electrical, mechanical and software aspects of a PAA system must be considered. Due to the vast number of choices and decisions required in designing a low-cost ground station, a design paradigm is documented. The purpose of using a PAA design paradigm is to break down the larger problem to be solved in smaller manageable parts in a chronologic sequence of design decisions. This paradigm is presented in Figure 3.1 and the structure of this design chapter is based on the sequence presented.

Requirements and Constraints
Identify mission requirements, ground station site and footprint, cost and other requirements.

Geometrical Configuration
Select geometry required for satellite pass coverage within defined location and footprint constraints.

Planar Face design
Focus on building block with the various sub-requirements.

Element Selection
Patch Design
Circular Polarization
Element Lattice

Beamforming Architecture
Determine appropriate beamforming architecture based on constraints with accompanying electronics.

Geodesic Structure
Design of supporting structure and corresponding parts.

Array Software
Determination of architecture and components, integration with ground station networks.

Figure 3.1: Design paradigm of a Phased Array Antenna for small satellites

3.1 Requirements and Constraints

This section identifies all requirements and constraints on which the PAA system is to be designed.

3.1.1 Mission Requirements

The origins of the UoMBSat project are in the form of a feasibility study conducted in 2016 for a PocketQube to host an ionospheric impedance probe [10]. From this study several design choices were set which paved the way for various related projects [136]. Abela [137] concluded that a Bit Error Rate (BER) of 10^{-5} is sufficient for the UoMBSat mission. Vassallo [138] further derived that the required SNR for achieving this BER is 10 dB and derived the mission link margins of Table 3.1.

	Uplink	Downlink
Received SNR	22.1dB	17 dB
Required SNR	10 dB	10 dB
Link Margin	**12.1dB**	**7 dB**

Table 3.1: Uplink and downlink communication link margin conclusions

The link margins of Vassallo [138] are derived from a detailed link budget calculation for uplink (ground to satellite) and the downlink (satellite to ground) communication. They assume that the UoMBSat mission will be granted an allocation in the UHF amateur satellite band of 435 MHz - 438 MHz as a result of a frequency coordination exercise with the International Amateur Radio Union (IARU). The typical bandwidth allocation is 20 kHz to 25kHz of usable bandwidth.

These link budgets were calculated with input from Abela [137] for BER, Agius [110] for receiver noise and losses and the author with regards to estimated gain and PAA configuration for antenna noise temperature calculations, which will be discussed later in this design chapter. The original calculations of [10] together with the updated detailed workings of Vassallo give rise to a set of specifications for the ground station antenna which is being formalized in Table 3.2. Every requirement is given a reference number which is used through the remainder of this dissertation.

Reference	Requirement or constraint	Value
Req.1	Centre Frequency	436.5 MHz
Req.2	Bandwidth	3 MHz
Req.3	Transmission Mode	Half Duplex
Req.4	Polarisation	RHCP
Req.5	Azimuth look angle	360°
Req.6	Elevation look angle	10° to 170°
Req.7	Axial Ratio	<3dB
Req.8	EIRP	56.0 dBm
Req.9	Gain	15 dBi
Req.10	Connector Insertion Loss	-0.4 dB
Req.11	Antenna noise temperature	600 K

Table 3.2 UoMBSat mission requirements

The PAA system will be designed mainly on these requirements. The detail of the link budgets will be presented and compared to the working of Vassallo towards in Chapter 5 once the antenna performance parameters have been determined.

3.1.2 Ground Station Site Selection

The ground station is to be sited at the University of Malta. In order to satisfy requirements Req.5 and Req.6 a site must be selected with unobstructed views over an elevation angle of 10° with 360° in azimuth. Two main sites for the ground station were considered. The highest site is the roof of the Biomedical Sciences Building, marked (1) in Figure 3.2. The second site is located at the top of an elevated room on the roof of Faculty of Engineering, marked (2) in Figure 3.2.
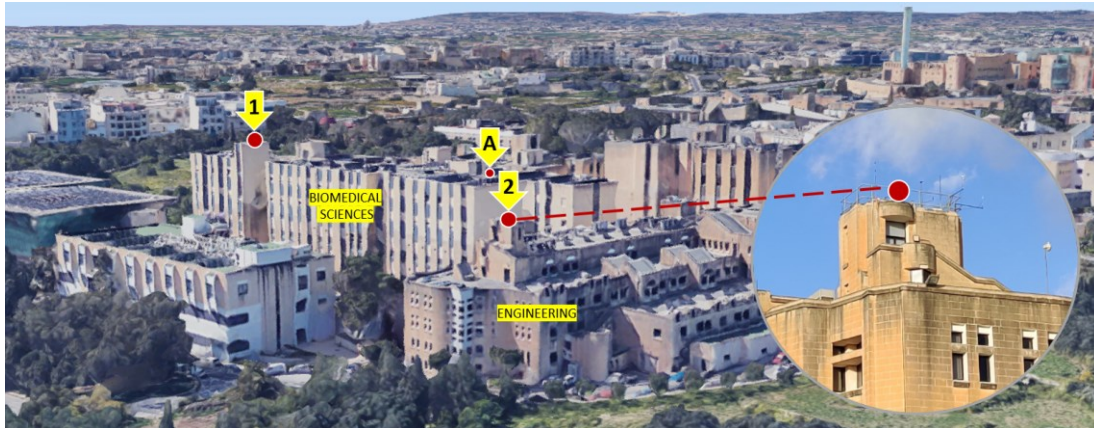
Figure 3.2: Aerial view of University of Malta and candidate ground station sites

Whilst in principle Site 1 was the preferred location due to it being the highest altitude point in the University offering unobstructed views, it created logistical difficulties due to it being in another faculty. Hence, Site 2 was identified for a site survey as it was within the Faculty of Engineering. The purpose of the site survey was primarily to determine whether it had sufficient clearance over 10° of elevation, particularly with regards to the Biomedical Sciences Building roof air conditioning units which from a visual inspection appeared to be the obstacle with the highest elevation, point marked (A) in Figure 3.4.

In 2017, a site survey was carried out on the roof of the Engineering Department at Site 2 of Figure 3.2 with coordinates 35° 54' 11.55" N, 14° 29' 6.92" E. A Total Station courtesy of the Department of Archaeology of the University of Malta was used. A Total Station is a tool used to measure horizontal and vertical angles during surveying. It is an electronic theodolite integrated with electronic distance measurement capabilities. The model of the Total Station used for this exercise is the Leica TS02.

For the readings to be taken, a virtual axis needs to be setup. A second point as a base reference point was located, the Dome of the Carmelite Church in Valletta

with precise coordinates 35° 54' 0.68", 14° 30' 44.18". Several readings in azimuth and elevation were taken with the Total Station with reference to the virtual axis.

Two points were created which roughly are situated in a West-East Direction. The maximum elevation of the buildings at various azimuth locations was surveyed with respect to the virtual axis set up.

Figure 3.3: Virtual axis reference for Total Station reading calculations

Following the site survey, the angle displacement between the virtual axis and real West-East axis was calculated and all measurements updated to reflect the real azimuth with respect to true North. The horizon outline is depicted in Figure 3.4.
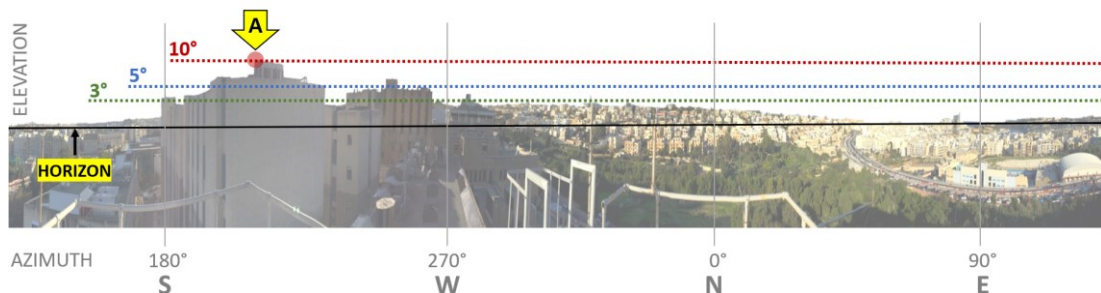
Figure 3.4: Horizon outline for ground station site

The obstacle with the highest elevation is the obstacle marked A in Figures 3.2 and 3.4 located at 213.9° South with an elevation of 10° 13'. Apart from approximately a 40° wide sector located South to Southeast of the site where the horizon is visible over 7°, the horizon outline is generally visible over 3° elevation. It is concluded that the site is adequate to serve for the UoMBSat mission. This site has subsequently been converted into a radio lab to host all ground station equipment.

3.1.3 Other Requirements and Constraints

The area on which the PAA antenna will be hosted measures circa 5 m × 2.75 m. The footprint of the designed antenna must not exceed these

dimensions. The antenna must be protected from weather particularly in terms of wind load and lightning due to the high elevation of the PAA.

As a result of the PAA architecture comprising of multiple antennas, a diagnostic capability mechanism is required to provide the ground station operator with feedback if a part of the PAA is malfunctioning. The PAA must also be designed in such a manner that allows individual parts to be replaced without dismantling the whole PAA. The system must be operated remotely.

The system must be designed with repeatability in mind to keep open the opportunity to have additional PAAs fabricated with collaborating institutions or alternative locations. The total cost of the PAA must not exceed ten thousand Euros for the capability to track one satellite. Nevertheless, the PAA must be designed in a manner that, even though such capability may not be immediately available, the underlying radio front end may be upgraded to support additional channels or configuration of combiners without physical modification of the PAA.

Reference	Requirement or constraint	Value
Req.12	Footprint	Length < 5 m Width < 2.75 m
Req.13	Weather Protection	N/A
Req.14	Diagnostics Capability	Required
Req.15	Ease of maintenance	Required
Req.16	Remote operation	Required
Req.17	Fabrication Repeatability	Required
Req.18	Cost	≈ EUR 10,000
Req.19	Multiple satellite simultaneous tracking	Scalability required

Table 3.3 Additional PAA system requirements

The constraints and requirements identified in Table 3.2 and Table 3.3 are considered at every step of the PAA design paradigm of Chapter 3 with Req.9 and Req.12 serving as the main fitness indicators between design stages.

3.2 Geometrical Configuration

To achieve Req.5 hemispherical coverage is required. The three approaches for hemispherical coverage discussed in Section 2.4.4 are considered. The approach to design an SPAA was immediately discarded due to the complexity of mounting antennas for the UHF operating frequency on a spherical surface and the associated requirement of a T/R module which would increase significantly costs and limit options. The approach of designing a faceted dome antenna was selected over a

multi-faceted geometrical configuration due to its property of retaining the advantages of a SPAA whilst leveraging existing planar manufacturing technology.

3.2.1 Polyhedron Selection

To avoid the necessity of needing to design different faces, simplifying the manufacturing process, a polyhedron with congruent faces is preferred. Polyhedrons having this property are known as Platonic solids. There are five Platonic solids as per Table 3.4.

The dihedral angle of a polygon is the angle between two adjacent polyhedron faces, from now on referred to as Planar Faces (PFs). The Sphericity Index Ψ [139] is a value which gives an indication of how close an object (particle) resembles a sphere through a ratio of their areas assuming they have the same volume. It is derived through the following formula:

$$\Psi = \frac{\pi^{\frac{1}{3}}\left(6V_p\right)^{\frac{2}{3}}}{A_p}$$
(3.1)

where V_p and A_p are the volume and area respectively of the object for which the sphericity index is required. The volumes and areas of platonic solids are well known, and the derived sphericity index values are listed in Table 3.4.

Name	Faces	Dihedral angle θ_d (approximate)	Maximum Steering Angle θ_{max}	Sphericity Index (approximate)
Tetrahedron	4	70.53°	109.47°	0.671
Hexahedron	6	90.00°	90.00°	0.806
Octahedron	8	109.47°	70.53°	0.846
Dodecahedron	12	116.57°	63.43°	0.910
Icosahedron	20	138.19°	41.81°	0.939

Table 3.4: Properties of Platonic solids

The tetrahedron (triangle pyramid), hexahedron (cube) and octahedron (square bipyramid) are essentially multi-faceted structures with a poor sphericity index. The dodecahedron and icosahedron polyhedrons both have a good sphericity index. The dodecahedron has twelve faces of pentagon shape with the icosahedron having twenty faces of equilateral triangle shape. A triangle is preferred to a pentagon as polygon shape as it simplifies the manufacturing process.

Furthermore, the dihedral angle is significantly larger in the icosahedron. This creates a significant advantage. Consider the arrangement in Figure 3.5. Let the

dihedral angle between PF 1 and 2 be θ_d. Let the angle from the broadside of PF1 or PF2 (z-axis) to the ground zenith be θ_i. The ground zenith is parallel to the intersection of both PFs on a common plane. Hence, the angle θ_i represents the maximum elevation scan angle required for a a PF in a scenario where one PF is used. However, the use of multiple PFs for BF is required, hence an extended scan angle must be considered. At Position 1, the satellite is pointing to the boresight of PF 1 so no beam steering is required on PF 1. On the other hand, the steering angle for PF 2 is $2\theta_i$. At Position 2, the satellite is pointing to the axis of the line of symmetry of the PF arrangement. In this case the steering angle required for both PF 1 and 2 to point to the satellite is θ_i. The relationship between θ_d and θ_i is shown in (3.2).
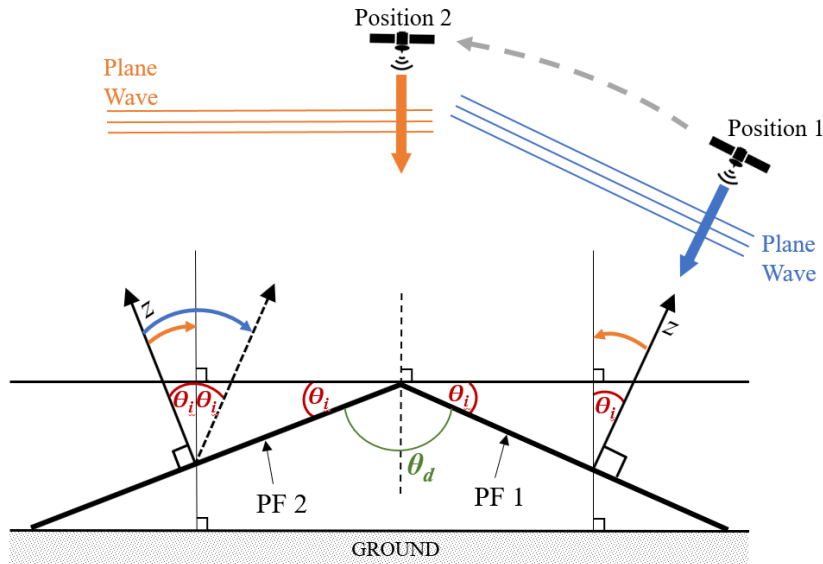
Figure 3.5: Effect of dihedral angle on steering angle from planar face boresight

The maximum steering angle θ_{max} required for a PF to point to the boresight of an adjacent PF may simply be derived from (3.2).

$$\theta_{max} = 2\theta_i = 180° - \theta_d \qquad (3.2)$$

The larger the dihedral angle θ_d, the less the faces are inclined to one another, resulting in a smaller maximum steering angle θ_{max}. In order to optimize the array gain it is desired that the maximum steering angle value required for the PF is less than the half of the HPBW of the PF. A smaller steering angle requirement allows the HPBW requirement also to be smaller, which finally results in a better spatial resolution of the main beam which is desired for BF applications.

Based on the smaller maximum steering angle requirement, the simple triangular shape for manufacturing of faces, that all faces are identical and the good sphericity the regular icosahedron is selected as the polyhedron of choice for the structure of the GDPAA.

3.2.2 Orientation

Let us take a closer look at the geometry of the icosahedron of Figure 3.6. An icosahedron's vertices consist of the vertices of three rectangles orthogonal to each other. The rectangles are golden rectangles, whereby the sides of the rectangle are in the golden ratio φ given by:

$$\varphi = \frac{1 + \sqrt{5}}{2} \tag{3.3}$$

Subsequently, the vertices of an origin-centered regular icosahedron with an edge length of 2 may be defined with the following Cartesian coordinates:

$$(0, \pm1, \pm\varphi)$$
$$(\pm1, \pm\varphi, 0)$$
$$(\pm\varphi, 0, \pm1)$$

The icosahedron has three types of axes of symmetry, one through the edge midpoint, one through the centre of the face and one through the vertex. Due to the orthogonal layout of the underlying structure of Figure 3.6, only the axis of rotation through the edge midpoint is also a line of symmetry. In order to keep the performance of the GDPAA equal from North to South, symmetry is desirable. Hence the icosahedron is positioned as per Figure 3.6 where the underlying golden rectangles represent the XY, XZ and YZ planes.
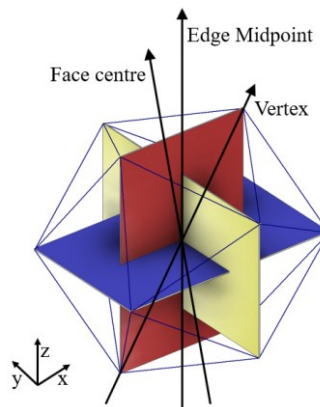
Figure 3.6: Geometry of a regular icosahedron denoting axes of rotation

53

3.2.3 Footprint

To determine the footprint of the GDPAA, the diameter d_{cs} of the circumscribed sphere of the icosahedron is used, such that the footprint of the GDPAA is a circle with a diameter of d_{cs}.
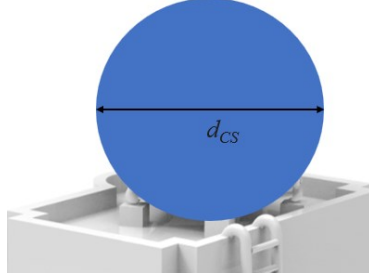
Figure 3.7: Diameter of icosahedron circumscribed sphere

The radius r_{ics} of the circumscribed sphere of an icosahedron may be obtained from the formula:

$$r_{ics} = b \ sin\frac{2\pi}{5} \qquad (3.4)$$

where b is the side length of the planar face of the icosahedron. According to Req.12 the footprint width must not exceed 2.75 m. Hence, the radius of the icosahedron must not exceed 1375 mm and from (3.4) the side length must not exceed 1446 mm.

3.3 Planar Face Design

The main constraint of the PF is meeting the footprint requirement Req.12. The available area for the design is an equilateral triangle with side length 1446mm. Considering that the half wavelength of the centre frequency of 436.5 MHz is 686.8 mm, the minimum number of elements required to perform BF must be selected. The icosahedron shape selected allows 360° azimuthal steering as per Req.5, However, 360° continuous azimuthal steering is also required at PF level, such that each individual PF can steer the beam to any location required. It has been numerically shown that this may be achieved with at least four elements [140]. With this knowledge, the first step is to select an antenna element type which is suitable for this purpose.

3.3.1 Element Selection

According to Req.9, the PAA is to have a minimum gain of 15 dBi. This may be achieved using more than one planar face simultaneously however in the design it is desired to come as close as possible to 15 dBi using one PF. The significance of coming close to such a gain is that the fewest number of PFs would be required to be

used simultaneously to track one satellite, allowing for the PAA to be used to track more than one satellite simultaneously (Req.19)

Theoretically, when antennas are stacked, the gain is doubled resulting in a 3 dB improvement. With four antenna elements this would be 6 dB, so the ideal antenna would have a theoretical gain of 9 dBi. Other criteria for selection of antenna element are:

- a HPBW which is greater than twice the maximum steering angle θ_{max} of 41.81°;

- bandwidth to cover the operating frequency of 435 MHz - 438 MHz;

- capability for circular polarization; and

- may be easily manufactured (Req.17) with low cost (Req.18)

Although the property of ESAs that they can be very small is attractive to the problem at hand, their low gain makes them inappropriate as the antenna element of the PF. On the contrary, Aperture antennas have high gain, making them attractive. However, large size is inhibitive to the required design. Aperture antennas include the Vivaldi antenna which is a common antenna used in phased array applications, However, Vivaldi antennas are used in applications where the wavelengths are significantly smaller. Broadband antennas are more suited to the application in terms of size however the gain is significantly lower than the required theoretical 9 dBi. Resonant antennas, on the other hand, provide a good compromise between the size and possible gain. Their physical size is generally half a wavelength before any miniaturization techniques are applied.

A linear polarized patch antenna has a theoretical directivity of almost 9 dB [141]. There are three components to this directivity:

1. The patch antenna comprises of a metallic patch on a ground plane with characteristics like radiating slots. In an ideal scenario and an infinite ground plane, all the power is concentrated into the front main lobe in the hemisphere of the boresight of the antenna. This gives rise to a 3 dB directivity improvement.

2. The radiating slots are like dipoles and are not isotropic, having a directivity of 2 dB to 3 dB.

3. The patch antenna consists of two slots, so a further 3 dB in directivity is achieved.

When the substrate between the metallic patch and substrate is air, such as the patch in Figure 2.25b, the electrical efficiency is optimised, and the theoretical gain of the antenna is also in the region of 9 dB.

Patch antennas offer versatility by having various shapes and are easy to manufacture on common PCB technology. Their low profile makes them suitable for use in PFs. They offer narrow bandwidth, however this is typically less than 5% [142] which is considered sufficient as band of interest is less than 1% operating frequency. The HPBW of patch antennas are typically 65°, i.e. ±32.5° from boresight. Assuming the boresight is perpendicular to the plane of the antenna, this comes close to the maximum steering angle θ_{max} of 41.81°. Various options for circular polarization exist. Although the patch antenna is typically used in applications with higher frequency bands, it meets all requirements and is selected as the antenna element for the PF. Despite the research being directed towards investigating PAAs onboard small satellites and in S-band, [143] concludes that the patch antenna is the most suitable antenna for satellite-GS communication links.

3.3.2 Patch Antenna Design

Once the antenna element has been selected, several design choices are required to maximize the use of the PF and to ensure it meets the various requirements. In its most basic form, a patch antenna consists of a radiating metal patch, underlying substrate and metal ground plane as per Figure 3.8.
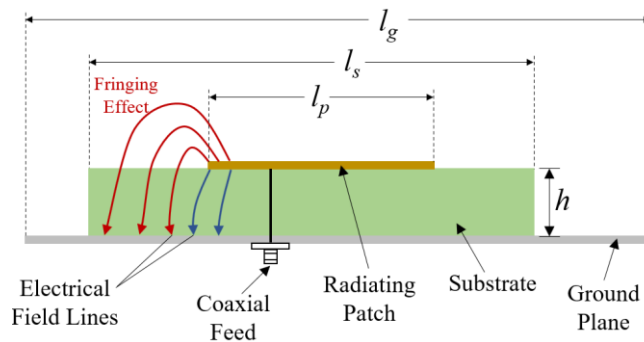
Figure 3.8: Patch antenna with fringing effect illustration

Patch Shape

The patch antenna can take a variety of shapes; square, rectangular, dipole, circular, elliptical, triangular, sector and ring. Often the metallic patch is selected in

one of these forms however with a rectangular ground plane. Considering the equilateral triangular shape of the PF, it is considered optimal if the patch antenna with corresponding ground plane is also an equilateral triangular. Triangular Patch Antennas (TPA) are, in general, known to be physically smaller at a fixed frequency compared to their rectangular and circular counterparts [144, 145]. An Equilateral Triangle Patch Antenna (ETPA) is selected as the patch geometry.

Ground Plane

Each ETPA may have its own dedicated ground plane or a common ground plane. A dedicated ground plane may increase antenna isolation as it avoids coupling through the common ground plane. On the other hand, as argued by Sharawo [146] this should be avoided as all antennas should have a common reference plane. A PF with a common ground plane also simplifies the manufacturing process and makes the GDPAA structure stronger. Aluminium is a lightweight and inexpensive material with good conducting properties. 1.5 mm sheet aluminium was selected as the ground plane material as it is inexpensive, readily available, and thin enough for sheet aluminium to be folded and easily transported.
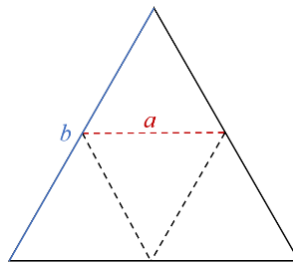
Figure 3.9: Planar face ground plane allocation for four ETPAs with maximum usage

In Section 3.2.3 it was established that the side length of the PF must not exceed 1446 mm. Whilst the ground plane is common, nonetheless each patch antenna must be allocated sufficient area within the ground plane. To maximize the use of the ground plane, one subdivision of the Sierpiński gasket [147] is carried out as per Figure 3.9. This gives four congruent triangles, hence $b = 2a$. Hence, one antenna should not occupy more than an area of equilateral triangle with a side length a of 723mm.

The equations provided in this section assume that the ground plane is infinite, with the fringing fields shown in Figure 3.8 not escaping the edge of the ground plane. In practice, an infinite ground plane is not possible, and the radiation pattern of the antenna is altered by the size of the ground plane. Preliminary

investigations are carried out via simulations in CST Microwave Studio (hereinafter referred to as CST) to investigate this property further. It is observed that a ground plane-to-patch ratio of 2:1 in terms of side length is adequate in terms of preserving a good front-to-back ratio on the antenna element. This ratio value also ensures that the elements are not too dense on the PF surface in order to minimize mutual coupling. The placement of antenna elements is discussed later in Section 3.3.4. This means that the side length of the radiating patch must not exceed 361 mm.

Side length

The base formula for the calculation of the resonant frequency f of an ETPA [148] is:

$$f_{mn} = \frac{2c}{3a\sqrt{\varepsilon_r}} \, (m^2 + mn + n^2)^{\frac{1}{2}} \tag{3.5}$$

where the subscript mn refers to the TM_{mn} transverse modes, a is the side length of the ETPA and ε_r the permittivity of the substrate between the radiating and ground planes. For the purposes of these calculations, it is assumed that the electric field is in the direction of propagation and the magnetic field is perpendicular (transverse) to the direction of propagation. Hence a transverse magnetic mode is used for our calculations, specifically the TM_{10} dominant mode where $m = 1$ and $n = 0$ meaning that the wave is travelling in a medium half a wavelength in the x-axis. In the TM$_{10}$ mode, (3.5) may be simplified to:

$$f_{10} = \frac{2c}{3a\sqrt{\varepsilon_r}} \tag{3.6}$$

In the remainder of this dissertation, the TM_{10} will be assumed. The permittivity of air, ε_0, is also being assumed to be that of vacuum, with the value of 1. Assuming air is used as a substrate for the patch antenna element, from (3.6) it may be derived that to achieve a resonant frequency of 436.5 MHz the side length a must be is 457.9 mm. This exceeds the maximum allowable side length of 361 mm, so a miniaturization technique must be adopted to reduce the size of the radiating patch.

Miniaturization

Antenna miniaturization techniques may be divided into two categories [149]: topology-based and material-based. Topology-based techniques revolve around modifying the geometry of the antenna in a way that the antenna is reduced in size

whilst maintaining good radiation characteristics in the frequency of interest. One common technique is meandering, whereby the radiating slot is modified such that it occupies a bent slot instead of a straight line, hence occupying less space. This technique however lowers the gain of the antenna. Another technique is to introduce a slot in the ground plane, which lowers the frequency, with a side effect of reducing directivity. The antenna may also be reactively loaded, which increases the electrical size of the antenna with the bandwidth significantly reduced. Despite the improvement in physical dimensions, topology-based techniques degrade the gain and bandwidth of the antenna significantly and could have an adverse effect on the mutual coupling between difference antenna elements. Hence this category of techniques is not considered suitable for the PF being designed.

The second category of antenna miniaturization techniques is material-based miniaturization. A metamaterial may be used as substrate whereby specific radiation characteristics may be obtained. Since they are not engineering materials, they are complex and expensive and were not considered further. Another technique is to select a substrate with a high refractive index n, calculated follows:

$$n = \overline{\varepsilon_r \mu_r} \tag{3.7}$$

where ε_r is the permittivity and μ_r is the permeability of the substrate. The required antenna size is inversely proportional to the refractive index due to the properties of the material slowing down the propagation of the EM wave, hence lowering the frequency. Since the relative permeability of materials used as substrates such as FR4 and Teflon is around 1, the permeability may be ignored for the purpose of determining the size of the antenna. The size of the antenna is normally inversely proportional to the square root of the relative permittivity of the substrate, as seen in (3.6). The main challenge of this technique is the degradation in efficiency as a result the dissipation of power through the substrate since dielectric losses contained in the variable e_{cd} in (2.15) and (2.16) contribute directly to the reduction of the antenna gain. The dissipation is measured by the loss tangent $\tan \delta$. A substrate must be chosen where a balance between antenna size reduction and efficiency degradation is maintained.

Substrate

Various substrates may be used for the patch antenna such as bakelite, ceramic or laminates. Khan and Nema [150] analyze five different dielectric

substrates on a microstrip patch antenna in terms of antenna performance. Several dielectric properties and results are presented in Table 3.5 together with a derived antenna size parameter which represents $1/n$.

	Bakelite	FR4	RO4003	Taconi TLC	RT Duroid
Relative Permittivity (ε_r)	4.78	4.36	3.4	3.2	2.2
Loss Tangent $(\tan\delta)$	0.03045	0.013	0.002	0.002	0.004
Antenna Size (% to antenna size with air substrate)	**45.7 %**	**47.9 %**	54.2 %	55.9 %	67.4 %
Bandwidth	12.5 %	10.12 %	7.59 %	8.8 %	15 %
Directivity	6.5 dBi	6.5 dBi	7 dBi	7 dBi	7.5 dBi
Radiating Efficiency	45.0 %	50.0 %	70.0 %	67.5 %	80.0 %
Gain	3 dBi	4 dBi	5 dBi	5.5 dBi	6.5 dBi

Table 3.5: Dielectric properties and antenna performance result comparison of five different dielectric substrates [150]

The smallest antenna is achieved through the bakelite and FR4 substrates which have the largest values of relative permittivity and reduce the size of the antenna by more than a half when compared to the equivalate antenna with an air substrate. These materials however also have the largest loss tangents which result in the highest losses and lower antenna gains.
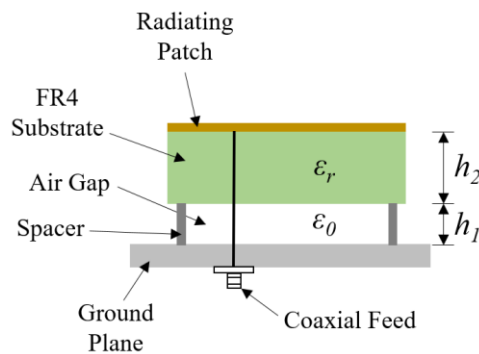
Figure 3.10: Patch antenna with substrate and additional air gap

FR4 is the preferred substrate material of the two as it is widely available, and the most common material used in PCBs making it easy to fabricate, satisfying Req.17. Apart from the substrate, the substrate thickness is an important consideration in the design of the PAA, as increasing the substrate thickness reduces the resonant frequency, which results in a smaller antenna size. Furthermore, the bandwidth is increased [151], although the side effect is that the efficiency is adversely affected. To compensate for the dielectric losses introduced by the FR4

substrate and additional thickness, an air gap between the substrate and ground plane may be inserted as per Figure 3.10. This increases the bandwidth [152] and maintains the gain [153].

Substrate Air Gap

In Figure 3.10, the height of the air gap in is h_1 and the height of the FR4 substrate is h_2. To cater for the combined effective permittivity of the dual-layer substrate of FR4 and air, ε_r in (3.5) is replaced with ε_{comb}, which is calculated by a heuristic relationship taken from the capacitance of the two dielectric layers [16], simplified as follows:

$$\varepsilon_{comb} = \frac{\varepsilon_r \varepsilon_0 (h_2 + h_1)}{\varepsilon_r h_1 + \varepsilon_0 h_2} \tag{3.8}$$

Hence, ε_r of (3.6) is replaced with ε_{comb} to give:

$$f = \frac{2c}{3a \sqrt{\varepsilon_{comb}}} \tag{3.9}$$

Introducing an air gap means that the FR4 substrate will no longer rest on the ground plane but must be suspended using spacers, as per Figure 3.10. The spacer material comprising of nylon is not included in any simulations during this study as simulations have shown that the effect is marginal in view of the operating frequency. Apertures in materials have been catered for, however, regardless of their minimal contribution to the end result. To preserve the sturdiness of the GDPAA design and to improve bandwidth to satisfy Req.2, a substrate thickness of 3.2 mm was selected for the FR4 substrate. Manufacturing a 3.2 mm thick PCBs is more expensive than its 1.6 mm counterpart however it is more robust and widely available. To minimize the area of the FR4 substrate, the substrate area is restricted to the size of the patch as per Figure 3.10 as opposed to a larger substrate, such that l_p of Figure 3.8 is equal to l_s. To reduce costs a 35-micron (one ounce copper per square foot) copper layer was selected. It must be noted that if the substrate is extended beyond the radiating patch, such that l_s is greater than l_p, the resonant frequency is lowered due to the electric fields inside of the fringing effect now needing to travel through the substrate, which lowers the frequency. This fact allows for further modification to be carried out prior to manufacturing the GDPAA should the resonant frequency want to be altered further without major redesign. In the

design of the GDPAA, attention has been given to allow for tuning to take place without any significant redesign of the PAA.

Using (3.7) and (3.8), it is possible to simulate the effect of air gap h_1 on the side length a which is represented in Figure 3.11. For a to be less than 361mm the airgap must be less than 3.5mm. Whilst a larger air gap improves bandwidth, the cost to manufacture the PCBs also increase. Hence, an air gap h_1 value of 2 mm was selected at this stage of the design process as it is considered as a good compromise between miniaturization and flexibility of choice of antenna element placement. The appropriateness of this value is confirmed when the element lattice is selected in Section 3.3.4.
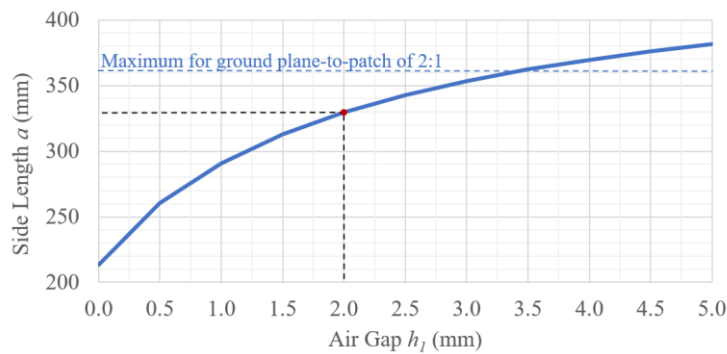
Figure 3.11: Effect of variable air gap h_1 on side length a

Fringing Effect Considerations

Equation (3.6) is based on the cavity model which assumes perfect magnetic walls. In reality, this is not the case and according to [145, 148] the most accurate model is the one proposed by [154] which amends the side length a to a_{eff} to cater for the fact that the antenna is electrically larger than its physical dimensions due to fringing fields. The value of a_{eff} is derived using (3.10).

$$a_{eff} = a + \frac{h}{\sqrt{\varepsilon_{comb}}} \qquad (3.10)$$

where h is the dual-layer substrate height $h_1 + h_2$ and ε_{comb} is the combined dielectric constant obtained from (3.8). The values given in Table 3.6 and (3.8) to (3.10) are used to compute the value of a. For an operating frequency of 436.5 MHz the side length a is 325.9 mm.

Parameter	Value
h_1	2.0 mm
ε_0	1.0
h_2	3.2 mm
ε_r	4.6
ε_{comb}	1.93
f	436.5 MHz

Table 3.6: Parameter values for the calculation of the effective side length a_{eff}

Chen et al. [155] propose another method to calculate a_{eff} with an improved accuracy of 1%, which is simplified as follows for the frequency f_{10}:

$$a_{eff} = a\left[1 + 2.199\left(\frac{h}{a}\right) - 12.853\left(\frac{1}{\sqrt{\varepsilon_{comb}}}\right)\left(\frac{h}{a}\right) + 16.436\left(\frac{1}{\varepsilon_{comb}}\right)\left(\frac{h}{a}\right)\right.$$
$$\left. + 6.182\left(\frac{h}{a}\right)^2 - 9.802\left(\frac{1}{\sqrt{\varepsilon_{comb}}}\right)\left(\frac{h}{a}\right)^2\right] \tag{3.11}$$

Using the same values of Table 3.6 and (3.8) the side length a is computed using (3.11). The value of a is 320.8 mm. The selected value will be finalized once the circular polarization discussed in Section 3.3.3 is considered.

Superstrate

The GDPAA will be exposed to weather conditions and to satisfy Req.13 weather protection is required. This is achieved through the addition of a radome which consists of a protective layer which does not adversely affect the EM waves being received or transmitted.

Typically, radomes consist of an additional structure which serves as an enclosure for the PAA. Due to footprint constraints, the protective layer is designed as a superstrate placed over the radiating patch in the vicinity of the radiating patch via the use of spacers in similar fashion to the substrate as featured in Figure 3.12.
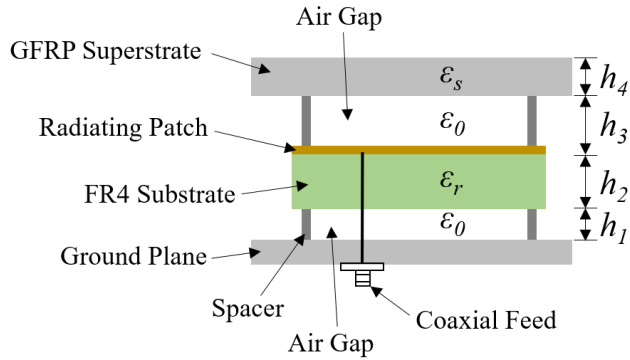
Figure 3.12: Patch antenna with substrate, superstrate, and air gaps

Glass Fibre Reinforced Polymer (GFRP), commonly referred to as fibreglass is a cheap, inexpensive, and commonly available plastic, widely used in a number of

industries. GFRP is made of a mixture of glass fibres and resin, and yields a plastic which is electromagnetically porous, rendering it transparent to EM waves. These properties make it suitable as the material for the radome.

A good study by [156] is performed on the input impedance and resonance characteristics of an ETPA with a superstrate at frequencies over 1 GHz. They conclude that typically a 2% to 4% resonance shift is expected with the presence of an additional superstrate. However, they do not discuss the impact of an air gap between the patch and superstrate which is desired to improve the bandwidth of the antenna. To assess such impact via simulations, the dielectric properties of the GFRP superstrate must be known.

The selected material was prefabricated in 3.5mm thick GFRP sheets by a local fibreglass supplier. The glass used is E-type chopped strand mat. General relative permittivity values of 6.2 and 4.3 for E-glass fibre and resin respectively are used. Various formulae exist to derive the relative permittivity ε_s because of the percentage of fibre present in the mixture [157]. The Wiener limit formula has been used as per the following formula:

$$\varepsilon_s = V_{fibre}\varepsilon_{fibre} + \left(1 - V_{fibre}\right)\varepsilon_{resin} \tag{3.12}$$

where V_{fibre} is the fibre volume fraction and ε_{fibre} and ε_{resin} the relative permittivity of fibre and resin respectively. Using (3.10) and an average V_{fibre} value of 0.58 the GFRP relative permittivity is 5.4. A simulation via CST was carried out to investigate the effect of varying the air gap on resonant frequency, bandwidth, and efficiency.
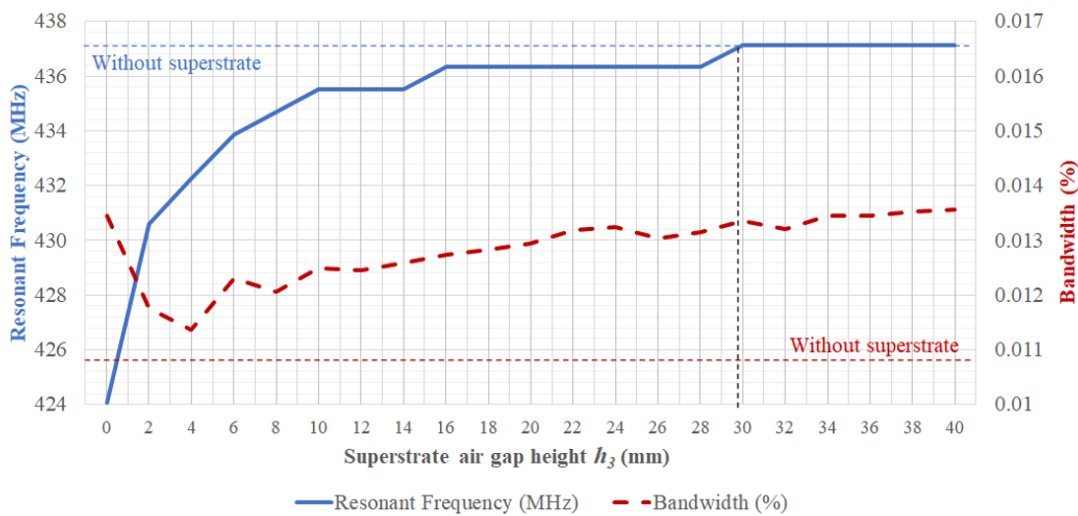
Figure 3.13: Effect of air gap variation between patch and superstrate on resonant frequency and bandwidth

In Figure 3.13 the resonant frequency (blue line) and bandwidth (red dashed line) are plotted against a variable air gap height h_3 for the superstrate. From Figure 3.13, for a single-layer GFRP superstrate of 3.5mm thickness with the previously discussed properties, two items may be concluded. Once the value of 30 mm has been reached for h_3, the resonant frequency is the same as a scenario where no superstrate is present. Furthermore, once the value of h_3 has reached 10 mm the bandwidth increases linearly.
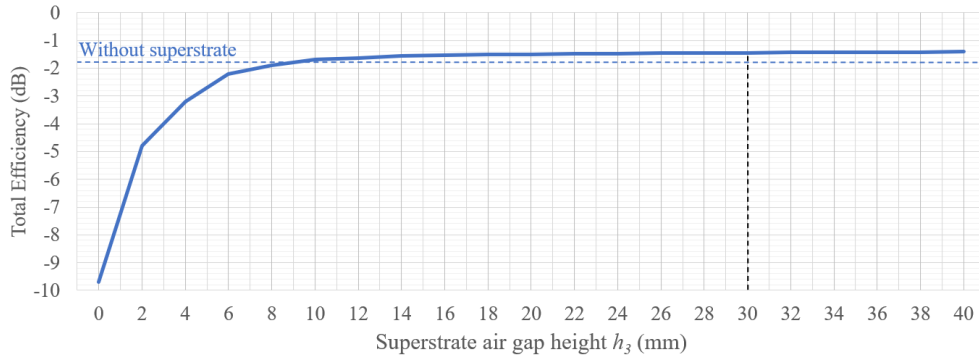
Figure 3.14: Effect of air gap variation between patch and superstrate on total efficiency

In Figure 3.14 the total efficiency of the patch antenna is plotted against a variable air gap height h_3 for the superstrate. It is noted that the efficiency of the antenna is significantly improved if an air gap is inserted between the radiating patch and GFRP superstrate. An air gap where height h_3 is greater than 9mm improves the efficiency of the antenna by approximately 0.5 dB when compared to an antenna without radome. The height h_3 of the air gap is selected to be 30mm.

In this section, the patch antenna has been designed. To make the patch complete, the final design decision is how the patch will be fed. This is discussed in the following section in the context of obtaining circular polarization.

3.3.3 Circular Polarization

The ground station phased array must be circularly polarized to avoid polarization mismatch losses and to satisfy Req. 4 RHCP is required. CP at a system level may be obtained in two ways. The first method is achieving CP at an array level via careful placement and rotation of linear polarized patch elements using the technique of Sequential Rotation. As an example, 90° for four antennas, 60° for six antennas, etc. These elements are fed through a feed network with a phase shift corresponding to the angle by which they are rotated. A good example is demonstrated by [158].

Alternatively, CP may be obtained by designing an antenna that achieves CP independently of the PF or PAA it forms part of. This is possible because the state of polarization of the individual element is preserved in the radiation pattern of the PF it forms part of [106]. This method is selected as it allows for more degrees of freedom in design by retaining the flexibility for the array to be repartitioned into sub-arrays without constraints. The concept of sequential rotation may still be utilized to improve on the AR when BF is carried out with the combined elements of two or more PFs.

The various methods of feeding the antenna will now be considered. These can be divided into four categories. The most common feeding method is the coaxial probe feed as per Figure 3.12. It consists of a connector, such as an SMA or BNC, whose inner conductor reaches the patch antenna and is soldered. The outer conductor is connected to the ground plane with additional soldering required. Additionally, the thicker the substrate (h_1 and h_2 combined) the longer the inner conductor must be resulting in additional losses. The location on the patch antenna is carefully selected to have an input impedance of 50 Ω which matches a 50 Ω feeder cable.

Another common feed type is the microstrip-line feed. This is basically an extension of the patch antenna with an intermediate quarter wave antenna which allows for good impedance matching although radiation may leak as a result and increase mutual coupling. This method provides many advantages on frequencies with short wavelengths as an entire planar face consisting of patches and feed lines can be manufactured on the same PCB with high precision and low cost. At the operating frequency of 435 MHz - 438 MHz however this is not practical as further enlargement of the antenna to cater for a transmission line is not affordable in terms of additional space requirements and is counter-productive to the miniaturization initiatives previously adopted. Additionally, PCBs are considerably more expensive to manufacture.

The third method, a variant of the microstrip line feed, is the proximity-coupled microstrip-line feed. Instead of the transmission line being an extension directly connected to the radiating patch, it is placed beneath the patch as an additional layer on the PCB embedded within the substrate or adjacent to it.

A fourth method is the aperture-coupled feed which consists of a microstrip line place on the opposite side of the ground plane, exciting the patch through an aperture in the ground plane.

In these last two methods the bandwidth is significantly increased, and radiation leakage is avoided. However, in both these methods additional PCB layers are required increasing costs.

The coaxial probe feed is selected as it is easy to use. It avoids spurious radiation [148] and the need for an external polarizer [159] or power combiner/splitter which directly translates to a reduced footprint. Due to the feeder cable being 50 Ω, the feed point must be placed at a specially selected 50 Ω point location. Feeding at a 50 Ω locus point results in maximum radiation because of perfect matching. The exact point or points for a dual feed antenna will be determined depending on what technique is chosen to achieve CP. Regardless of which technique is chosen, the underlying principle consists of splitting the signal into two distinct parts and inserting a phase delay of 90° between them.

One approach is to feed the antenna through two feed points with the insertion of a phase shifter capable of introducing the phase delay. This introduces an additional layer of complexity and is not desired. The other approach is to modify the properties of the patch in a certain way that the TM_{10} mode is split into two near-degenerate orthogonal resonant modes. The resulting effective excited patch surface current path in the x and y direction are not the same, so the x-directed resonant mode and y-directed resonant mode will result in a different resonant frequency. At the centre frequency, a 90° phase shift will exist. If both modes also have equal amplitude, this results in circular polarization.

The properties of the ETPA may be modified by altering the geometry in several ways. Methods include altering the aspect ratio of the sides of the triangle [160] as per Figure 3.15a, truncating the tip [161] or tips of the triangle as per figures 3.15b and c, or alternatively inserting a defective structure such as a slot or notch as per Figures 3.15d and e. The truncated-tip method is selected as it is easy to manufacture, allowing for post-manufacturing tuning.
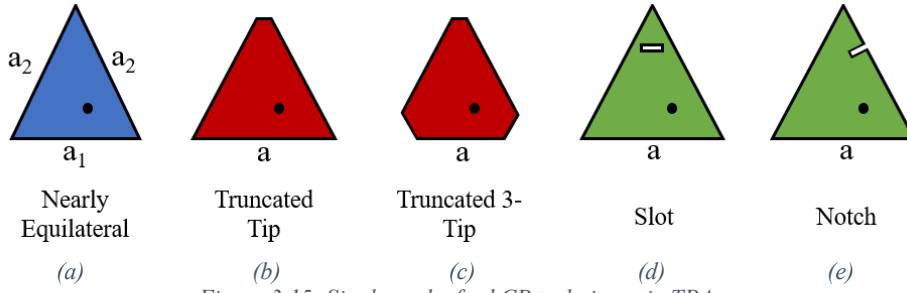
Figure 3.15: Single probe feed CP techniques in TPAs

The tip truncation method was proposed by [161] where it was observed that CP may be achieved by truncating one of the tips and then adjusting the length of the new side to approximately a factor of 0.09 of the remaining sides. However, [161] also concludes that the AR bandwidth is largely dependent on the thickness of the substrate. The frequency of operation in this work was in the region of 1.7 GHz to 2.38 GHz, with the truncation ratio (TR) decreasing to approximately 0.08 as the frequency decreased.
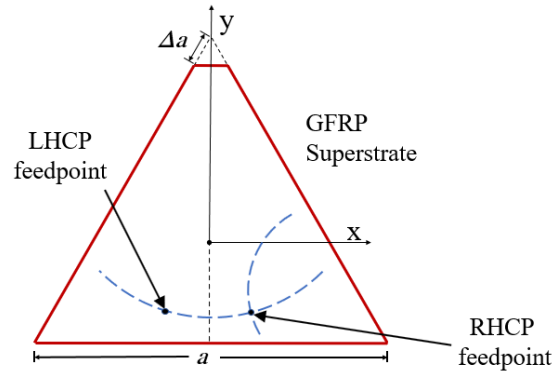
Figure 3.16: Truncated-tip ETPA with single-feed probe

The desired frequency for the best AR is located at the centre of the x-directed resonant mode and y-directed resonant mode. Hence, the patch antenna properties must be modified such that the x-directed mode resonates at the lower frequency. To determine this frequency, the simulated bandwidth of the patch antenna as per Figure 3.13 is considered. At 436.5 MHz the bandwidth is circa 1.34%. The resonant frequencies of the antenna must lie on the edges of the bandwidth range, which are 433.6 MHz and 439.4 MHz.

The values in Table 3.6 were used substituting the value of f with the lower resonant frequency of 433.6 MHz. Equations (3.8) and (3.11) were used to derive a new value of side length a of 323.4 mm. This value was rounded upwards to 324 mm. This allows for manufacturing imprecision tolerances, as the side can easily be abraded if required.

Simulations were carried out for an ETPA design with truncated tip as per Figure 3.16 with the new side length a of 324 mm and with truncation ratio Δa. Through an optimization technique carried out via the parameter sweep function of CST, an optimum AR was found when the truncation ratio had a value of 0.062.

The 50 Ω feed point needs to be determined. This is the point of intersection of the loci of the 50 Ω feed point positions of the excited resonant modes. The feed point loci may be found via a series of field equations [162] to give the input impedance, which are based on the cavity model bounded by a magnetic wall. However, this study does not cater for additional air gaps which are known to have a significant impact on the impedance as shown by [163]. This is confirmed through CST simulations comparing the impedance for the antenna without a superstrate for scenarios with and without air gap h_1. The Smith chart of Figure 3.17 clearly shows that with the same feed point, the impedance changes dramatically.
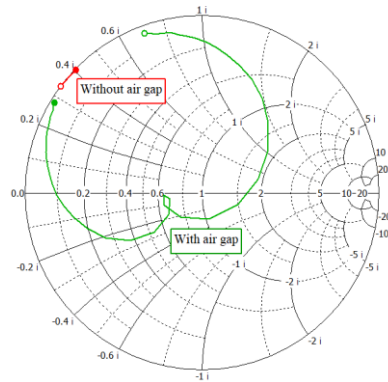
Figure 3.17: Smith chart demonstrating change in impedance for the same ETPA feed point with and without air substrate

Hence, like the works of [164] and [161] the ideal feed point is determined experimentally. The equations given in [162] are used to determine an initial set of loci which are further refined through MATLAB and subsequently CST via the parameter sweep functionality comparing the feed point location with the impedance values using a Smith chart and the AR. A good balance of AR and input impedance was found at the location $x = 30$ mm and $y = -21$ mm from the centroid of the triangle as per Figure 3.16 for RHCP. The LHCP feed point is found at the mirror location with the y-axis as line of symmetry, where $x = -30\ mm$ and $y = -21$ mm.

The patch antenna was designed using Altium Designer and both RHCP and LHCP feed points where catered for. Gerber and drill files were submitted to a foreign supplier for the manufacturing of the patch antennas on a one layer 3.2mm

TG130 FR4 board with 35-micron copper and a top red solder mask for aesthetic purposes.

3.3.4 Element Lattice

All element parameters have been identified and are summarized in Table 3.7. Now that the antenna element has been designed the final step is to select the optimum placement of the elements on the PF and optimize the lattice configuration.

The basic goal that is required to be achieved is the placement of antennas in the designated PF triangle area with the largest amount of antenna isolation possible to minimize the mutual coupling between antennas and improve the performance of the antenna.

Properties	Symbol	Values	Unit
Triangle side length	a	324.0	mm
Truncation ratio	Δa	0.062	-
RHCP feed point location	x, y	30.0, -21.0	mm
Ground plane thickness	-	1.5	mm
Ground plane: patch area ratio	-	2.0	-
Substrate air gap height	h_1	2.0	mm
FR4 substrate height	h_2	3.2	mm
FR4 relative permittivity	ε_r	4.6	-
Copper layer thickness	-	0.036	mm
Superstrate air gap height	h_3	30.0	mm
GFRP superstrate height	h_4	3.5	mm
GFRP relative permittivity	ε_s	4.93	-

Table 3.7: Properties of designed truncated-tip ETPA

Let us first consider the dimensions of the patch antenna and corresponding ground plane of Figure 3.18. The truncated tip is omitted for simplification purposes. The value of a is 324 mm and using the Pythagorean theorem the value of R is 187.06 mm. Using Euler's theorem the relationship between the circumradius R and the inradius r is $R = 2r$. The height of the patch, $R + r$, is therefore 280.59 mm.
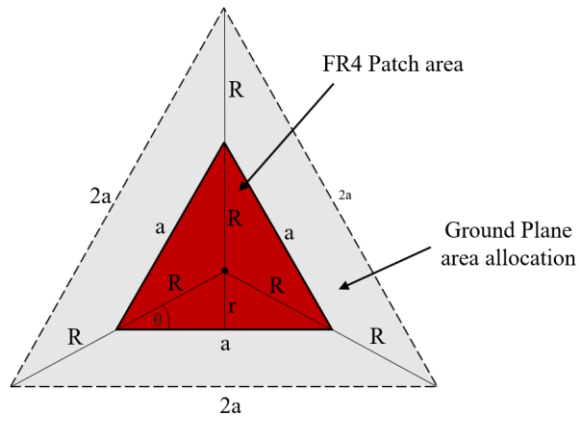
Figure 3.18: Geometry of patch without truncated tip

Let us consider the triangular lattice configuration of Figure 2.16c and place four antenna elements on such a lattice. These elements and their corresponding ground plane allocations must be enclosed within an equilateral triangle with side length b to conform to the PF geometry previously designed.
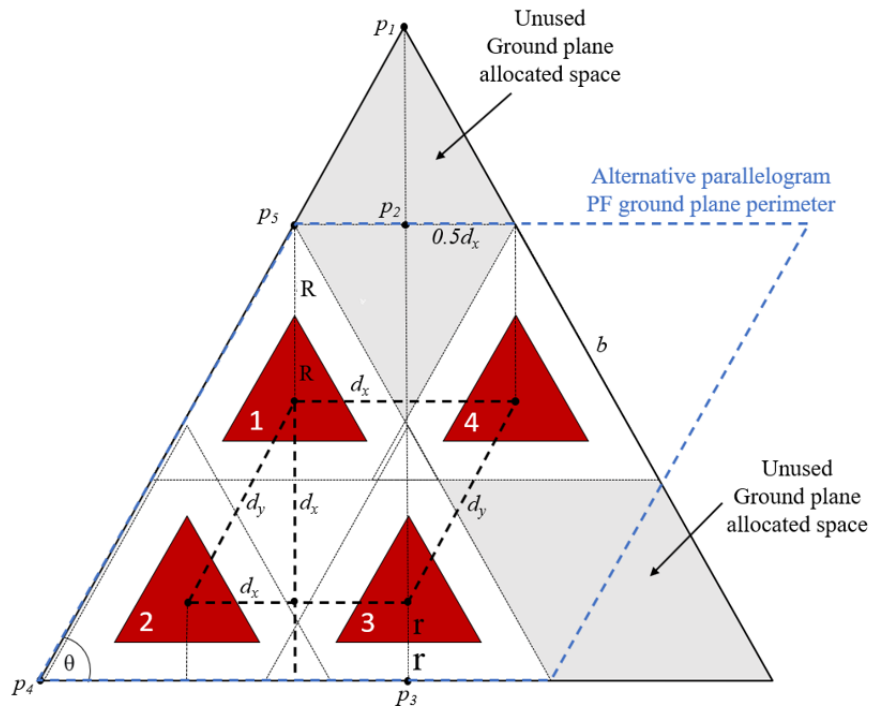
Figure 3.19: Fitting four elements arranged in a triangular lattice on an equilateral planar face

To fit the four elements inside an equilateral triangle, a side length b, as per Figure 3.19 is required. For the avoidance of doubt, the sides of patches 2 and 3 are not perfectly aligned with patches 1 and 4. This is since the angle between d_x and d_y is equal to 63.43° (arctan 2) as opposed to the 60° angle between sides of an ETPA.

From Section 3.2.3 it has been concluded that the value of b must not exceed 1446 mm. To meet this constraint, the element spacing d_x must be calculated through the following formulas:

$$\sin\Theta = \frac{p_1 p_3}{b} \tag{3.13}$$

$$p_1 p_2 = \frac{d_x}{2}\tan\Theta \tag{3.14}$$

$$p_2 p_3 = 3R + d_x \tag{3.15}$$

Re-arranging (3.13) to (3.15), d_x may be expressed as:

$$d_x = \frac{b\sin\Theta - 3R}{1 + \frac{\tan\Theta}{2}} \tag{3.16}$$

From (3.16), with a value of $b = 1446$ mm, the maximum distance between antenna elements d_x can be 370.36 mm which equates to 0.539λ through the use of (2.4). The distance between elements d_y is 414.08 mm or 0.603λ. A simulation was carried out in CST to assess the mutual coupling for the S_{32} parameters for d_x and the S_{12} parameter for d_y. These are plotted as the blue lines in Figure 3.20.
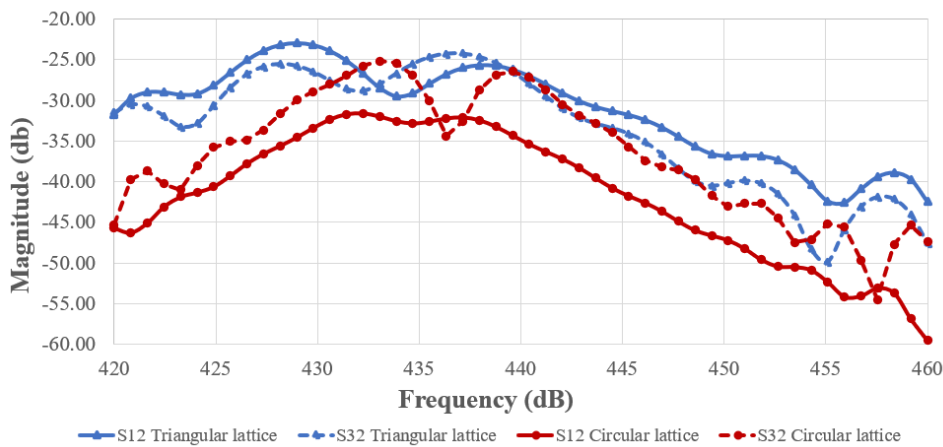
Figure 3.20: Mutual coupling simulation results comparison for PF with triangular and circular lattice with same side length b

From Figure 3.20 it is visible that the mutual coupling is in the range of -25 dB. Considering that the transmission mode of Req.3 is half-duplex, an antenna isolation of -25 dB may be considered suitable. However, in order to improve the isolation and also to reduce further the physical dimensions of the PF, an alternative arrangement for the placement of antennas was investigated. Rather than needing to introduce an additional mutual coupling technique which may complicate further the manufacturing process, the preferred solution was to better utilize the ground plane

space of Figure 3.19. Hence, the elements were placed in a circular lattice configuration with one centre element and three elements on an outer concentric ring as per Figure 3.21.
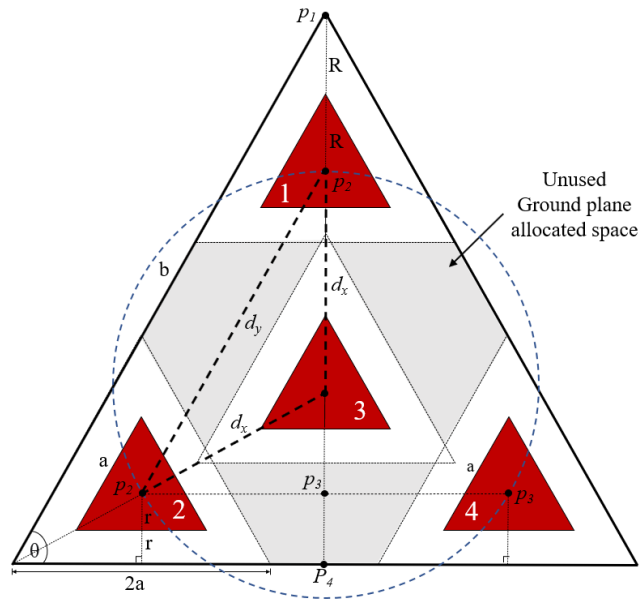
Figure 3.21: Placing four ETPAs in a circular lattice with a common equilateral triangle ground plane

The element spacing d_x may be expressed through the following formula:

$$d_x = \frac{b}{\sqrt{3}} - 2R \tag{3.17}$$

From (3.17) with a value of $b = 1446$ mm the maximum distance between antenna elements d_x can be 460.73 mm which equates to $0.671\,\lambda$. The distance between elements d_y is 798.01 mm or $1.162\,\lambda$. A smaller value of d_x of $0.65\,\lambda$ is selected to slightly decrease the side length b. This allows some room for the GDPAA structure to be inserted adjacent planar faces. The effect of mutual coupling on the planar face with circular lattice configuration is plotted via the red lines in Figure 3.20.

It is clear that there is major improvement in mutual coupling by up to 10 dB. This results from the different lattice configuration which increases the antenna element spacing. Furthermore, the author has shown in a recent publication [165] that even when the antenna element distance d_x is kept constant between both lattice configurations ($0.65\,\lambda$), the circular lattice demonstrates an improvement in antenna isolation over its triangular counterpart. The ground plane in the referenced study consists of a parallelogram rather than an equilateral triangle, marked in blue in Figure 3.19, however the lattice configuration is the same.

The counter-effect of increasing antenna element spacing is increasing grating lobes. In practice, the PF will not be required to perform beam steering at end-fire but rather to the maximum steering angle θ_{max} from the broadside of the PF as suggested by [93]. In Section 3.2.1 it has been established that θ_{max} is 41.81°. Hence a simulation for the radiation pattern of the circular lattice configuration was carried out in CST to ensure that whilst the mutual coupling has improved, the grating lobes are acceptable at θ_{max}. Figure 3.22 demonstrates that FNBW of the combined four elements of the PF without beam steering is greater than the maximum steering angle required hence the grating lobes are not an issue in this design.

To further validate the proposed design, the distance d_a for neighboring patches on adjacent PFs with a common side was considered as per Figure 3.23. An additional 20mm is added to the value of R due to physical design considerations of how the ground planes are designed to be mounted as per Figures 3.26 and 3.27. The element spacing d_a is 386.85mm or 0.563λ is considered sufficient as it exceeds the 0.539λ element spacing investigated for the triangular lattice configuration. The mutual coupling effect of the restricted spacing of elements on adjacent PFs will be further investigated in Section 5.1.4.
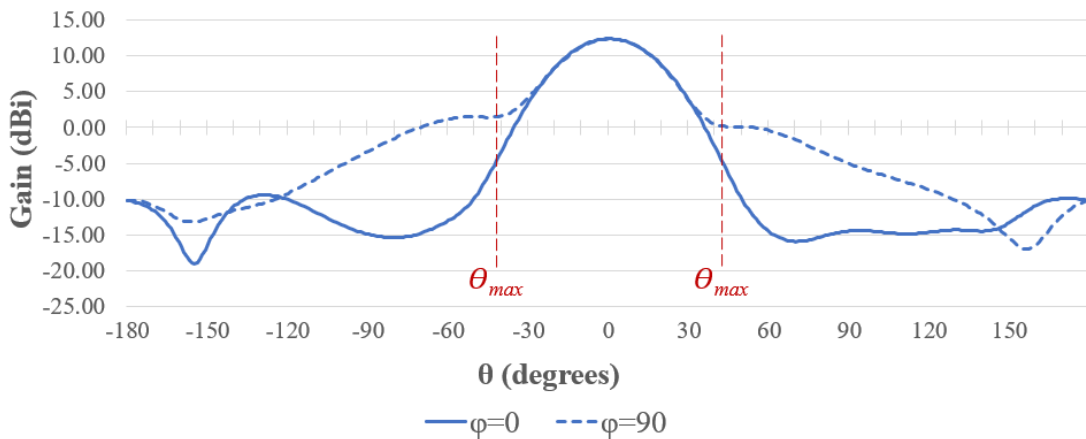
Figure 3.22 Preliminary far field gain inspection at maximum steering angle θ_{max} for $\varphi=0°$ and $\varphi=90°$
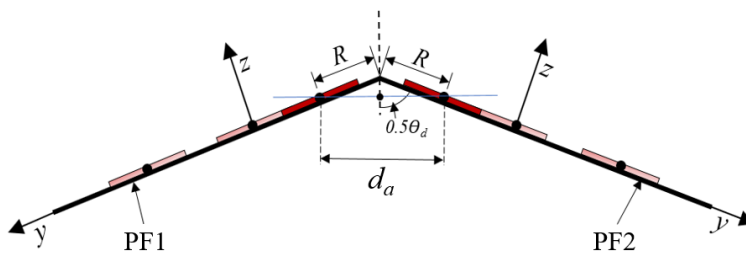
Figure 3.23: Distance d_a of antenna elements between two adjacent PFs

74

Equations (3.16) and (3.17) are used with a value of d_x of 446.43 mm (0.65λ) to allow the physical properties of the circular lattice arrangement to be compared to the triangular lattice. From the area of a triangle formula and (3.4) the values of Table 3.8 are derived. By placing four truncated-tip ETPAs in a circular lattice, a savings of ~22% on PF area and ~12% on the footprint of the icosahedron on its triangular counterpart. By using this lattice configuration with an antenna element spacing d_x of 0.65λ, the design parameters provided in Table 3.7 are considered fit for purpose and are used to produce the PF of the GDPAA.

Properties	Triangular Lattice	Circular Lattice
Side length b	1609.92 mm	1421.23 mm
PF area	1,122,300 mm^2	874,640 mm^2
PF area ratio	1.0	0.779
Icosahedron radius r_{ics}	1531.12 mm	1351.67 mm
r_{ics} ratio (footprint ratio)	1.0	0.883

Table 3.8: Physical properties comparison of triangular lattice and circular lattice arrangement with common value of d_x = 446.43mm or 0.65λ

The ground plane layer was exported from CST as per Figure 3.24 and manufactured at a local aluminium supplier using plasma cutting technology on 1.5mm sheet aluminium.
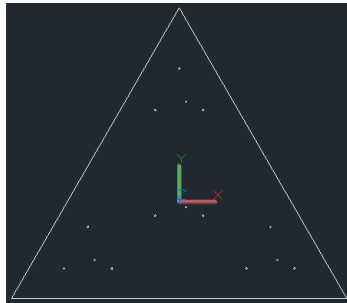
Figure 3.24: CST export of PF ground plane layer

3.4 Geodesic structure

Now that the PF has been designed, it must be fitted into the icosahedral structure which consists of a series of vertex joints and rods as illustrated from a custom-built scaled model in Figure 3.25a. GFRP material is selected once again as being the material of choice for the rods due its property of being radio transparent and at the same time robust and fit for a supporting structure. GFRP threaded rods have been sourced with a thickness of 17 mm as per Figure 3.25b.

A number of options for the vertex joints have been designed or modified to the 17 mm GFRP rod and printed using Polylactide (PLA) filament in conjunction

with a Creality Ender 5 3D printer. Various prototypes were manufactured as per Figure 3.25c including versions with long support for the rods (black prototypes) and inserting a webbed support (blue prototype). They were tested by inserting two rods into the joints and exerting manual pressure until they snapped. This technique demonstrated that the design that was found to be the most robust was a design for an icosahedron pipe joint available under the Creative Commons License [166]. For a 100% infill the part requires 49 g of PLA material. This is the white part of Figure 3.25c.

(a)   (b)   (c)

Figure 3.25: (a) GFRP threaded rod (b) prototypes of matching vertex joints: (b) short rod support version with flat vertex (c) webbed and long rod support versions

Once the icosahedron structure has been designed the planar face must be affixed to the GFRP rods. Considering that the air gap between the radiating patch and the superstrate is only 30 mm (h_3) and the need for this air gap to be consistent across all the surface of the PF, the superstrate is secured to the PF using nylon bolts, nuts and spacers as per Figure 3.26a. The superstrate and ground plane are then inserted into appropriate slots in a custom-built part with Autodesk Inventor Pro as per 3D render of Figure 3.26b. For a 100% infill the part requires 163 g of PLA material. A 25 mm hole is drilled into the GFRP superstrate on top of each feed point and sealed with a purposely designed cover. The purpose of this cover is to facilitate the physical inspection of the feed points for the quality of soldering joints should an anomaly be revealed from routine inspection.
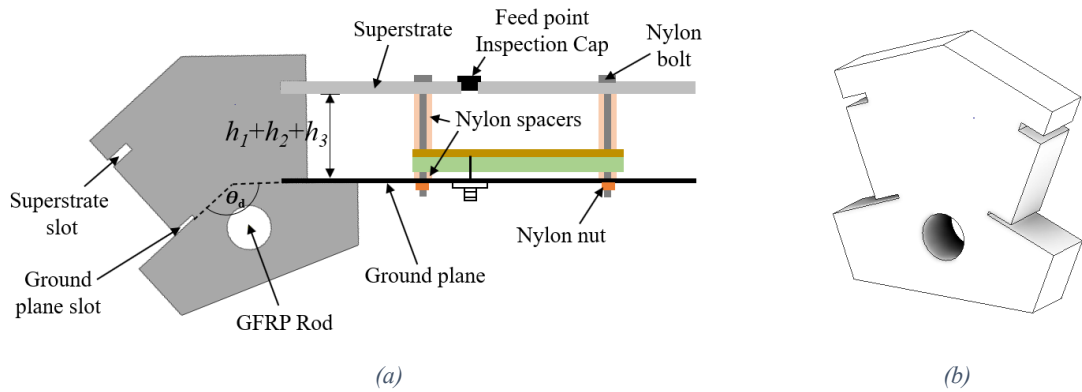
Figure 3.26: Design view of PF dihedral joint (a) Cross-sectional view with PF components (b) 3D render

A minimum of three parts are required for one GFRP rod as per Figure 3.27a. The purpose is to minimize the warping of the aluminum ground plane. Once the GDPAA is assembled, a strip of GFRP material will be laid in-situ on the icosahedron edges, ie. between PFs, to stabilize further the structure and to render it waterproof.
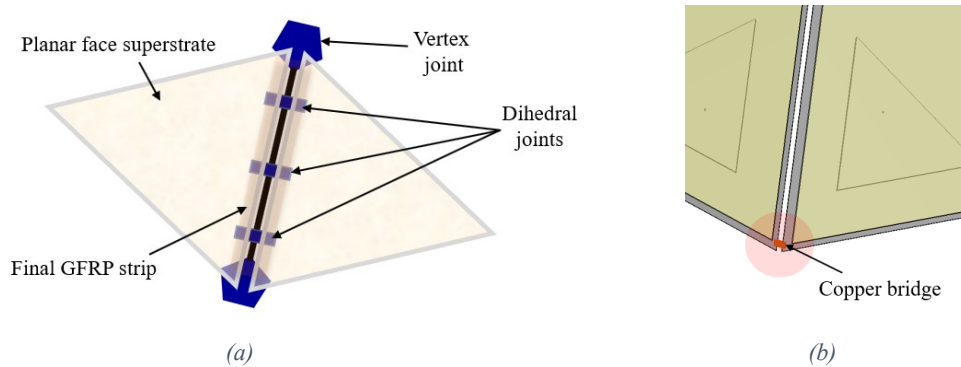
Figure 3.27: (a) Top view of rod, dihedral, and vertex joint assembly (b) Copper bridge for planar face ground plane continuity

A short copper bridge link towards the edge of adjacent PFs will join ground planes such that all ground planes are connected and have the same potential as per Figure 3.27b. A cable from one of the bottom PF ground planes will then be connected to a dedicated high current capacity earth electrode with low impedance 25 mm^2 conductors in the ground station room below the GDPAA. This structure is envisaged to mitigate the effect of indirect lightning strikes.

Based on the orientation of the icosahedron as previously discussed, the final GDPAA structure will rest on two vertices which in turn are placed on supporting stones as per Figure 3.28. The structure will be further secured by two additional supporting rods and four supporting cables. It is envisaged that the structure will be lifted into place through two hoisting rings.
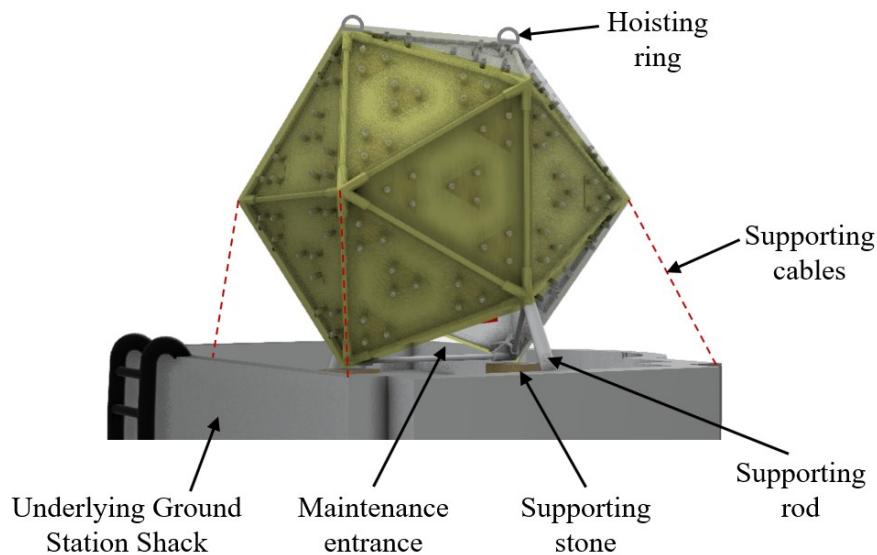
Figure 3.28: 3D representation of GDPAA and underlying support structure

3.5 Beamforming Architecture

An analogue beamformer is selected as the main BF architecture. This is due to two main reasons. Firstly, considering that the PAA is to be a low-cost system, an analogue BF architecture eliminates the used of DAC/ ADC pairs or SDRs for each antenna element which would significantly introduce costs. The SDR components often comprise of more than half the cost of the system [41]. Secondly, although support for multi-satellite tracking is required, it is envisaged that one beam will be required per PF where analogue BF is the common architecture in use. In [167] the author concluded that, an ABF architecture with capability for both phase and amplitude variation can be considered a good compromise for the mission at hand.

Nonetheless, a certain degree of flexibility is desired on each antenna element by retaining control not only on the phase but also on the amplitude. Instead of a series of phase shifters and step attenuators, a decision was taken to utilize a 4-channel DDS. This allows an element of adaptive BF to be carried out, provided a feedback mechanism allows the power level to be returned to adjust the weights.
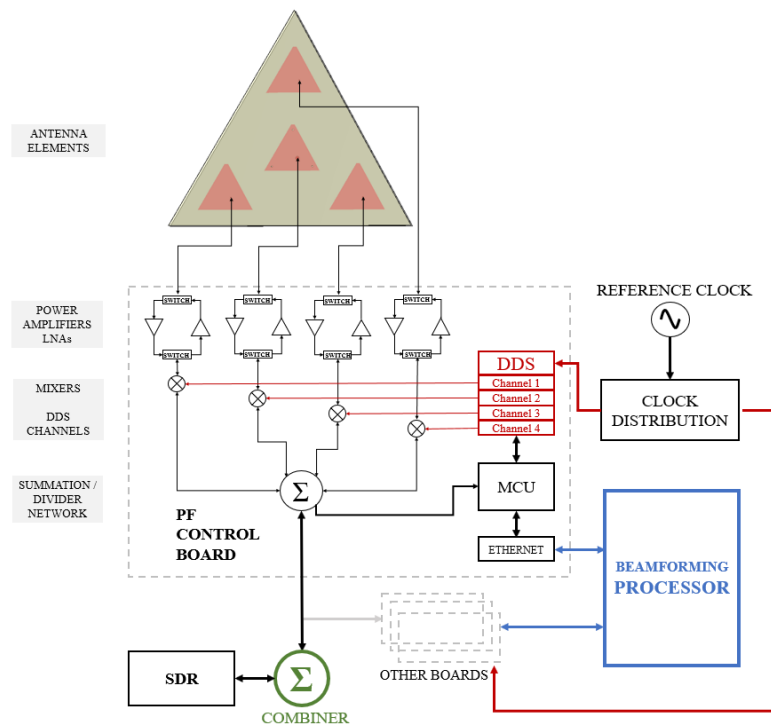
Figure 3.29: System block diagram of analogue BF architecture for GDPAA

Figure 3.29 shows the high-level analogue BF architecture design. The system starts with a reference clock, which is distributed to every DDS in the system. It is very important that all DDS reference the same clock. Four-channel DDSs are commercially available so the system was designed to utilize four-channel DDSs in order to avoid additional clock distribution circuits. Additionally, since one PF contains four channels, it is convenient to map one four-channel DDS device to one PF.

The individual antenna elements will be connected to a series of switches to alternate between the use of a power amplifier for transmission or LNA for reception. For the receiver signal chain, the amplified signals received from the antennas will be mixed with a phased carrier signal provided by the DDS.

The DDS is controlled by the BF Processor (via an intermediate microcontroller unit (MCU) over an ethernet interface. The BF Processor controls the phase for phase shifting, amplitude for additional complex weights if required, and frequency to cater for the doppler shift. A similar concept applies for the transmission signal chain. The output of the four phase-shifted signals is summed at a PF level, and further summed to form one signal which is fed to the SDR for demodulation or to separate hardware for down conversion before the signal is

demodulated and further processed. The BF Processor is a collection of software components discussed further in Section 3.6.

Based on the above-mentioned high-level system design, the design of the radio front end was carried out by Agius [110] with regular discussions and consultations. The low-cost 4-channel 500MSPS AD9959 chip from Analog Devices is selected as DDS. It has a 32-bit frequency tuning word, 14 bits of phase offset and 10-bit DACs which is considered adequate for this design. Most importantly, it has four interleaved cores with each core having its own registers, which allow for the channels to have different phase, amplitude, and frequency control.

Agius designed the system to comprise of four module types each with its own PCB. Various components have been selected for the desired frequency or operation. The first board is the Element Control Board which comprises of two AD9959 DDSs controlled by a PIC MCU and mixers. It also contains a divider and combiner capable of handling a modulated IF signal at 50 MHz via differential input and output. It provides an ethernet interface for communication with the BF processor. An abstraction layer of software within the MCU would allow the BF processor to control the various DDSs over ethernet.

The Element Control Boards (ECBs) are connected to two T/R Conditioning Boards, one on each side of the ECB as per Figure 3.30. The purpose of the T/R Conditioning Boards is to contain the amplification blocks, filters, and switches for each channel. The reason for the split by Agius is for flexibility and redundancy. This allows for a different T/R Conditioning Board to be designed for a different frequency range utilizing the underlying ECB. Furthermore, in the case of lightning it is envisaged that the components on the T/R Conditioning Board would fail first, being closer to the antenna elements in the signal chain. It is easier to replace this board on its own.

The ECBs are fed with a 10 MHz reference signal from the Reference Distribution Board, whose role is to provide each ECB with a synchronized reference from one original 10 MHz signal. Similarly, the Power Distribution board distributes power to the ECB.
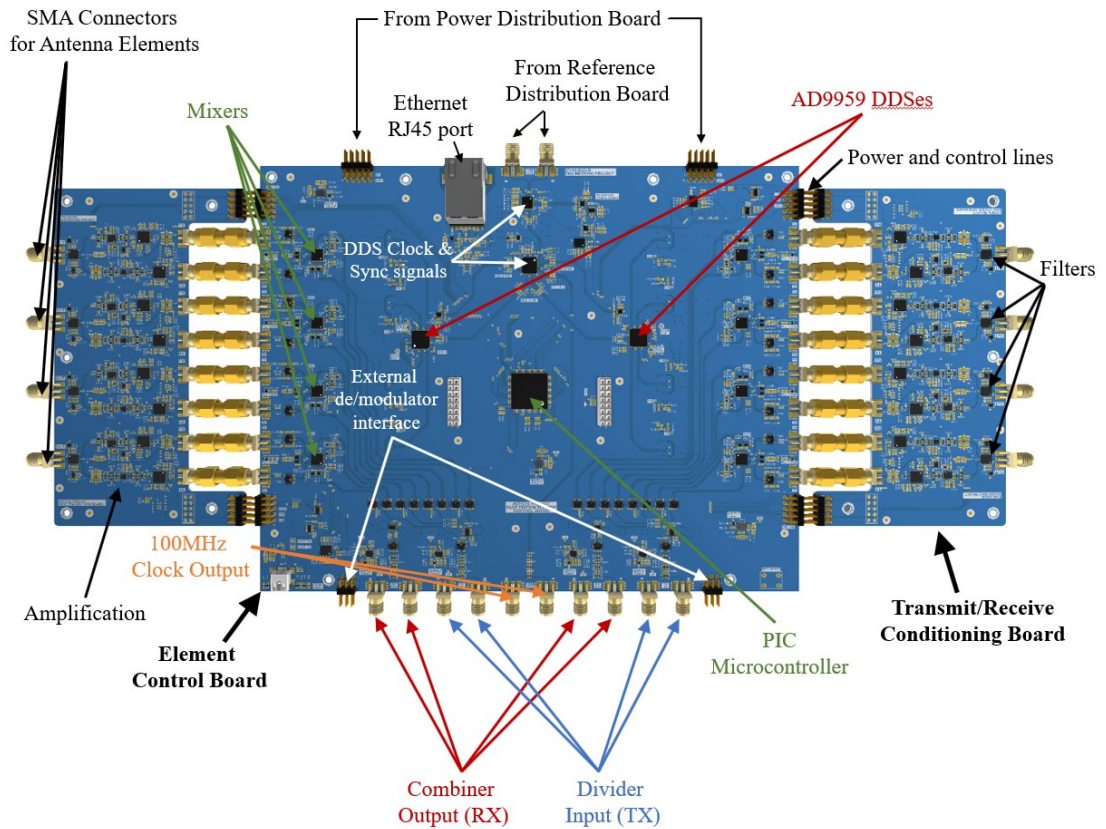
Figure 3.30: Element Control Boards and T/R Conditioning Board

The four boards are designed to be mountable and stacked. The initial system designed by Agius comprises of four ECBs, each separated by a shielding layer, which is in turn may drive eight PFs. The system may be upgraded by redesigning the Reference and Power Distribution boards to accommodate a maximum of nine ECBs. This allows for eighteen PFs to be utilized as two PFs are not utilized in the GDPAA as per Figure 3.28 which allows for an entrance into the interior of the GDPAA for inspection and maintenance purposes. The stacked boards are shown in Figure 3.31.

The inputs and outputs of the various ECBs of Agius need to be further externally divided or combined, respectively. Following on the work of Agius, Abela [168] designed a digital combiner and divider using Field Programmable Gate Arrays which would allow the BF processor to effectively select which combination of PF signals should be combined or divided. This work corresponds to the combiner component marked in green in Figure 3.29.
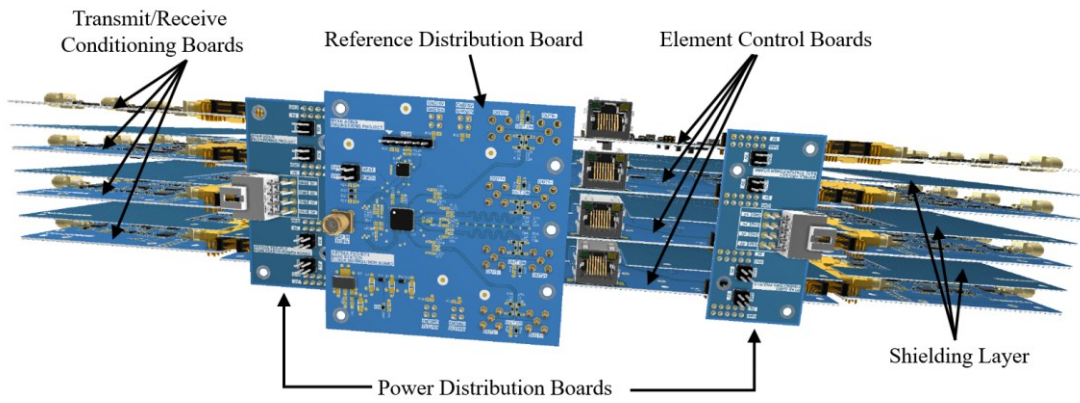
Figure 3.31 Front-end system stack comprising of Reference and Power Distribution Boards, ECBs, T/R Conditioning Boards and shielding layers

3.6 Array Software

3.6.1 Ground Station Software Architecture

For the GS to operate, it requires a series of components some of which out of scope of this project. Figure 3.32 demonstrates how these components interact together.
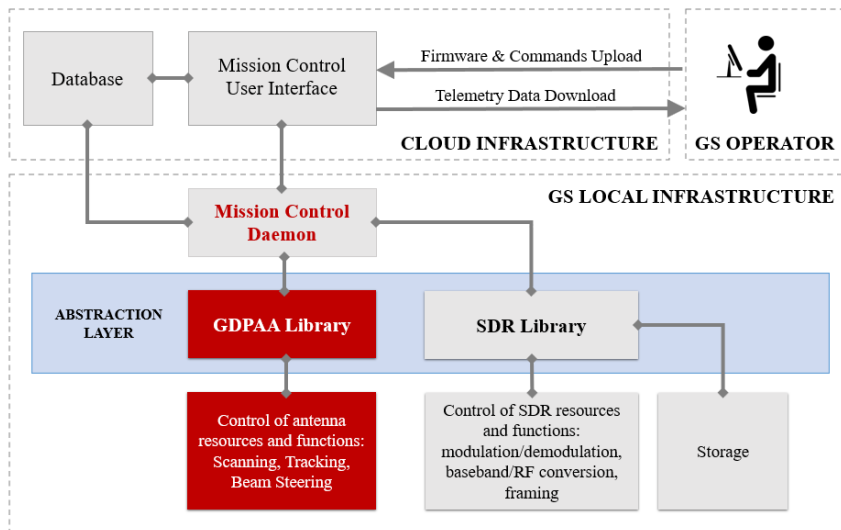
Figure 3.32 Complete GS architecture

The overall concept is based on the notion of a GS operator being able to access the system remotely for the full set of TT&C functions which include both the downloading of telemetry data and the upload of Firmware and commands. These functions will be available via a Mission Control User Interface.

It was originally desired that various components of the SatNOGS GSN would be leveraged to provide the user experience for the GS operator. However, as a result of the new MT.25 data link layer protocol implemented by Vassallo [138] for the uplink, direct control of the uplink chain is required, and a software dashboard

based on the same technology used by SatNOGS (Grafana) is being developed by the University to serve as a Mission Control Interface. Nonetheless, the software is designed in a way that allows the PAA to be plugged in easily into the SatNOGS GSN without any further development.

The interface leverages an underlying Mission Control Daemon (referred to as *daemon*) which controls the ground station via two underlying libraries and stores the information in a central database. It is envisaged that the database and interface components are stored in a cloud infrastructure, whilst the daemon is hosted locally to continue to function in the eventuality of an interruption of connection with the interface.

The data and corresponding modulated signal are generated through the SDR library currently being developed by Vassallo as a continuation of his work. For transmission, the output of the SDR will be a 50 MHz modulated signal which enters the front-end of the PAA designed by Agius. The PAA is subsequently controlled via a GDPAA library of functions designed and implemented by the author, further described in the remainder of this chapter and in Appendix 1. For the system to be demonstrated, part of a basic daemon is implemented in order to demonstrate the GDPAA library in use and carry out various tests as per Chapter 4.

Unfortunately, the system designed by Agius was not fully implemented in terms of a physical working prototype or the provision of the interface specification required to control the AD9959 DDSs via the PIC MCU. To proceed with the design and testing of the GDPAA an alternative mechanism had to be found. An AD9959-PCBZ development board for the AD9959 chip was acquired and tested. However, an alternative setup comprising of a COTS PCB with an embedded ST Microelectronics MCU and AD9959 chip in conjunction with an RTL-SDR was used as the preferred solution. This will be discussed further in Chapter 4. The underlying software is nonetheless very similar, with only minor modifications required once a working solution of the PAA front-end is delivered.

3.6.2 GDPAA Library

A GDPAA library must be implemented as an abstraction layer, to allow the daemon to utilize the antenna without the underlying complexities.
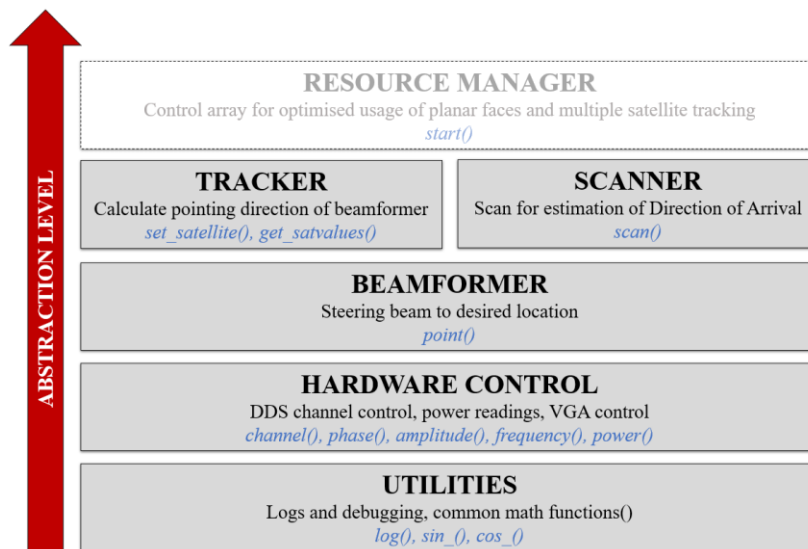
Figure 3.33: GDPAA Library functional architecture

The functions are grouped together in logical categories. The lower levels are functions intended to be consumed by other higher-level functions, which create a layer of abstraction for the daemon to utilize. At this stage of the project, due to time constraints, all the functions have been implemented within the same module as methods. It is envisaged that in the future, certain methods will be upgraded to object classes for enhanced flexibility and for multiple code versions to be used, such as is the case of the Beamformer where more complex beamformers may be utilized.

Python Version 3.7 has been selected as the programming language for the development of the GDPAA library. It has a simple syntax and fast execution. More importantly, it is commonly used in satellite applications and is inter-alia widely supported by the satellite and amateur communities. Various libraries for arithmetical functions, hardware control and ephemeris calculations are available, making it the language of choice. The category functions will now be discussed.

3.6.3 Utilities

The first functions developed are intended to avoid the duplication of code. At present these comprise of a function to store logs in a log file (*log()*) and functions to return the sine and cosine values for an angle in degrees (*sin_()* and *cos_()*). The various functions make regular use of the *log()* function for debugging purposes for the ground station operator.

3.6.4 Hardware Control

The hardware control control functions serve two main purposes: control of the DDS and the SDR.

Eventually, when this is developed by other parties within the ASTREA group, the radio front-end will have its own interface via the PIC MCU which internally control the two AD9959 chips. For this dissertation, functions were developed to interface to the alternative DDS setup described briefly in Section 3.6.1.

The phase, amplitude and frequency of the AD9959 are controlled via the interface of the COTS board through the *phase()*, *amplitude()* and *frequency()* functions respectively. The AD9959 chip, natively supports all settings to be stored in buffers and only one IOUPDATE command is required to re-program all the channels with all the required variables accordingly. The COTS board implementation requires that only one value for any one channel may be changed at any point in time. Hence, an additional function *channel()* changes the channel of the DDS before an instruction to change the phase, amplitude or frequency may be issued. No information is available in the specification of the COTS board however the delay between the changes of the individual channels is not considered to be material for the purposes the BF function described in the upcoming Section 3.6.5.

For the GDPAA to estimate the DOA, a feedback mechanism is to return the received power level. At this stage, such mechanism is being considered in the form of a hardware implementation within a new combiner being developed by an other student within the ASTREA group. This will be implemented at a PF level which is considered sufficient. In order for the system to be tested, a function *power()* has been implemented which returns the power level reading directly from an RTL-SDR which is selected as software radio.

The RTL-SDR is low cost SDR based on a Realtek RTL2832U chipset. A Python wrapper 'pyrtlsdr' is available for the 'librtlsdr' driver of the SDR. The RTL-SDR only outputs 8-bit IQ components per sample, so the accuracy is improved by taking several readings and returning the mean power. Increasing the accuracy slows down the execution time of the function.

The power reading is achieved via the 'matplotlib.pyplot.psd' function. This function is normally used to plot the power spectral density (PSD) P_{xx} by using Welch's average periodogram method. The maximum sample rate of the RTL-SDR is 3.2 mega samples per second (MS/s). A sampling rate of 2.04 MS/s has been chosen to reduce the effect of samples being dropped, which is more than sufficient considering we are only interested in reading the PSD for a specific frequency. 2^{14}

samples are read for every power reading, resulting in one reading every 8 ms, which is considered as a good compromise in terms of accuracy against speed and allowing the samples to be processed on a low-end processor. This will not be discussed further as the RTL-SDR is only used as a temporary solution for testing which will be discussed further in Chapter 4. The RTL-SDR produces a DC spike on the centre frequency which is misleading for power measurements. Hence, an offset of 50 kHz was introduced to shift the centre frequency.

Agius had planned for a data line between the ECB and T/R Conditioning Board to be able to control the VGAs from the PIC MCU and expose such functionality to the BF Processor. It is not envisaged that this functionality will be used as the amplitude of different channels may be controlled through the AD9959.

3.6.5 Beamformer

The beamformer is implemented through the *point()* method. The phase adjustments of elements 1, 2 and 4 in Figure 3.21 are calculated with respect to the central element 3. The coordinate system used is the azimuth-elevation.

To establish the phase calculations required, the incoming signal is considered in the form of a plane wave discussed in Section 2.1.5 and shown in Figure 2.9. The additional distance travelled to reach the individual elements depending on the azimuth and elevation angle of the incoming wave is computed. This is possible through knowledge of the distance between antenna elements d_x together with the frequency. The additional distances travelled with respect to the centre element as a ratio of the wavelength of the centre frequency, provide the phase differences for elements 1, 2 and 4 with respect to the centre element through the following equations:

$$Phase_1 = \frac{d_x cos\,\Theta\,cos(\varphi + 180)}{\lambda} \times 360 \tag{3.18}$$

$$Phase_2 = \frac{d_x cos\,\Theta\,sin(\varphi + 30)}{\lambda} \times 360 \tag{3.19}$$

$$Phase_4 = \frac{d_x cos\,\Theta\,sin(30 - \varphi)}{\lambda} \times 360 \tag{3.20}$$

where $d_x = 446.43$ mm, θ is the angle of elevation where $0°$ is the horizon and $90°$ is the zenith, φ is the angle of azimuth where $0°$ is North and turning clockwise, and λ is the centre frequency of the signal required. The coordinate system used in (3.18) -(3.20) and the respective software implementation is the horizontal

coordinate system. The value of $Phase_3$ is 0. A further computation within the method determines the element closest to the signal and adjusts the phases such that they are normalised with respect to the element closest to the incoming signal. This is done to ensure there are no negative phase values as the phase value to be passed to the AD9959 must be positive.

The maximum steering angle θ_{max} of the PF has been established at 41.81° so the minimum elevation is 48.19°. The maximum distance the plane wave needs to additionally travel to reach the last element is when the DOA angle is at the minimum elevation and distance d_y is maximum, such as at 60° clockwise from North in azimuth. The computed distance via trigonometric functions is 505.35 mm which translates to 0.736λ or 264.89°. This is within the capability of the DDS as a 360° phase shift is possible.

This function has been developed to deliver a proof-of-concept. The function must be eventually upgraded to take into consideration the orientation of the PF withing the GDPAA in the calculation of phases. Equations (3.18) - (3.20) will need to be modified to reflect this orientation together with the addition of an extra equation and subsequent phase calculation for the centre element.

A power level reading is returned at a PF level rather than an element level. Hence, it is not possible to use a system of complex weights featuring amplitude control.

3.6.6 Tracker

The tracker module is designed to consist of two main functions; *set_satellite()* and *get_satvalues()*. The purpose of the *set_satellite()* function is to obtain a fresh set of TLEs for a satellite that is to be acquired, if such TLEs are known. The TLEs are obtained via API from a well known established radio amateur with callsign N2YO who offers an API for satellite tracking. The code may easily be modified to utilize a TLE calculated by the University should this be required.

The PyEphem astronomy library for Python is used for ephemeris calculations. It allows the creation of a satellite object when provided with an updated TLE. The *get_satvalues()* function utilizes this satellite object by referencing the observer properties declared towards the beginning of the module to return a computation for a number of values for the satellite. The prime purpose is to return the azimuth and elevation angles of the satellite at any point in time with respect to

the ground station for the beamformer to steer the beam appropriately via the *point()* function. One of the properties returned from the PyEphem satellite computations is the angular velocity Δv, which is the relative velocity of the satellite when compared to the ground station. This value allows the doppler frequency correction Δf to be calculated for the satellite frequency f via the following formula:

$$\Delta f = \frac{\Delta v}{c} f \tag{3.21}$$

This value is returned via the *get_satvalues()* function. In this implementation, since full control of the SDR is available, the doppler frequency shift correction is being catered for as an adjusted frequency when the *point()* function is called. However, when the system is finally integrated with all other components of Figure 3.32 it may be decided to cater for doppler shift by reading the correct value from the acquired samples. In either case, the recommended option for improved beamformer accuracy is for the *point()* function to be provided with the adjusted frequency, despite the correction being minimal, in the range of a few kilohertz.

The *get_satvalues()* function also returns various other parameters when called; latitude, longitude and altitude of the relative position of satellite on the ground, range of the satellite to the ground station and an indicator as to whether the satellite is in the earth's shadow. The purpose of these parameters is purely for visualization purposes for any rendering required by the mission control interface.

Both functions may be enhanced further such that the *set_satellite()* function would return the satellite object and subsequently the *get_satvalues()* would require such object as an input parameter. This would allow multiple satellite values to be simultaneously computed in multiple-satellite applications.

3.6.7 Scanner

The PAA is required to electronically scan the hemisphere to estimate the DOA of a satellite. This is carried out on a PF level, whereby the field of view must be scanned. The maximum steering angle θ_{max} of the PF has been established at 41.81° which is being rounded to 40° for this implementation. For 40° of elevation and full azimuthal scanning, which will be referred to as the search area, fourteen thousand four hundred and forty measurements are required which is not considered practical considering that the average pass according to Vassallo [138] at the expected altitude of UoMBSat is expected to last over between six minutes. This is

further confirmed by [169]. The search time must only consist of a fraction of the total pass time, as a long search time would yield inaccurate results due to the constantly changing position of the satellite. Hence, a heuristic search strategy is adopted.

Three heuristic iterations are carried out. The first iteration consists of dividing the search area into twelve azimuthal segments and four elevation segments as per Figure 3.34a. These segment sizes have been selected to be smaller than the HPBW of the antenna as indicated in Figure 3.22. A power level is obtained for the angle of arrival in the centre of each of the forty-eight segments to determine the segment with the highest power level. Each segment comprises of 30° in azimuth and 10° in elevation.

<table>
<tr><td>(a)</td><td>(b)</td></tr>
</table>
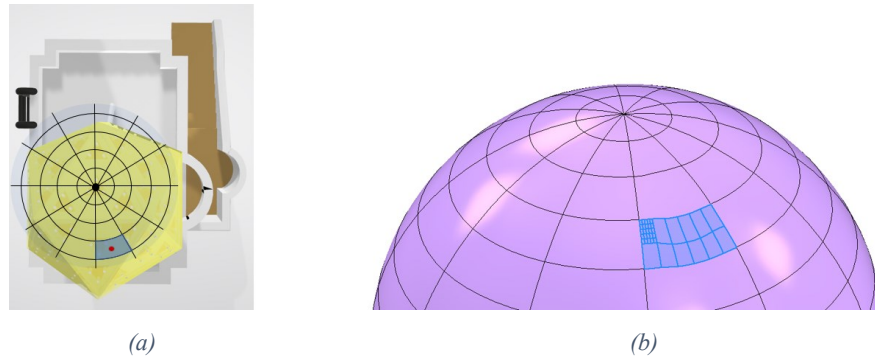
Figure 3.34: Scanner heuristic search by dividing search area into segments over 3 iterations (a) 2D view for 1ˢᵗ iteration (b) 3D view for 2ⁿᵈ and 3ʳᵈ iterations

The second iteration consists of splitting the selected segment into six parts in azimuth and two parts in elevation giving twelve segments of 5×5 degrees as per Figure 3.34b. Like the first iteration, a power reading is obtained for the angle of arrival at the centre of the segment. The third iteration consists of obtaining a power reading for each angle of arrival possibility on the 5×5 grid resulting in thirty-six readings. The selected heuristic iterations require ninety-six angle of arrival readings in total, reducing the number of readings by a factor of circa one hundred and fifty of the total possible combinations.

It is important to note that the satellite is a moving target. Consider the satellite on the exact edge of adjacent search segments A and B as per Figure 3.35. The satellite is travelling North, toward the centre of segment B. In the first iteration, the highest power level could be detected at the centre of segment A and subsequently the second and third iterations would home in on segment A, whilst the DOA of the satellite is now in segment B.
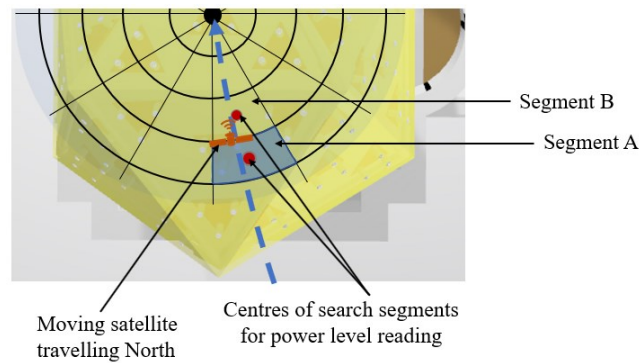
Figure 3.35: Moving satellite situated on the border of adjacent search segments

Due to time constraints, the scanner logic was not refined further to cater for this eventuality. Two options have nonetheless been considered as a solution to this scenario. In the first option, the second and third iterations would cater for the search areas of segments to be widened to overlap the adjacent segments as a tolerance for a moving satellite or satellite situated on the segment border. The disadvantage is that it would take more power level readings, although by a small margin. The second option would be for the scanner to have a memory of the iterative values and detect whether the power level in subsequent iterations has remained the same, increased or decreased. If the power level has remained the same or increased, this is due to the more accurate look angle returning a higher power level. If the power level is reduced, this could be a clear indication of this anomaly, and the iterative step may be reversed. This may also increase the amount of power level readings, however this approach gives more options for further optimization of the beamformer and is preferred.

3.6.8 Resource Manager

It is desired that the system has the flexibility to combine or divide the signal from any number of PFs in the system. Such functionality will require the implementation of a digital combiner which has been developed by Abela [168] and will be finalized through additional work by the ASTREA group. Once such functionality becomes available, the designed GDPAA Library software may be upgraded to host the concept of resource manager which at this stage has not been implemented due to its dependency on the combiner in development.

This function would retain oversight for the management of the different PFs and will contain the logic required to allocate different PFs to form sub-arrays which in turn could track multiple satellites. In this scenario additional transceivers will be required. It will serve as the final layer of abstraction for the daemon such that the

GDPAA will be treated as one system referenced via the GDPAA library, without the need for the daemon to manage the complexity of the underlying geometric configuration. For the purposes of daemon development, the functions previously described will be backward compatible for TT&C operations on one satellite. Upgrades to the library in terms of functions for multiple satellite tracking and more advanced control on the GDPAA, such as control of the active sector of the GDPAA.

Conceptually, the Resource Manager will determine the eligibility of the various PFs in satellite pass calculations. This will include whether the PF is a contributing PF to the satellite pass in terms of the satellite falling within its field of view or whether the PF is functioning correctly and not already committed to another conflicting satellite pass. To maximise the use of the GDPAA, the active sector and PFs in use may be dynamically changed in order to accommodate a particular TT&C requirement improving efficiency. This concept has also been investigated by [170]. The Resource Manager may also cater for graceful degradation of the GDPAA due to malfunctioning elements and provide health status metrics for an enhanced GS Operator experience. Once implemented, health functions for diagnostic purposes may return the status of the different components.

3.6.9 SatNOGS Integration

The SatNOGS open-source client [171] contains all the blocks required in order to successfully download telemetry data from a satellite of choice. For antennas with rotating capability, the SatNOGS client, via a hamlib rotctld command, sends the pointing location to the rotator interface controller, such as the Yaesu GS-232.

The GDPAA library *point()* function is the equivalent of the rotator interface controller and in order for the PAA to be used on the SatNOGS system an additional *satnogs()* function has been developed. This function accepts incoming TCP connections and parses incoming requests according to the rotctld protocol. Figure 3.36 demonstrates how these two functions integrate into the SatNOGS system.

The system was implemented however cannot be utilized due to two main reasons. Firstly, the SatNOGS client does not cater for a LO offset greater than one quarter of the sample rate. The maximum sampling rate of the RTL-SDR is 3.2 MS/s so the LO offset cannot be more than 0.8 MS/s. This is inadequate considering that the frequency of the DDS will be in the megahertz range. Various alternative approaches have been discussed with SatNOGS developers and the reference

'SoapySDR' source code [172] has been modified, however it requires further investigation [173]. Secondly, the SatNOGS client is not capable of passing the frequency as a parameter via the Rotctld interface, as under normal circumstances a mechanically steerable antenna does not require knowledge of the frequency.
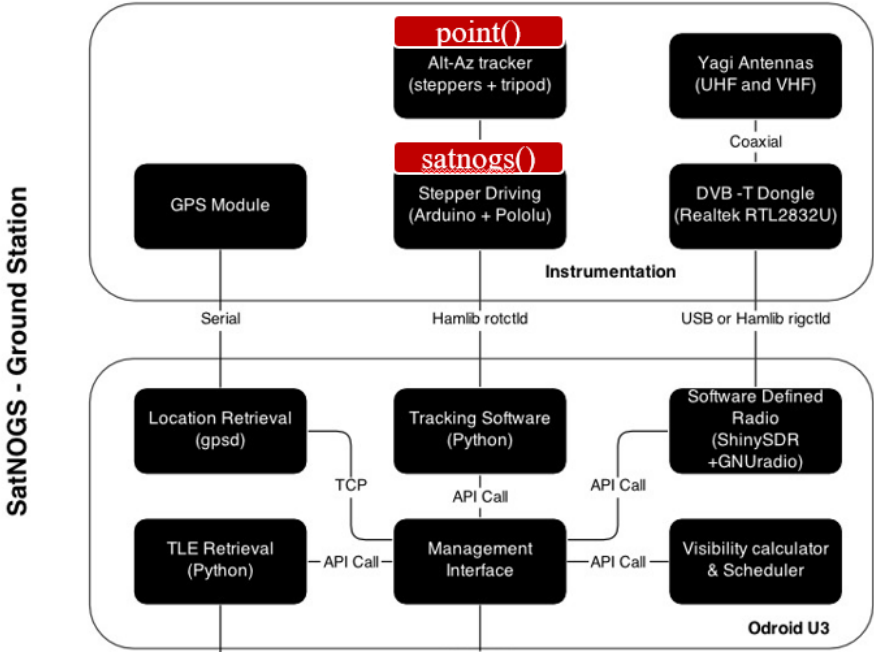
Figure 3.36 Part of the SatNOGS system design visualization with developed functions

3.7 Design Stage Conclusions

In this chapter a paradigm for the design of the PAA has been presented and the flow of the chapter has been based on the sequence of design steps according to this paradigm. First, the requirements and constraints of the research problem have been presented. A site selection was chosen, the overall dimensions of the PAA were restricted to the physical footprint constraint dimensions.

Subsequently the geometrical configuration was selected where a geodesic dome with an underlying icosahedron configuration was selected as the basis for the design. Several design choices on the antenna element and the placement of the respective elements within the faces of the icosahedron followed. Four truncated-tip patch antennas with FR4 board as substrate were manufactured and assembled on a common aluminium ground plane. An additional GFRP layer was mounted on the planar face to serve as a protecting radome, via the use of a system of custom designed 3D parts printed with PLA material. A fully functional PF was assembled and prepared for the subsequent testing as per Figure 3.37.
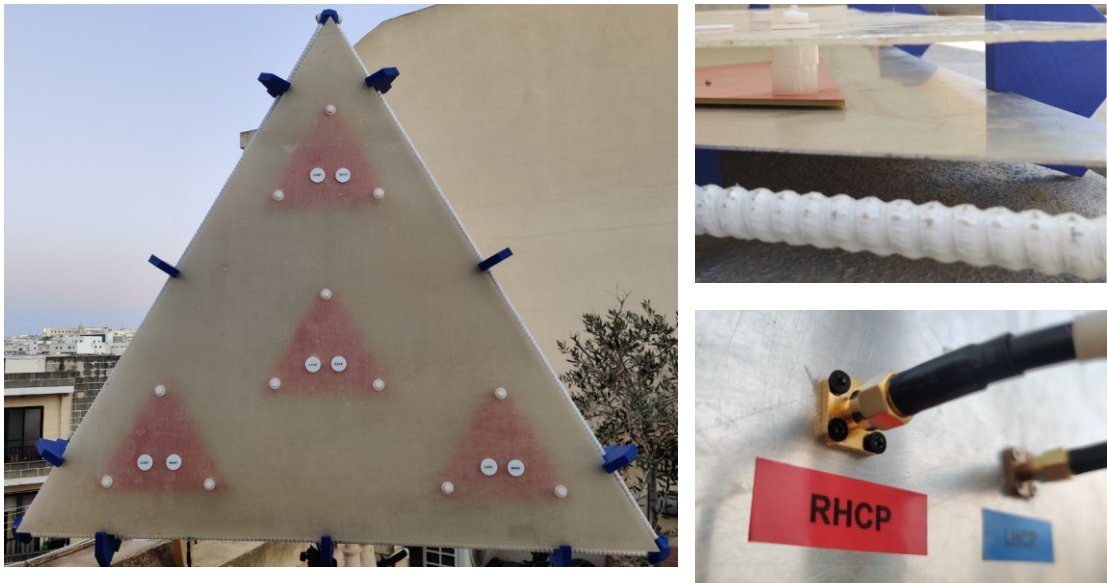
Figure 3.37: Final assembled planar face with corresponding GFRP superstrate, rods,3D printed joints and RHCP/LHCP feed points

Once the physical aspects of the system have been addressed, an analogue BF architecture was selected as the preferred architecture to drive the required phase shifting for the PAA to operate. The underlying front-end electronics to drive the PAA have been designed through separate projects of the ASTREA group.

Finally, the software aspect was addressed. A GDPAA library was designed and implemented in the Python programming language with supporting documentation. The system is described at a system and unit level. It is designed to integrate easily to the SatNOGS network. The basic PAA functions for BF, tracking and scanning were developed, together with an additional interface to an external SDR. This was put into place to allow for a fully working prototype to be produced and subsequently tested. The methodology for the generation and testing of simulated and measured results for the antenna element, PF and GDPAA, inclusive of BF tests, are discussed in Chapter 4.

Chapter 4: Testing Methodology

This chapter describes the methodology and approach used to test the PAA designed in the previous section. It describes the tools used, the tests carried out and the approach taken to ensure that the results of such tools are reliable. During this project, testing was an iterative process and interim results to aid the design process have been generated via the use of simulations. This chapter is divided into four main sections. First the computational electromagnetic software tools to carry out simulations are described along with the methodology applied to reliability of results. A receiver signal chain for the testing of software and BF is setup and described. The instruments and tools for measuring the results are then discussed and finally the tests carried out to produce the results.

4.1 Simulations

Throughout the design stage, 3D Electromagnetic simulation software tools have been used extensively. Various tools are available on the market, with two commonly used tools being MATLAB and CST Microwave Studio (CST). Throughout the course of this study, it has been found that although both tools provide similar functionality, they have different strengths and both tools have been leveraged.

4.1.1 EM Simulation Software

To effect EM simulations, MATLAB is a programming and numeric computing platform used extensively worldwide. It has various capabilities in different segments made available through toolbox add-ons. The Antenna Toolbox is a set of tools for design, analysis and visualization of antenna elements and arrays, and various options for the simulation of PAAs are available [174]. Via an inbuilt Antenna Designer, it is possible to design and obtain various impedance, S-Parameters, current and 3D radiation patterns in a very short timeframe, although it does not allow the addition of multi-layer substrates or superstrates via the designer. A phased array toolbox and respective antenna array designer also allows the fast iteration of designs; however this is limited due to the lattice options restricted to a choice of triangular and lattice.

This tool was used in the initial stages of this study in designing various antenna types discussed in Section 2.5 to facilitate the high-level selection of the most appropriate antenna element of for the PAA. The processing capabilities of

MATLAB were also used to compute the approximate intersection of 50Ω loci as discussed in Section 3.3.3.

CST is tool used for 3D EM modelling. It is acknowledged by MATLAB as being the most efficient and accurate in terms of computational solutions for 3D EM designs [175] and an interface between MATLAB and CST exists via CST's Visual Basic macro language. An antenna may easily be designed in MATLAB and the simulation run in CST to take advantage of both tools and has been used for initial prototyping. CST offers more EM solver options. It has powerful adaptive meshing techniques with superior control over various parameters for discretizing the mesh structure than MATLAB. From tests carried out, it is observed that inconsistent results are obtained in MATLAB when calculating S-Parameters on different frequency vectors as a result of auto-meshing that occurs on the antenna object. The matter was confirmed with MATLAB technical support as per Appendix 3.

In the early stages of the project, a prototype square patch antenna element was designed and manufactured on 1.6 mm FR4 board. Various corrections for the effective permittivity or side length were not considered at that stage and the resultant patch was resonant on 423 MHz. This patch was used to compare simulations produced by CST and MATLAB against measurements via the use of a VNA. This comparison is presented in Figure 4.1, whereby it has been noted that the CST simulation is closer to the VNA measurement. The additional control on simulation parameters, the extended choice of EM solvers and the proximity of simulated results to the measured results resulted in the choice of the CST tool for the remainder of EM simulations presented in this study.
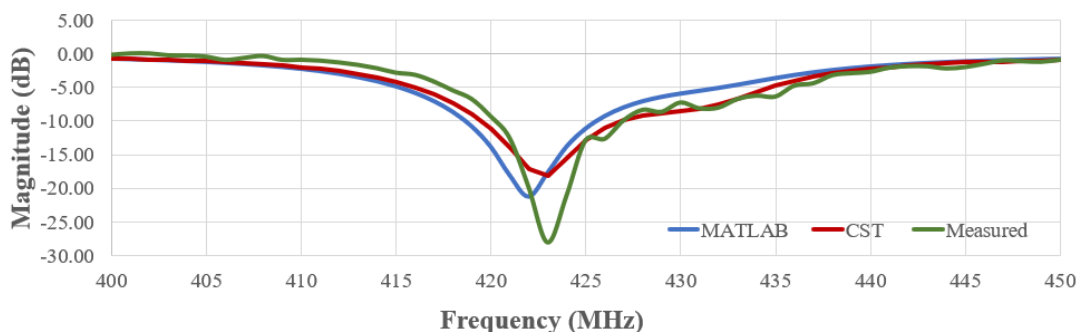
Figure 4.1: Comparison of MATLAB and CST simulations against actual measurements for a protype ETPA

4.1.2 EM Solvers

In this section the computation methods for the generation of simulations are described. All EM solvers essentially consist of discretization calculations of

Maxwell's equations in different forms, CST offers a wide range of solvers serving different purposes. The time domain and frequency domain solvers have been used in this study.

Time domain solvers are based on the progression of EM fields at discrete points in space and time. Two-time domain solvers are available in CST, the Transient Solver (TS) and the TLM solver. The TS is based on the Finite Integration technique, which as the name implies is based on a discretization calculation using the integral form of Maxwell's equations. It is the most versatile solver and the fastest, as the frequency behaviour across the required frequency range can be derived in one calculation run.

The way this works is by dividing the problem to be solved into smaller finite parts. The antenna is enclosed in a bounding box which is broken down into several mesh cells of a specific shape as per Figure 4.2. The TS utilizes a hexahedral mesh, so basically the mesh consists of various cubes whose size are controlled by the user through various parameters. The smaller the hexahedron, the finer the mesh and the more accurate the result.
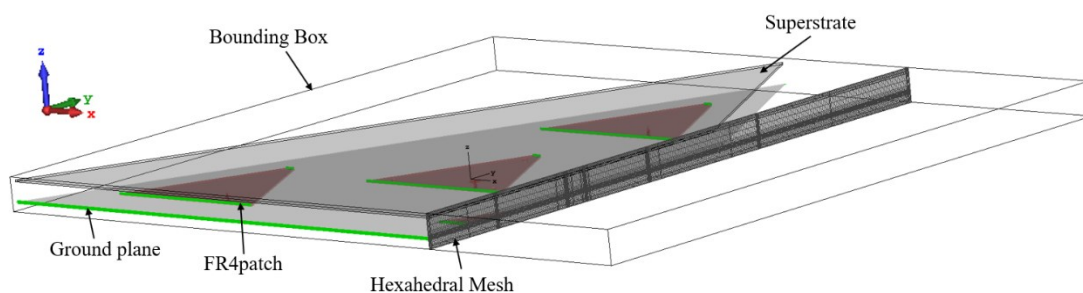
Figure 4.2: View of primary hexahedral mesh cut in the X-plane with bounding box

This mesh, known as the primary mesh, is used to calculate electric grid voltages and magnetic facet fluxes. CST automatically sets an orthogonal mesh for the calculation of magnetic grid voltages and dielectric facet fluxes [176]. Maxwell's equations are then used as the base to solve the EM field problems on the cells. The transient solver also uses various techniques for accuracy such as the Perfect Boundary Approximation. This is a technique whereby when there is more than one material in a cell, the average of the material properties is used depending on their fill ratio. This is important for the application described in this dissertation as the feed point structure is circular. A port is setup on the feed point in such a way that a signal may be sent to the port, and the voltages and currents are monitored through the incident and reflected signals calculated through the Discrete Fourier Transform.

When the signals propagate through the structure being analysed, due to numerical errors, the signal will not reduce to zero. The greater the reduction of the signal results in improved accuracy. A compromise between processing time and accuracy is required.

The TLM solver shares many features of the transient solver with an efficient meshing algorithm capable of reducing the number of cells required. In this study, the TS has been used for all simulations where possible. However, it has one limitation. All the ports must be located on the same cartesian plane which allows it to be used to carry out simulations on one PF, but not on two PFs or more, since the ports are located on planes oriented with an inclination equal to the dihedral angle from each other. The Frequency Domain Solver (FDS) allows such simulations. It is based on the Finite Element method which is used to solve partial differential equations within a boundary. The cell shape for a Finite Element method mesh is a tetrahedron. In this study this solver was used to simulate the radiation patterns of two adjacent PFs. Similar to the TS, the mesh of the frequency domain solver may be directly controlled through various parameters.

4.1.3 Mesh Independence Testing

Modern EM solvers increase the simulation control for the user but also increase the complexity. The user has to set the appropriate combination of parameters. It is relatively easy for the outcome of the simulation to be incorrectly modified via inappropriate parameter values. Hence, two main methods have been used throughout this study to ensure the reliability of simulated results. The first is Mesh Independence Testing (MIT) discussed in this section. In the following section continuous validation will be discussed.

The accuracy of the simulations is largely dependent on the mesh size which causes discretization errors. Hence, MIT, also known as grid independence testing, is undertaken prior to commencing the recording of simulated results. As the size of the underlying mesh cell decreases, the accuracy increases. On the other hand, the processing time increases. To find the best compromise, an exercise needs to be undertaken to perform a simulation with various iterations where the cell size is varied. The processing time is recorded, together with the difference in results for each iteration and compared. The S-parameters are used as the criterion for measuring the difference. When the difference between results is below an accepted

tolerance and meets the stop criteria, then the mesh cell size need not be reduced further.

CST offers adaptive mesh refinement capability which allows an initial mesh to be set and then automatically refined according to set parameters. Various mesh independence tests have been run and the final test will be now presented. The maximum size of the mesh cell is expressed as a fraction of the wavelength of the highest frequency of the calculation, which is 30 cells per wavelength. The range of 420 MHz to 460 MHz is used for this test. The minimum allowed size of the mesh cell is expressed as a fraction of the maximum cell size which was set to 1/20.

The adaptive meshing function is set to allow a minimum number of three passes and a maximum of seven, with the full range of S-parameters used as stop criteria. The maximum delta S value is expressed as a ratio. It was set to 0.01, meaning that if the difference between the S-Parameter values of the pass being computed is more than 1% of the previous pass values, the S-parameters would have been considered to converge and no further iterations of the test are required. The minimum number of delta S checks is set to three. The refinement strategy is set to expert system based with a mesh increment of three. The test was run on an AMD Ryzen 9 3950X 16-Core Processor with 64 GB of DDR4 3600 MHz RAM with Windows 10 Home operating system. The test performance results are presented in Figures 4.3 to 4.5 .

Every iteration increases further the number of cells. In the last pass, the cells per wavelength value have increased to 48, resulting in a mesh of 7.6 million cells as opposed to 2.8 million cells in the first pass, as per Figure 4.4. In Figure 4.5 it may also be seen that the solver time increases linearly to the same effect from almost four hours in the first pass to twelve hours in the seventh pass.
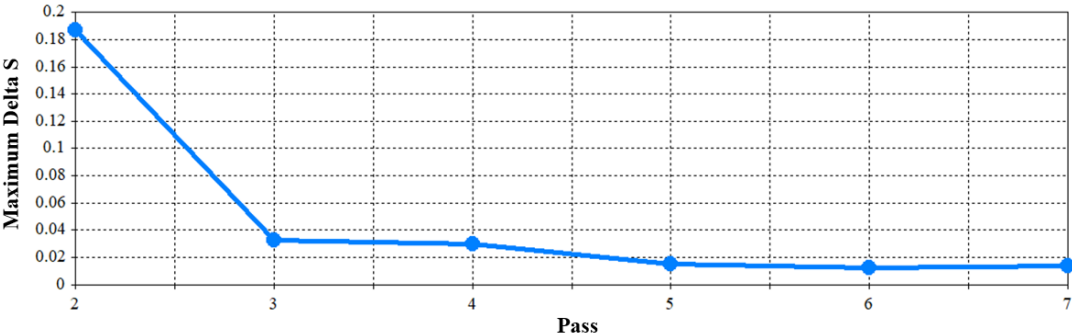
Figure 4.3: MIT result: maximum delta S per iteration pass

98

It is easily observable from Figure 4.3 that the mesh used in the first pass provides inaccurate results because of the large delta S value. The iterations significantly improve this value until the fifth pass, after which the results are similar, although the number of mesh cells used and consequently the solver time required are significantly larger. Hence, a mesh with a maximum cell size of 42 cells per wavelength is considered adequate for our study, with a total value of circa 6 million hexahedral cells being used in the EM solver computation and a total processing time of circa ten hours. The same mesh fineness is used in the author's published work [165].
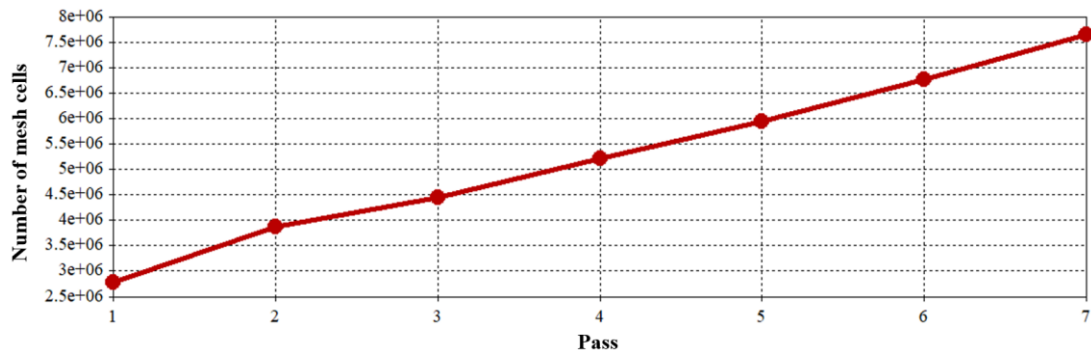
Figure 4.4: MIT result: number of mesh cells per iteration pass
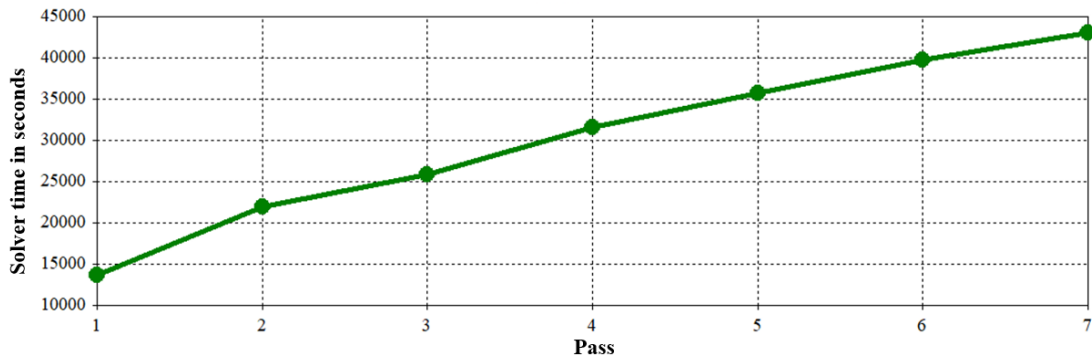
Figure 4.5: MIT result: solver time in s per iteration pass
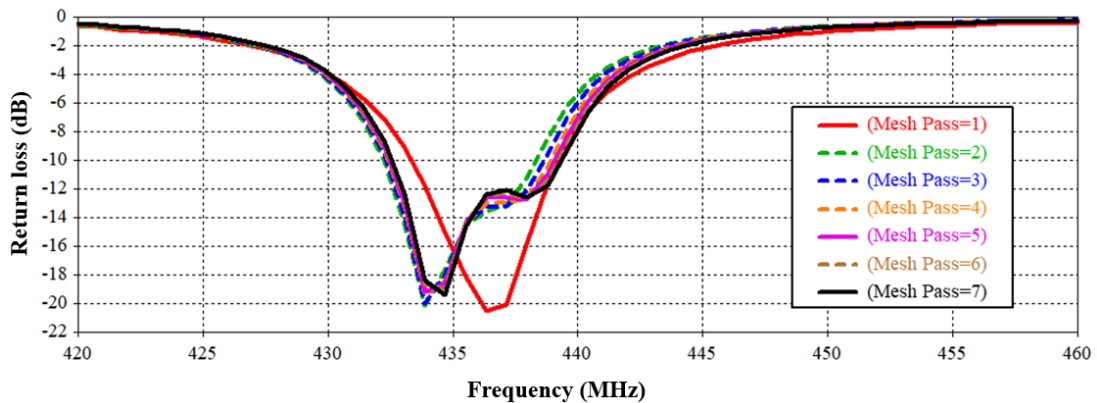
Figure 4.6: MIT result: S_{33} parameter per iteration pass

The S-Parameters of the different passes are shown in Figure 4.6 which confirms the conclusion that the fifth pass is adequate. It is observed in Figure 4.7 that the mesh refinement has a marginal effect on the radiation pattern.
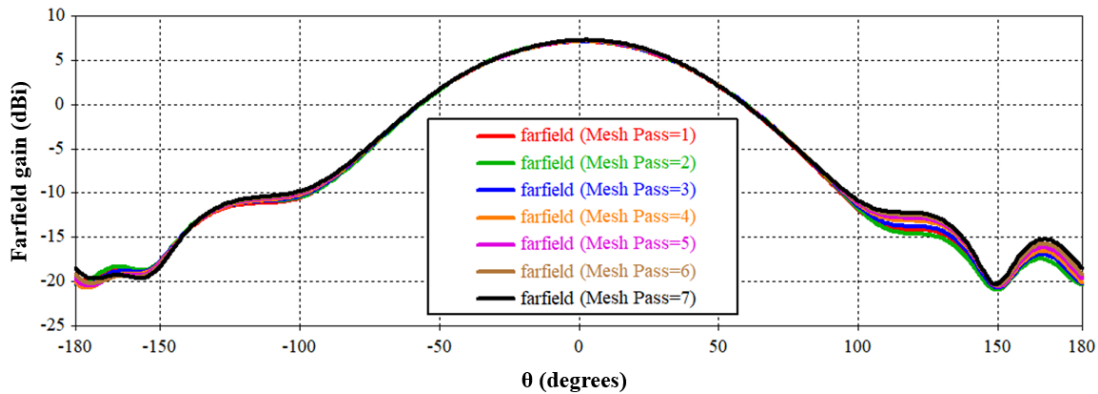
Figure 4.7: MIT result: Cartesian farfield gain plot for φ=0° on port 3 for the frequency 436.5 MHz per iteration pass

In this section the results of MIT for the TS are presented. MIT has also been carried out on the FDS however the test results are considered out of scope of this dissertation and are not presented further. As a general observation, it is found that there is a slight variance between solver results and some comparisons are made in Sectios 5.1.3 and 5.1.6.

4.1.4 Simulation of multiple PFs

To simulate certain properties of the GDPAA, a structure of two or more PFs may be simulated in CST. Figure 4.8 considers the scenario of two adjacent PFs. This creates a real representation of two PFs joined together via a common rod and dihedral joints as per Figure 3.27a. The PFs are azimuthally displaced by 180° and are inclined to each other by the dihedral angle θ_d.
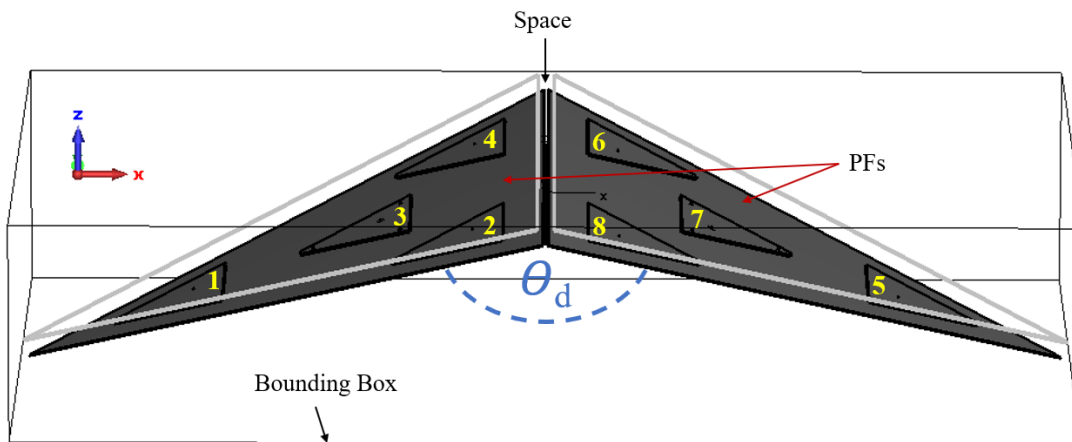
Figure 4.8: Simulation geometry setup of two azimuthally opposing PFs

CST offers a convenient functionality to create a customised array in the form of an array task as part of a simulation project. The coordinates of the different PFs are provided through a tab separated value file which imported to CSV. The PF structure is replicated and eight ports are available for EM simulations, one for each antenna element. These are marked with yellow numbers in Figure 4.8. The solver used for simulations of two PFs is the FDS due to its ability to perform simulations on ports not located on the same cartesian plane, like the ports of the antenna elements in the two-PF setup of Figure 4.8.

With the simulation hardware setup described in Section 4.1.4, it was found that to retain a suitable mesh size and a good accuracy solver order, a maximum of two PFs could be simulated before running out of memory. This is because due to the number of additional mesh cells required as a result of an additional PF.

4.1.5 Continuous Validation

Throughout the design process various antenna prototypes have been constructed. Various patches were manufactured using different parameters as per Table 4.1 and featured in Figure 4.9.

Different ground planes, dielectrics and patch materials were used to aid the design process. At each stage, measurements of S-parameters were compared to simulations to give the confidence that the simulations are reliable, prior to the final measurements being taken for the generation of the results of Chapter 5. Overall, the results are in good agreement with measured results.

Type	Internal Ref	Ground Plane	Substrate and height	Patch	Patch Type
Element	V0	Aluminium	Air	Aluminium	Square
Element	Patch V1	Copper	FR4 1.6 mm	Copper	Truncated square
Element	ETPA V2	Copper	FR4 3.2 mm	Copper	Truncated-tip ETPA
Element	ETPA V3	Aluminium	FR4 3.2 mm	Copper	Truncated-tip ETPA
Element	ETPA V3.1	Aluminium	PLA 2 mm	Aluminium Foil	Truncated-tip ETPA
PF	PF V1	Aluminium	FR4 3.2 mm	Copper	Truncated-tip
Element	ETPA V4	Aluminium	Air/ FR4 3.2 mm	Copper	Truncated-tip ETPA
PF	PF V2	Aluminium	Air/ FR4 3.2 mm	Copper	Truncated-tip ETPA

Table 4.1: Prototypes for continuous validation with modified physical properties

The ETPA and PF marked in blue in Table 4.1 are the final product used in the assembly of the PF and have been featured in Figure 3.37.
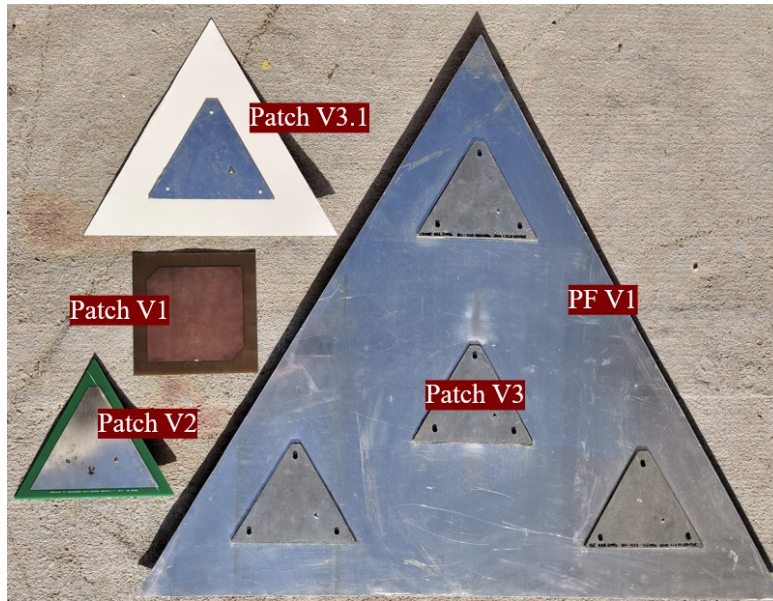
Figure 4.9: Patch and PF prototypes for continuous validation

4.2 Measuring Instruments and Tools

Various tools have been used for this project to measure S-parameters, frequency count, phase difference, power levels and to carry out experiments in general. These include a VNA, two oscilloscopes and a spectrum analyzer.

VNA

The main tool used for the measurement of antenna parameters was a VNA. The model is the miniVNA Tiny of Figure 2.8c which has been purchased towards the beginning of the project. This tool has been used extensively for the performance measurement of all prototypes and the final PF. The VNA has two ports, one for the device under test (DUT) and one for the detector (DET). When one antenna is being tested as a single-port device it is connected to the DUT port.

To measure the S-Parameters S_{ij} of a multi-port device, antenna j is connected to the DUT port where the signal is excited, and antenna i is connected to the DET port where the signal is captured. Internally, the VNA has a directional coupler at the DUT port, so the antenna connections must be switched to measure the coupling effect on each other. The S-Parameters presented in this study were captured in this way. It is interesting to note that the underlying waveform generator within the miniVNA Tiny is the AD9951, a one-channel DDS similar to the four-channel DDS used in the PAA and in this project.

An important step prior to using the VNA is to provide sufficient time for the electronic devices to warm up and stabilize, and to calibrate the device before each reading. The ports are connected to the end of the cables at the location where the antenna would be connected. This is to ensure that the delay and impedance characteristics are included in the calibration.

The VNA contains a calibration kit which includes a 50Ω dummy load. The manufacturer procedure is followed for reflection calibration as per Figure 4.10 and for transmission calibration as per Figure 4.11. The operating frequency range of the miniVNA Tiny is 1 MHz - 3 GHz. There are two modes of operation.

In the first mode the number of calibration data samples is not linearly distributed along the frequency of operation but concentrated in certain frequency bands. Between the operating frequency of 429 MHz - 442 MHz two thousand data samples are collected, one every 6.5 kHz, which is considered sufficient.

In the second mode, the calibration data samples are evenly spread. The first mode was selected for this study.
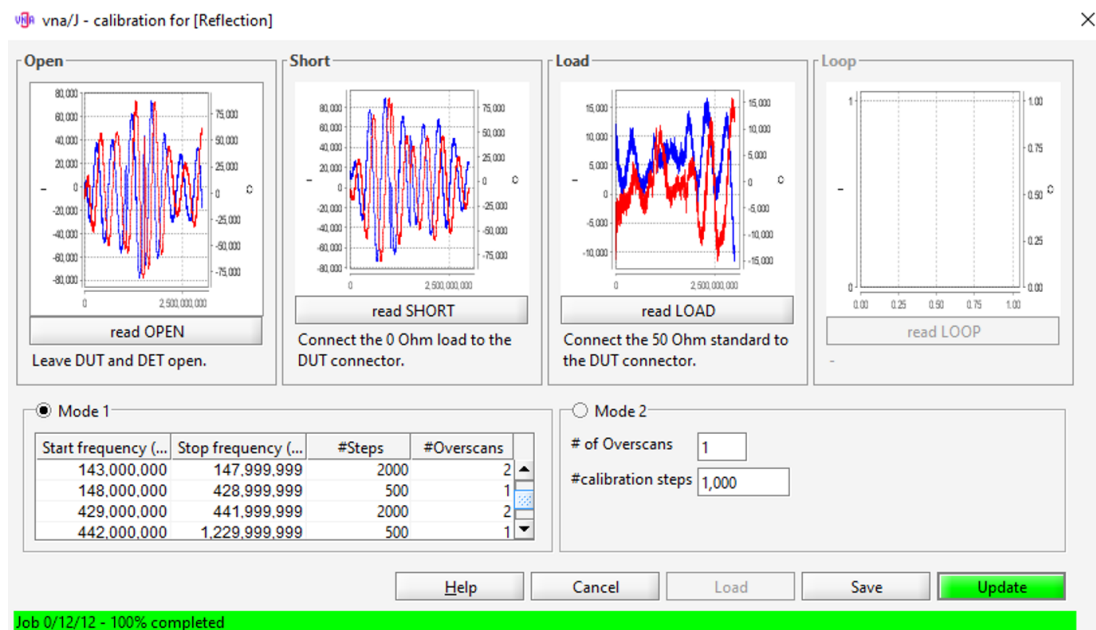
Figure 4.10: Calibration setup for miniVNA Tiny operating in reflection mode
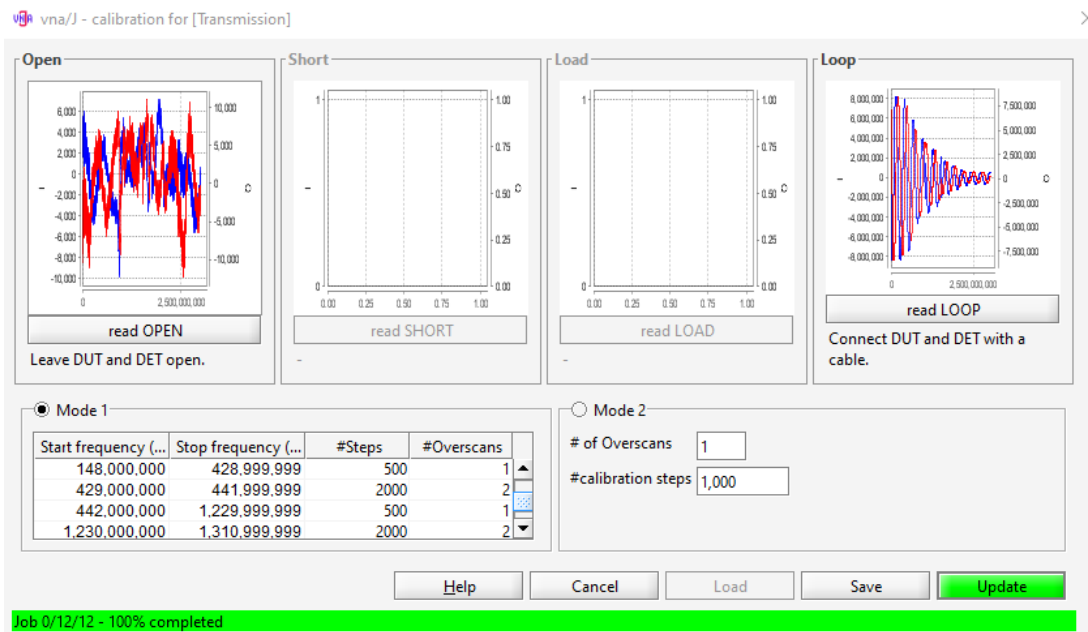
Figure 4.11: Calibration setup for miniVNA Tiny operating in transmission mode

Oscilloscopes

The Tektronix TDS2024C is 4-channel digital oscilloscope with a bandwidth of 200 MHz and a sample rate of up to 2 GS/s. It has been used during experiments carried out with AD9959 development boards primarily to debug the system and verification of output clocks from the boards. It is also used to verify the frequency accuracy of the DDS, together with the phase difference of the DDS and combiner.

The Hameg HM204 is a 2-channel analogue oscilloscope with a bandwidth of 20 MHz which has been used for day-to-day use to verify the state of various devices particularly during the software development cycle.

Spectrum Analyzer

The Anritsu MS2724B [177] is a high-performance handheld spectrum analyzer operating in the frequency range of 9 kHz to 20 GHz. It is capable of running in an automatic mode whereby measurements are captured and saved to an external USB drive creating one file for every set of measurements. The spectrum analyzer was provided courtesy of the University of Malta's Department of Physics and was used to carry out radiation pattern testing as described in Method 2 of Section 4.4.1.

4.3 BF Setup

As previously mentioned in Section 3.6.1, a separate project by Agius [110] which consisted of the radio front-end for the PAA was not made available towards

the end of this project. To address the gap a workaround solution was devised consisting of COTS RF modules in a limited amount of time. This will be described further in this section.

Considering that the purpose of this intermediate design is temporary, only the receiver signal chain was implemented. The proposed signal chain of Agius [110] is displayed in Figure 4.12.
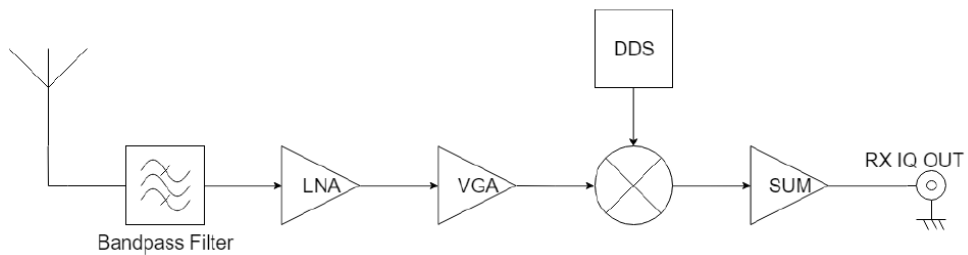
Figure 4.12: Block diagram of the receiver signal chain of Agius' radio front-end

The signal chain flow has been respected with two main modifications. The variable gain amplifier was omitted since the amplitude will be controlled via the DDS. Following the summation of signals, the combined output is directly fed to an SDR rather than an output an intermediate IQ stream. The implemented block diagram is shown in Figure 4.13. The actual setup is shown in Figure 4.14.
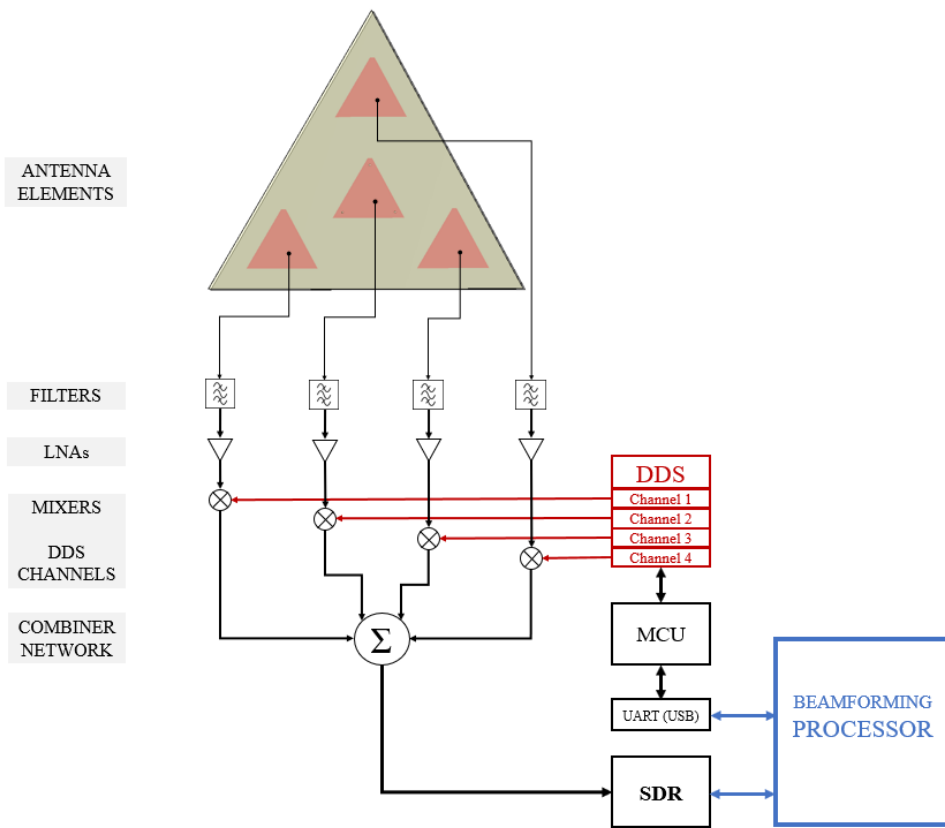
Figure 4.13: Block diagram of the proof-of-concept BF receiver signal chain
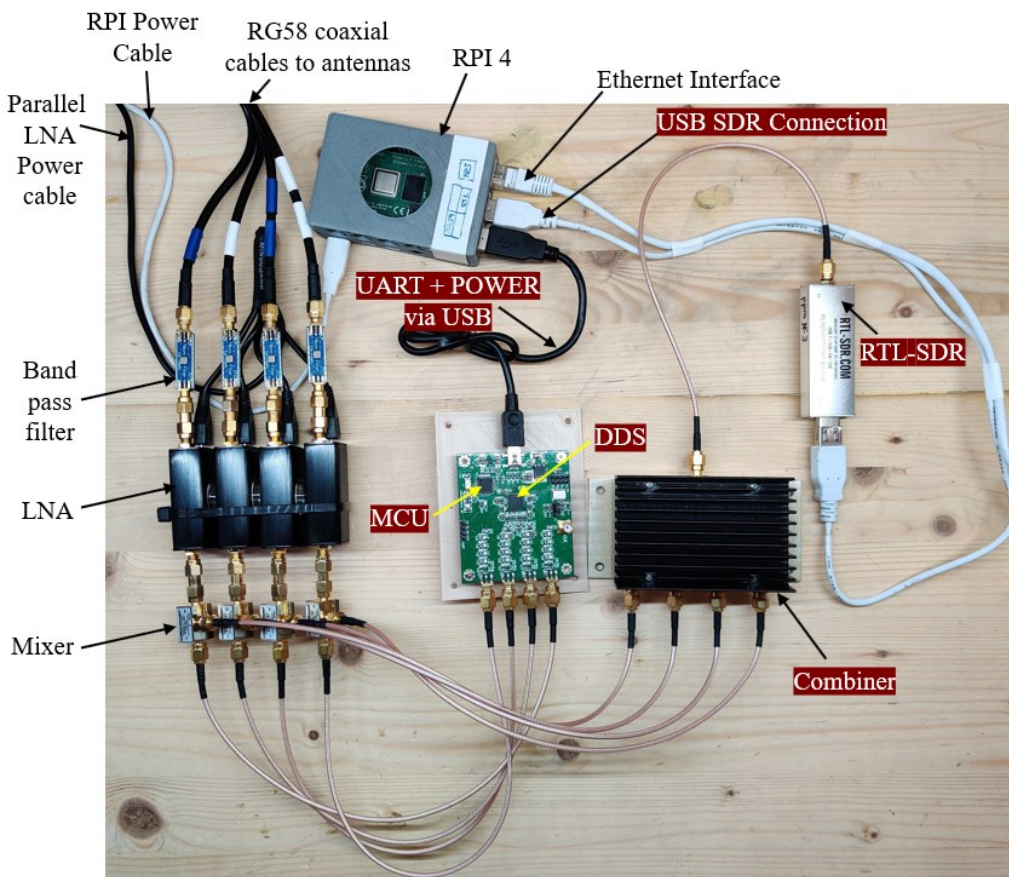
Figure 4.14: Actual proof-of-concept BF receiver signal chain

Bandpass Filter

The four antennas of the PF are connected via the RHCP feed point using four 5 m RG58 50Ω coaxial cables. The TST 1408 saw filter [178] is used as a bandpass filter, with a usable bandpass of 425 MHz - 445 MHz and a 2 dB insertion loss at 430 MHz - 440 MHz. This is confirmed via a VNA reading as per Figure 4.15a.

<table>
<tr><td>(a)</td><td>(b)</td></tr>
</table>
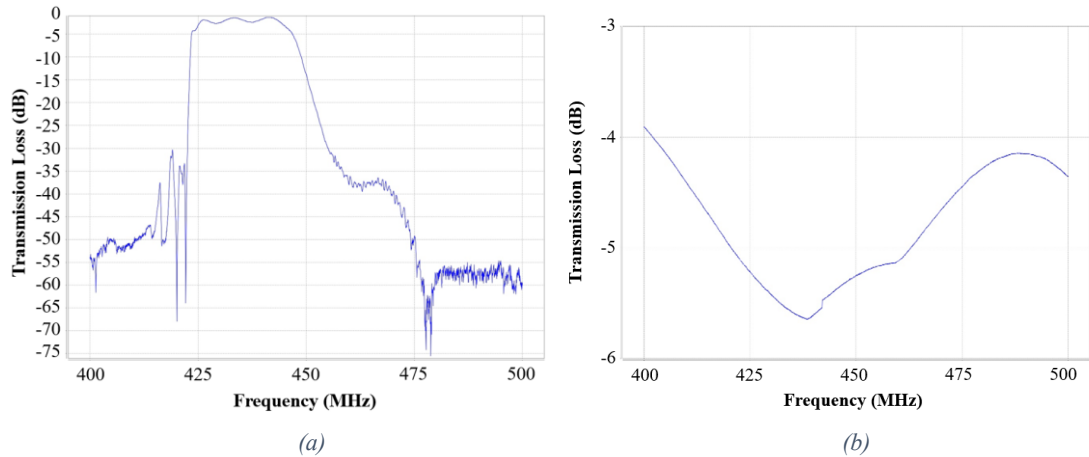
Figure 4.15: Transmission Loss for (a) TST 1408 saw filter (b) Nooelec wideband LNA attenuated by 30 dB

LNA

The selected LNA is the Nooelec LaNA wideband low noise amplifier [179]. It operates within the frequency range of 20 MHz - 4000 MHz. It offers 24 dB of gain at 435 MHz with a noise figure of 0.8 dB and a noise temperature T_n of 67 K. It is fed with a supply voltage of 5 V via a micro-USB port and a custom-built parallel power cable splitting the power between four devices. The gain was verified via the VNA and a 30 dB attenuator, as per Figure 4.15b.

Mixer

The amplified RF signal is fed to the RF port of the Mini-Circuits coaxial frequency mixer ZX05-1L-S+ [180]. This mixer has an operating frequency range of 2 MHz - 500 MHz. At 436.5 MHz the conversion loss is between 5.5 dB and 6.5 dB, depending on the power difference between the LO and RF signals.

An AD9959 module from Elecdemo [181] was purchased, housing an AD9959 chip and ST Microelectronics STM32 MCU. The MCU receives a set of AT commands via a UART interface over USB. The schematic diagram and command

set have been obtained directly from the seller and are attached in Appendix 4. Due to the unavailability of adequate documentation, the module was not used with an external clock but through the onboard reference crystal. The module is powered via USB. The channel output of the AD9959 module is connected to the LO input of the mixer.

Combiner

The four outputs of the mixer are connected to the Mini-Circuits high power combiner ZB4CS-440-12W [182]. The operating frequency is 100 MHz - 440 MHz and it has a low insertion loss of typically 0.6 dB. The base unbalance at 436.5 MHz is circa 1.7°.

SDR

The combined received signal is fed into an RTL-SDR device. The selected SDR is the RTL-SDR v3 [183]. It has an RTL2832U 8-bit ADC and operates in the frequency range of 500 kHz - 1766 MHz. An 8-bit DAC resolution translates to a dynamic range of 42 dB which is low however sufficient for the experiments carried out in this study. The automatic gain control functionality of the RTL-SDR is overridden to a manual gain setting of 19.7 dB. This value is generally accepted as being the gain with the best sensitivity performance. Due to its popularity the RTL-SDR is widely supported in various applications and software libraries. The third version of the RTL-SDR has been selected as it incorporates a temperature compensated oscillator (TCXO). The temperature drift of the TCXO is around one part per million (PPM) which improves significantly on previous models. To cater for the factory frequency offset, the device must be calibrated.

Calibration may be affected through a number of methods. The selected method is to utilize an SDR application such as SDR# [184]. A −10 dB signal is generated through a Baofeng BF-F8HP handheld radio with 1 Watt of power (30 dBm) and a 30 dBm attenuator so as not to damage the circuitry due to the close vicinity of transmitter and receiving device. A dipole antenna was used connected to the RTL-SDR and the centre frequency of the signal observed. The frequency correction is modified until the centre of the transmitted frequency matches the desired centre frequency as per Figure 4.16. It was found that that device frequency correction is 3PPM. This value is configured in the RTL-SDR parameter section of the GDPAA module discussed in Section 3.6. This calibration step is considered to

be important as the RTL-SDR is primarily used as a mechanism to detect the power level via the *power()* function.
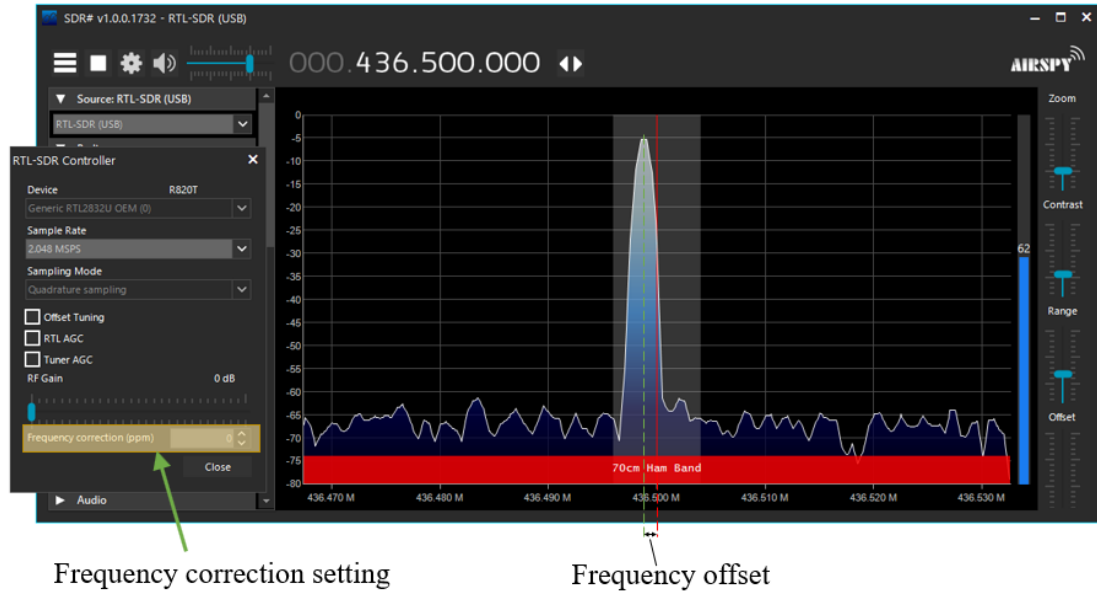
Figure 4.16: Selected calibration method of RTL-SDR device for frequency correction

The final net gain of the receiver signal chain setup is estimated to be 38.3 dB as per Table 4.2.

Device	Gain/loss (dB)	Net gain/loss (dB)	Source
RG58 cable	-1.5	-1.5	[185]
Bandpass filter	- 2.0	- 3.5	[178]
SMA coaxial connector	-0.2	- 3.7	[138]
LNA	24.0	20.3	[179]
SMA coaxial connector	-0.2	20.1	[138]
Mixer	-6.5	13.6	[180]
SMA coaxial connector	-0.2	13.4	[138]
Combiner	5.4	18.8	[182]
SMA coaxial connector	-0.2	18.6	[138]
SDR	19.7	**38.3**	-

Table 4.2: Net gain calculation of beamformer receiver signal chain setup

4.4 PAA Performance and BF tests

To allow the simulated results via CST to be validated against actual results, actual measurements must be taken. It is standard practice for antenna measurements to be taken in an anechoic chamber. Such chambers are rooms designed in a way to absorb any reflections from transmitting test antennas to ensure more accurate

measurement of signals received in the Device Under Test (DUT). They also isolate the test antennas from external noise in the environment. An anechoic chamber is available in the Department of Physics at the University of Malta. Unfortunately, it can only support frequencies of 700 MHz and higher therefore not being an option for this study.

As the best alternative an open area site was selected. An open area site minimises neighbouring noise from reaching the antenna under test. It also minimises the power being absorbed back into the antenna because of reflection. A second approach was taken to carry out measurements via an aerial method using an Unmanned Aerial Vehicle (UAV) for a portion of the radiation pattern. Both these methods in the context of their role in measuring various parameters will now be discussed.

4.4.1 Radiation Patterns

Method 1

For a full radiation pattern to be measured, a test setup was devised as per Figure 4.17. A reference antenna is connected to the DUT port of the VNA which generates a signal, and the PF is connected to the DET port of the antenna. The antennas are rotated according to the test being carried out, and the power received by the PF measured. With sufficient readings, different radiation patterns may be derived. Unlike the horizontal coordinate system used for BF and ephemeris calculations discussed earlier, for the purposes of measuring results for comparison with EM simulations, the Ludwig [186] coordinate system is used, also known as the spherical theta-phi coordinate system. What is previously measured as the azimuth in terms of the x-y plane is referred to as φ where $\varphi = 0°$ is located on the x-axis and increases in the direction of the y-axis (counter-clockwise) up to a complete turn of 360°. What is previously referred to as elevation in terms of the x-z plane is referred to as θ where $\theta = 0°$ is located on the z-axis. It increases to a maximum of 180° in the direction of the positive x-axis and decreases to a minimum of $-180°$ in the direction of the negative x-axis.
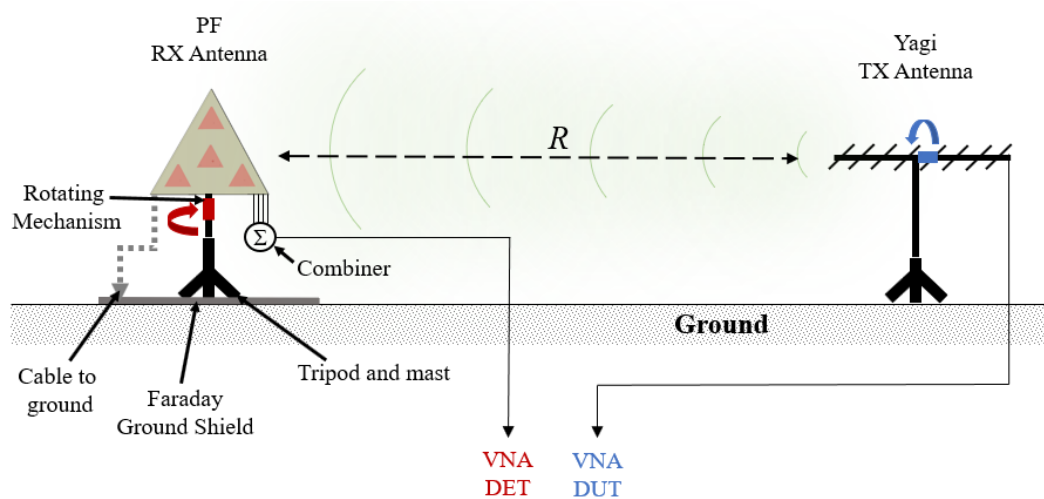
Figure 4.17: Setup for the measurement of radiation patterns

The reference antenna used is a 10-element Arrow II Alaskan [187] Yagi-Uda. A Yagi-Uda was selected because of its directionality and the standard HPBW for a 10-element Yagi is small at 40°. This focuses the signal into the direction of the PF minimizing reflection of surrounding objects and the ground. This antenna is also linearly polarised, which allows for different readings to be taken in different orientations. It has a low reflection loss of -32 dB on the centre frequency and was measured with the VNA prior to the tests being conducted as per Figure 4.18.

The custom mounting for the Yagi-Uda antenna is shown in Figure 4.19. The mounting was built using PVC pipe T-section and 3D custom parts. This allows the boom of the Yagi-Uda to be rotated on its axis to a degree of precision according to the rotation marker of Figure 4.20a. The rotation marker allows for readings every 10°. It was mounted on a tripod and mast 1.6 m above the ground.
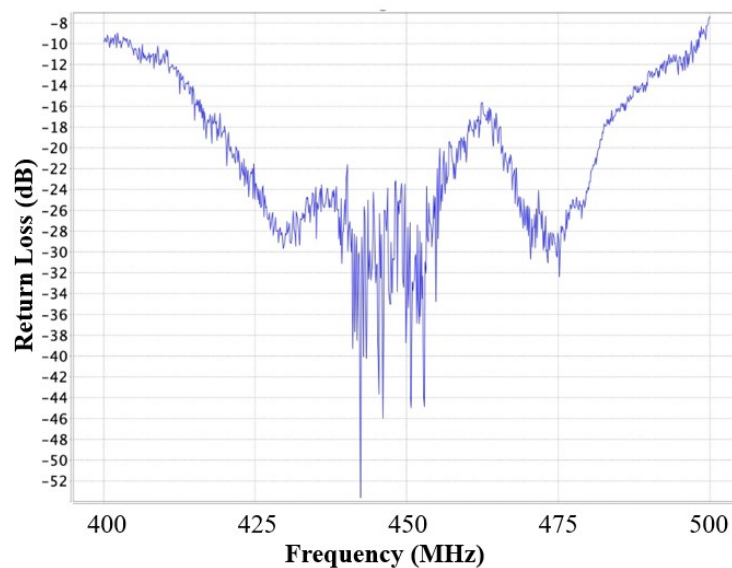
Figure 4.18: Measured return loss of reference Yagi-Uda antenna

111

Figure 4.19: Rotating mechanism for reference antenna

The PF was also mounted on a mast 1.6 m above the ground via a heavy-duty tripod. To minimize the effect of ground reflection a Faraday ground shield of dimensions 1500 mm × 2400 mm was placed beneath the PF with a mesh cell size of 12 mm × 12 mm. The ground plane of the PF was connected to the ground shield. The mast consists of several poles which allow them to be rotated without movement of the tripod base. The rotation marker band of Figure 4.20b was affixed to the mast such that an accurate rotation of the mast can be measured like the boom of the reference antenna also with 10° readings.

(a)   *(b)*

Figure 4.20: Rotation markers (a) reference antenna boom rotation for θ (b) PF mast rotation for θ

Six sets of tests are carried out, three of which to test one individual antenna element and the other three for the PF. For the individual element, the combiner of Figure 4.17 is not used, and the centre element (Port 3) is connected directly to the DET port of the VNA. All measurements apply to the 436.5 MHz frequency.

The first three tests are intended to measure the performance of an individual antenna. The first test consists of a farfield gain measurement with $\varphi = 0°$ and varying θ. The reference antenna is set oriented horizontally and the PF is rotated as per Figure 4.17. For every increment of 10° the power is recorded via the VNA. Thirty-six readings allow for a $\varphi = 0°$ cut to be plotted. In the second test the reference antenna is rotated 90° such that is now vertically oriented. Similarly, the PF is rotated and a $\varphi = 90°$ cut may be derived. The third test comprises of the broadside of the PF pointing to the reference antenna such that $\theta = 0°$. The reference antenna is rotated counterclockwise such that thirty-six readings are also obtained for a $\varphi = 0°$ cut. The three tests are repeated for the PF, whereby the four antennas are connected to the combiner, which in turn is connected to the DET port of the VNA.

112

Method 2

A second method was devised to create a 3D radiation pattern of the field of view for the maximum steering angle of the PF via the use of a UAV. The model used for this test was the DJI Matrice 600 PRO [188], courtesy of the University of Malta's Department of Geosciences. The UAV is capable of carrying a 6 kg payload with battery autonomy of circa 20 minutes. The necessary permits in terms of location and flight were obtained and the tests were carried out in the site marked A in Figure 4.21 and the test was carried out with Farhat [189] and the Department of Geosciences.

Figure 4.21: Site of UAV testing for radiation pattern measurement and BF test

The test was designed for a horizontal dipole resonating on 436.5 MHz and a signal generator with 17 dBm of power to be mounted on the UAV. The antenna PF was mounted horizontally, raised 1.1 m from the ground through additional GFRP rods as per Figure 4.22. The same Faraday ground shield used for Method 1 was used to avoid the reflection of power from the soil of the field into the back lobe of the PF. The four antenna elements were connected to the combiner via four identical 5-metre RG58 cables site. The output was fed into the Anritsu spectrum analyzer.
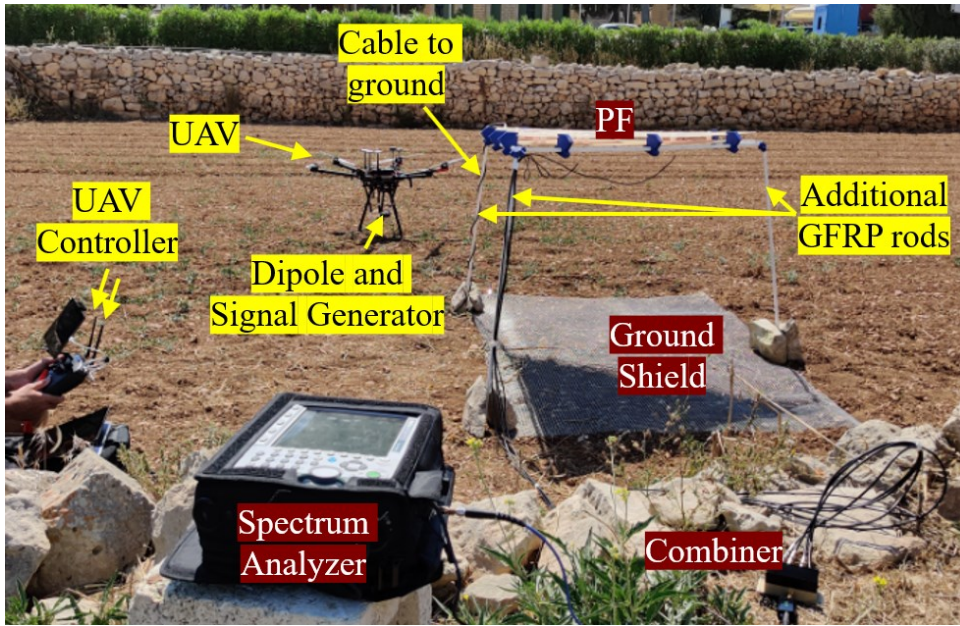
Figure 4.22: Field test setup of PF and UAV

The purpose of the test was to measure four elevation cuts with different readings of φ with fixed values of $\theta = 40°$, $\theta = 30°$, $\theta = 20°$ and $\theta = 10°$. A series of waypoints for the UAV are created as shown in Table 4.3.

The UAV flight path is determined through a user designer interface which allows concentric circles to be set and waypoints created as required. The reference point of the UAV was set to the centre of the PF. The UAV operator must provide the ground radius of the flight path required for the elevation cut, and the altitude. The values were calculated using basic trigonometric functions maintaining a constant distance of the UAV to the reference point of 40 m. This distance was carefully selected to avoid neighboring objects. The speed of the UAV was set to 2 m/s and the dwell time on each waypoint at 3 s. The waypoints from this interface are shown in Figure 4.23. They are also plotted in 3D using MATLAB and are shown in Figure 4.24.

θ value	φ step	Radius	Total Unique
40°	20°	40 m	18
30°	20°	40 m	18
20°	20°	40 m	18
10°	36°	40 m	10
0°	0°	40 m	1
Total			65

Table 4.3: Spherical coordinate UAV waypoints
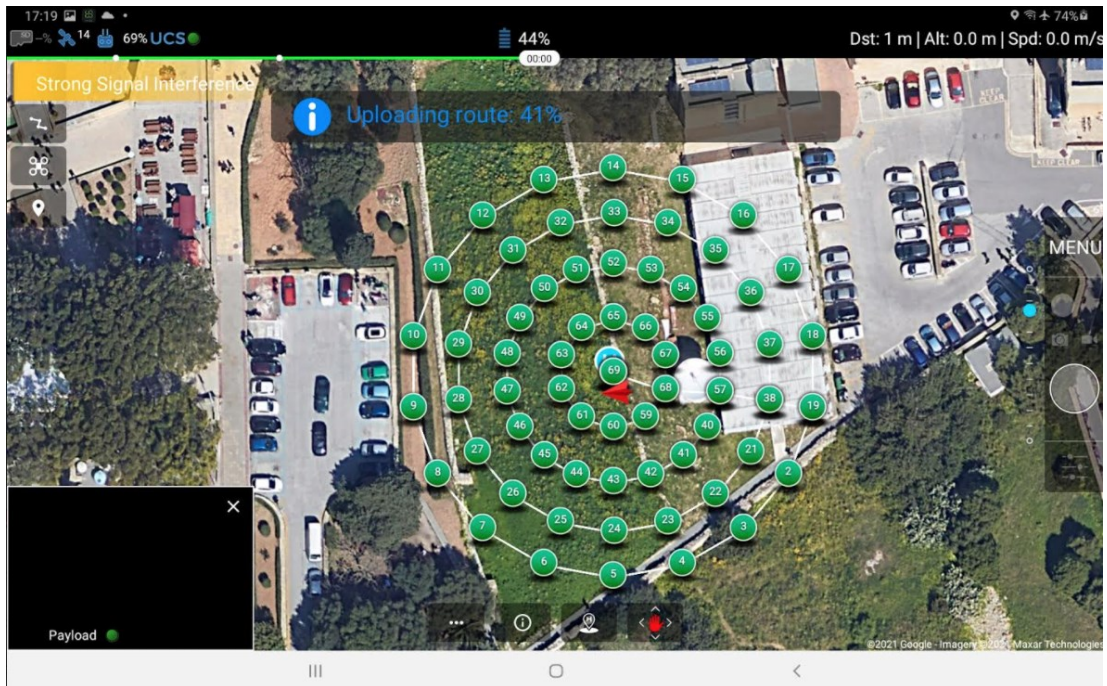
Figure 4.23: Screenshot of flight path showing waypoints from UAV designer interface

The transmitting dipole mounted on the UAV was set to continuously transmit a carrier wave during the duration of the entire test. The spectrum analyzer was set in automatic mode to capture a set of spectrum readings. By ensuring both UAV and spectrum analyze are synchronized to a common time, a power measurement for every location is subsequently possible via post-processing.
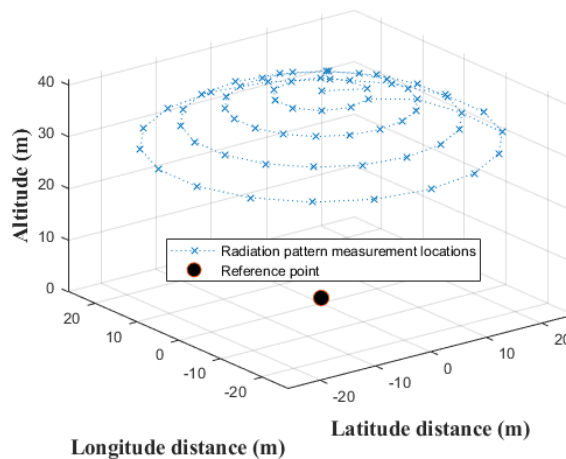
Figure 4.24: UAV 3D flight path plotted in MATLAB

4.4.2 S-parameters

For the measurement of S-parameters a similar setup to the one presented in Figure 4.17 for the PF is utilized. Considering the VNA is a 2-port device, all combinations of S-parameter measurements must be carried out for S_{ij} where the i port is connected to the DET port and the j port is connected to the DUT port.

Sixteen different measurements are taken to complete the full S-parameter set of the PF 4-port network.

4.4.3 Beamforming

In order to test the beamformer, testing in software and in hardware was carried out.

Beamformer software testing

The beamformer is implemented via the *point()* function which calculates the phase shifts via the implementation of equations (3.18) to (3.20). To test whether the equations are correct and whether their implementation is error free four values of azimuth and four values of elevation were selected giving 16 pairs of horizontal coordinates.

$$Azimuth\ values = [0° \quad 90° \quad 180° \quad 270°]$$

$$Elevation\ values = [48.19° \quad 60° \quad 70° \quad 80°]$$

The *point()* function was used to obtain the phase shift of the four antenna elements. The computed phase shifts were translated to Ludwig 3 coordinates and used to compute farfield elevation cuts for the phase-shifted combined radiation patterns of the individual antenna elements. A farfield elevation cut with a step size of 10° up to the maximum steering angle θ_{max} of 41.81° was produced for $\varphi = 0°$ and $\varphi = 90°$. These simulations allow the software implementation of the beamformer to be verified and the results are presented in Section 5.2.

Beamformer hardware testing

The interface to the AD9959 DDS described in Section 4.3, and the respective hardware control functions of *channel(), phase()* and *amplitude()* were tested via the Hameg HM204 oscilloscope. The channel, phase and amplitude of the four channels were changed for various values and verified on the oscilloscope for correctness. The values are arbitrary and their selection does not constitute part of the test.

In order to test the workaround setup described in Section 4.3 the configuration of Figure 4.25 was setup. The outdoor setup experiment is similar to the one proposed by Sumantyo and Takahashi [190]. It consists of a transmitting antenna mounted on a roof. A standard dipole resonating at 435 MHz was used for

the test. The DUT (PF) is mounted on the top of a car. By moving the car accordingly, various azimuth and elevation angles may be obtained.

(a)   *(b)*
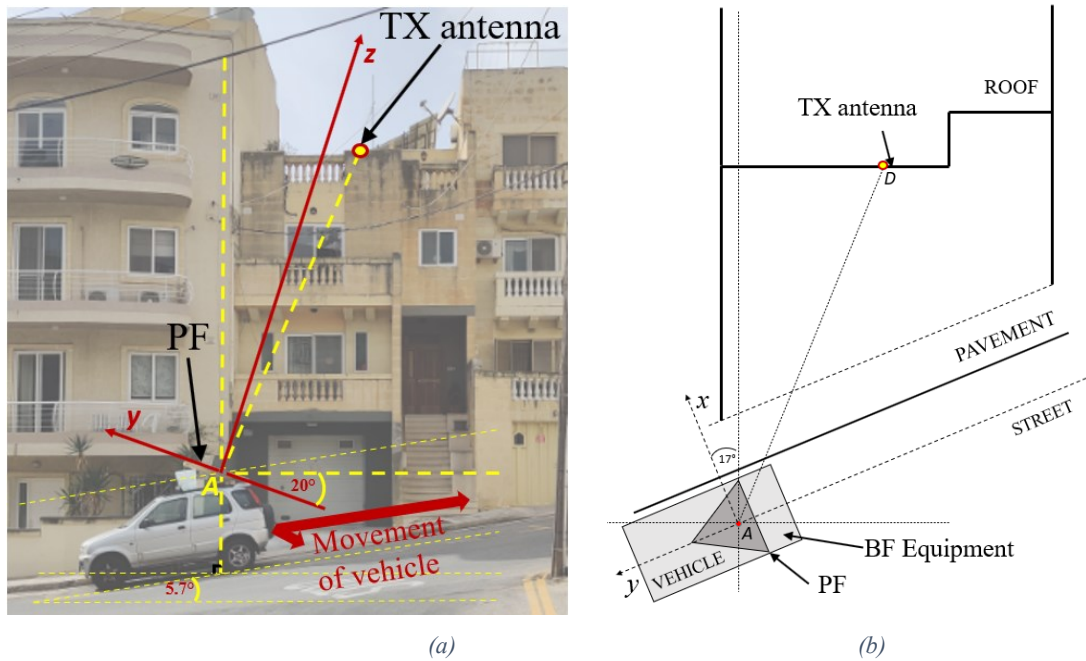
Figure 4.25: BF system testing setup(a) side view (b) top view

The car was moved to obtain three elevation angles:

- $Elevation = 48°$ to simulate a scenario of when the beam is being steered at the maximum steering angle θ_{max} (PF2 steering to position 1 in Figure 3.5);

- $Elevation = 21°$ to simulate a scenario of when the beam is being steered in the intersection of PFs (PF2 steering to position 2 in Figure 3.5);

- $Elevation = 10°$ to simulate an overhead pass

It must be mentioned that the way the *scan()* function has been implemented assumes a scenario whereby the object for which an estimation of DOA is being carried out emits a continuous signal. Hence, an assumption is made whereby when a power reading is made via the *power()* function, there is always a signal to read. In a real-life scenario, a satellite does not emit a constant signal but a beacon. In this scenario, the *scan()* function must be upgraded to allow sufficient time for a signal to be transmitted between power readings, the maximum of which is derived from the word speed of the beacon in terms of the pause between characters.

4.4.4 Small Satellite Observations

Part of the equipment used in the BF setup described in Section 4.3 was also used to validate that the PF has been assembled correctly and the PF has adequate

gain to operate in a real-life scenario. The SatNOGS station [81] previously described in Section 2.2.3 was configured to have a static antenna without rotating capability. A receiver chain was setup comprising of band pass filters, LNAs and the combiner, with the combined output connected to the RTL-SDR. The PF was setup to point to East in azimuth and 45° in elevation. Satellite observations were scheduled via the SatNOGS web user interface [191] on a variety of satellites to assess the capabilities of the assembled PF without BF capability.

In this chapter the testing methodology has been described. Various instruments and software tools have been used, with emphasis on controls and verifications at various stages to ensure that simulations and measurements are reliable. This included MIT for the verification of simulations. Chapter 5 will present the results obtained through the various testing methods obtained in this chapter.

Chapter 5: Results and Discussion

The results of the various simulations and tests carried out will now be presented and discussed. First, results obtained on different PAA parameters are presented with corresponding observations. A section is dedicated to BF where simulations results are presented and analyzed. Another section is dedicated to noise calculations based on the selected orientation of the GDPAA geometric configuration. Finally, a link budget and cost analysis are presented.

Measurements taken to assess the performance of the PF have been taken by combining the four antenna elements through the use of the Mini-Circuits combiner described in Section 4.3. In this chapter, this setup will be referred to as the *combined elements*. The antenna at the centre of the PF, marked "3" in Figure 5.1, will be referred to as the *centre element*.

5.1 PAA parameter performance

In this section various antenna parameters will be presented and discussed for both the individual element and PF. Unless otherwise specified, the simulated results are carried out using the TS previously described in Section 4.1.2. Throughout this section, the coordinate system in use is the Ludwig 3 as per Figure 5.1.
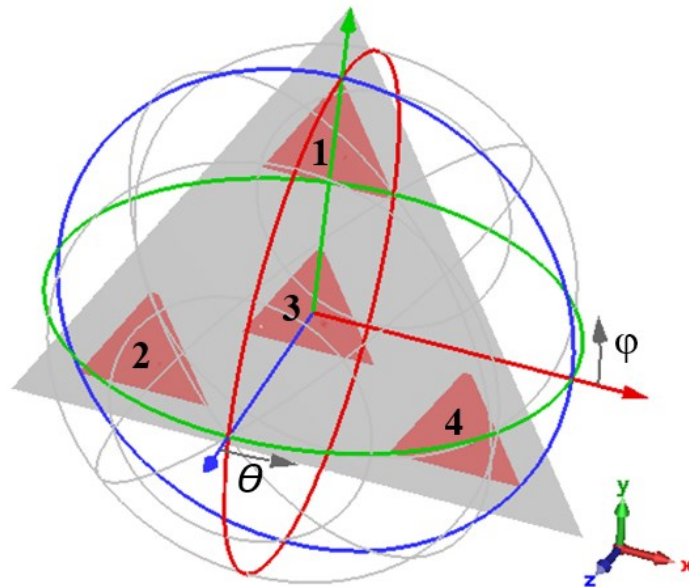
Figure 5.1: Ludwig 3 Coordinate system for simulated and measured results

5.1.1 Return Loss and Bandwidth

The return loss and bandwidth of the individual and combined antenna elements will next be discussed. In Figures 5.2a to d, the reflection parameters S_{11}, S_{22}, S_{33} and S_{44} are plotted for simulated and measured values respectively.

From Figure 5.2 , the simulated values show that the lowest return loss occurs at ~434 MHz. This is close to the design frequency of 433.6 MHz, which corresponds to the x-resonant mode described in Section 3.3.3. The light red bands in Figure 5.2 highlight the operating frequency band of interest (435 MHz - 438MHz).
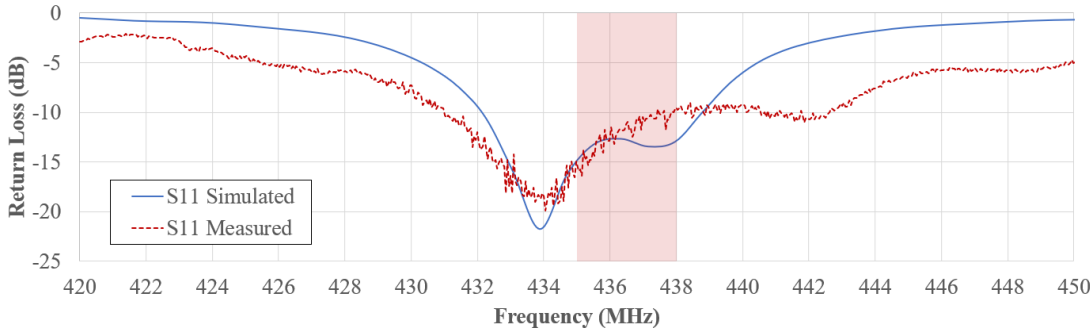
(a)
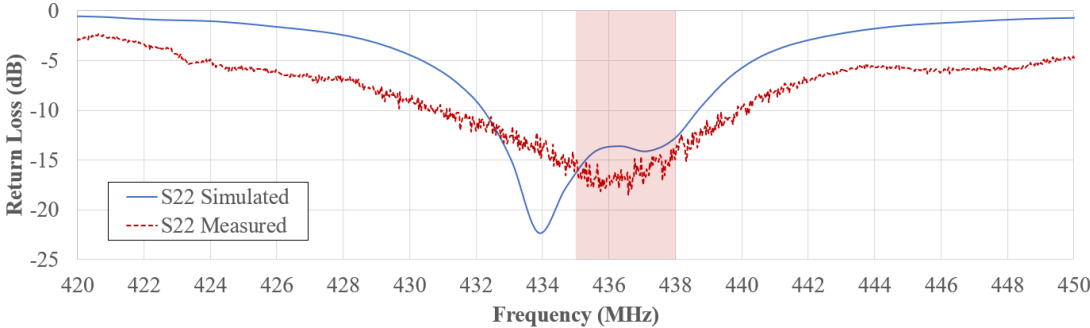
(b)
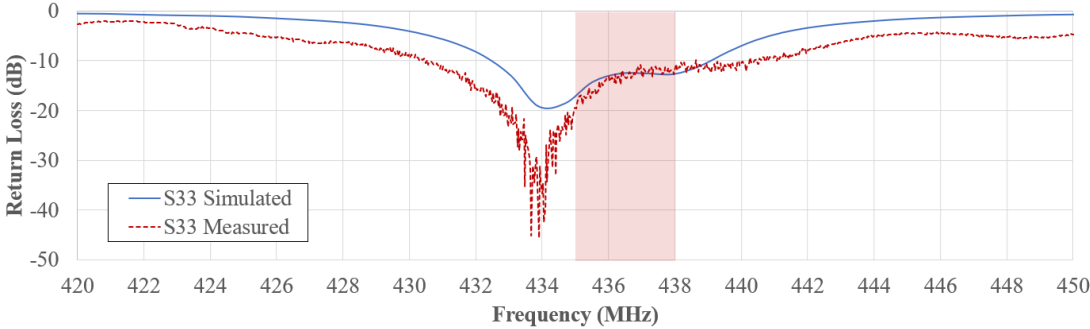
(c)
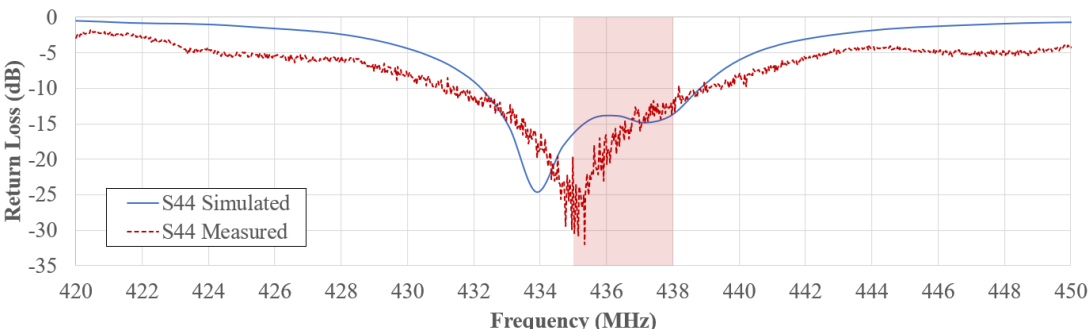
(d)

Figure 5.2: Comparison of simulated and measured return loss for the antenna elements via parameter (a) S_{11} (b) S_{22} (c) S_{33} (d) S_{44}

The measured values corresponding to antenna elements 1 and 3 shown in Figures 5.2 a and c respectively show good agreement with the simulated values. The measured minimum return loss for antenna elements 2 and 4 occur at 436 MHz and 435 MHz respectively, as per Figures 5.2 b and d. The largest variance in the minimum return loss occurs at antenna element 4 where there is a deviation in the minimum return loss of 2.4 MHz, this corresponds to a 0.55% deviation minimum return loss. This is deemed adequate when one considers that the accuracy of (3.11) to calculate side length a_{eff} is 1%. Figure 5.2 also shows that the measured bandwidth results are better than the simulated results on all the individual antenna elements.

The variance between the shape of the return loss pattern between simulated and actual results for elements 2 and 4 as per Figures 5.2 b and d is attributed mainly to the sensitivity of the air gap h_1 of Figure 3.12 between the ground plane and the FR4 substrate. In Figure 3.11 it has been shown that varying the air gap h_1 by even 0.1 mm has a considerable effect on the side length of the antenna and hence its resonance and return loss. From various experiments and measurements carried out requiring frequent movement of the assembled PF, the author has observed that, with the current setup of nylon spacers between the ground plane and FR4 substrate of Figure 3.12, the air gap h_1 is subject to a variance in the order of a few micrometres. After the final assembly of the GDPAA is complete, the nylon bolts of Figure 3.26a must be tightened or loosened to tune the air gap accordingly.
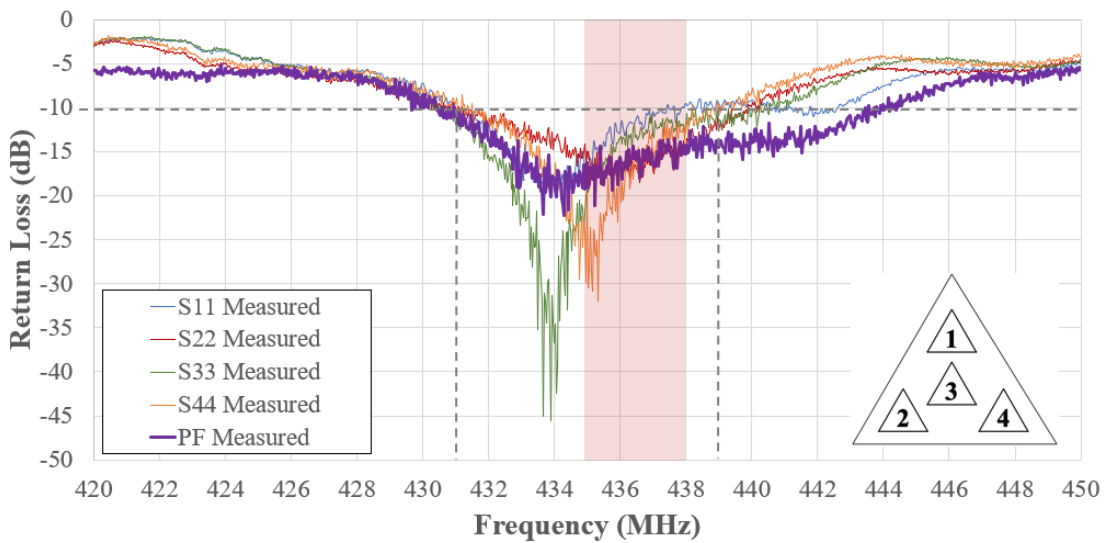
Figure 5.3: Measured return loss for individual and combined antenna elements

Figure 5.3 presents the measured return loss for the individual antenna elements compared against the measurement for the PF via the combined antenna

elements through the use of the Mini Circuits combiner described in Section 4.3. The edge frequencies at which the antenna elements have a −10 dB loss is recorded in Table 5.1.

From Table 5.1 and Figure 5.3 it may be noted that all the antenna elements have a bandwidth of more than 8 MHz. This is advantageous when compared to the 3 MHz bandwidth requirement of Req.2. This represents a bandwidth of 2% which is in line with expectations for patch antennas as previously discussed in Section 3.3.1. Also, from Table 5.1 and Figure 5.3 it may be noted that when the power is combined, the bandwidth of the PF exceeds 3%.

Antenna Element	Lower frequency with −10 dB loss	Higher frequency with −10 dB loss	Bandwidth (MHz)	Bandwidth (%)
1	431.0	442.6	11.6	2.7
2	430.6	440.1	9.5	2.2
3	430.5	441.1	10.6	2.4
4	431.1	439.4	8.3	1.9
PF	429.7	444.4	14.7	3.4

Table 5.1: Measured bandwidth for individual and combined antenna elements

5.1.2 Impedance

The impedance of the centre antenna element will be presented and analysed via the S_{33} parameter. In the impedance Smith chart of Figure 5.4, the input impedance Z_{in} is plotted relative to the characteristic impedance of the transmission line Z_0, which is 50Ω and located at the centre of the chart.
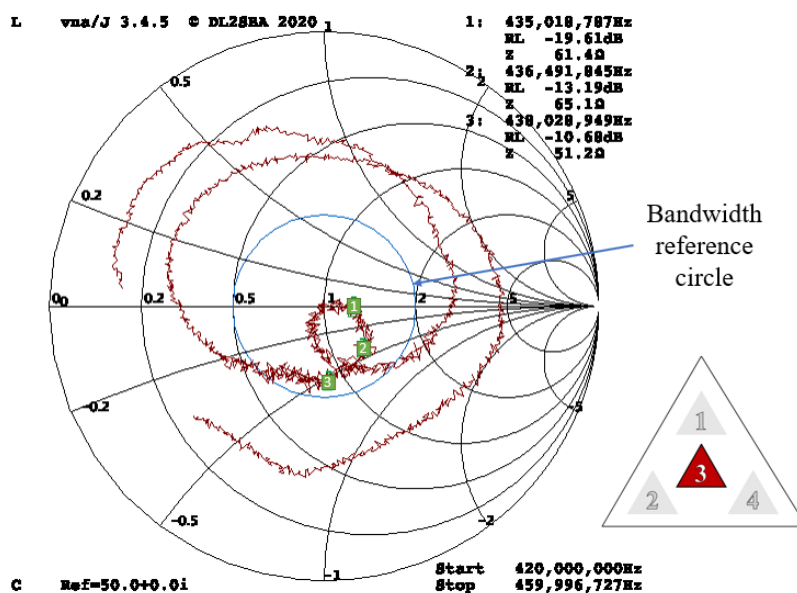
Figure 5.4: Impedance Smith chart for impedance measurements for the centre antenna element 3

Markers 1, 2 and 3 in Figure 5.4 represent readings close to 435 MHz, 436.5 MHz and 438 MHz respectively. It is immediately visible that all three points fall within the bandwidth reference circle equivalent to -10 dB return loss discussed previously in Section 5.1.1. The frequency at the prime center of the Smith chart is 434 MHz, which corresponds to the lowest return loss observed in Figure 5.2. The measurement confirms that the antenna element designed to resonate on 433.6 MHz has good impedance matching with an input impedance of 48 Ω.

The antenna also has good impedance matching within the frequency band 435 MHz - 438 MHz represented through complex impedance markers 1, 2 and 3. It may be observed that the complex impedances of these points are capacitive.

A loop is noted towards the centre of the impedance Smith chart in Figure 5.4. According to Lu et al. [159], this signifies that two resonant modes are excited at close frequencies making CP radiation possible.
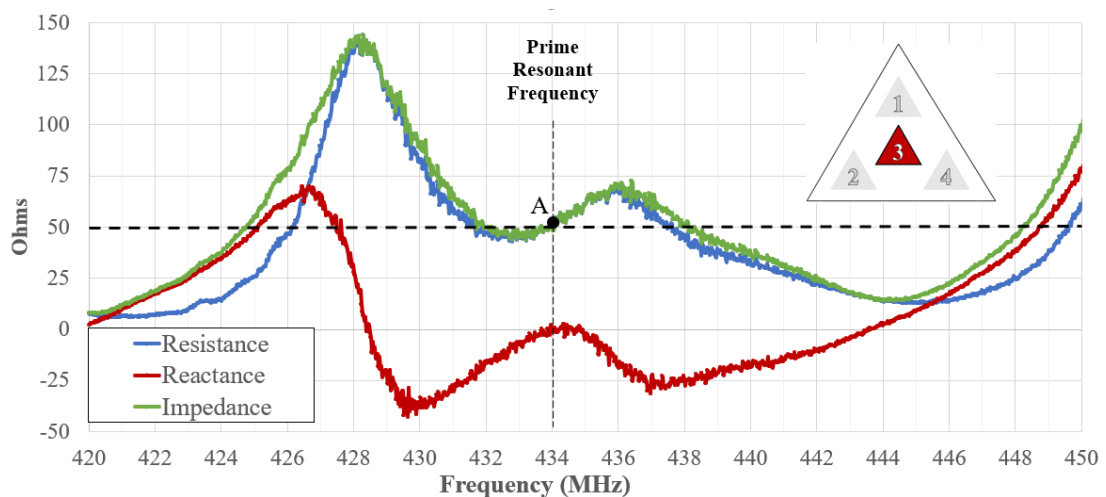
Figure 5.5: Measured resistance, reactance and impedance parts for the centre antenna element

To better analyse the complex impedance at various frequencies of interest, the real (resistance) and imaginary (reactance) parts are plotted together with the impedance in Figure 5.5. It may be noted that the prime resonant frequency of the antenna is at 434 MHz, marked as point A. At this point, the reactance is zero, and the impedance consists solely of resistance with the voltage and current being completely in phase. Resonance also occurs at 428.5 MHz and 443.5 MHz. However, from Table 5.1 it may be noted that these frequencies fall outside the usable bandwidth of the centre element which lies between 430.5 MHz and 441.1 MHz. This is due to poor impedance matching caused by the electrical resistance at the antenna's feed point at those frequencies.

In the single feed point configuration selected, the location of the feed point is crucial to the impedance of the antenna at various frequencies. In Figure 5.6, simplified versions of the basic ETPA configuration of Figure 3.16, and the simulated return loss for the centre element of Figure 5.2 are presented.
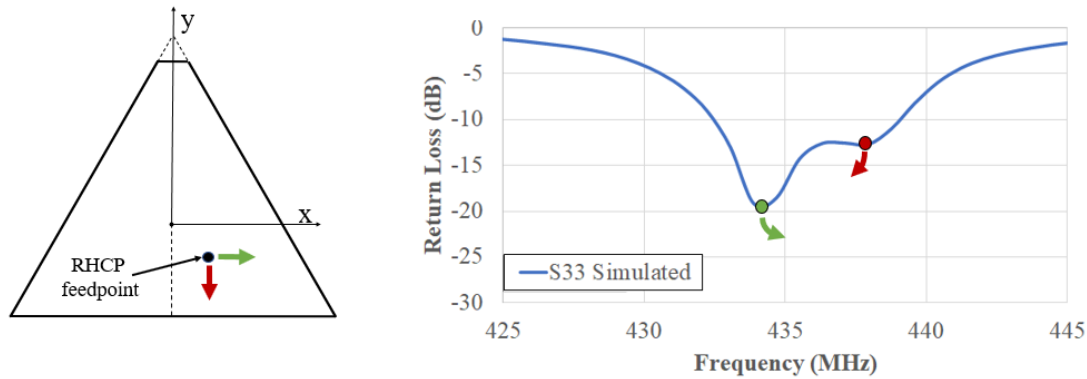
Figure 5.6: Observed effect of change of feed point location on return loss

During the continuous validation stage of Section 4.1.5 it has been observed that the dips in return loss are directly controlled through feed point location, as the placement of the feed point has a direct relationship with the impedance. Shifting the RHCP feed point to the right, in the positive x-axis, results in the dip of the lower frequency in the return loss to shift to a higher frequency. Similarly, shifting the RHCP feed point downwards, in the negative y-axis, results in the dip of the higher frequency in the return loss to shift to a lower frequency. The location of the dips has a direct effect on the reflected power in the antenna and hence the efficiency of power radiated. Varying the feed point location effects the x-directed and y-directed resonant modes. The frequency at which the antenna must radiate CP must be placed within the centre of such dips.

The impedance of the PF when part of a larger structure has also been investigated. Figure 5.7 shows two curves. The curve marked 'TS' in Figure 5.7 shows the simulated complex impedance for the four individual antenna elements of the PF using the TS, which is the solver used to generate the return loss simulations of Figure 5.2. There is good agreement between the measured results of Figure 5.5 and the simulated results, with point A being a 50 Ω point at 434 MHz in both Figures 5.5 and 5.7 .

The second curve marked 'FDS' in Figure 5.7 shows the simulated complex impedance for eight individual antenna elements in a two PF setup using the FDS. Two observations are made. Firstly, the complex impedance simulation curves of the

TS and FDS are similar. A shift of 1 MHz to 2 MHz is observed, with the 50 Ω point A of the TS curve being shifted by 1 MHz to point B in the FDS curve. Secondly, with the exception of antenna element 7, the impedance curve of all antenna elements is similar. Hence, it may be concluded that the impedance of the antenna elements does not significantly change when the PF is placed into a larger GDPAA structure.
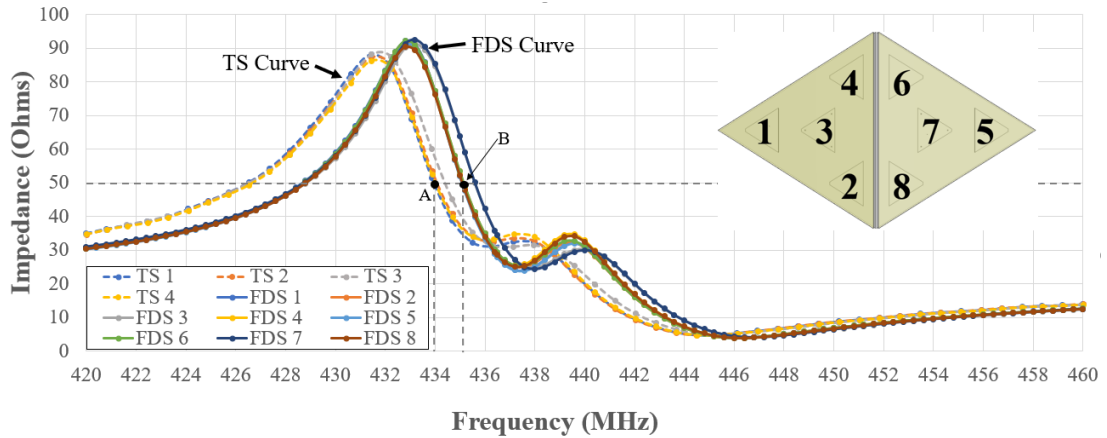
Figure 5.7: Simulated impedance with FDS of individual antenna elements in a two PF setup of 8 ports compared to the simulated impedance with TS of individual antenna elements in a one PF setup of 4 ports

5.1.3 VSWR

In Section 5.1.1, the return loss of the antenna elements measured through the miniVNA Tiny have been discussed. The miniVNA tiny also returns the VSWR values, calculated from the ratio of the incident to reflected power. The VSWR values for the frequency range 435 MHz - 438 MHz are shown in Figure 5.8. It is observed that all four antenna elements have a good VSWR value of less than 2 for the whole band. It is also observed that the VSWR deteriorates as the frequency increases, due to it distancing itself from the main resonant point of 434 MHz.
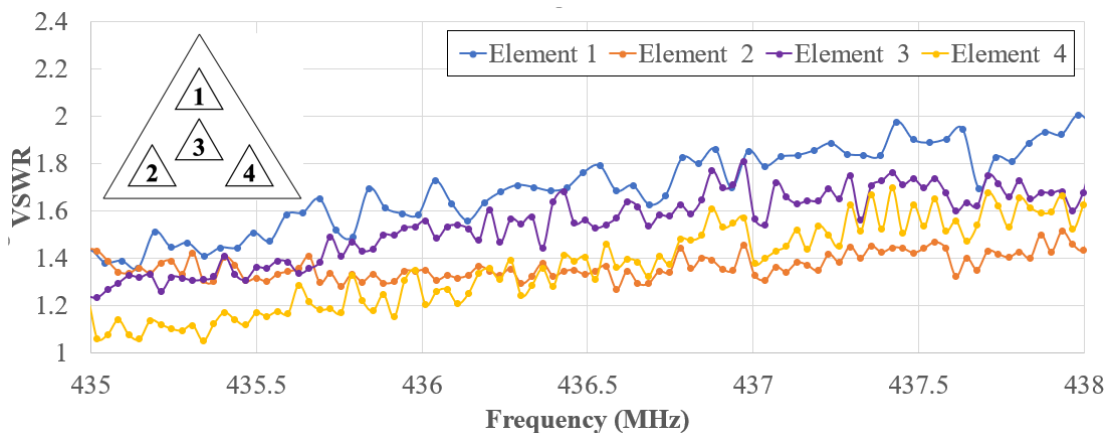
Figure 5.8: Measured VSWR on the four antenna elements of the PF
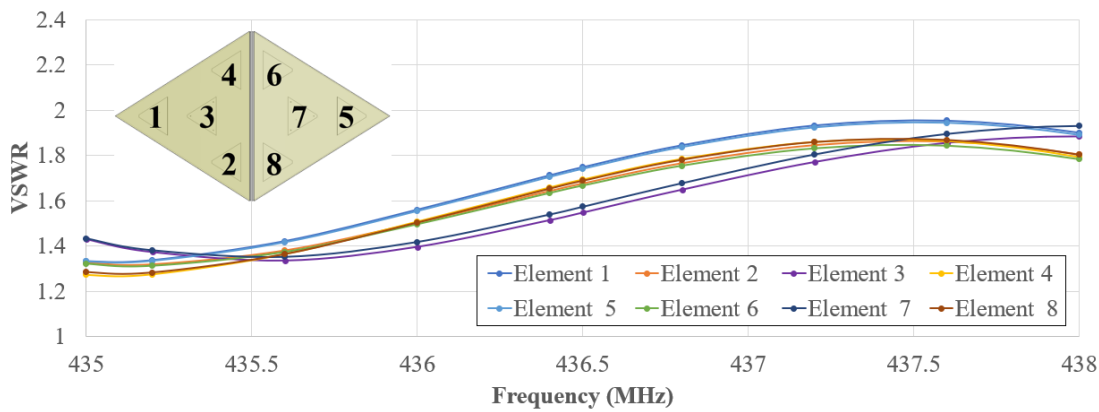
Figure 5.9: Simulated VSWR on the eight antenna elements of the two PF setup given in Figure 4.8

Figure 5.9 shows the simulated values of eight antenna elements of the two PF setup using the FDS. The values also represent a similar pattern for all the eight antenna elements with a VSWR value of below 2. It may be concluded that all the elements of the PF have good VSWR and it is indicated that this property is preserved then the PF forms part of a larger GDPAA structure.

5.1.4 Mutual Coupling

The effect of mutual coupling will now be discussed. The PF contains four antenna elements which, as per Figure 3.21 are separated with distance d_x or d_y from each other. Since the i and j ports in a S_{ij} port network are reciprocal, there are six different S-parameter sets that need to be considered. The S-parameter values representing the mutual coupling between devices is presented in Figure 5.10.
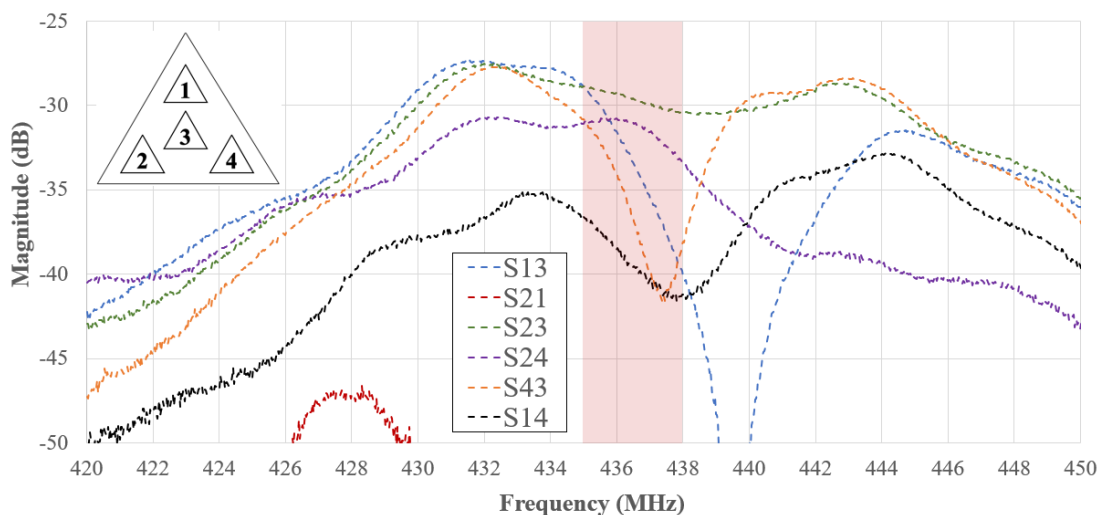
Figure 5.10: Measured S-parameter values representing the mutual coupling between elements in a PF

The highest value of coupling within the operating frequency band of interest (435 MHz - 438 MHz) is almost -29 dB which occurs within the S_{13} and S_{23} parameters. This value is acceptable and shows there is good isolation due to the increased element spacing discussed in Section 3.3.4. The highest coupling occurs

126

between the elements which involve the centre element which are separated by a distance of d_x. The simulation values and measurements for elements separated by a distance of d_x are shown in Figure 5.11. Values obtained through simulations and measurements are in agreement, with a constant frequency shift in the magnitude dip noted. This effect is more evident in the S_{13} and S_{43} parameters and is attributable to the variance in measured return loss of Figure 5.2. Since the dip has shifted to a frequency of approximately 2 MHz higher, it causes an improvement in the mutual coupling in the frequency band of interest (435 MHz - 438 MHz) for the antenna elements separated by a distance of d_x.
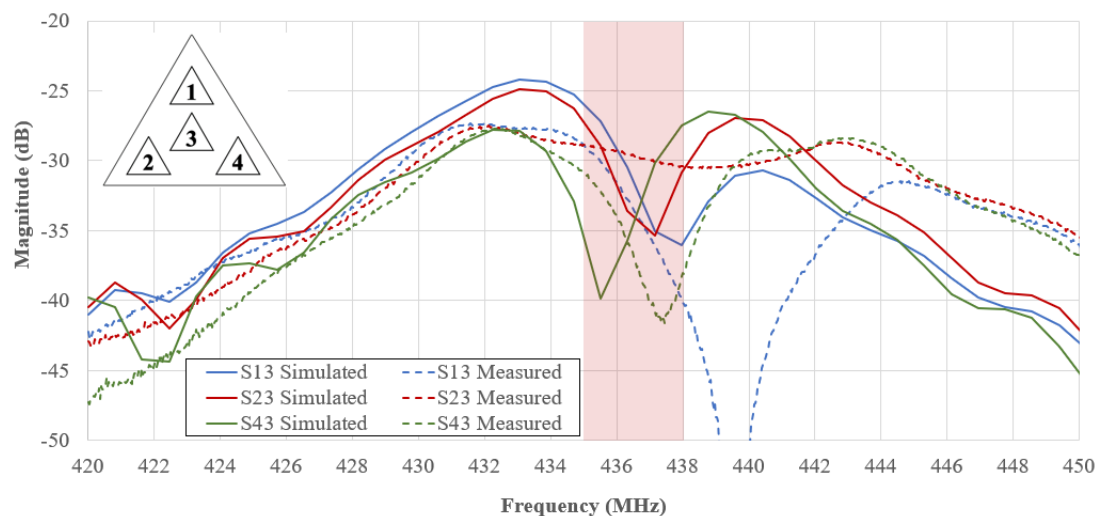
Figure 5.11: Simulations and measurements for antenna elements separated by distance dx

The same exercise is carried out for the antenna elements which do involve the centre element and separated by a distance of d_y. The results are presented in Figure 5.12, where it may be confirmed that the mutual coupling on elements separated by a distance of d_y is improved with respect to the elements separated by a distance of d_x. A significant deviation is noted between on the simulation and measured result for the S_{13} parameter. The measured S_{13} parameter values were compared to the measured S_{31} parameter values to establish whether measurement was as a result of operator error. However, the values were found to be in close agreement. The exact reason for the deviation of the simulation and measured result is not known. However, it is suspected that this may be due to an inaccurate simulation being returned by the TS solver as a result of the discretization of the mesh structure created by the various parameters that have been set.
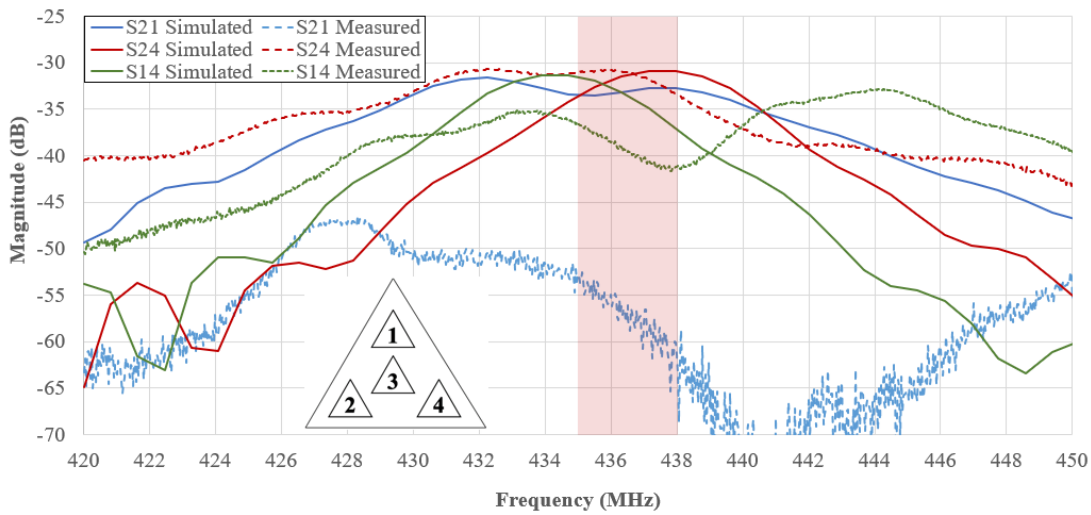
Figure 5.12: Simulations and measurements for antenna elements separated by distance dy

In order for the analysis of the effect of mutual coupling on antenna elements to be complete, an additional scenario must be considered of when the elements are separated by distance d_a as given in Figure 3.23. This distance corresponds to the distance of adjacent antenna elements which are located on different PFs. In the configuration of Figure 4.8, the antenna element pairs {2,8} and {4,6} are separated by distance d_a.
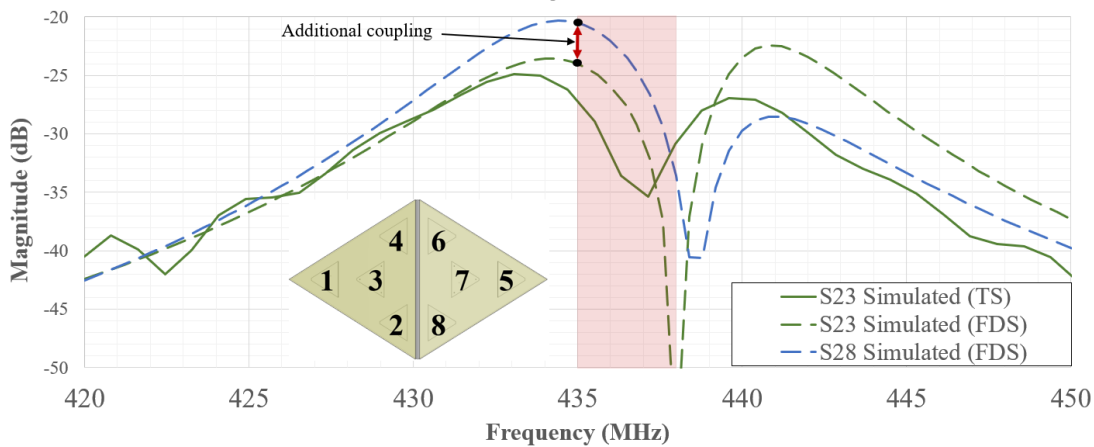
Figure 5.13: Comparison of mutual coupling effect on elements separated by distance dx and da

The solid green line of Figure 5.13 represents the simulated value of the S_{23} parameter already presented in Figure 5.11. This set of simulations were generated via the TS. The dashed green line represents the same simulated value of the S_{23} parameter via the two PF setup using the FDS. As observed in Figure 5.7 for the complex impedance, a shift of 1 MHz is also noted between the TS and FDS simulations. Otherwise, the results obtained through the simulations using the two solvers are similar. On the basis of the similarity of results between the TS and FSD simulations, the simulated S_{28} may be relied on to serve as an indication of the

128

mutual coupling of elements separated by distance d_a. Within the operating frequency band of interest (435 MHz - 438 MHz), the highest mutual coupling has a magnitude of -20 dB and occurs at 435 MHz. Whilst more coupling is present in these elements, it is nonetheless considered an acceptable value in terms of the antenna elements having sufficient isolation. Overall, between measurements of mutual coupling on intra-PF antenna elements, and simulations of intra-PF antenna elements, it is concluded that the PAA has sufficient antenna isolation and the levels of mutual coupling are acceptable.

5.1.5 Polarization

For the PAA to be circularly polarized, the AR must be kept below 3dB for the entire scan angle range of the PF. This consists of the range $\varphi = 0°$ to $\varphi = 360°$ and $\theta = 0°$ to $\theta = \theta_{max}$, where $\theta_{max} = 41.81°$. Hence, the AR is analysed by varying both φ and θ.

The effect of φ on the AR is investigated by normalising various power measurements for values of φ to 0 dB when $\theta = 0°$. Subsequently these values are converted to a power ratio using the inverse form of (2.6). Measured values are shown in Figure 5.14 for both the centre element and the combined elements.
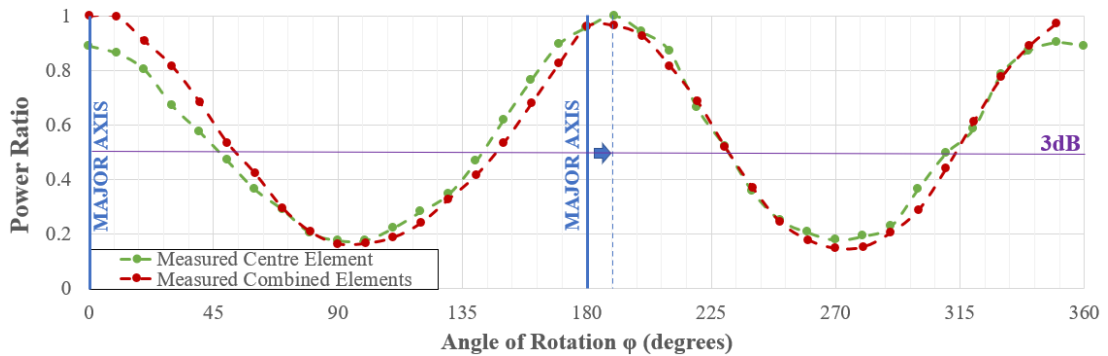
Figure 5.14: Cartesian plot of power ratio for varying angle of rotation φ for centre element and combined elements

The AR for both the centre element and the combined elements are very similar. This proves the important assertion of Section 3.3.3 where it was stated the CP is possible on a PF because the state of polarization of the individual element is preserved in the radiation pattern of the PF it forms part of.

The purple reference line in Figure 5.14 represents the point of half power magnitude where the loss is 3 dB. It may be seen that the AR is within 3 dB for only circa half the angles of rotation. At its lowest point, the average AR at opposing angles is 8.1 dB.

Figure 5.14 shows consistent results in terms of symmetry of measured power around the major axis when $\varphi = 0°$. In the case of $\varphi = 180°$, a shift in the axis to $\varphi = 190°$ is observed. The major axis and shift are denoted with the blue vertical lines in Figure 5.14. The magnitude is expected to be periodic and symmetrical around the major axis. Similar patterns on both sides of the axis give the additional comfort that the measurements are reliable. Figure 5.15 is the polar representation of Figure 5.14 for the combined elements only. In Figure 5.15 it may be noted that the major axis of the right hemisphere is at $\varphi = 0°$. However, in the left hemisphere the major axis seems to occur between measurements for $\varphi = 180°$ and $\varphi = 190°$. Analysis using a windowing technique on the measurements reveals that the major axis occurs when $\varphi = 0°$. Nevertheless, due to the measurements taken every $10°$ increments of φ, it is indicated that there could be a slight shift in the major axis towards $\varphi = 10°$.
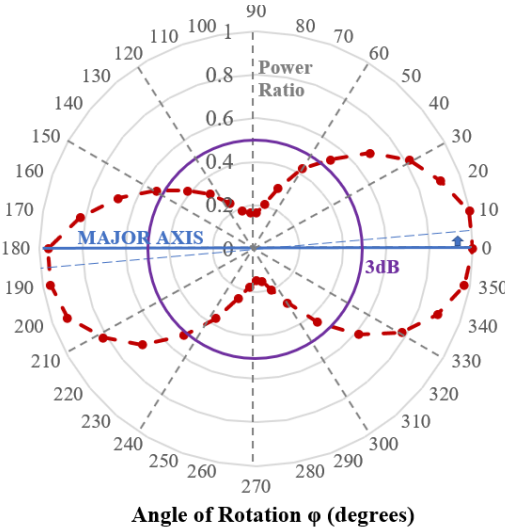
Figure 5.15: Polar plot of power ratio for varying angle of rotation φ for the combined elements

From Figures 5.14 and 5.15 it may be concluded that the PF is elliptically polarized with its major axis along $\varphi = 0°$ and AR = 8 dB.

The effect of φ on the AR of the PF has been investigated. The polarization of the PF may also be effected with the scan angle, hence the effect of θ on AR will now be investigated. Figure 5.16 shows the simulated AR for the frequencies 435 MHz, 436.5 MHz and 438 MHz. The simulated values show the effect of different values of θ for when $\varphi = 90°$ for the combined elements.
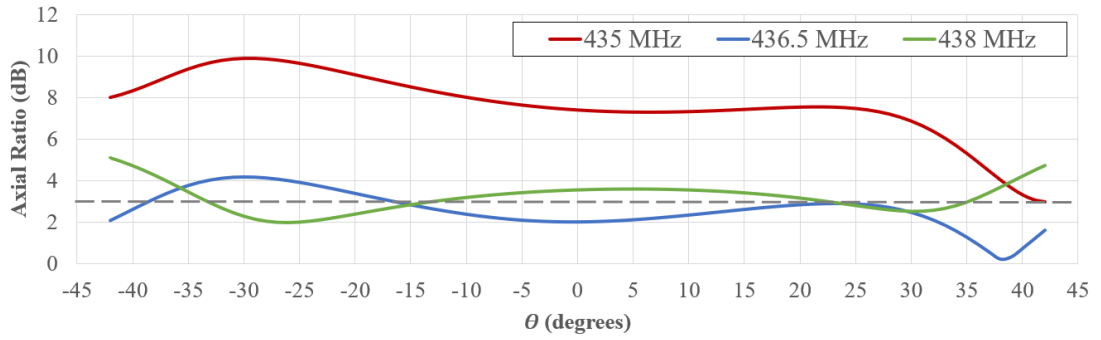
Figure 5.16: AR simulations for combined elements for frequencies 435 MHz, 436.5 MHz and 438 MHz when φ=90°

From Figure 5.16 it may be noted that for the frequencies 436.5 MHz and 438 MHz, varying θ up to θ_{max} does not have an adverse effect on the AR, with the AR being below 5 dB. On the other hand, the AR at 435 MHz degrades further than the 8 dB mark for negative values of θ. From the previous results this is expected. It is concluded that reducing the truncation ratio to 0.062 shortens the y-directed resonant mode effectively reducing the AR bandwidth.

5.1.6 Gain

The gain of an antenna is inclusive of both directivity and total efficiency. Hence, in order to give a more accurate representation of the performance of the PAA, and to enable comparison between simulation and measurement results, an analysis is presented on the gain of the individual antenna element and combined elements. Gain simulations on the two-PF setup are also presented. The effect of BF on the gain of the antenna is discussed later in Section 5.2.

(a)

(b)
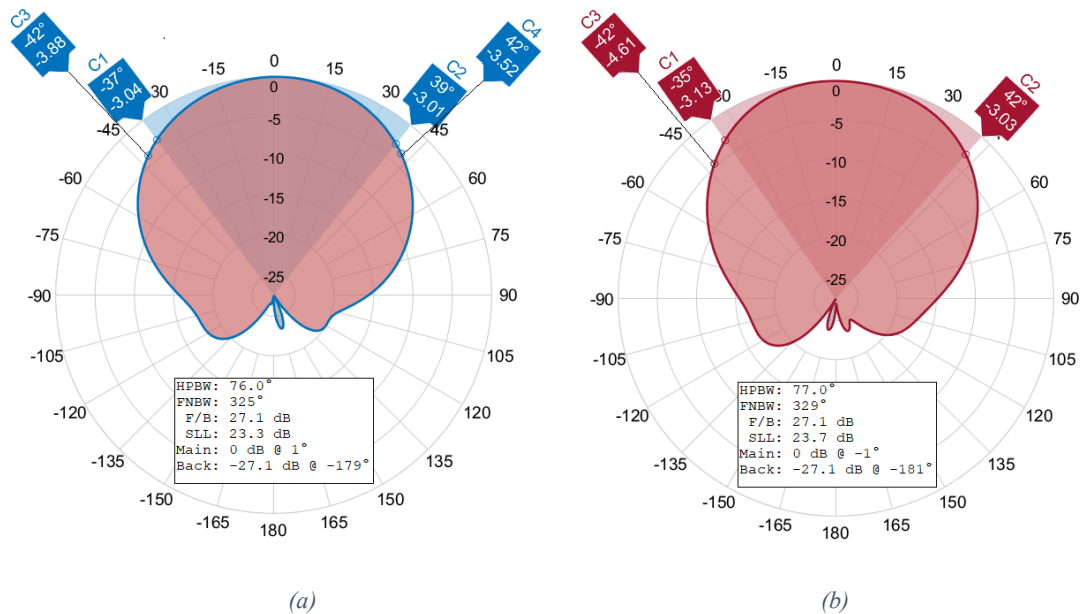
Figure 5.17: Simulated farfield normalised gain elevation cuts for centre element (a) φ=0° (b) φ=90°

Let us first consider the simulated normalised farfield gain for the centre element. Figures 5.17a and b show the elevation cuts of when φ=0° and φ=90° respectively.

The desired field of view of the patch element is 84°, which is twice the maximum steering angle θ_{max} of 41.81°. Figure 5.17a shows that the simulated HPBW at $\varphi = 0°$ is 76°. This is visible through the markers C1 and C2. The gain at the desired field of view is −3.88 dB and −3.52 dB, represented by the markers C3 and C4 respectively.

Figure 5.17b shows that simulated HPBW for $\varphi = 90°$ is 77°. Whilst the HPBW is only 1° more than its counterpart of the $\varphi = 0°$ in Figure 5.17a, it may be observed that the antenna performs better on the right-hand side of the main lobe in Figure 5.17b. The elevation angle at which the HPBW limit occur on the right-hand side coincides with θ_{max}. The gain at the desired field of view on the left-hand side of the main lobe is −4.52 dB as per marker C3. This means that the there is a shift in the main lobe to the right-hand side although the main lobe direction is located at −1°.

The simulations shown in Figure 5.17 utilize the TS. The simulated gain of the centre element is 7.2 dB. The antenna element HPBW is one of the most important parameters of the PAA. This is because, regardless of the HPBW of the combined elements which will now be analysed, the HPBW of the steered beam is dependant and limited on the pattern of the individual antenna element. This concept is explained clearly and proven via simulations in Section 5.2. The SLL of the antenna element is −23.3 dB when $\varphi = 0°$, and −23.7 dB when $\varphi = 90°$. These values are considered sufficient and above minimum SLL of −20 dB as noted in Section 2.1.2.

Figures 5.18a and b show the comparison of the simulated TS result of Figures 5.17a and b to measurements, when $\varphi = 0°$ and $\varphi = 90°$ respectively. These figures also show a second set of simulations using the FDS.

In Figure 5.18a, when $\varphi = 0°$, good agreement between simulation and measurement results is observed. Whilst the simulation values for the main lobe are the same for the TS and FDS, it is observed that there is better agreement between measurement values compared to the results obtained using the FDS simulation for the side lobe. The similarity of measurement values compared to simulations results

obtained using the FDS solver is also repeated when $\varphi = 90°$ in Figure 5.18b. However, when $\varphi = 90°$, the main lobe for measured results is observed to have the highest power between the readings at $\theta = 10°$ and $\theta = 20°$. This is partly attributable to the fact that the antenna gain is better on the right hand side of the main lobe as observed in Figure 5.17b. It could also be due to the elliptical major axis rotation shift noted in Section 5.1.5. Similar results are also observed in the measurements of the combined elements as shown in Figure 5.19 when $\varphi = 0°$, and when $\varphi = 90°$ in Figure 5.20. Hence, it is indicated that the variation in the main beam measurements compared to simulations is due to the major axis rotation shift.
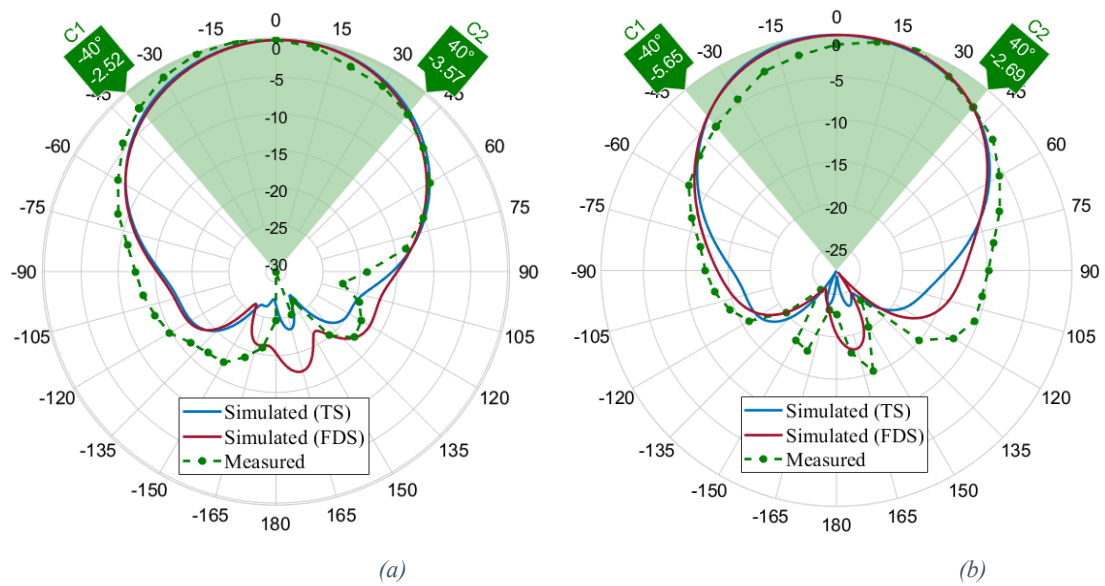
Figure 5.18: Simulated vs measured farfield normalised gain elevation cuts for centre element (a) φ=0°
(b) φ=90°

In Figures 5.18a and b, the gain is analysed through the gain markers C1 and C2 which indicate the gain at the elevation angle 40°, being the closest measurement to θ_{max}. From the measured results, it is concluded that when $\varphi = 0°$ the gain performance meets requirements, as the values of markers C1 and C2 in Figures 5.18a are −2.52 dB and −3.57 dB. These are sufficiently close to the −3 dB HPBW value. When $\varphi = 90°$, a shift in gain observed in the right-hand side on the lobe. Post-manufacturing calibration of the antenna is required to correct the observed variance in the mean beam measurements from the simulation. This should balance the gain values −5.65 dB and −2.69 dB of markers C1 and C2 of Figure 5.18b such that they are both closer to the −3 dB HPBW value.

Similar simulation and measurement results are presented for the four combined elements of the PF and are shown in Figures 5.19 and 5.2 . However, a cartesian plot is used instead of a polar plot in order to better illustrate the

observations. In the elevation cut $\varphi = 0°$ of Figure 5.19, the measured results indicate a broader main beam compared to that obtained through simulation using both TS and FDS. This is attributed to the combined effect of the individual antenna elements having a broader main beam as per the observations of Figure 5.18a. Agreement between simulation and measured results is noted for the deep nulls. The desired field of view with scan angle θ_{max} from broadside is represented in the light red band in the figure.

The processing of results took place some days after the actual measurements and the difference in the measured and simulated main lobe for values of θ greater than 40° is unknown. One possible reason is failure of the miniVNA Tiny in losing its calibration, described in Section 4.2, as the measurements carried out for the PF took place towards the end of the measurement session. The measurements took place towards the end of this study and it was not possible to repeat the experiment due to time constraints.
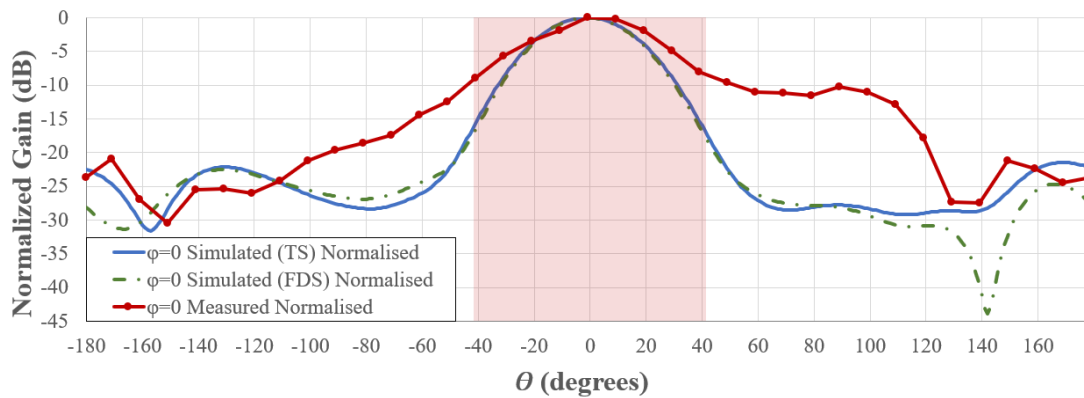
Figure 5.19: Simulated vs measured farfield normalised gain elevation cut for combined elements when φ=0°
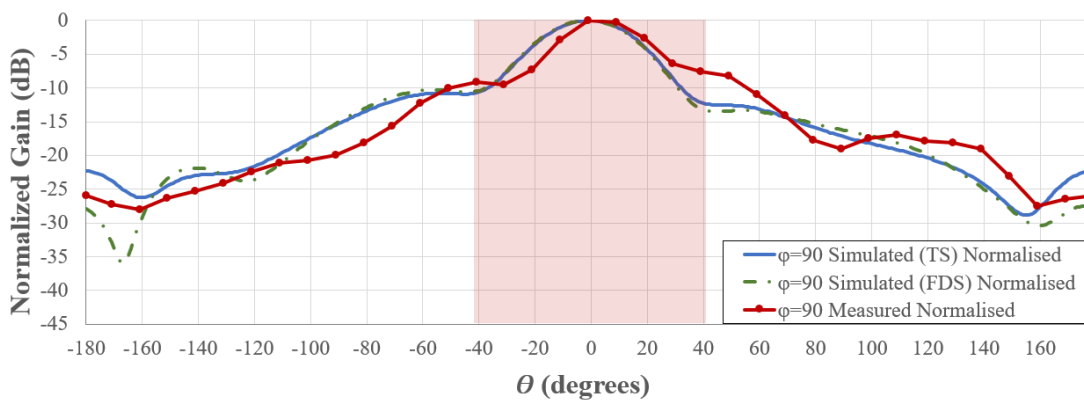
Figure 5.20: Simulated vs measured farfield normalised gain elevation cut for combined elements when φ=90°

In the elevation cut $\varphi = 90°$ shown in Figure 5.20, a shift in the main beam direction is observed with the maximum power occurring between the measurements

134

taken at $\theta = 0°$ and $\theta = 90°$. The shift from shift $\theta = 0°$ is less than the observed main beam shift of the centre element antenna of Figure 5.18b. This is possible since only the elevation cuts for the centre element have been measured, which may be averaged out in the measurements for the combined elements. The simulated gain of the combined elements is 12.4 dB.

A 3D farfield normalised gain pattern for the centre antenna element and the combined elements obtained through simulation are presented in Figure 5.21. From Figures 5.21a and b it may be noted that, the gain for both the centre element and PF respectively, are consistent for all values of φ.

(a)   (b)
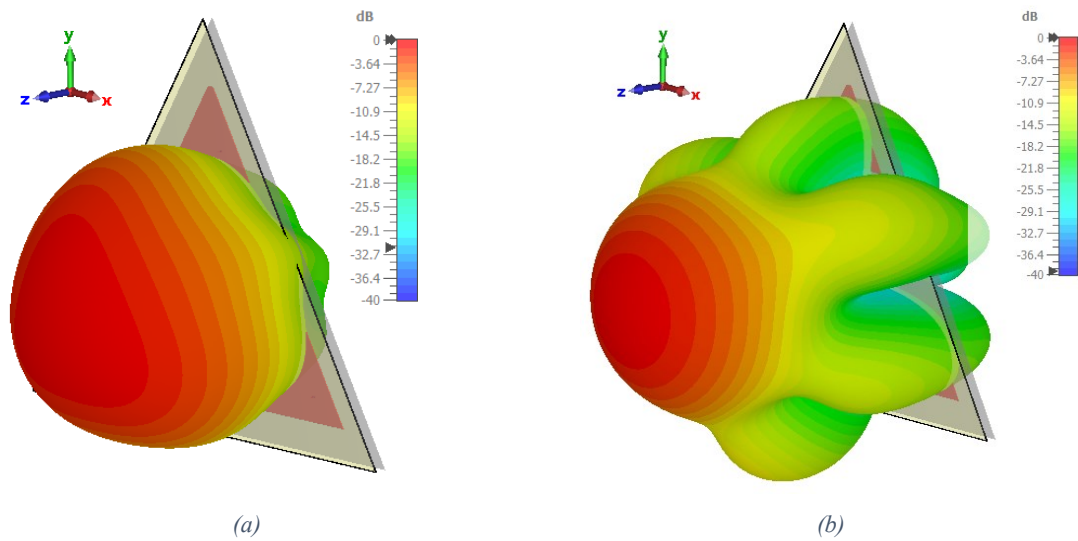
Figure 5.21: Simulated 3D Farfield Normalised Gain for (a) Centre Element (b) PF without BF

The UAV testing carried out in order to establish a 3D pattern of the combined antenna elements as per the second method of Section 4.4.1 proved unsatisfactory. Unfortunately, the signal generator mounted on the UAV malfunctioned and was replaced with an FM transmitter available on site transmitting an audio tone. The test was not expected to render any reliable results, however it was still carried out to validate the test setup. The normalised power measurements corresponding to the UAV waypoints of Figure 4.23 are displayed in Figure 5.22. The results are inconclusive and will not be discussed further.
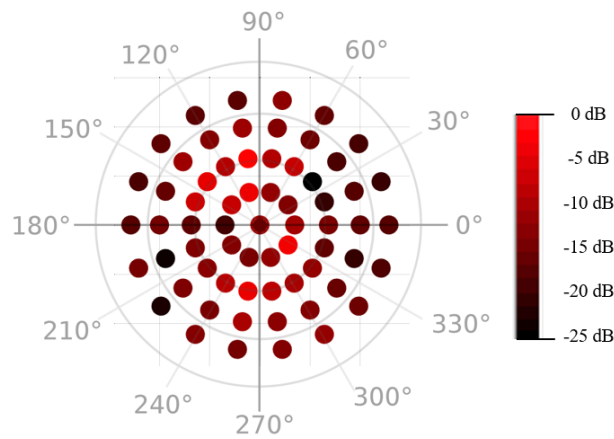
Figure 5.22: Normalised power measurements for UAV waypoints

Several observations of small satellites have been carried out at various stages of the continuous validation process described in Section 4.1.5 [192] using the method described in Section 4.4.4. BisonSat [193] is an amateur 1U small satellite which transmits telemetry using RHCP on 437.375 MHz. The FSK modulation scheme with a baud rate of 9600 bps is used. This is also the polarization, modulation scheme and baud rate of the UoMBSat mission [138]. An observation successfully received telemetry transmissions [194] which were encoded in an AX.25 packet, at a maximum elevation of 45°. To ensure that the SNR is adequate, the AX.25 packet content was compared to the same observation [195] from a reliable SatNOGS station network with over 100,000 observations to date and operated by one of the founders of the SatNOGS network located in Greece [196]. This station uses a helical antenna resonant to 438 MHz.

The result is encouraging as the content of the AX.25 packets is identical. As a result, it is proven that the PF setup is functioning as intended and has adequate gain to decode real telemetry on a similar small satellite even in a one-PF setup scenario.

5.2 Beamforming

In Section **Error! Reference source not found.** it has been described that a set of elevation angles were selected in order to carry out beamformer software. The data and observations as a result of the simulation exercise via post-processing in CST are presented in Table 5.2 and Figure 5.23.

θ (degrees)	Element Phase Shift (degrees)				PF Gain (dBi)	Normalized gain (dB)	Main Lobe Direction (degrees)	Pointing Loss (dB)
	1	2	3	4				
-41.81 ($-\theta_{max}$)	135.099	0.000	135.099	270.198	9.8	-2.6	-31	1.0
-30	101.325	0.000	101.325	202.650	11.0	-1.4	-23	0.4
-20 ($\sim\theta_i$)	69.310	0.000	69.310	138.621	11.8	-0.6	-16	0.1
-10	35.190	0.000	35.190	70.380	12.3	-0.1	-8.0	0.0
0	0.000	0.000	0.000	0.000	12.4	0.0	0	0.0
10	35.190	70.380	35.190	0.000	12.3	-0.1	8	0.0
20 ($\sim\theta_i$)	69.310	138.621	69.310	0.000	12.0	-0.4	16	0.1
30	101.325	202.650	101.325	0.000	11.3	-1.1	23	0.3
41.81 (θ_{max})	135.099	270.198	135.099	0.000	10.1	-2.3	31	0.7

Table 5.2: BF simulated data when φ=0°
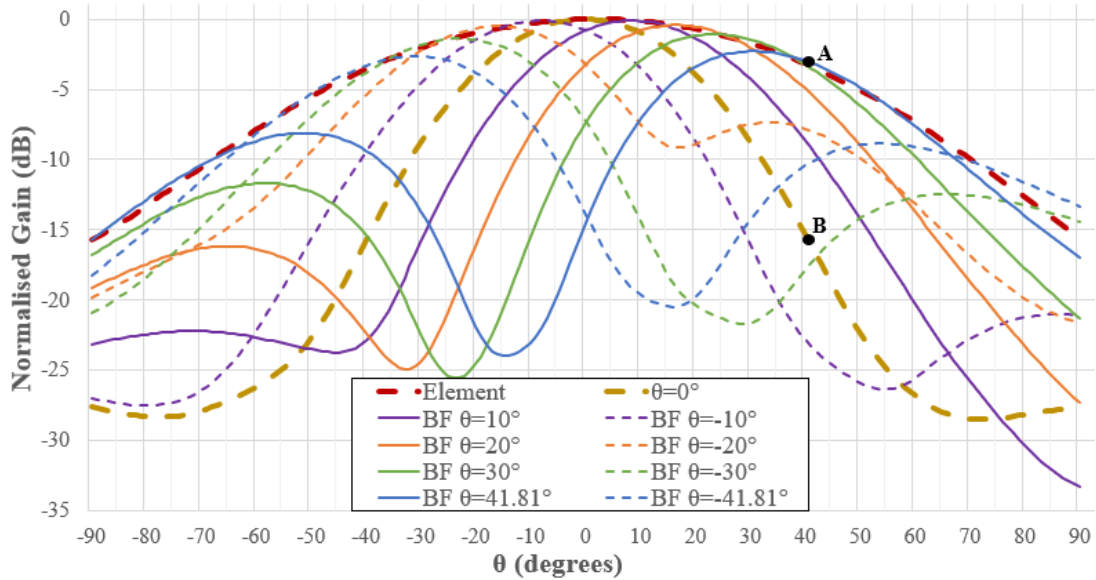
Figure 5.23: Comparison of simulated normalised gain for PF beam steering pattern gain when φ=0°

In Figure 5.23 the simulated far field gain pattern when $\varphi = 0°$ for the centre element has been normalised to 0 dB and represented via the red dashed line. The simulation for the combined elements without BF has also been normalised to 0 dB and corresponds to the TS simulation pattern presented in Figure 5.19. This is

marked through the dashed gold line in Figure 5.23. The BF patterns are all normalised with respect to combined elements and the same normalisation factor has been used.

From Figure 5.23 various observations are made. Firstly, it is easily noted that the pattern of the main beam at the different values of θ is determined by the contour of the antenna element pattern, in this case the element under review is the centre element. This is a significant improvement over the pattern of the combined elements without BF. The BF patterns are normalised and are not indicative of the gain of the BF with respect to one antenna element. The BF main beam pattern being determined by the contour of the individual antenna element is expected and is also documented clearly by Sheldon [41] in a similar work. Hence, the HPBW of the antenna element becomes the limitation of the steered beam pattern.

It may also be observed that the gain in the steered beam is much stronger at the steered angle θ when compared to the same angle θ for the combined elements without BF. Point A represents the normalised gain of -3.0 dB when the beam is steered to θ_{max}. Point B represents the normalised gain of -16.8 dB. This constitutes an increase of almost 14 dB which is one of the main advantages of BF. In Figure 5.23 it may also be observed that the side lobe increases significantly with increased values of θ. The side lobe pattern is also determined by the contour of the main lobe pattern of the antenna element. From Table 5.2 it is noted that at the maximum steering angle θ_{max}, the total gain loss with respect to boresight, inclusive of pointing loss, is 3 dB and 3.6 dB on both sides of boresight.

A similar analysis is carried out for BF when $\varphi = 90°$. The BF patterns are shown in Figure 5.24 with the same colour coding scheme. Relative data is presented in Table 5.3 from where it is noted that at the maximum steering angle θ_{max}, the total gain loss with respect to boresight, inclusive of pointing loss, is 3.6 dB and 3.2 dB on both sides of boresight. The observations noted between the beamformed pattern, antenna element and combined element pattern when $\varphi = 90°$ are the same as previously discussed for when $\varphi = 0°$.
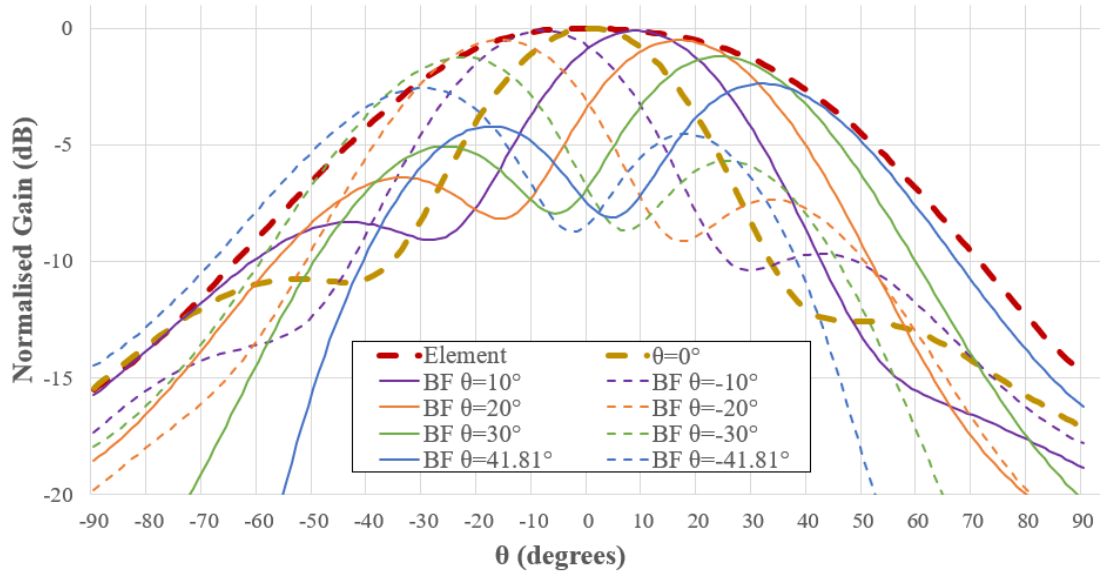
Figure 5.24:Comparison of simulated normalised centre element simulated gain against PF beam steering pattern gain when φ=90°

θ (deg)	Element Phase Shift (degrees)				PF Gain (dBi)	Norm-alized Gain (dB)	Main Lobe Direction (degrees)	Poi-nting Loss (dB)
	1	2	3	4				
-41.81 ($-\theta_{max}$)	233.999	0.000	78.000	0.000	9.8	-2.6	-30	1.0
-30	175.500	0.000	58.500	0.000	11.2	-1.2	-23	0.5
-20 ($\sim\theta_i$)	120.049	0.000	40.016	0.000	11.9	-0.5	-16	0.1
-10	60.951	0.000	20.317	0.000	12.3	-0.1	-8	0.1
0	0.000	0.000	0.000	0.000	12.4	0.0	0	0.0
10	0.000	60.951	40.634	60.951	12.3	-0.1	9	0.0
20 ($\sim\theta_i$)	0.000	120.049	80.033	120.049	11.9	-0.5	17	0.1
30	0.000	175.500	117.000	175.500	11.2	-1.2	24	0.4
41.81 (θ_{max})	0.000	233.999	155.999	233.999	10.0	-2.4	32	0.8

Table 5.3: BF simulated results when φ=90°

From these simulations, it is proven that the beamformed radiation pattern is as good as the radiation pattern of the underlying antenna elements. The simulated gain of the PF is 12.4 dB at boresight. When BF is used, the results given in Tables Table 5.2 and 5.3 show that the worst case simulated gain value from for the steering angle 20° ($\sim\theta_i$) is 11.7 dB and for θ_{max} is 8.8dB. Since there is good agreement

between simulations and measured results for the antenna element, it is anticipated that the radiation patterns of the PAA at a PF level will match the simulations presented in this chapter. It may be concluded that the implemented BF function *point()* operates as intended. Field tests for the beamformer hardware testing described in Section 4.4.3 proved to be inconclusive with no clear indication of estimation of DOA. It is suspected that this is due to two main factors: the reflection-free environment under which the test was carried out and the poor dynamic range of the RTL-SDR device in the workaround setup.
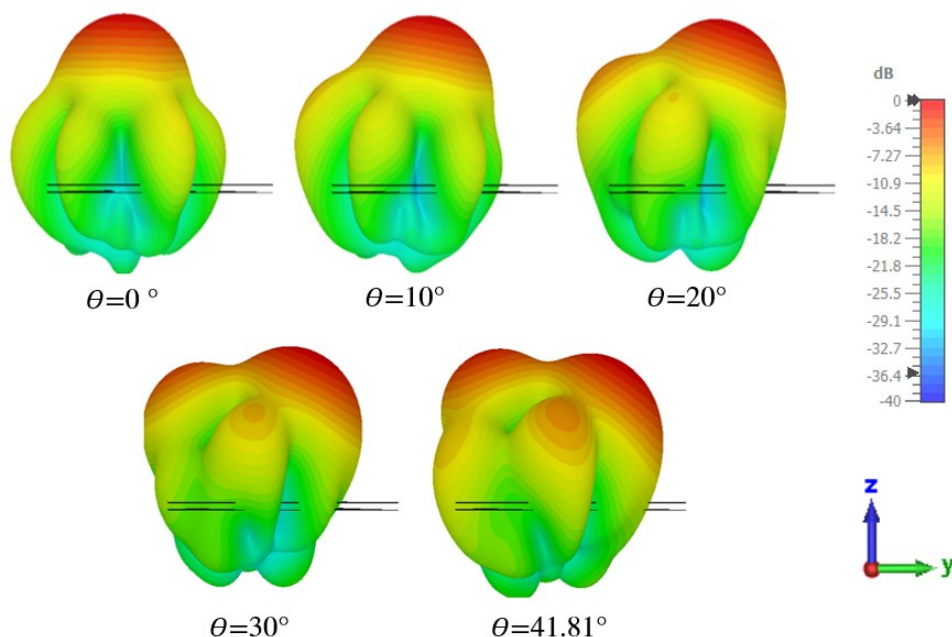
Figure 5.25: Simulated 3D farfield normalised gain BF 3D patterns for φ = 90°

Figure 5.25 shows the simulated 3D farfield normalized gain BF patterns for progress values of positive θ when $\varphi = 90°$. The view in Figure 5.25 is a side view, enabling this reader to obtain a 3D equivalent view of the BF patterns of Figure 5.24. From this figure it may be conclude that apart from the side lobes already observed in Figure 5.24, an additional side lobe starts developing for values of $\theta > 20°$. It is not anticipated that his causes any undesired result.

The number of PFs that the beamformer will utilize will depend on the orientation of the incoming plane wave from the satellite and whether the incoming incident angle relative to the PF is less than the capability of the PF, which is θ_{max}. Four scenarios may be considered, depending on where the incoming signal is pointing to:

i.   Axis of rotation of the vertex

ii.   Axis of rotation of the edge midpoint

iii. Axis of rotation through the centre of the face

iv.   Any other point not mentioned above

The axes of rotation are also defined in Section 3.2.2 and Figure 3.6. An example of when the incoming plane wave is pointing to the axis of rotation of the vertex is shown in Figure 5.26. In this scenario, which is the best case scenario, the incoming wave is in the field of view of five PFs. Hence, five PFs are utilized to form the active sector to receive or transmit the signal.
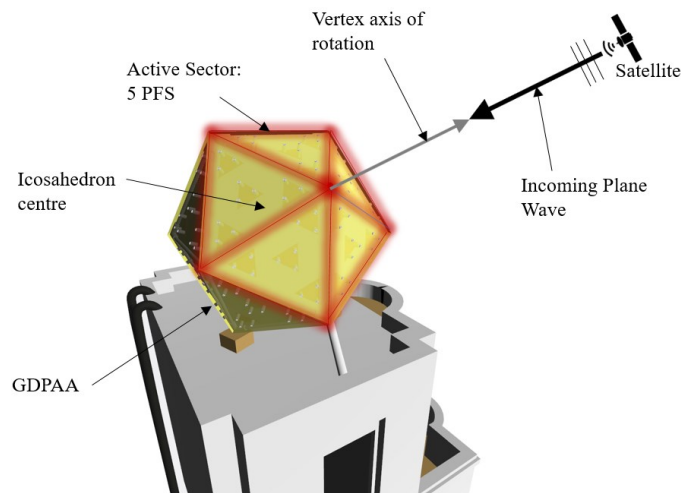
Figure 5.26: Active sector illustration of GDPAA when incoming plane wave is in the direction of the vertex axis of rotation

Hence, the gain of the PAA is not fixed, but may vary depending on the angle of arrival and the selection by the GS operator as to how many PFs to activate to form the active sector. For the purposes of establishing the PAA gain for link budget calculations, best-case and worst-case scenario estimates are calculated.

In the best-case scenario shown in Figure 5.26, five PFs will steer the beam to an angle of $\varphi = 0°$ and $\theta = \theta_i$. From Table 5.2, the gain of one PF at this angle of arrival is 11.9 dB including pointing loss. Hence, an active sector of five PFs provides a maximum theoretical gain of a further 6.9 dB. 5.7 dB is used as a more realistic figure, being a 75% increase in theoretical power due to efficiency degradation, phase error and other losses. This gives a best-case scenario PAA gain of 17.6 dBi.

On the other hand, a worst-case scenario may be considered when the angle of arrival is incident to an axis of rotation corresponding to the midpoint centre. In this case, two PFs at minimum may be used where the beam is steered to $\varphi = 90°$

and $\theta = -\theta_i$. From Table 5.3, the gain of one PF at this angle of arrival is 11.8 dB. Two PFs provide a maximum theoretical gain of 3 dB. However, a 75% increase is also considered due to losses so 2.3 dB is expected due to efficiency losses and phase error. Although more PFs can be used to contribute to the active sector, the worst-case scenario of the PAA is a gain of 14.1 dBi.

5.3 Noise Calculations

Discussions were held with Vassallo, who is working on the system's transceiver [138], to determine the noise floor of the receiver signal chain of the GDPAA. To determine the noise floor, the antenna temperature of the GDPAA must be calculated. The purpose of this section is to outline the basis of the calculations that were provided to Vassallo from which the antenna noise temperature requirement Req.11 of 600 K originated.

The temperature will largely depend on the PFs in use, as these have different orientations. Let us consider the GDPAA structure based on the orientation selected in Figure 3.6 in Section 3.2.2 which is reproduced with triangular faces in Figure 5.27. The orientation of three PFs are considered: pointing to elevation angle of 69°, pointing to elevation angle of 21°, and pointing to elevation angle of 0° (horizon).
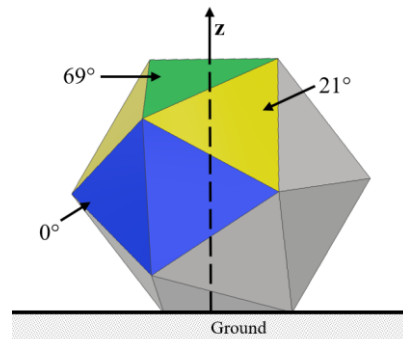
Figure 5.27:Orientation of PFs in GDPAA

The azimuth direction of the PFs is not relevant to these calculations and hence the x and y axis are omitted in Figure 5.27. The temperature varies from the component contributing to that temperature. The sky, horizon and ground all have different temperatures. Their temperature contributions in the calculation of the PF temperature are based on the orientation of the lobes of the patch antenna element, which in turn is dependent on the elevation angle from ground. The following temperatures have been used: 10K for the sky temperature at the operating frequency of the PAA [197] and values of 150 K and 300 K for the horizon and ground temperatures [198].

The contribution of the sky, horizon and ground are calculated as a percentage of their contribution to the lobes of the patch antenna element. Subsequently, based on the above established temperatures, the contributing temperatures are summed to provide a total antenna temperature for the PF in use. As per Table 5.4, the total temperature of the PF does not exceed 113 K. With this data, Vassallo [138] derives a resultant final antenna temperature of 600 K.

PF Elevation	Sky Contribution		Horizon Contribution		Ground Contribution		Total Temperature
	%	Temper-ature	%	Temper-ature	%	Temper-ature	
69°	89%	8.9K	7%	10.5K	4%	12K	32K
21°	53%	5.3K	22%	33.0K	25%	75K	113K
0°	53%	5.3K	23%	34.5K	24%	72K	112K

Table 5.4: Sky, horizon and ground contributions for antenna temperature of the PF by elevation

5.4 Final Link Budget

Various discussions have been carried out in terms of link budgets with Vassallo [138] who has documented the full calculations in his work. In order to facilitate the calculation of link budgets, a popular tool [199] from the Radio amateur Satellite Corporation (AMSAT) for link budget calculation has been used since the start of this project. The main contributing factors for gains and losses are listed in the aggregated uplink and downlink budgets given in Tables 5.5 and 5.6 respectively.

Parameter	Value	Total Value
Ground Station EIRP		56.0 dBm
Channel Losses		
FSPL	-151.8 dB	
Polarization Loss	-3.0 dB	
Pointing Loss	-1.1 dB	
Total Channel Losses		- 155.9 dB
Received power at satellite antenna		-99.9 dBm
Receiver contributions		
Satellite Antenna gain	2.2 dB	
Connector Insertion Loss	-0.2 dB	
Filter Insertion Loss	-2.8 dB	
Total receiver contributions		-0.8 dB
Received power signal level		-100.7 dBm
System noise floor power level		(-122.8 dBm)
Received SNR		22.1 dB
Required SNR		(10.0 dB)
Link Margin		**12.1 dB**

Table 5.5: UoMBSat Uplink budget

For the calculation of FSPL, a satellite orbit altitude of 550 km was considered with a 10° elevation pass. Atmospheric losses, ionospheric losses and rain fall attenuation are taken into consideration. The required SNR of 10 dB originates from the requirement to achieve a bit error rate of 10^{-5} [138]

In the uplink budget Vassallo [138] had planned for ground station EIRP of 56 dBm. Since EIRP is inclusive of the antenna gain, the PAA performance previously described does not affect the value of the ground station EIRP and this link budget remains unmodified. Table 5.6 shows the downlink budget for UoMBSat. There are three main variances from the uplink budget of Vassallo [138], marked in red.

Parameter	Value	Total Value
Satellite Transmitter		
Power amplifier output power	32 dBm	
Antenna gain	2.2 dB	
Connector insertion loss	-0.2 dB	
Satellite EIRP		34.0 dBm
Channel Losses		
FSPL	-151.8 dB	
Polarization Loss	-3.0 dB	
Pointing Loss	-1.1 dB	
Total Channel Losses		- 155.9 dB
Received power signal level at GS		-121.9 dBm
Ground Station		
GDPAA gain (minimum)	14.1 dBi	
Connector Insertion loss	-0.4 dB	
Additional Polarization loss	-5.0 dB	
Ground Station gain		8.7 dB
Received power signal level		-113.2 dB
System noise floor power level		(-124.3 dB)
Received SNR		11.1 dB
Estimated BF SNR Gain		5.0 dB
Required SNR		(10.0 dB)
Link Margin		**6.1 dB**

Table 5.6: UoMBSat worst case downlink budget

The first variation is the GDPAA gain. From Section 5.2 it has been established that the worst-case scenario gain for the PAA is 14.1 dBi instead of the original 15 dBi gain requirement of Req.9, although this may be increased to 17.6 dBi depending on the angle of arrival.

The second variation is the additional polarization loss. Vassallo [138] has already accounted for a 3 dB polarization loss from a satellite point of view should

the CP capability fail due to one of the dipoles malfunctioning. An additional 5 dB polarization loss has been added to the downlink budget in Table 5.6, which is considered to be a worst-case scenario budget. This is to account for a potential 8 dB loss as a result of the AR conclusions in Section 5.1.5. This is in the eventuality that IARU satellite frequency coordination exercise allocates to the UoMBSat project a frequency in the lower end of the band of interest (435 MHz - 438 MHz) where the AR is higher.

The third variation is the addition of an estimated SNR gain introduced by the BF technique. A detailed calculation of the estimated SNR introduced by the beamformer has not been included in the scope of this dissertation. For the purposes of the downlink budget in Table 5.6, 5 dB of SNR gain has been assumed. In their work, Sheldon et al. [41] have measured an improvement of in excess of 5 dB on a four-channel UHF PAA. The SNR gain could be increased by more than 5 dB, however this figure has been used for conservative purposes.

When the downlink budget of Table 5.6 is compared to the downlink budget of Vassallo [138], the downlink margin is reduced by 0.9 dB (from 7 dB to 6.1 dB) which is considered acceptable.

5.5 Cost Analysis

An analysis of all known costs to date is presented in Table 5.7. It is based on the GDPAA being fully assembled consisting of eighteen PFs.

The cost of the GDPAA does not include the SDR required to operate the system, as this could vary significantly in cost. The cost of a good quality SDR such as the Ettus N210 [62] is in the region of EUR2,500. In order to remain within a tight budget of EUR 10,000, the full eighteen PFs may not be required for full hemispherical coverage and may be initially reduced. Hemispherical coverage will remain, however with reduced gain. The cost savings could subsidize the cost of the SDR.

Item	Cost EUR (ex VAT)	Qty	Sub-total (EUR)	Total (EUR)	Notes
PF					
Aluminium Ground plane	59.32	18	1,068		1
1-layer FR4 3.2mm PCBs	80.55	18	1,450		2
GFRP panel	50.84	18	915		
Nylon spacers assortment	50	1	50		
				3,483	
GDPAA Structure					
GFRP rods	6.21	30	186		
PLA: Vertex joint	1.47	12	17		3
PLA: Dihedral Joint	4.89	30	145		4
Final GFRP Strips	500	1	145		
				494	
Radio Front End					
ECB + Shield	375	9	3,375		
T/R Conditioning Board	40	18	720		
Other boards	200	1	200		5
Combiner	500	1	500		6
				4,795	
Others					
RG58 Cables (per metre)	1	500	500		
16U Wall mountable rack panel	350	1	350		
Miscellaneous	200	1	200		7
				1,050	
GRAND TOTAL				**9,822**	

Notes:
1. Inclusive of plasma cutting
2. Inclusive of shipping
3. PLA Cost of EUR30/kg
4. PLA Cost of EUR30/kg
5. Reference distribution and power boards
6. Estimated cost
7. Includes SMA Connectors and cable ties

Table 5.7: Cost analysis of GDPAA

In this chapter, the PAA was analysed from the viewpoint of various parameters, where simulations and measurement results were presented and discussed. Simulations from two different solvers, TS and FDS, were presented for the centre element, combined elements and a two-PF setup. A discussion has been

held on various parameters; return loss, bandwidth, impedance, VSWR, mutual coupling, polarization and gain. Overall, there is good agreement between simulations and measured results.

BF simulations have been presented for elevation angles within the field of view of interest in scenarios of where $\theta = 0°$ and $\theta = 90°$. The results of a BF test were inconclusive and due to time constraints the test could not be repeated.

Noise calculations to derive the antenna temperature have been provided. A link budget for uplink and downlink has been presented and compared to the last UoMBSat link budget prepared by Vassallo [138]. A detailed cost analysis has also been provided showing the various costs envisaged for the final GDPAA to be assembled.

Chapter 6: Conclusions and Future Work

In order to conclude this dissertation a summary will now be provided, followed by the main conclusions and key contributions. Future work considerations are also listed.

6.1 Summary

The UHF amateur satellite band of 435 MHz - 438 MHz is a popular choice of operating frequency for small satellites due to the lower cost of underlying electronics and instrumentation. Support for this operating frequency is ubiquitous in university and the radio amateur community. Various ground stations have been reviewed and the conventional means of tracking satellites is a mechanically steerable Yagi-Uda antenna, or series of them ganged together.

PAAs offer various advantages such as graceful degradation, increased SNR and interference suppression. However, despite these advantages, few advances have been made in the community for PAAs operating in this frequency due to an array of associated complexities. These include additional electronic components, T/R modules, synchronization of clocks, calibration and other items. As a result, the costs are inhibitive. Last but not least, the wavelength at this frequency is relatively large at 70cm. This makes the assembly and handling of **bulky** structures more complex, and a larger footprint for the PAA is required.

A GDPAA based on an icosahedron as the underlying geometrical structure is proposed. Each triangular face is mounted with four single-feed truncated-tip ETPAs placed in a circular lattice with a common triangular ground plane. All joints are designed to be 3D printed. Robust GFRP rods are used for the basic structure. A GFRP layer is added to the triangular planar faces to provide a protective radome to the structure. This design allows for the GDPAA to be locally planar, which is a well-known technology, but globally spherical. This allows for full hemispherical coverage to be obtained without moving parts. Four-channel DDSs are used in the underlying technical design, which allows the designed RF analogue beamformer to control the antenna elements with the required phase and amplitude if desired. An artist impression of the GDPAA is shown in Figure 6.1.
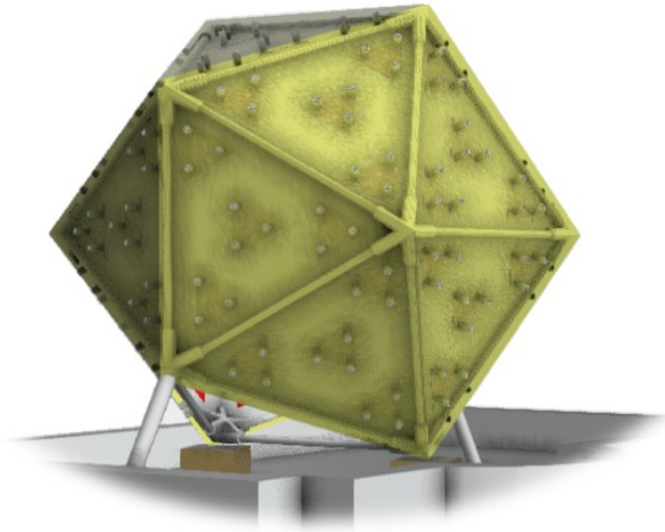
Figure 6.1: Artist impression of UoMBSat GDPAA

Overall, there is good agreement between simulations and measured results. The measured bandwidth of the PAA exceeds 8 MHz, which equates to 2% of the centre frequency 436.5 MHz. The PAA has a measured VSWR value of less than 2 for the whole band of interest (435 MHz - 438 MHz). The measured effect of mutual coupling is generally less than -26 dB however the coupling increases to -20 dB for antenna elements located next to each other but on different PFs. The GDPAA is RHCP, with the measured axial ratio being 8 dB at 435 MHz, improving with the increase in frequency to 5 dB at 438 MHz. The simulated gain on one antenna element is 7.2 dBi and on one PF without BF 12.4 dBi. After BF is taken into consideration, the simulated gain for the GDPAA ranges from 14.1 dBi to 17.6 dBi. One PF has a calculated noise temperature of 113 K. Whilst the axial ratio may be improved, the performance of the parameters of the PAA are considered fit for purpose of the UoMBSat mission requirements and constraints, which are being summarised in Table 6.1.

The uplink margin is 12.1 dB and downlink margin is 6.1 dB. Both margins are considered acceptable to operate a ground station for small satellites. The GDPAA may be placed within a restricted footprint of $2.75\ m\ \times 2.75m$. The total cost of the GDPAA is estimated to be within the region of EUR 10,000. This dissertation challenges the status quo in ground station antennas for small satellites and proves that a **physically compact and low cost** PAA in UHF frequency is technically and commercially feasible.

Reference	Requirement or constraint	Value	Requirement or constraint met status	Comments
Req.1	Centre Frequency	436.5 MHz	Yes	
Req.2	Bandwidth	3 MHz	Yes	> 8 MHz
Req.3	Transmission Mode	Half Duplex	Yes	
Req.4	Polarisation	RHCP	Yes	Support also for LHCP, untested.
Req.5	Azimuth look angle	360°	Yes	
Req.6	Elevation look angle	10° to 170°	Yes	Theoretically 0° to 180°
Req.7	Axial Ratio	<3 dB	No (without impact)	5 dB to 8 dB AR, factored into downlink budget and link margin is adequate
Req.8	EIRP	56.0 dBm	Yes	Possible
Req.9	Gain	15dBi	Partial	Worst case 14.1 dBi, best case 17.6 dBi, factored into downlink budget and link margin is adequate
Req.10	Connector Insertion Loss	-0.4 dB	Yes	
Req.11	Antenna noise temperature	600K	Yes	
Req.12	Footprint	Length < 5m Width < 2.75m	Yes	
Req.13	Weather Protection	N/A	Yes	Radome protection
Req.14	Diagnostics Capability	Required	Yes	Via software and access design
Req.15	Ease of maintenance	Required	Yes	Feed point inspection covers, GDPAA bottom entrance for maintenance
Req.16	Remote operation	Required	Yes	Web-based Software implementation
Req.17	Fabrication Repeatability	Required	Yes	Easy to source materials
Req.18	Cost	≈ EUR 10,000	Yes	
Req.19	Multiple satellite simultaneous tracking	Scalability required	Yes	

Table 6.1: UoMBsat mission requirements and constraints checklist

6.2 Conclusions

From the phased array ground station antenna designed in this dissertation the following may be concluded:

1. It is possible to design a PAA for operation in the UHF frequency with relatively low cost. The cost of the GDPAA, inclusive of structure, antennas and underlying electronics is in the region of EUR 10,000 for the entire GDPAA including structure, antennas, and underlying electronics.

2. The cost of the GDPAA is in the same region of a conventional ground station built from sourcing individual parts. It is five times cheaper than the current market price of a complete COTS GS, with the added benefits of a PAA.

3. Phase shifting may be carried out via COTS components comprising of primarily four-channel DDSs.

4. Through the proposed design, the PAA is repeatable, can be distributed in kit form and is easily reconstructable at other GS locations.

5. The proposed system is functionally scalable and through its software design is interoperable with other GSNs and UoMBSat software components.

6. Post manufacturing tuning of the antennas is possible and an element of on-site calibration is required on installation. The system is designed in a way whereby further modifications may be made with minimal impact, such as the relocation of feed point or design modification of the ETPA.

7. Through the miniaturization of the design, a reduced footprint is obtained and the PAA may be placed within a constrained footprint of 2.75 m × 2.75 m.

8. The software implementation design allows the interoperability with other systems and allows for software functions for post-installation maintenance and health diagnostics to added. BF algorithms may be easily added with a plug-and-play approach.

9. The performance of the antenna may be adjusted by the size of the active sector in terms of the number of simultaneous PFs used to steer the beam.

10. *The main requirements for the UoMBSat mission have been met. The GDPAA designed in this dissertation is considered fit for purpose to be used as the GS for the upcoming UoMBSat mission.*

6.2.1 Main Contributions

The main contributions described within this dissertation are summarized as follows:

1. At a high level, this work addresses the design of all components of a phase array ground station antenna for small satellites. The works of Agius [110] and Abela [168] have originated from this project. This work may serve as a comprehensive reference for a GS designer for small satellites looking to implement any part of a PAA.

2. A site survey has been carried out which has allowed for the ASTREA team to decide the location of the UoMBSat GS.

3. A novel design for a low-cost GDPAA with reduced footprint has been published as part of this work [165]. It has been found that if the individual antenna elements are placed in a circular lattice, the footprint is reduced and the overall array performance and antenna isolation are improved.

4. Design and build of four antenna elements has been made, assembling a fully functional higher-level building block PF. Measurements are in good agreement with simulation results.

5. An analogue beamformer has been designed implemented on a PF level.

6. A Python GDPAA library has been designed with the various functions required to operate a PAA; namely the beamformer, tracker and scanner.

7. Various tests have been designed which lay the groundwork for further validation of implemented components.

6.3 Future Work

This work has covered all project objectives originally anticipated. However, during the various phases of this work, various items have been observed that may be improved upon. These are listed below.

1. The AR of the ETPA can be improved by reconsidering the truncation ratio of the ETPA and relocating the feed point. This will directly improve the link budget to the effect of 5 dB. The existing work serves as a reference point for the validation of simulations for this exercise.

2. The technique of sequential rotation may be considered to orientate the antenna elements on a PF in a different direction such that better CP may be obtained through alternate positioning.

3. One may consider increasing the thickness of the ground plane aluminium such that warping is reduced to avoid beam squinting. This is preferred to adding more dihedral joints which could also give a similar result.

4. A 3D printed coarse mesh or other electromagnetically porous layer may be added between the ground plane and the FR4 substrate to guarantee that the substrate air gap remains precise and stable to within a fraction of a millimetre, as this has been found to have an effect on the performance of the antenna.

5. Further multiple-PF simulations may be carried out in CST to include radiation patterns. The radiation patterns simulated in CST may be imported in MATLAB for further processing including a simulation on the anticipated SNR gain. Beam eccentricity may be investigated further from such simulations.

6. Carbon fiber filled materials may be used to 3D print tougher vertex joints. High-quality wear resistant printer nozzles are available to allow printing with such highly abrasive materials.

References

[1] H. Heidt, J. Puig-Suari, A. Moore, S. Nakasuka and R. Twiggs, "CubeSat: A new generation of picosatellite for education and industry low-cost space experimentation," 2000.

[2] "The Cubesat Program," [Online]. Available: https://www.cubesat.org/about. [Accessed 15 03 2021].

[3] A. Toorian, K. Diaz and S. Lee, "The cubesat approach to space access," in *2008 IEEE Aerospace Conference*, 2008.

[4] J. Bouwmeester and J. Guo, "Survey of worldwide pico-and nanosatellite missions, distributions and subsystem technology," *Acta Astronautica,* vol. 67, p. 854–862, 2010.

[5] T. Villela, C. A. Costa, A. M. Brandão, F. T. Bueno and R. Leonardi, "Towards the thousandth CubeSat: A statistical overview," *International Journal of Aerospace Engineering,* vol. 2019, 2019.

[6] "Nanosats," [Online]. Available: https://www.nanosats.eu/#figures. [Accessed 19 04 2021].

[7] Y. Rahmat-Samii, V. Manohar and J. M. Kovitz, "For Satellites, Think Small, Dream Big: A review of recent antenna developments for CubeSats.," *IEEE Antennas and Propagation Magazine,* vol. 59, p. 22–30, 2017.

[8] QB50, "QB50 Home Page," [Online]. Available: https://www.qb50.eu/index.html. [Accessed 03 25 2021].

[9] University of Malta, "First Maltese PicoSatellite prototypes to undergo qualification at French Space Agency," 03 10 2019. [Online]. Available: https://www.um.edu.mt/newspoint/news/features/2019/10/firstmaltesepicosatellite prototypestoundergoqualificationatfrenchspaceagency. [Accessed 15 12 2020].

[10] D. Cachia, J. Camilleri, M. A. Azzopardi, M. Angling and A. Sammut, "Feasibility Study of a PocketQube Platform to Host an Ionospheric Impedance Probe," in *the ESA/CNES 4S Symposium: Small Satellites go Viral*, 2016.

[11] Alba Orbital, "http://www.albaorbital.com/launch," [Online]. Available: http://www.albaorbital.com/launch. [Accessed 21 02 2021].

[12] I. Vertat, R. LInhart, M. Pokorny, J. Masopust, P. Fiala and J. Mraz, "Small satellite ground station in Pilsen—experiences with VZLUSAT-1 commanding and future modifications toward open reference ground station solution," in *Radioelektronika (RADIOELEKTRONIKA), 2018 28th International Conference*, 2018.

[13] S. Speretta, T. Pérez Soriano, J. Bouwmeester, J. Carvajal Godínez, A. Menicucci, T. G. Watts, P. P. Sundaramoorthy, J. Guo and E. K. A. Gill, "Cubesats to pocketqubes: Opportunities and challenges," in *Proceedings of the 67th*

International Astronautical Congress (IAC), 2016.

[14] S. Hitefield, Z. Leffke, M. Fowler and R. W. McGwier, "System overview of the Virginia Tech Ground Station," in *2016 IEEE Aerospace Conference*, 2016.

[15] T. S. Tuli, N. G. Orr and R. E. Zee, "Low cost ground station design for nanosatellite missions," in *Proceedings of the North American Space Symposium*, 2006.

[16] D. Parker and D. C. Zimmermann, "Phased arrays-part 1: theory and architectures," *IEEE transactions on microwave theory and techniques,* vol. 50, p. 678–687, 2002.

[17] D. Parker and D. C. Zimmermann, "Phased arrays-part II: implementations, applications, and future trends," *IEEE Transactions on microwave theory and techniques,* vol. 50, p. 688–698, 2002.

[18] P. Rocca, G. Oliveri, R. J. Mailloux and A. Massa, "Unconventional phased array architectures and design methodologies—A review," *Proceedings of the IEEE,* vol. 104, p. 544–560, 2016.

[19] U. Nielsen, "Tomographic Techniques for Radar Ice Sounding," Danmarks Tekniske Universitet (DTU), 2015.

[20] C. C. Hernandez, V. Krozer, J. Vidkjaer and J. Dall, "POLARIS: ESA's airborne ice sounding radar front-end design, performance assessment and first results," 2009.

[21] C. F. du Toit, M. Deshpande and R. F. Rincon, "Advanced antenna design for NASA's EcoSAR instrument," in *Phased Array Systems and Technology (PAST), 2016 IEEE International Symposium on*, 2016.

[22] I. S. Association and others, "145-2013-IEEE standard for definitions of terms for antennas," *IEEE, New York, NY,* 2013.

[23] W. L. Stutzman and G. A. Thiele, Antenna theory and design, John Wiley & Sons, 2012.

[24] C. A. Balanis, Antenna theory: analysis and design, John wiley & sons, 2016.

[25] P. Delos, B. Broughton and J. Kraft, "Phased Array Antenna Patterns—Part 2: Grating Lobes and Beam Squint," *26 Phased Array Antenna Patterns—Series,* p. 39, 2020.

[26] S. W. Ellingson, Electromagnetics, Vol. 2, Virgina Tech Publishing, 2020.

[27] C. T. Keyer, "Best Swr Meter For Ham Radio (1)5 Best SWR Meters for HAM Radio (Reviews Updated 2021) February 18, 2020," [Online]. Available: https://www.cwtouchkeyer.com/best-swr-meter-for-ham-radio/. [Accessed 04 04 2020].

[28] Microwaves 101, "S-Parameters," [Online]. Available: https://www.microwaves101.com/encyclopedias/s-parameters#:~:text=S%2Dparameters%20are%20defined%20for,to%20the%20nu

mber%20of%20ports.. [Accessed 04 04 2021].

[29] University of Malta, "Electromagnetics Research Group Laboratory Resources," [Online]. Available: https://www.um.edu.mt/research/electromagnetics/laboratoryresources. [Accessed 04 04 2021].

[30] I. Uchendu and J. R. Kelly, "Survey of beam steering techniques available for millimeter wave applications," *Progress In Electromagnetics Research,* vol. 68, p. 35–54, 2016.

[31] J. Kim, J. Jeong and S. Jeon, "Improvement of Noise Performance in Phased-Array Receivers," *ETRI Journal,* vol. 33, p. 176–183, 2011.

[32] B. H. Stenhaug, "Antenna system for a ground station communicating with the ntnu test satellite (nuts)," 2011.

[33] Ø. Karlsen, "Ground station considerations for the AMOS satellite programme," 2017.

[34] J. Kalde, "UHF communication system for cubesatellite," 2015.

[35] H. Vangli, "Construction of a remotely operated satellite ground station for low earth orbit communication," 2010.

[36] M. Fischer and A. L. Scholtz, "Design of a Multi-mission Satellite Ground Station for Education and Research," 2010.

[37] A. Wickramanayake, *Design, development and operation of a student ground station,* 2007.

[38] D. Ichikawa, "CubeSat-to-Ground Communication and Mobile Modular Ground-Station Development," *University of Hawaii,* 2006.

[39] C. Cooper, R. Fevig and J. Patel, "The CubeSat ground station at the university of arizona," in *Proceedings of the 16th AIAA/USU Conference on Small Satellites*, 2002.

[40] California Polytechnic State University, "PolySat Earth Station," [Online]. Available: https://www.polysat.org/earth-station/. [Accessed 22 03 2021].

[41] C. Sheldon, J. Bradfield, E. Sanchez, J. Boye, D. Copeland and N. Adams, "UHF Phased Array Ground Stations for Cubesat Applications," 2016.

[42] Francois Visser, "United Nations Office for Outer Space Affairs," 13 12 2017. [Online]. Available: http://www.unoosa.org/documents/pdf/psa/activities/2017/SouthAfrica/slides/Presentation63.pdf. [Accessed 05 01 2021].

[43] Yaesu, "Yaesu G-5500 Instruction Manual," [Online]. Available: https://www.yaesu.com/downloadFile.cfm?FileID=8814&FileCatID=155&FileName=G%2D5500%5FIM%5FENG%5FE12901004.pdf&FileContentType=application%2Fpdf. [Accessed 03 03 2021].

[44] A. T. S.A., "Tonna 435MHz 2x19 Element Instruction Manual," [Online]. Available: http://www.radiomanual.info/schemi/ACC_antenna/Tonna_435_2x19crossed_user .pdf. [Accessed 22 03 2021].

[45] Yaesu, "G-1000DXA User Manual," [Online]. Available: https://www.yaesu.com/downloadFile.cfm?FileID=16800&FileCatID=155&FileN ame=G%2D800DXA%5F1000DXA%5F2800DXA%5FOM%5FENG%5FEAA67 X101%5F2102B%2DBS.pdf&FileContentType=application%2Fpdf. [Accessed 22 03 2021].

[46] SPID Elektronik, "BIG-Ras User Manual," [Online]. Available: http://cdn.spid.net.pl/manuale/Manual-BIG-RAS-EN.pdf. [Accessed 22 03 2021].

[47] Yaesu, "GS-232 Manual," [Online]. Available: http://www.radiomanual.info/schemi/YAESU_ACC/Yaesu_GS-23_GS-232_user.pdf. [Accessed 21 03 2021].

[48] Celestrak, "Satellite Tracking Software Index," [Online]. Available: https://www.celestrak.com/software/satellite/sat-trak.php. [Accessed 21 03 2020].

[49] DX Zone, "Software," [Online]. Available: https://www.dxzone.com/catalog/Software/. [Accessed 21 03 2021].

[50] DK1TB, "SatPC32," [Online]. Available: http://www.dk1tb.de/indexeng.htm. [Accessed 22 03 2021].

[51] Space-Track.Org, "API Documentation," [Online]. Available: https://www.space-track.org/documentation#/api. [Accessed 21 03 2021].

[52] Celestrak, "NORAD Two-Line Element Sets," [Online]. Available: https://www.celestrak.com/NORAD/elements/. [Accessed 22 03 2013].

[53] NASA, "Browse APIs," [Online]. Available: https://api.nasa.gov/. [Accessed 21 03 2021].

[54] Rhodesmill.org, "PyEphem astronomy library for Python," [Online]. Available: https://rhodesmill.org/pyephem/. [Accessed 23 03 2021].

[55] B. M. Zieliński, "A comparison of various types of TNC controllers," *IFAC Proceedings Volumes,* vol. 42, p. 80–85, 2009.

[56] Kantronics, "KPC-9612 Plus manual," [Online]. Available: https://kantronics.com/wp-content/uploads/2018/10/KPC-9612Plus-Manual-RevG.pdf. [Accessed 22 03 2020].

[57] ICOM, "IC-910H," [Online]. Available: http://www.icomamerica.com/en/products/amateur/satellite/910h/specifications.as px. [Accessed 22 03 2021].

[58] Icom, "IC-9100," [Online]. Available: http://www.icomamerica.com/en/products/amateur/satellite/9100/specifications.as px. [Accessed 22 03 2021].

[59] Yaesu, "VHF/UHF Amateur Radio Equipment," [Online]. Available: https://www.yaesu.com/pdf/201805_V_UHF_Amateur_Radio.pdf. [Accessed 22 03 2021].

[60] O. Vassallo, "Design of a software radio hardware platform for a picosatellite," 2018.

[61] GNU Radio, "About GNU Radio," [Online]. Available: https://www.gnuradio.org/about/. [Accessed 22 03 2021].

[62] Ettus Research, "About Ettus Research," [Online]. Available: https://www.ettus.com/about/. [Accessed 22 03 2021].

[63] FUNCube Donle, "FUNcube Dongle Pro+ User Manual (V4)," [Online]. Available: http://www.funcubedongle.com/MyImages/FCD2ManualV4.pdf. [Accessed 22 03 2021].

[64] RTL-SDR, "ABOUT RTL-SDR," [Online]. Available: https://www.rtl-sdr.com/about-rtl-sdr/. [Accessed 22 03 2021].

[65] Great Scott Gadgets, "HackRF One," [Online]. Available: https://greatscottgadgets.com/hackrf/one/. [Accessed 22 03 2021].

[66] ISISPACE, "Full Ground Station Kit VHF/UHF/S-band," [Online]. Available: Full Ground Station Kit VHF/UHF/S-band. [Accessed 22 03 2021].

[67] Alba Orbital , "Ground Station Solutions," [Online]. Available: http://www.albaorbital.com/ground-station. [Accessed 22 03 2021].

[68] ISISPACE, "Satellite-as-a-service," [Online]. Available: https://www.isispace.nl/satellite-as-a-service/. [Accessed 22 03 2020].

[69] Alba Orbital, "Alba Connect Network," [Online]. Available: https://www.albaorbital.com/albaconnect. [Accessed 22 03 2021].

[70] Amazon Web Services, "AWS Ground Station," [Online]. Available: https://aws.amazon.com/ground-station/. [Accessed 22 03 2021].

[71] Leaf Space, "Subscribe To Our Shared Ground Station Network," Leaf Space, [Online]. Available: https://leaf.space/leaf-line/. [Accessed 25 03 2021].

[72] M. Krynitz, "The ground station of the future," *Acta Astronautica,* vol. 67, p. 1252–1254, 2010.

[73] European Cooperation for Space Standardization, "Active Standards," [Online]. Available: https://ecss.nl/standards/active-standards/. [Accessed 24 03 2021].

[74] K. Leveque, J. Puig-Suari and C. Turner, "Global educational network for satellite operations (GENSO)," 2007.

[75] European Space Agency, "Global Educational Network for Satellite Operations," [Online]. Available: http://www.esa.int/Education/Global_Educational_Network_for_Satellite_Operations. [Accessed 23 03 2021].

[76] github/aerospaceresearch, "Distributed Ground Station Network," [Online].
      Available: https://aerospaceresearch.net/?page_id=1122. [Accessed 25 03 2021].

[77] ThumbSat / ThumbNet, "ThumbNet," [Online]. Available:
      https://www.thumbsat.com/thumbnet. [Accessed 25 03 2021].

[78] UNISEC, "UNISEC GSN-WG," [Online]. Available:
      http://www.astro.mech.tohoku.ac.jp/~gsn/en/. [Accessed 25 03 2021].

[79] D. J. White, I. Giannelos, A. Zissimatos, E. Kosmas, D. Papadeas, P. Papadeas, M.
      Papamathaiou, N. Roussos, V. Tsiligiannis and I. Charitopoulos, "SatNOGS:
      satellite networked open ground station," 2015.

[80] Libre Space Foundation, "Our Projects," [Online]. Available:
      https://libre.space/projects/. [Accessed 23 03 2021].

[81] SatNOGS, "124 - 9H1Y-70cm-PlanarFace-FR4_ETPAx4," [Online]. Available:
      https://network.satnogs.org/stations/124/. [Accessed 23 03 2021].

[82] Hamlib, "Ham radio control libraries," [Online]. Available:
      https://github.com/Hamlib/Hamlib/wiki. [Accessed 23 03 2021].

[83] UpSAT, "UPSat Command and Control," 19 07 2016. [Online]. Available:
      https://upsat.gr/?p=328&fbclid=IwAR00GWKNQk6SvyHc3xxbV4-EuzGh-
      fB6AkLddmnNoBfYmPDWkQK54RSYAJI. [Accessed 23 03 2020].

[84] UpSAT, "UpSAT Overview," [Online]. Available: https://upsat.gr/?page_id=9.
      [Accessed 23 03 2021].

[85] B. P. Kumar, C. Kumar, V. S. Kumar and V. V. Srinivasan, "A spherical phased
      array antenna with unequal amplitude excitation for satellite application," in *2017
      IEEE International Conference on Antenna Innovations & Modern Technologies
      for Ground, Aircraft and Satellite Applications (iAIM)*, 2017.

[86] R. Martínez Rodríguez-Osorio and M. A. Salas Natera, "On the Use of Ground
      Antenna Arrays for Satellite Tracking: Architecture, Beamforming, Calibration
      and Measurements," 2010.

[87] B. Tomasic, J. Turtle and S. Liu, "The Geodesic Sphere Phased Array Antenna for
      Satellite Communication and Air/Space Surveillance-Part 1," 2004.

[88] B. Tomasic, J. Turtle, R. Shiang Liu, S. Schmier, P. Bharj and P. Oleski, "The
      geodesic dome phased array antenna for satellite control and communication -
      subarray design, development and demonstration," USA, 2003.

[89] J. S. Herd and M. D. Conway, "The Evolution to Modern Phased Array
      Architectures," *Proceedings of the IEEE,* vol. 104, p. 519–529, 2016.

[90] S. Ghosh and D. Sen, "An inclusive survey on array antenna design for millimeter-
      wave communications," *IEEE Access,* vol. 7, p. 83137–83161, 2019.

[91] L. Jin, H. Wang and others, "Investigation of different types of array structures for
      smart antennas," in *2008 International Conference on Microwave and Millimeter*

Wave Technology, 2008.

[92] C. Wolff, "Phased Array Antenna," [Online]. Available: https://www.radartutorial.eu/06.antennas/Phased%20Array%20Antenna.en.html. [Accessed 05 04 2021].

[93] E. Sharp, "A triangular arrangement of planar-array elements that reduces the number needed," *IRE Transactions on Antennas and Propagation,* vol. 9, p. 126–129, 1961.

[94] N. H. Noordin, A. O. El-Rayis, N. Haridas, B. Flynn, A. T. Erdogan and T. Arslan, "Triangular lattices for mutual coupling reduction in patch antenna arrays," in *2011 Loughborough Antennas & Propagation Conference*, 2011.

[95] M. Kiani-Kharaji, H. R. Hassani and S. Mohammad-Ali-Nezhad, "Wide scan phased array patch antenna with mutual coupling reduction," *IET Microwaves, Antennas & Propagation,* vol. 12, p. 1932–1938, 2018.

[96] G. Dadashzadeh, A. Dadgarpour, F. Jolani and B. S. Virdee, "Mutual coupling suppression in closely spaced antennas," *IET microwaves, antennas & propagation,* vol. 5, p. 113–125, 2011.

[97] E. Rajo-Iglesias, O. Quevedo-Teruel and L. Inclan-Sanchez, "Mutual coupling reduction in patch antenna arrays by using a planar EBG structure and a multilayer dielectric substrate," *IEEE Transactions on Antennas and Propagation,* vol. 56, p. 1648–1655, 2008.

[98] P. Ioannides and C. A. Balanis, "Uniform circular and rectangular arrays for adaptive beamforming applications," *IEEE Antennas and Wireless Propagation Letters,* vol. 4, p. 351–354, 2005.

[99] H. Schippers, J. Verpoorte, P. Jorna, A. Hulzinga, A. Meijerink, C. Roeloffzen, R. G. Heideman, A. Leinse and M. Wintels, "Conformal phased array with beam forming for airborne satellite communication," 2008.

[100] G. Buttazzoni and R. Vescovo, "Reducing the Sidelobe Power Pattern of Linear Broadside Arrays by Refining the Element Positions," *IEEE Antennas and Wireless Propagation Letters,* vol. 17, p. 1464–1468, 2018.

[101] K. Y. Reddy, R. B. Kumar, M. Jijenth, K. K. Suman, V. S. Gangwar and A. K. Singh, "Synthesis of randomly spaced planar antenna array with low peak side lobe level (PSLL) using Modified Genetic Algorithm," in *2017 IEEE International Conference on Antenna Innovations & Modern Technologies for Ground, Aircraft and Satellite Applications (iAIM)*, 2017.

[102] G. Kiesel, E. Strates and C. Phillips, "Beam forming with a reconfigurable antenna array," in *Phased Array Systems and Technology (PAST), 2016 IEEE International Symposium on*, 2016.

[103] P. Fortescue, G. Swinerd and J. Stark, Spacecraft systems engineering, John Wiley & Sons, 2011.

[104] G. Knittel, "Choosing the number of faces of a phased-array antenna for hemisphere scan coverage," *Antennas and Propagation, IEEE Transactions on,* vol. 13, p. 878–882, 1965.

[105] J. Kmetzo, "An analytical approach to the coverage of a hemisphere by n planar phased arrays," *Antennas and Propagation, IEEE Transactions on,* vol. 15, p. 367–371, 1967.

[106] D. Sengupta, T. Smith and R. Larson, "Radiation characteristics of a spherical array of circularly polarized elements," *Antennas and Propagation, IEEE Transactions on,* vol. 16, p. 2–7, 1968.

[107] M. Sierra-Pérez, A. Torres, J. L. Masa, M. Gómez and I. Montesinos, "Geoda: Adaptive antenna array for satellite signal reception," 2007.

[108] L. D. Poles, J. P. Kenney and E. Martin, "UHF phased-array measurements in snow," *IEEE Antennas and Propagation Magazine,* vol. 46, p. 181–184, 2004.

[109] M. Biswas and A. Mandal, "The effect of radome on resonance characteristics of triangular patch antenna," *International Journal of Engineering Science and Technology (IJEST),* vol. 3, p. 536–546, 2011.

[110] R. Agius, *Design of the Radio Front End of a UHF Phased Array System,* 2019.

[111] W. E. S. Ong, "Commercial off the shelf direct digital synthesizers for digital array radar," 2005.

[112] L. Jiaguo, W. Manqin, J. Xueming and F. Zhengxing, "Active phased array antenna based on DDS," in *Phased Array Systems and Technology, 2003. IEEE International Symposium on*, 2003.

[113] Y. Yusuf and X. Gong, "A low-cost patch antenna phased array with analog beam steering using mutual coupling and reactive loading," *IEEE Antennas and Wireless Propagation Letters,* vol. 7, p. 81–84, 2008.

[114] L. Segers, B. da Silva, A. Braeken and A. Touhafi, "Cloud-Based Acoustic Beamforming Emulator for FPGA-Based Sound Source Localization," in *2018 4th International Conference on Cloud Computing Technologies and Applications (Cloudtech)*, 2018.

[115] A. K. Bhattacharyya and others, "Phased array antennas," in *Floquet analysis, synthesis, BFNs, and active array systems*, Wiley Online Library, 2006.

[116] A. Badawy, T. Khattab, D. Trinchero, T. ElFouly and A. Mohamed, "A Simple Angle of Arrival Estimation Scheme," *arXiv preprint arXiv:1409.5744,* 2014.

[117] J. Mailloux Robert, Phased Array Antenna Handbook, vol. 19, Emerald Group Publishing Limited, 1999.

[118] L. C. Godara, "Applications Of Antenna Arrays To Mobile Communications, Part I: Performance Improvement, Feasibility, And System Considerations," *Proceedings of the IEEE,* vol. 85, p. 1029–1030, 1997.

[119] M. Salucci, L. Poli, A. F. Morabito and P. Rocca, "Adaptive nulling through subarray switching in planar antenna arrays," *Journal of Electromagnetic Waves and Applications,* vol. 30, p. 404–414, 2016.

[120] M. A. Ingram, R. Romanofsky, R. Q. Lee, F. Miranda, Z. Popovic, J. Langley, W. C. Barott, M. U. Ahmed and D. Mandl, "Optimizing satellite communications with adaptive and phased array antennas," 2004.

[121] Y. Cheng, M. Haardt, H. Henniger, R. Metzig and E. Diedrich, "Interference Suppression and Electronic Tracking Using Antenna Arrays at Satellite Ground Stations," in *Smart Antennas (WSA), 2013 17th International ITG Workshop on*, 2013.

[122] Toner Cable Equipment Inc. , "WH Series Helical Antennas," [Online]. Available: https://www.tonercable.com/pdf/Wade_WH_Series_Helical_Antennas.pdf. [Accessed 20 04 2021].

[123] M. Mirmozafari, "DESIGN AND IMPLEMENTATION OF A PHASED ARRAY ANTENNA FOR MULTI-MISSION APPLICATIONS," 2018.

[124] M. Mirmozafari, S. Saeedi, H. Saeidi-Manesh, G. Zhang and H. H. Sigmarsson, "Direct 3-D Printing of Non-Planar Linear Dipole Phased Array Antennas," *IEEE Antennas and Wireless Propagation Letters,* 2018.

[125] A. J. Fenn, D. J. Pippin, C. M. Lamb, F. G. Willwerth, H. M. Aumann and J. P. Doane, "3D printed conformal array antenna: simulations and measurements," in *Phased Array Systems and Technology (PAST), 2016 IEEE International Symposium on*, 2016.

[126] M. Khosronejad and G. G. Gentili, "Design of an Archimedean spiral UHF antenna for pulse monitoring application," in *2015 Loughborough Antennas & Propagation Conference (LAPC)*, 2015.

[127] I. O. Farhat, K. Z. Adami, Y. Zhang, A. K. Brown, C. V. Sammut and I. C. on Electromagnetics in Advanced Applications (ICEAA), *Ultra-wideband tightly coupled fractal octagonal phased array antenna,* Institute of Electrical and Electronics Engineers Inc., 2013.

[128] Schwarzbeck, "UHALP 9108A," [Online]. Available: http://schwarzbeck.de/en/antennas/logarithmic-periodic-broadband-antennas/standard-lpda/205-uhalp-9108-a.html. [Accessed 21 04 2021].

[129] U. o. Malta, "Radio Telescope," [Online]. Available: https://www.um.edu.mt/library/oar/bitstream/123456789/19383/1/THINK%2c%202016-17%20-%20A2.pdf. [Accessed 21 04 2021].

[130] A. S. Inc., "SAS-584 Datasheet," [Online]. Available: https://www.ahsystems.com/datasheets/SAS-584-Horn-Antenna-Datasheet.pdf. [Accessed 21 04 2021].

[131] Wikiwand, "Vivaldi Antenna," [Online]. Available: https://www.wikiwand.com/en/Vivaldi_antenna. [Accessed 21 04 21].

[132] T.-H. Chio and D. H. Schaubert, "Parameter study and design of wide-band widescan dual-polarized tapered slot antenna arrays," *IEEE Transactions on Antennas and Propagation,* vol. 48, p. 879–886, 2000.

[133] W. J. Otter, B. P. Pirollo, R. I. Henderson and R. A. Lewis, "Multi-octave BAVA radiating elements for use in modular phased array antennas," in *2009 3rd European Conference on Antennas and Propagation*, 2009.

[134] A. Presse, J.-M. Floch and A.-C. Tarot, "Flexible VHF/UHF Vivaldi Antenna for Broadband Applications," *Progress In Electromagnetics Research,* vol. 52, p. 37–43, 2015.

[135] T. Ödman and P. Hallbjörner, "Vivaldi antenna with low frequency resonance for reduced dimensions," in *2013 7th European Conference on Antennas and Propagation (EuCAP)*, 2013.

[136] University of Malta, "ASTREA Student Research Projects," [Online]. Available: https://www.um.edu.mt/research/astrionics/projects. [Accessed 24 04 2021].

[137] A. Abela, "Design of LDPC Codec for the FX.25 Pico-satellite Link," University of Malta, 2019.

[138] O. Vassallo, "Design of a Software Radio for a Pico-Satellite," University of Malta, 2021.

[139] H. Wadell, "Volume, shape, and roundness of rock particles," *The Journal of Geology,* vol. 40, p. 443–451, 1932.

[140] T. Ohira and K. Gyoda, "Electronically steerable passive array radiator antennas for low-cost analog adaptive beamforming," 2000.

[141] D. Orban and G. J. K. Moernaut, "The basics of patch antennas, updated".

[142] K. F. Lee, K. M. Luk and H. W. Lai, Microstrip patch antennas, World Scientific, 2017.

[143] K. Dang, "Phased array antenna investigation for CubeSat size satellites," 2016.

[144] Y. S. H. Khraisat and M. M. Olaimat, "Comparison between rectangular and triangular patch antennas array," in *2012 19th International Conference on Telecommunications (ICT)*, 2012.

[145] M. M. Olaimat and N. I. Dib, "Improved formulae for the resonant frequencies of triangular microstrip patch antennas," *International Journal of Electronics,* vol. 98, p. 407–424, 2011.

[146] M. S. Sharawi, "Current misuses and future prospects for printed multiple-input, multiple-output antenna systems [wireless corner]," *IEEE Antennas and Propagation Magazine,* vol. 59, p. 162–170, 2017.

[147] Brittanica, "Wacław Sierpiński," [Online]. Available: https://www.britannica.com/biography/Waclaw-Sierpinski. [Accessed 15 06 2021].

[148] K.-F. Lee, K.-M. Luk and J. S. Dahele, "Characteristics of the equilateral triangular patch antenna," *IEEE Transactions on Antennas and Propagation,* vol. 36, p. 1510–1518, 1988.

[149] M. Fallahpour and R. Zoughi, "Antenna Miniaturization Techniques: A Review of Topology-and Material-Based Methods," *IEEE Antennas and Propagation Magazine,* vol. 60, p. 38–50, 2018.

[150] A. Khan and R. Nema, "Analysis of five different dielectric substrates on microstrip patch antenna," *International journal of computer applications,* vol. 55, 2012.

[151] L. C. Paul, M. S. Hosain, S. Sarker, M. H. Prio, M. Morshed and A. K. Sarkar, "The effect of changing substrate material and thickness on the performance of inset feed microstrip patch antenna," *American Journal of Networks and Communications,* vol. 4, p. 54–58, 2015.

[152] V. Sharma, B. Sharma, V. K. Saxena, K. B. Sharma and D. Bhatnagar, "Modified rectangular patch antenna with air-gap for improved bandwidth," in *2008 International Conference on Recent Advances in Microwave Theory and Applications*, 2008.

[153] A. Gupta and P. K. S. Pourush, "Microstrip array antenna with and without airgap in plasma environment," 2001.

[154] J. Helszajn and D. S. James, "Planar triangular resonators with magnetic walls," *IEEE Transactions on Microwave Theory and Techniques,* vol. 26, p. 95–100, 1978.

[155] W. Chen, K.-F. Lee and J. S. Dahele, "Theoretical and experimental studies of the resonant frequencies of the equilateral triangular microstrip antenna," *IEEE transactions on antennas and propagation,* vol. 40, p. 1253–1256, 1992.

[156] M. Biswas and D. Guha, "Input impedance and resonance characteristics of superstrate-loaded triangular microstrip patch," *IET microwaves, antennas & propagation,* vol. 3, p. 92–98, 2009.

[157] Z. Li, A. Haigh, C. Soutis, A. Gibson and R. Sloan, "Dielectric constant of a three-dimensional woven glass fibre composite: analysis and measurement," *Composite Structures,* vol. 180, p. 853–861, 2017.

[158] K. K.-M. Chan, A. E.-C. Tan and K. Rambabu, "Decade bandwidth circularly polarized antenna array," *IEEE transactions on antennas and propagation,* vol. 61, p. 5435–5443, 2013.

[159] J.-H. Lu, C.-L. Tang and K.-L. Wong, "Single-feed slotted equilateral-triangular microstrip antenna for circular polarization," *IEEE Transactions on antennas and propagation,* vol. 47, p. 1174–1178, 1999.

[160] Y. Suzuki, N. Miyano and T. Chiba, "Circularly polarised radiation from singly fed equilateral-triangular microstrip antenna," in *IEE Proceedings H (Microwaves, Antennas and Propagation)*, 1987.

[161] C.-L. Tang, J.-H. Lu and K.-L. Wong, "Circularly polarised equilateral-triangular microstrip antenna with truncated tip," *Electronics Letters,* vol. 34, p. 1277–1277, 1998.

[162] R. K. Vishwakarma, J. A. Ansari and M. K. Meshram, "Equilateral triangular microstrip antenna for circular polarization dual-band operation," 2006.

[163] V. G. Kasabegoudar and K. J. Vinoy, "A broadband suspended microstrip antenna for circular polarization," *Progress In Electromagnetics Research,* vol. 90, p. 353–368, 2009.

[164] J.-H. Lu, C.-L. Tang and K.-L. Wong, "Circular polarisation design of a single-feed equilateral-triangular microstrip antenna," *Electronics Letters,* vol. 34, p. 319–321, 1998.

[165] C. Grech, M. A. Azzopardi and V. Buttigieg, "Circular lattice design for UHF geodesic dome phased array antenna with reduced footprint," in *2020 International Symposium on Antennas and Propagation (ISAP)*, 2021.

[166] David1729, "Icosahedron Pipe Joint," Cults3d.com, [Online]. Available: https://cults3d.com/en/3d-model/various/icosahedron-pipe-joint. [Accessed 19 05 2021].

[167] J. Bouwmeester, T. Walkinshaw, A. Paliwoda, C. Pires, S. McAndrew, R. C. Prajapati, S. Lorquet, F. Paez, K. Kumar, A. Dunn, I. Daradimos and C. Grech, *Presentations of the 2nd PocketQube Workshop (Delft, 2018),* DataverseNL, 2018.

[168] L. Abela, "Digital antenna array combiner and divider using FPGAs," 2020.

[169] J. Nieves-Chinchilla, R. Martínez, M. Farjas, R. Tubio-Pardavila, D. Cruz and M. Gallego, "Reverse engineering techniques to optimize facility location of satellite ground stations on building roofs," *Automation in Construction,* vol. 90, p. 156–165, 2018.

[170] B. Shiang Liu, J. Tomasic and J. Turtle, "The geodesic dome phased array antenna for satellite operations support - antenna resource management," 2007.

[171] Libre Space Foundation, "satnogs-client Gitlab page," [Online]. Available: https://gitlab.com/librespacefoundation/satnogs/satnogs-client. [Accessed 29 04 2020].

[172] Pothos, "SoapySDR project," [Online]. Available: https://github.com/pothosware/SoapySDR/wiki. [Accessed 05 12 2020].

[173] Libre Space Foundation, "SATNOG_LO_OFFSET greater than 0.25 x sample rate," [Online]. Available: https://community.libre.space/t/satnogs-lo-offset-greater-than-0-25-x-sample-rate/6886/11. [Accessed 30 03 2021].

[174] H. Chen and R. Gentile, "Phased array system simulation," in *Phased Array Systems and Technology (PAST), 2016 IEEE International Symposium on*, 2016.

[175] Mathworks, "CST Microwave Studio," [Online]. Available: https://www.mathworks.com/products/connections/product_detail/cst-microwave-

studio.html. [Accessed 27 01 2021].

[176] CST, "CST Studio Suite Help," Simulia, 2021.

[177] Anritsu, "Spectrum Master MS2724B," [Online]. Available: https://dl.cdn-anritsu.com/en-us/test-measurement/files/Brochures-Datasheets-Catalogs/datasheet/11410-00407R.pdf. [Accessed 15 06 2021].

[178] Tai-Saw Technology Co. ltd. , "TA1408A filter," [Online]. Available: https://www.rfmw.com/datasheets/taisaw/ta1408a%20_rev.1.0_.pdf. [Accessed 22 01 2021].

[179] Noelec Inc, "Lana Datasheet revision 1," [Online]. Available: https://www.nooelec.com/store/downloads/dl/file/id/92/product/315/lana_datasheet_revision_1.pdf. [Accessed 13 12 2020].

[180] Mini-Circuits, "ZX05-1L-S+ datasheet," [Online]. Available: https://www.minicircuits.com/pdfs/ZX05-1L-S+.pdf. [Accessed 01 03 2021].

[181] Elecdemo, "AD9959 module," [Online]. Available: https://www.aliexpress.com/item/33002306603.html. [Accessed 06 09 2020].

[182] Mini-Circuits, "ZB4CS-440-12W Data Sheet," [Online]. Available: https://www.minicircuits.com/pdfs/ZB4CS-440-12W.pdf. [Accessed 15 01 2021].

[183] RTL-SDR, [Online]. Available: https://www.rtl-sdr.com/wp-content/uploads/2018/02/RTL-SDR-Blog-V3-Datasheet.pdf. [Accessed 02 02 2021].

[184] airspy.com, "SDR Software download," [Online]. Available: https://airspy.com/download/. [Accessed 15 09 2019].

[185] QSL.net, "Coax Calculator," [Online]. Available: https://www.qsl.net/co8tw/Coax_Calculator.htm. [Accessed 06 07 2021].

[186] A. Ludwig, "The definition of cross polarization," *IEEE Transactions on Antennas and Propagation,* vol. 21, p. 116–119, 1973.

[187] Arrow Antennas, "Arrow II Satellite antenna," [Online]. Available: http://www.arrowantennas.com/inst/146437-10_All%20Suffixes_Instruction_Sheet.pdf. [Accessed 03 07 2020].

[188] DJI, "Matrice 600 Pro," [Online]. Available: https://www.dji.com/mt/matrice600-pro. [Accessed 15 06 2021].

[189] I. Farhat, D. Cutajar, K. Z. Adami and C. Sammut, "Field Trials for Ultrawideband Antenna," in *2018 2nd URSI Atlantic Radio Science Meeting (AT-RASC)*, 2018.

[190] J. S. Sumantyo, K. Ito and M. Takahashi, "Dual-band circularly polarized equilateral triangular-patch array antenna for mobile satellite communications," *IEEE Transactions on Antennas and Propagation,* vol. 53, p. 3477–3485, 2005.

[191] Libre Space Foundation, "Satnogs Network," [Online]. Available: https://network.satnogs.org/. [Accessed 15 01 2018].

[192] Libre Space Foundation, "Observations - Station 124," [Online]. Available: https://network.satnogs.org/observations/?norad=&observer=&station=124&start= &end=. [Accessed 30 05 2021].

[193] Salish Kootenai College, "BisonSat," [Online]. Available: https://cubesat.skc.edu/. [Accessed 05 01 2021].

[194] Libre Space Foundation, "Observation #3837959," [Online]. Available: https://network.satnogs.org/observations/3837959/. [Accessed 25 03 2021].

[195] Libre Space Foundation, "Observation #3838292," [Online]. Available: https://network.satnogs.org/observations/3838292/. [Accessed 25 03 21].

[196] Libre Space Foundation, "SatNOGS Network Station 6," [Online]. Available: https://network.satnogs.org/stations/6/. [Accessed 25 03 2021].

[197] A. Hérique, B. Agnus, E. Asphaug, A. Barucci, P. Beck, J. Bellerose, J. Biele, L. Bonal, P. Bousquet, L. Bruzzone and others, "Direct observations of asteroid interior and regolith structure: science measurement requirements," *Advances in Space Research,* vol. 62, p. 2141–2162, 2018.

[198] R. A. Meyers, Encyclopedia of physical science and technology, Academic, 2002.

[199] AMSAT, "Tools for Spacecraft and Communication Design," [Online]. Available: https://www.amsat.org/tools-for-calculating-spacecraft-communications-link-budgets-and-other-design-issues/. [Accessed 04 10 2017].

Appendix 1: GDPAA Library

Module gdpaa()

This module contains all the required functions in order to operate the UoMBSat Phased Array Antenna. It is designed to be used by the Ground Station daemon.

Functions

log (pfref, text)

Writes a record to the log file with the timestamp, planar face reference number and respective data.

Category	Utilities
Parameters	• **pfref** – Planar face reference number, values from 1 to 18. A PF reference of '0' is to be used when the log is not related to a PF. • **text** – The data that is to be written to the log file.
Returns	None

sin_ (angle)

Returns the sine value for an angle provided in degrees.

Category	Utilities
Parameters	• **angle** – Angle in degrees.
Returns	Sine value.

cos_ (angle)

Returns the cosine value for an angle provided in degrees.

Category	Utilities
Parameters	• **angle** – Angle in degrees.
Returns	Cosine value.

channel (port,value)

Sends a command to the AD9959 via a COTS STM32 interface to switch the channel. To be replaced with the instruction set to the Element Control Board once this is available.

Category	Hardware control
Parameters	• **port** – The serial port of the USB Uart connection to the STM32 microcontroller. • **value** – The DDS Channel reference number.
Returns	None

phase (port,value)

Sends a command to the AD9959 via a COTS STM32 interface to change the phase of the selected channel. To be replaced with the instruction set to the Element Control Board once this is available.

Category	Hardware control
Parameters	• **port** – The serial port of the STM32 UART interface over USB. • **value** – Phase in degrees.
Returns	None

amplitude (port,value)

Sends a command to the AD9959 via a COTS STM32 interface to change the amplitude of the selected channel. To be replaced with the instruction set to the Element Control Board once this is available.

Category	Hardware control
Parameters	• **port** – The serial port of the STM32 UART interface over USB. **value** – Amplitude as a percentage expressed as an integer (100 being 100% for maximum amplitude).
Returns	None

frequency (port,value)

Sends a command to the AD9959 via a COTS STM32 interface to change the frequency of the selected channel. To be replaced with the instruction set to the Element Control Board once this is available.

Category	Hardware control
Parameters	• **port** – The serial port of the STM32 UART interface over USB **frequency** – Frequency in hertz.
Returns	None

power (accuracy,freq)

Obtains a number of power readings for a selected portion of the band depending on a specified accuracy and returns the mean power of the readings.

Category	Hardware control
Parameters	• **accuracy** – Number of power readings required for accuracy purposes • **freq** – The frequency for which the power reading is to be returned
Returns	Power in dBm for frequency

point (phi,theta,freq)

Changes the phase of the four channels of one DDS based on a provided azimuth, elevation and frequency.

Category	Beamformer
Parameters	• **phi** – Azimuth angle in degrees, where zero degrees points North on the y-axis, with degrees increasing clockwise (x-axis being 90 degrees) • **theta** – Elevation angle in degrees, where 0 degrees is the endfire of the antenna (x-axis) with degrees increasing clockwise such that the z-axis (broadside) is 90 degrees • **freq** – The centre frequency of the signal of interest
Returns	None

set_satellite(norad_id)

Creates a PyEphem satellite object using TLEs obtained from a call to the N2YO satellite API.

Category	Tracker
Parameters	• **norad_id** – NORAD catalogue number of the satellite to be tracked
Returns	None

get_satvalues(freq)

Function to return the coordinates of the satellite primarily for pointing purposes in conjunction with the beamformer. A derived value of the doppler frequency correction is also returned together with a number of other useful parameters for displaying purposes on the mission control interface.

Category	Tracker
Parameters	• **freq** – The frequency of the satellite being tracked
Returns	An array with the following elements: [0] Azimuth angle in degrees [1] Elevation angle in degrees [2] Doppler frequency correction [3] Ground latitude (Visualization) [4] Ground longitude (Visualization) [5] Altitude (Visualization) [6] Range from ground station (Visualization) [7] Eclipsed state, True when satellite is in earth's shadow (Visualization)

scan(accuracy,freq)

Function to scan the field of view of the planar face and return the coordinates and power level. This function carries out a heuristic approach to scan the entire field of view of the planar face in the minimum time possible.

Category	Scanner
Parameters	• **accuracy** - Number of power readings required for accuracy purposes • **freq** – The frequency of the satellite being tracked
Returns	An array with the following elements: [0] Azimuth angle in degrees of highest power level [1] Elevation angle in degrees of highest power level [2] Power level in dBm

satnogs(freq)

Function to receive ROTCTL azimuth and elevation pointing instructions over a TCPIP connection from the Satnogs client. Such instructions are rerouted to the beamformer via the point() function.

Category	Other
Parameters	• **freq** – The frequency of the satellite being tracked
Returns	None

Appendix 2: Code

```python
# Module name:  gdpaa.py

# Version:      1.0

# Author:       Charles Grech (9H1Y)

#

# Description:      This module contains all the necessary functions in
order to use the UOMBSAT Ground Station PAA.

#


# Import required modules
from pylab import *

from rtlsdr import RtlSdr

import matplotlib.pyplot as plt

import matplotlib

import numpy as np

import math

import time

from datetime import datetime

import serial

import ephem

from ephem import degree

import requests

import sys

import socket


# Set ground station location and API key
api_key = "REDACTED KEY FOR DOCUMENTATION" # N2YO.com API KEY

observer = ephem.Observer()

observer.lat = '35.896' # 9H1Y Radio Shack on locator JM75FV

observer.lon = '14.475' # 9H1Y Radio Shack on locator JM75FV

observer.elevation = 35 # 9H1Y Radio Shack on locator JM75FV


# RTL-SDR PARAMETERS
# This section is temporary as this module also covers the direct control of
the SDR.
sdr = RtlSdr()

sdr.freq_correction = 3 # PPM correction of RTL-SDR in use

center_offset = 50e3

sample_rate = 2.04e6

sdr.sample_rate = sample_rate

sdr.gain =  19.7

num_samples =  16*1024

nfft = 1*1024

sp1 = serial.Serial(port = "/dev/ttyACM0", baudrate=9600, bytesize=8,
```

```python
                    timeout=10, stopbits=serial.STOPBITS_ONE)


# DDS general settings

# At this stage these are set directly as a result of direct interface to
the AD9959

dds_freq = 5.0e6

amp = 100


# [TO IMPLEMENT] The resource manager needs a function to tell the array to
track. As a minimum the following params need to be sent:

# - The object to track (NORAD ID)

# - whether the object is to be tracked automatically or whether a TLE is to
be forced which is not yet available in the databases,

#   in which case an array object needs to be passed with the TLEs

# - whether doppler frequency correction is required or not


# ASSET CONFIGURATION AND INITIALIZATION

# The intial asset consists of one planar face whose broadside is the

# z-axis.


# ********** UTILITIES FUNCTIONS **********


# Function to write to logfile (Syntax: PF reference number, details)

def log(pfref,text):
        filename = "gdpaa_log2.txt"

        with open(filename, 'a') as file_object:
file_object.write(datetime.now().strftime("%d-%m-%Y %H:%M:%S") + " PF-" +
str(pfref) + " " + text + "\n")


# Function to return sin of angle in degrees

def sin_(angle):
        return math.sin(math.radians(angle))


# Function to return cosine of angle in degrees

def cos_(angle):
        return math.cos(math.radians(angle))


# ********** HARDWARE CONTROL FUNCTIONS **********


# Function to change channel on AD9959 via STM32 Microcontroller board

def channel(port,value):
        port.write(bytes(("AT+CHANNEL+" + str(value) + "\r\n"),'utf-8'))
```

```python
# Function to change phase on AD9959 via STM32 Microcontroller board
def phase(port,value): # in degrees
        value = round(value/360*16383)
        s = "AT+PHA+" + str(value) + "\r\n"
        port.write(bytes(s,'utf-8'))


# Function to change amplitude on AD9959 via STM32 Microcontroller board
def amplitude(port,value): # in %
        value = round(value/100*1023)
        s = "AT+AMP+" + str(value) + "\r\n"
        port.write(bytes(s,'utf-8'))


# Function to change frequency on AD9959 via STM32 Microcontroller board
def frequency(port,value): #in Hz
        s = "AT+FRE+" + str(value) + "\r\n"
        port.write(bytes(s,'utf-8'))


# Function to return the power level from the RTL-SDR
def power(accuracy,freq):


        sdr.center_freq = freq - center_offset - dds_freq
        power_readings = []
        x=1
        while x <= accuracy:
                samples = sdr.read_samples(num_samples)
                #Find the position within the array of the frequency of
interest taking into consideration the offset
                array_pos =
round((((sample_rate/2)+center_offset)/sample_rate)*num_samples)
                power, psd_freq = psd(samples, NFFT=nfft,
Fs=sdr.sample_rate/1e6, Fc=sdr.center_freq/1e6)
                array_pos =
round((((sample_rate/2)+center_offset)/sample_rate)*nfft)
                power_readings.append(power[array_pos])
                x=x+1
        power_dBm = 10*np.log(10*np.mean(power_readings))
        return (power_dBm)


# Function to initialize AD9959 DDS via STM32 Microcontroller board and set
initial channel settings
def start():
        try:


                # PLACEHOLDER SECTION
                # Calibration settings for measured clock distribution
```

```python
            variances to DDS channels


            # CONFIGURE PF 1

            pfref = 1

            sp1_string = "" # Used to hold data coming over UART

            # Get Board Version

            sp1.write(b"AT+VERSION\r\n")

            sp1_string = sp1.readline()

            log(pfref,"STM32 AD9959 Board Version: " +
str.strip(str(sp1_string.decode('Ascii'))))

            print(sp1_string)

            # Crystal Reference Frequency

            sp1.write(b"AT+REF+25000000\r\n")

            sp1_string = sp1.readline()

            log(pfref,"Setting Crystal Reference Frequency..." +
str.strip(sp1_string.decode('Ascii')))

            # Set Multiplier

            sp1.write(b"AT+MULT+20\r\n")

            sp1_string = sp1.readline()

            log(pfref,"Setting Multiplier... " +
str.strip(sp1_string.decode('Ascii')))

            # Set the module to work in dot frequency

            sp1.write(b"AT+MODE+POINT\r\n")

            sp1_string = sp1.readline()

            log(pfref,"Setting Dot Frequency Mode..." +
str.strip(sp1_string.decode('Ascii')))

            # Set initial channel settings

            channel(sp1,1); amplitude(sp1,amp); phase(sp1,0);
frequency(sp1,dds_freq)

            channel(sp1,2); amplitude(sp1,amp); phase(sp1,0);
frequency(sp1,dds_freq)

            channel(sp1,3); amplitude(sp1,amp); phase(sp1,0);
frequency(sp1,dds_freq)

            channel(sp1,4); amplitude(sp1,amp); phase(sp1,0);
frequency(sp1,dds_freq)

            log(pfref,"LO (AD9959) channels set to " + str(dds_freq) +
"Hz")

            log(pfref,"Amplitude on all channels set to " + str(amp) +
"%")

            log(pfref,"Phase on all channels set to 0 degrees")

            return (0,"")


    except Exception as err:

            print(type(err))

            print(err.args)

            print(err)

            return (1, err) # At present, only 1 is returned as error
code. Future work: List of error codes.
```

176

```python
# Beamformer implementation

# At this stage the resources of the GDPAA consist of 1 Planar Face.

# PHI=0 is the Y-Axis of the antenna, PHI=90 is the X-Axis of the antenna,
turning clockwise.

# THETA=90 at broadside and THETA=0 at end-fire.


def point(az, el, freq):

    sdr.center_freq = freq - center_offset - dds_freq

    # Element spacing - for the time being assumed perfect between all
elements

    # will need to cater for manufacturing errors in the future

    dx = 446.4263 # variable es in CST workings

    lmbd = 299792458/freq*1000   # in mmm

    # At this stage since there is 1 PF the phases are calculated in
terms of their reference to the centre element.

    # FUTURE WORK: Change coordinates to centre of icosahedron as centre
of coordinate system

    #

    # calculate phases 1(N), 2(SW), 3(C), 4(SE) in relation to the centre
element 3,*360/lmbd converts distance to phase

    p1 =
math.cos(math.radians(el))*dx*math.cos(math.radians(az+180))*360/lmbd

    p2 =
math.cos(math.radians(el))*dx*math.sin(math.radians(az+30))*360/lmbd

    p3 = 0

    p4 = math.cos(math.radians(el))*dx*math.sin(math.radians(30-
az))*360/lmbd


    # Normalization of phase shift with respect to the element closest to
the antenna N

    phases = [p1,p2,p3,p4]

    p1 = p1-min(phases)

    p2 = p2-min(phases)

    p3 = p3-min(phases)

    p4 = p4-min(phases)

    print(p1,p2,p3,p4)


    # set phases

    channel(sp1,1); phase(sp1,p1);

    channel(sp1,2); phase(sp1,p2);

    channel(sp1,3); phase(sp1,p3);

    channel(sp1,4); phase(sp1,p4);


    return()


# Function to create a satellite object using TLEs
```

```python
def set_satellite(norad_id):
    url = "https://api.n2yo.com/rest/v1/satellite/tle/" + str(norad_id) +
"&apiKey=" + api_key
    req = requests.get(url)
    if req.status_code == requests.codes.ok:
        resp = req.json()
        tle_name = resp['info']['satname']
        tle = resp['tle'].splitlines()
        tle_line1 = tle[0]
        tle_line2 = tle[1]
    else:

        print("Error with code".format(req.status_code))


    global satellite
    satellite = ephem.readtle(tle_name, tle_line1, tle_line2)
    log(0,"NORAD ID: " + str(norad_id))


# Function to return coordinates of satellite to be tracked, together with
other paramaters for visualization of mission control interface
def get_coords(freq):
    now = datetime.utcnow()
    observer.date =now
    satellite.compute(observer)
    print(satellite.range)
    print(satellite.range_velocity)
    doppler_fc = freq * satellite.range_velocity / 299792458
    return
(satellite.az,satellite.alt,doppler_fc,satellite.sublat,satellite.sublong,sa
tellite.elevation,satellite.range,satellite.eclipsed)


# Function to estimate DOA
def scan(accuracy,freq):


    # Look angle is 41 degrees in elevation


    header = "Phi, Theta, Frequency, Accuracy, dB Value"
    log(0,header)


    # Timer to measure total scan time
    start = time.time()


    # ITERATION 1
    power_ = []; az_ = []; el_ = []
    el = 55
    while (el<90):
```

```python
        az = 15
        while (az<360):
                point(az,el,freq)
                pow = power(accuracy,freq)
                power_.append(pow)
                az_.append(az)
                el_.append(el)
                log(1,"," + str(az) + "," + str(el) + "," + str(freq) +
"," + str(accuracy) + "," + str(pow))
                az = az + 30
        el = el + 10


max_power = np.amax(power_)
max_pos = power_.index(max_power)
print("Max power is " + str(power_[max_pos]) + "dBm at AZ:" +
str(az_[max_pos]) + " EL:" + str(el_[max_pos]))


# ITERATION 2
a = 1
az = az_[max_pos]-12.5
el_stored = el_[max_pos]-2.5
power_ = []; az_ = [];    el_ = []
while (a<=6):
        e = 1
        el = el_stored
        while (e<=2):
                point(az,el,freq)
                pow = power(accuracy,freq)
                power_.append(pow)
                az_.append(az)
                el_.append(el)
                log(1,"," + str(az) + "," + str(el) + "," + str(freq) +
"," + str(accuracy) + "," + str(pow))
                el = el + 5
                e = e + 1
        az = az + 5
        a = a + 1


max_power = np.amax(power_)
max_pos = power_.index(max_power)
print("Max power is " + str(power_[max_pos]) + "dBm at AZ:" +
str(az_[max_pos]) + " EL:" + str(el_[max_pos]))


# ITERATION 3
a = 1
```

```python
        az = az_[max_pos]-2.5
        el_stored = el_[max_pos]-2.5
        power_ = []; az_ = [];    el_ = []
        while (a<=6):
            e = 1
            el = el_stored
            while (e<=6):
                point(az,el,freq)
                pow = power(accuracy,freq)
                power_.append(pow)
                az_.append(az)
                el_.append(el)
                log(1,"," + str(az) + "," + str(el) + "," + str(freq) +
",", + str(accuracy) + "," + str(pow))
                el = el + 1
                e = e + 1
            az = az + 1
            a = a + 1


        max_power = np.amax(power_)
        max_pos = power_.index(max_power)
        end = time.time()
        result = "Scanned in "+ str(np.round(end-start,2)) + "s. Strongest
signal of " + str(max_power) + "dB at AZ:" + str(az_[max_pos]) + " EL:" +
str(el_[max_pos])
        print(result)
        log(1,result)
        return(az_[max_pos],el_[max_pos],power_[max_pos])


# Function to serve as a bridge for Satnogs Client
def satnogs(freq):
        # Create and bind TCP/IP socket
        sock = socket.socket(socket.AF_INET, socket.SOCK_STREAM)
        server_address = ('localhost', 10000)
        print(sys.stderr, 'starting up on %s port %s' % server_address)
        sock.bind(server_address)
        # Listen for incoming connections
        sock.listen(1)


        while True:
            # Wait for comman
            connection, client_address = sock.accept()
            try:
                print("Request from  ", client_address)
                # Set default azimuth and elevation angles
```

180

```python
                      az = 0.0
                      el = 90.0
                      buffer = ""
                      while True:
                              data = connection.recv(1)
                              if data:
                                      d = data.decode('utf-8')
                                      if d == "\n":
                                              if d == "\dumpstate":
                                                      print("Dump detected")

        connection.sendall(bytes("9H1Y ASTREA BEAMFORMER V1.0\n",'utf-8'))
                                              else:
                                                      if buffer == "p":
                                                              position =
bytes(str(az) + " " + str(el) + "\n",'utf-8')

        connection.sendall(position)

                                                              print("p detected")
                                                      else:
                                                              if buffer[0] == "P":

        sp2=buffer.find(' ',2)

                                                                      az =
buffer[2:(sp2-1)]

                                                                      el =
buffer[sp2+1:]

                                                                      print("P
detected with AZ:",az," EL:",el)

                                                                      # CALL TO
BEAMFORMER

        point(az,el,freq)

                                                      else:
                                                              print("Other
data detected: ",buffer)
                                              buffer = ""
                                      else:
                                              buffer = buffer + d
                              else:
                                      break
              finally:
                      # Clean up the connection
                      connection.close()
```

```python
# daemon.py

# This python script is used for testing. It also serves as a demonstration
for the GS Daemon as to

# how to interact with the GDPAA module and its different methods.


####
import time
import gdpaa


# Initiate the AD9959 and the SDR
freq = 436500000
start = gdpaa.start()
if (start[0] != 0): # exit if error, or take alternative action if required
        print (start[1])
        sys.exit()


# Simple command to point to a specific location
 el = 50
 az = 0
 while az < 360:
        while el<90:
                gdpaa.point(az,el,freq)
                p = gdpaa.power(3,freq)
                print("az: " + str(az) + "el: " + str(el) + " " + str(p))
                el = el + 1
        el = 50
        az = az + 10


# Sample flow code to track and point to a satellite
 gdpaa.set_satellite(39090)
x = 1
while x<10:
        t = gdpaa.get_coords(freq)
        az = t[0]
        el = t[1]
        doppler = t[2]
        if el<0:
        #Location of PF - pointing AZ 107 and EL 56
                print("Satellite below horizon:  ",el)
        else:
                print("Satellite in view:        ",el)
                # POINT TO TARGET
                # The t array has the azimuth and elevation of the satellite
which must be translated to the reference point of the PF.
                gdpaa.point(az,el,freq+doppler)
```

```python
        time.sleep(1)
        x = x+10


#gdpaa.scan(3,436500000)
gdpaa.point(0,80,436500000)


#gdpaa.satnogs(436500000)
```

Appendix 3: MATLAB Case 03615672

MathWorks®

Support

My Service Requests

<< View All Service Requests

Details

Case Number	03615672
Subject	Antenna Toolbox inconsistent reults

Description	I am running the following script:

```
clear all;
L = 0.1548;
W = L;
a = 0.0027;
h = 0.00156;
groundplane_length = 0.1997;
groundplane_width = groundplane_length;
patch = antenna.Rectangle('Length',L,'Width',W );
patch.Center = [ 0 0 ];
toprightcorner = antenna.Polygon('Vertices',[(L/2)-a,(W/2),0; (L/2),(W/2),0; (L/2),(W/2)-a,0]);
bottomleftcorner = antenna.Polygon('Vertices',[(-L/2)+a,(-W/2),0; (-L/2),(-W/2),0; (-L/2),(-W/2)+a,0]);
patch = patch - toprightcorner - bottomleftcorner;
board = antenna.Rectangle('Length',groundplane_length,'Width',groundplane_width);
groundplane = board;
pcbantenna = pcbStack;
pcbantenna.BoardThickness = h;
pcbantenna.BoardShape = board;
pcbantenna.Layers = {patch,dielectric('FR4'),groundplane};
pcbantenna.FeedLocations = [-(L/2) 0 1 3];
sobj = sparameters(pcbantenna,400e6:254939:600e6,50);
rfplot(sobj);
```

If I run this script the result in Image1.png is obtained. If I change the upper limit of the RF plot from 600e6 to 700e6 and rerun I obtain the image in Image2png

```
sobj = sparameters(pcbantenna,400e6:254939:700e6,50);
```

As may be seen the results are not the same. The magnitude of the trough in the 600Mhz plot is circa -10dB, in the 700Mhz plot it is -20dB, the frequency of the trough is not the same. Additionally, in the 600Mhz plot a significant trough was detected at circa 590Mhz which was not detected in the 700Mhz plot.

Status	Resolved	Product	Antenna Toolbox
Date/Time Opened	15 May 2019 11:41 AM GMT	Product Release	R2019a
Date/Time Closed	16 May 2019 6:06 PM GMT	Product Version	4.0
License Number		Platform	Windows x64
⑦ View My Licenses		Operating System	Windows 10

Communication History   Add Comment

Subject	Type	Message Date
Re: Antenna Toolbox inconsistent reults [ref:_00Di0Ha1u._5000Z1CwRmW:ref]	Email	16 May 2019 5:46 PM

Suggested Answers

Title

Attachments   Attach File

File Name	Uploaded Date
image2.png	15 May 2019 11:41 AM GMT
image1.png	15 May 2019 11:41 AM GMT
output_of_ver.txt	15 May 2019 11:41 AM GMT

Create New Service Request

Email Details

Message Date	5/16/2019 6:01 PM
From	support@mathworks.com
To	charles@grech.space
CC	

Subject	Re: Antenna Toolbox inconsistent reults [ref:_00Di0Ha1u._5000Z1CwRmW:ref]

Body	Hello Charles,

I am writing in reference to your Technical Support Case #03615672 regarding 'Antenna Toolbox inconsistent reults'.

I understand that you are getting inconsistent results when trying RFPLOT the same antenna with different frequency vectors.

The reason for the inconsistency is because when the "sparameters" function is called, there is some amount of auto-meshing that occurs on the antenna object. The meshing maximum edge length is dependent on the maximum frequency of the frequency vector input to the function.

This causes the difference that we are observing when viewing the response of the S-Parameters of the transmission line.

As the meshing is automatically done, we cannot control it and may see unexpected or undesired results.

I suggest manually defining the meshing like you had originally been doing for this particular example.

Set the maximum edge length to 0.2, and the growth rate to 0.3.

You can do that by the following command:

mesh(pcbantenna,'MaxEdgeLength',0.2,'GrowthRate',0.3);
I have modified your code with the above line and the results are nearly identical, with differing amounts of frequencies displayed. I am attaching the script to this email.

Please feel free to reach out to me if you have additional questions.

Sincerely,
Sanjay Arikatla
MathWorks Technical Support

Please preserve the Reference ID in further correspondence on this query. This allows our systems to automatically associate your reply to the appropriate Case.

If you have a new technical support question, please submit a new request here:
http://www.mathworks.com/support/servicerequests/create.html

Self-Service: https://www.mathworks.com/support/contact_us.html
File Exchange and MATLAB Answers: http://www.mathworks.com/matlabcentral/

ref:_00Di0Ha1u._5000Z1CwRmW:ref

Appendix 4: Elecdemo AD9959 module schematic and command set
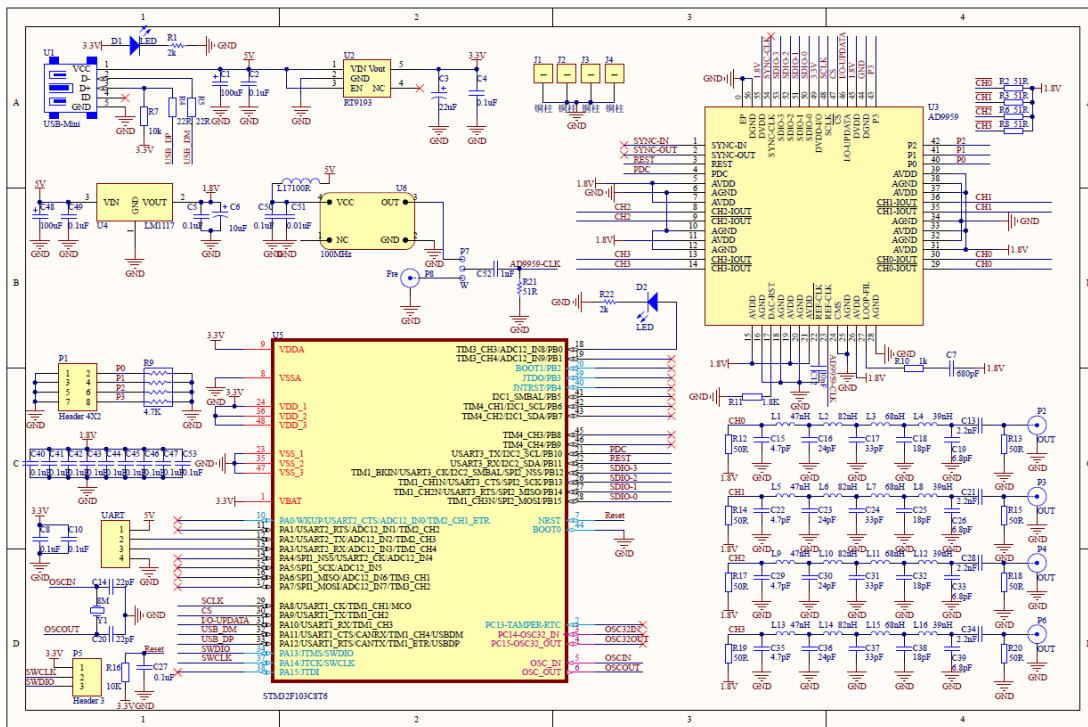
Instruction	Description	Parameter Range	Unit	Response	
AT\r\n	Test Instruction	No	No	OK	
AT+RESET\r\n	Reset	无	无	OK	
AT+VERSION\r\n	Version read	无	无	+VERSION=1.0-20180103	
AT+CHANNEL<+PRA>\r\n	Channel Cotrol	1/2/3/4	无	+CHANNEL=当前工作模式	
AT+REF<+PRA>\r\n	Reference crystal frequency setting	10-125	MHz	+REF=当前晶振参考频率	
AT+MULT<+PRA>\r\n	Multiplier setting	1~20	倍	+MULT=当前时钟倍频数	
AT+MODE<+PRA>\r\n	Operating mode	POINT/SWEEP/FSK2/FSK4/AM	无	+MODE=当前工作模式	
AT+FRE<+PRA>\r\n	Dot Fr	1-200,000,000	Hz	+FRE=当前输出频率	Command to enter the dot frequency mode
AT+AMP<+PRA>\r\n	Dot frequency amplitude	0-1023	无	+AMP=当前输出幅度	
AT+PHA<+PRA>\r\n	Point frequency phase	0-16383 (corresponding to 0-	无	+PHA=当前输出相位	
AT+STARTFRE<+PRA>\r\n	扫频开始频率	1-ENDFRE	Hz	+STARTFRE=当前扫频开始频率	
AT+ENDFRE<+PRA>\r\n	扫频结束频率	STARTFRE-200,000,000	Hz	+ENDFRE=当前扫频结束频率	
AT+STARTAMP<+PRA>\r\n	扫频开始幅度	0-1023	无	+STARTAMP=当前扫频开始幅度	Command to enter the sweep mode
AT+ENDAMP<+PRA>\r\n	扫频结束幅度	0-1023	无	+ENDAMP=当前扫频结束幅度	
AT+TIME<+PRA>\r\n	扫频间隔时间	0-9999	ms	+TMIE=当前扫频间隔时间	
AT+STEP<+PRA>\r\n	扫频间隔频率	1-200,000,000	Hz	+STEP=当前扫频间隔频率	
AT+SWEEP<+PRA>\r\n	扫频开关	ON/OFF	无	+SWEEP=当前扫频状态	
AT+FRE1<+PRA>\r\n	2FSK模式频率1	1-200,000,000	Hz	+FRE1=当前设置频率	2FSK模式指令（所有通道都可设置为2FSK
AT+FRE2<+PRA>\r\n	2FSK模式频率2	1-200,000,000	Hz	+FRE2=当前设置频率	
AT+FRE1<+PRA>\r\n	4FSK模式频率1	1-200,000,000	Hz	+FRE1=当前设置频率	4FSK指令（通道一与通道二可设置为4FSK）
AT+FRE2<+PRA>\r\n	4FSK模式频率2	1-200,000,000	Hz	+FRE2=当前设置频率	
AT+FRE3<+PRA>\r\n	4FSK模式频率3	1-200,000,000	Hz	+FRE3=当前设置频率	
AT+FRE4<+PRA>\r\n	4FSK模式频率4	1-200,000,000	Hz	+FRE4=当前设置频率	
AT+FRE<+PRA>\r\n	AM频率	1-200,000,000	Hz	+FRE=AM输出频率	AM模式指令
AT+DEP<+PRA>\r\n	AM debugging depth	0-100	%	+DEP=当前调制深度	
AT+RATE<+PRA>\r\n	AM modulation rate	20-600	Hz	+RATE=AM调制速率	
AT+AM<+PRA>\r\n	AM switch	ON/OFF	无	+AM=当前AM状态	

Features	Send	Return	备注
Comms test	AT\r\n	OK	
Read Version	AT+VERSION\r\n	+VERSION=1.0-20180103	
Set the module to work in dot frequency mode	AT+MODE+POINT\r\n	OK	These three commands can set the output
Set the current channel to channel one	AT+CHANNEL+1\r\n	OK	
set frequence value	AT+FRE+20\r\n	+FRE=当前频率值	
设置当前通道为通道二	AT+CHANNEL+2\r\n	OK	
设置频率值	AT+FRE+30\r\n	+FRE=当前频率值	